

Studies of Floating Strip Micromegas Detectors  
in Proton and Carbon Ion Beams  
with a Fast Gas Mixture

Studien zu Floating Strip Micromegas Detektoren  
unter Bestrahlung mit Protonen und Kohlenstoff-  
Ionen mit einer Schnellen Gasmischung



Masterarbeit an der Fakultät für Physik  
der  
Ludwig-Maximilians-Universität München

vorgelegt von  
**Felix Klitzner**  
geboren in Gräfelfing

München, den 16.03.2016



Gutachter: Prof. Dr. Otmar Biebel



## Abstract

In this thesis, novel floating strip Micromegas detectors are studied in detail in proton and carbon beams. A Ne:CF<sub>4</sub> based gas mixture has been used as detector gas for all measurements to further increase the already excellent high-rate capabilities of this detector. This increases both the electron drift velocity and the ion mobility in the amplification region by a factor of three compared to typical Ar:CO<sub>2</sub> based detector gases.

Hit efficiencies above 98% are observed for optimized field configurations during measurements with 23 MeV protons at the tandem accelerator in Garching. Single plane angular resolutions of  $\left(\begin{smallmatrix} +3 \\ -2 \end{smallmatrix}\right)^\circ$  are determined using the  $\mu$ TPC method for tracklet reconstruction.  $\mu$ TPC based alternative hit positions improve the spatial resolution for inclined particle tracks above 10° at drift fields below 500 V/cm.

Measurements have been carried out at the Heidelberg Ion Therapy center with high-rate carbon beams with energies between 88 MeV/u and 430 MeV/u. The Micromegas detectors have been operated without drift voltage applied. An optimum hit efficiency of  $(97.5 \pm 0.1)\%$  has been determined. A single layer time resolution of  $(8.53 \pm 0.07)$  ns is observed. As no drift voltage was applied, optimum values for the spatial resolution better than 220  $\mu$ m are determined independent of the track inclination for all investigated angles up to 35°. Radiographies of a PMMA step phantom and a slab phantom with four tissue equivalent layers have been successfully acquired with a floating strip Micromegas tracking system and a scintillator layer based particle range telescope.

Floating strip Micromegas with two-dimensional strip readout structure were characterized at the tandem accelerator with 20 MeV protons. The pulse height of the bottom, perpendicular readout strip layer is estimated to be smaller than 11.4% of the parallel strip readout layer. Nevertheless, an optimum angular resolution of  $\left(\begin{smallmatrix} +1.6 \\ -1.2 \end{smallmatrix}\right)^\circ$  is observed for both readout layers. The resolution is better than  $\left(\begin{smallmatrix} +4 \\ -3 \end{smallmatrix}\right)^\circ$  for both layers for drift fields up to 1.33 kV/cm with corresponding electron drift velocities up to 0.109 mm/ns.



## Kurzfassung

In dieser Arbeit werden neuartige floating strip Micromegas Detektoren detailliert unter Bestrahlung mit Protonen und Kohlenstoff-Ionen studiert. Eine Ne:CF<sub>4</sub> basierte Gasmischung wurde als Detektorgas für alle Messungen verwendet um die exzellente Hochratenfähigkeit dieses Detektors weiter zu verbessern. Dabei ist die Elektronen Driftgeschwindigkeit und die Ionenmobilität bis zu drei mal größer als bei herkömmlich verwendeten Driftgasen auf Ar:CO<sub>2</sub> Basis.

Bei Messungen mit 23 MeV Protonen am Tandem Beschleuniger in Garching wurden für optimierte Drift- und Verstärkungsfelder Treffer-Effizienzen von über 98 % bestimmt. Eine  $\mu$ TPC-basierte Winkelrekonstruktion erlaubte die Spursteigung der Teilchen mit einer Auflösung von  $\left(\begin{smallmatrix} +3 \\ -2 \end{smallmatrix}\right)^\circ$  zu rekonstruieren. Eine alternative  $\mu$ TPC-basierte Methode die Position des Teilchendurchgangs zu bestimmen, zeigte, dass sich die Ortsauflösung für Spursteigungen über 10° und Driftfelder kleiner als 500 V/cm damit verbessern lässt.

Am Heidelberger Ionenstrahl Therapie Zentrum wurden Messungen mit Kohlenstoff-Ionen von 88 MeV/u bis 430 MeV/u Strahlenergie durchgeführt. An die Micromegas Detektoren wurde dabei keine Driftspannung angelegt. Optimale Treffer-Effizienzen von  $(97.5 \pm 0.1) \%$  und eine intrinsische Zeitauflösung von  $(8.53 \pm 0.07)$  ns wurden bestimmt. Da keine Driftspannung anlag, konnte eine Ortsauflösung unter 220  $\mu$ m für alle untersuchten Teilchenspurwinkel bis zu 35° erreicht werden. Radiographien eines PMMA Stufenphantoms, sowie eines Phantoms mit vier gewebeähnlichen Lagen wurden erfolgreich mit einem floating strip Micromegas Spursystem und einem Szintillatorlagen basierten Teilchen Reichweiten-Teleskop aufgenommen.

Zwei-dimensionale floating strip Micromegas wurden am Tandem Beschleuniger mit 20 MeV Protonen vermessen. Dabei wurde festgestellt, dass die Pulshöhe der tiefer gelegenen, senkrecht orientierten Streifenlage weniger als 11.4 % der Pulshöhe der parallelen Streifenlage beträgt. Nichtsdestotrotz konnte eine optimale Winkelauflösung von  $\left(\begin{smallmatrix} +1.6 \\ -1.2 \end{smallmatrix}\right)^\circ$  für beide Streifenlagen rekonstruiert werden. Die Auflösung ist besser als  $\left(\begin{smallmatrix} +4 \\ -3 \end{smallmatrix}\right)^\circ$  für alle Driftfelder bis zu 1.33 kV/cm, was einer Elektronen Driftgeschwindigkeit bis zu 0.109 mm/ns entspricht.



# Contents

<b>1</b>	<b>Introduction and Motivation</b>	<b>1</b>
1.1	Micromegas Detectors . . . . .	1
1.2	Floating Strip Micromegas in Medical Application: Ion Transmission Tomography . . . . .	2
<b>2</b>	<b>Theoretical Background</b>	<b>4</b>
2.1	Particle Interaction with Matter . . . . .	4
2.1.1	Charged Particles . . . . .	4
2.1.2	Photons . . . . .	6
2.2	Charge Carrier Drift and Amplification in Gaseous Detectors . . . . .	7
2.3	Multiple Scattering of Charged Particles . . . . .	9
<b>3</b>	<b>The Floating Strip Micromegas Detector</b>	<b>10</b>
3.1	Internal Structure . . . . .	10
3.2	Signal Formation . . . . .	11
3.3	Mesh Transparency and Detection Efficiency . . . . .	13
3.4	Discharges . . . . .	14
3.5	Two-Dimensional Floating Strip Readout Anode . . . . .	14
3.6	High-density APV25 front-end electronics . . . . .	16
<b>4</b>	<b>Signal Analysis - Methods</b>	<b>18</b>
4.1	Signal Reconstruction: Pulse Height and Timing . . . . .	18
4.2	$\mu$ TPC Method . . . . .	19
4.2.1	Selection of Data Points and Weighting . . . . .	20
4.2.2	Angle Reconstruction . . . . .	21
4.3	Determination of Drift Velocity . . . . .	22
4.3.1	Inverting the $\mu$ TPC Method . . . . .	22
4.3.2	Signal Timing Distribution . . . . .	22

4.4	Determination of Hit Position . . . . .	24
4.4.1	Centroid Method . . . . .	24
4.4.2	$\mu$ TPC Method . . . . .	25
4.5	Track Fitting . . . . .	27
4.5.1	Track Reconstruction via Analytic $\chi^2$ -Minimization . . . . .	27
4.5.2	Combinatorial Kalman Filter Based Track Reconstruction . . . . .	27
4.6	Detector Alignment . . . . .	27
4.6.1	High Precision Coordinate $\mathbf{x}$ and $\mathbf{y}$ . . . . .	29
4.6.2	Distance $\mathbf{z}$ Between Detector Layers . . . . .	29
4.6.3	Relative Rotations Around $\mathbf{y}$ -Axis and $\mathbf{z}$ -Axis . . . . .	29
4.7	Determination of Spatial Resolution . . . . .	30
4.7.1	Residual Distribution for Two Layers . . . . .	30
4.7.2	Track-Based Geometric Mean Method . . . . .	31
4.7.3	Track Interpolation Method . . . . .	31
<b>5</b>	<b>Investigation of a Ne:CF<sub>4</sub> 80:20 vol.% Gas Mixture at the Tandem Accelerator</b> . . . . .	<b>33</b>
5.1	Testbeam Setup . . . . .	33
5.2	Pulse Height Behavior . . . . .	34
5.3	Efficiency . . . . .	38
5.4	Drift Velocity . . . . .	40
5.5	Track Angle Reconstruction and Angular Resolution . . . . .	43
5.6	Spatial Resolution . . . . .	47
5.7	2D-Imaging . . . . .	50
5.8	Summary . . . . .	56
<b>6</b>	<b>High-Rate Tracking and Imaging at the Heidelberg Ion Therapy Center with Carbon Beams</b> . . . . .	<b>57</b>
6.1	Setup . . . . .	57
6.2	Pulse Height Behavior and Hit Efficiency . . . . .	59
6.3	Signal Timing . . . . .	65
6.4	Track Reconstruction and Spatial Resolution . . . . .	69
6.5	Ion Transmission Radiography . . . . .	82
6.5.1	Radiography: Step Phantom . . . . .	84
6.5.2	Radiography: Slab Phantom . . . . .	87
6.6	Summary . . . . .	92

---

<b>7</b>	<b>Characterization of a Two-Dimensional Floating Strip Micromegas at the Tandem Accelerator</b>	<b>94</b>
7.1	Setup . . . . .	94
7.2	Signal Characteristics . . . . .	95
7.3	3D Track Reconstruction in a Single Layer . . . . .	101
7.4	Conclusions . . . . .	106
<b>8</b>	<b>Summary and Outlook</b>	<b>108</b>
	<b>Bibliography</b>	<b>110</b>
<b>A</b>	<b>Tracking Methods</b>	<b>113</b>
A.1	$\chi^2$ -Minimization . . . . .	113
A.2	Kalman Filter Based Track Reconstruction . . . . .	114



# Chapter 1

## Introduction and Motivation

In this thesis, the performance and behavior of floating strip Micromegas<sup>1</sup> detectors is investigated. Measurements with a new, considerably faster detector gas mixture under irradiation with proton and carbon beams are presented. A recently developed, two-dimensional readout anode is tested for the first time and the performance is discussed.

The research on floating strip Micromegas detectors for medical imaging applications is motivated and radiographies of phantoms, acquired with a floating strip Micromegas tracking system, are presented.

In the following, Micromegas detectors are introduced as a suitable upgrade for detectors at particle accelerators like the LHC<sup>2</sup>, where good spatial resolution under continuous high rate background irradiation is required.

### 1.1 Micromegas Detectors

Micromegas detectors are radiation detectors, used for applications in the high energy physics where particle tracks have to be determined precisely. Detectors at modern particle accelerators like the LHC encounter continuously rising collision rates (RunII<sup>3</sup>) due to larger bunch filling and better beam transport and focusing. Due to the correspondingly increasing particle and background hit rates, new gaseous detectors with superior position and time resolution than the currently used wire chambers are required. Micromegas are high-rate capable, high resolution micro-mesh gaseous detectors, based on parallel plate avalanche chambers proposed by Giomataris et al. [1996].

A typical Micromegas detector consists of a 6 mm wide drift region between the cathode and the conductive micro-mesh with an electric field with 0.8 kV/cm and an approximately 0.1 mm wide amplification region between the mesh and the anode with an electric field on the order of 39 kV/cm. The anode readout structure consists of strips, see Fig.1.1.

The traversing particle produces electron/ion pairs which then will not recombine but will drift towards their corresponding electrodes. For an electron, created near the

---

<sup>1</sup>Micro mesh gaseous detector

<sup>2</sup>Large Hadron Collider

<sup>3</sup>Increase of center of mass energy and collision rate from 8 TeV and 20 MHz in 2012 to 13 TeV and 40 MHz in 2015.

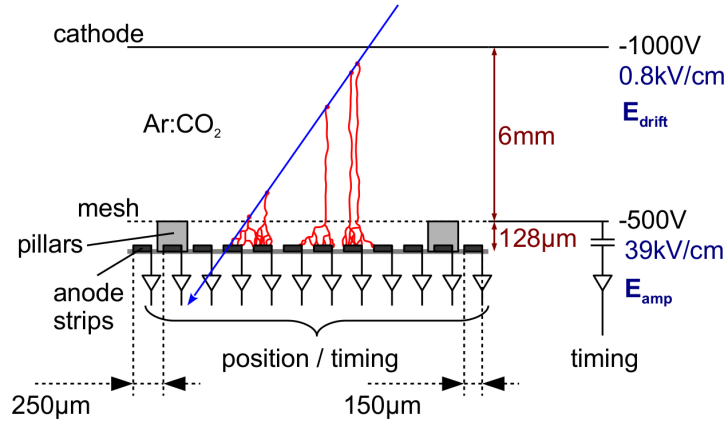


Figure 1.1: Cut through a standard Micromegas: The blue line represents the trajectory of the ionizing particle, creating electron/ion pairs in the active area filled with a typically used detector gas Ar:CO<sub>2</sub>. The electrons (red line) drift towards the micro-mesh and trigger the charge avalanche in the amplification region. Picture taken from [J.Bortfeldt, 2014].

cathode, the maximum drift time to the mesh will be about 100 ns. As soon as it passes the micro-mesh, it will be accelerated albeit with a much higher electric field. The electron therefore gains enough energy to create ion/electron pairs via impact ionization. Pairs created this way will also ionize the gas, again creating electron/ion pairs that will trigger the so called Townsend avalanche effect. Electrons created in this amplification process will reach the anode in less than 1 ns.

The signal on the readout structure is induced by the movement of the charges between the micro mesh and the anode. It is possible to precisely measure the particle hit position and timing by reading out every strip individually.

The advantage of Micromegas detectors is thus on the one hand the very fast formation and accessibility of the signal on the readout electronics, which is in the order of 100 ns. On the other hand, space-charge effects known from the up to today used wire chambers, are avoided because of the fast drain of positive ions in the only  $\mathcal{O}(0.1 \text{ mm})$  thin amplification region [Olive et al., 2014b].

## 1.2 Floating Strip Micromegas in Medical Application: Ion Transmission Tomography

In the following, a brief overview of the advantages of ion-based radiography is given. The general physical advantages of ion beam therapy in oncology are due to the finite range of ions in tissue. This allows for a precise dose delivery in the tumor region. Imaging the patient at the treatment site before or during the treatment improves the accuracy delivered dose in tissue and avoids range uncertainties due to the usage of X-ray calibration curves [Rinaldi, 2011].

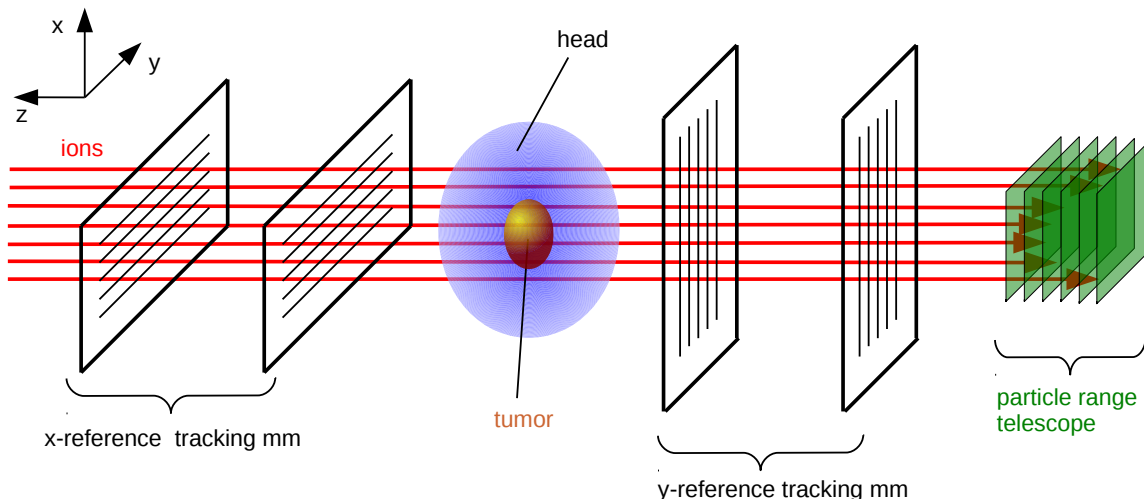


Figure 1.2: The concept of ion beam radiography: An ion beam (red lines) with sufficient energy is traversing a patient (blue), losing energy accordingly to the tissue properties. The residual particle energy  $\Delta E$  is measured via a particle range telescope behind the floating strip Micromegas (mm) tracking system, providing the contrast information of the image. The figure is describing the case of one-dimensional readout Micromegas, where at least one detector for each dimension is necessary to reconstruct a full 3-d particle trajectory. Recently, successful measurements with floating strip Micromegas, equipped with two-dimensional readout anodes, showed, that their application could improve the tracking efficiency could be improved and lower the material budget at the same time.

The dose of ion transmission radiographies compared to conventional X-ray computed tomographies is approximately a factor of 50-100 lower [Schneider et al., 2004]. The basic idea behind ion transmission tomography is illustrated in Fig. 1.2. An ion beam with sufficient energy is traversing a patient, losing energy mostly in inelastic Coulomb collisions with atomic electrons, which is well described by the Bethe-Bloch-equation (see section 2.1.1). The residual ion energy can then be measured in a particle range telescope, which can be e.g. several layers of scintillating material or conventional energy calorimeters equipped with fast readout electronics. The trajectory of the traversing particle can be acquired by a tracking floating strip Micromegas reference system, which allows highly efficient one-by-one registration of particles and a full 3-d track reconstruction at particle fluxes up to  $7 \text{ MHz/cm}^2$ . These only low material budget detectors show excellent spatial and temporal resolution. Novel floating strip Micromegas have been introduced and the physics and performance was studied in detail by [J.Bortfeldt, 2014]. The internal structure and signal formation, as well as advantages compared to standard Micromegas are summarized in chapter 3.

# Chapter 2

## Theoretical Background

### 2.1 Particle Interaction with Matter

Detecting particles and photons is possible through their interactions with matter. These interaction processes can be used as a basis for a specific detector concept. In the case of Micromegas detectors, the detection processes of the transversing particle in the active gas volume of the detector behaves differently for charged and neutral particles (such as photons).

#### 2.1.1 Charged Particles

Charged particles interact with matter via excitation of bound electrons, Cherenkov radiation, bremsstrahlung, production of transition radiation and ionization. The latter is of greater importance for Micromegas detectors as the created electron ion pairs can directly be detected within the active volume.

The average energy loss of charged particles per unit length is well described by the Bethe-Bloch formula [Grupe and Shwartz, 2008]

$$\left\langle \frac{dE}{dx} \right\rangle = -4\pi N_A r_e^2 m_e c^2 \rho \frac{Zz^2}{A\beta^2} \left( \frac{1}{2} \ln \frac{2m_e c^2 \beta^2 \gamma^2 T_{max}}{I^2} - \beta^2 - \frac{\delta}{2} \right) \quad (2.1)$$

with  $r_e$ : classical electron radius;  $m_e$ : electron mass;  $c$ : speed of light;  $\rho$ ,  $Z$ , and  $A$ : density, atomic number and atomic weight of the absorbing material;  $z$ ,  $\beta = v/c$  and  $\gamma = 1/\sqrt{1-\beta^2}$ : charge in units of  $e$  and velocity  $v$  of incident particle;  $T_{max} \approx 2m_e c^2 \beta^2 \gamma^2$ : maximum energy transfer to an electron in a single collision. Values for the mean excitation energy  $I$  of the absorbing material and the density correction factor  $\delta$  can be found in [Sternheimer et al., 1984]. The mean excitation energy  $I$  can thus either be determined experimentally, or approximated by empirical formulas [Poskus, 2010] that relate  $I$  to the atomic number  $Z$  of the considered element, following:

$$I \approx 9.2 \cdot Z + 4.5 \cdot Z^{1/3} \quad [\text{eV}]. \quad (2.2)$$

If the absorbing material is composed of several mono atomic chemical elements,  $I$  can be expressed by the mean excitation energies of the constituent elements, with

$$I = \sum_{j=1}^N c_j I_j. \quad (2.3)$$

$I_j$  is the mean excitation energy of the element  $j$ , determined via Eq. (2.2), and  $c_j$  the relative number of atoms of element  $j$  in a compound of  $N$  elements of the absorbing material.

The Bethe-Bloch equation is usually given in units  $\text{MeV}/(\text{cm}^2/\text{g})$  with  $dE/d\chi_0 = dE/(\rho \cdot dx)$ , because it is then largely independent of the properties of the absorbing material. Following the equation, the energy loss decreases like  $1/\beta^2$  in the low-energy domain and reaches a minimum of ionization in the  $\beta\gamma \approx 4$  regime. Relativistic particles ( $\beta \approx 1$ ) which have an energy corresponding to that minimum are called *minimum-ionizing particles* (MIPs). The energy loss of MIPs is on the order of  $2 \text{ MeV}/(\text{cm}^2/\text{g})$  for almost all absorber materials. Further increasing  $\beta\gamma$  leads to a relativistic rise of the energy loss because of the logarithmic term in the brackets [Grupe and Schwartz, 2008]. Fig. 2.1 shows the dependence of the Bethe-Bloch equation on  $\beta\gamma$  of a singly charged particle in an Ar:CO<sub>2</sub> 93:7 vol.% and a Ne:CF<sub>4</sub> 80:20 vol.% gas mixture, respectively.

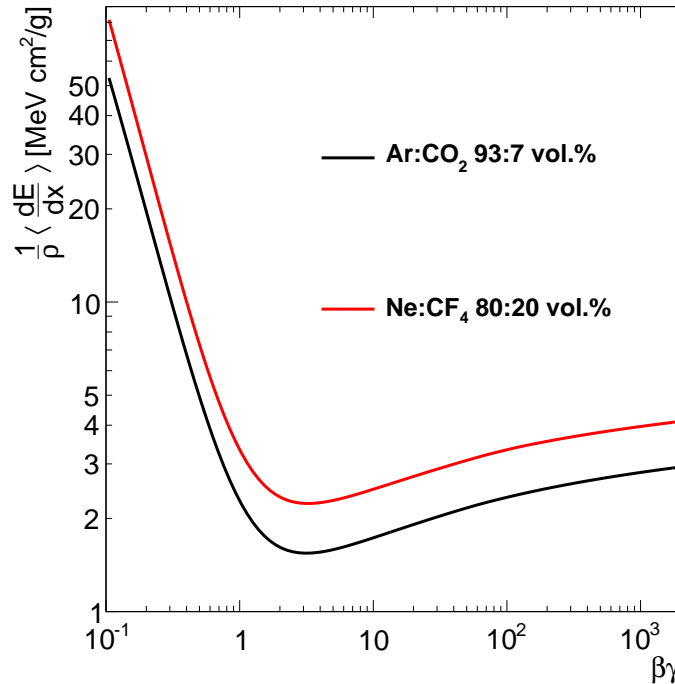


Figure 2.1: Energy loss of a singly charged particle versus  $\beta\gamma$  in the range  $0.1 < \beta\gamma < 2000$  for an Ar:CO<sub>2</sub> 93:7 vol.% (black) and a Ne:CF<sub>4</sub> 80:20 vol.% (red) gas mixture. The mean excitation energy of CF<sub>4</sub> has been calculated with Eq. (2.2) and Eq. (2.3). The Sternheimer coefficients of CF<sub>4</sub> have been approximated by F<sub>2</sub>-gas taken from [Groom, 1993].

In the case of thin absorber materials, it has been argued by [Bichsel, 1988] that strong fluctuations around the average energy loss exist because of the large energy transfers to target electrons. The most probable energy-loss in a layer of thickness  $d$  can then be described by

$$\left. \frac{\Delta E}{\Delta x} \right|_p = 2\pi N_{Ar} r_e^2 m_e c^2 z^2 \frac{Z}{A} \cdot \frac{\rho}{\beta^2} \left( \ln \frac{2m_e c^2 \gamma^2 \beta^2}{I} + \ln \frac{\xi}{I} + 0.2 - \beta^2 - \delta \right) \quad (2.4)$$

with  $\xi = 2\pi N_A r_e^2 m_e c^2 z^2 \frac{Z}{A} \cdot \frac{\rho}{\beta^2} \cdot d$ . The energy-loss distribution for a thin absorber material e.g. a gaseous detector is strongly asymmetric but can be well described by a Gaussian convoluted *Landau distribution*. When increasing the absorber thickness the tail of the landau distribution is reduced and for very thick absorbers it can be approximated by a Gaussian distribution [Gruppen and Shwartz, 2008].

## 2.1.2 Photons

As photons do not carry electric charge, their interaction with matter is fundamentally different from ionization processes of charged particles. Photons are either absorbed via photoelectric effect and pair production, or scattered via Compton scattering. As these effects are pure statistical processes, one can not define a definite range for photons in matter. A collimated photon beam with intensity  $I_0$  hits a layer of thickness  $x$  and attenuates exponentially in it according to

$$I(x) = I_0 \cdot \exp^{-\mu x} \quad , \quad (2.5)$$

with the absorbing material dependent *mass attenuation-coefficient*  $\mu$  in units  $\text{g}/\text{cm}^2$ . It is related to the cross sections of the possible interaction processes  $\sigma_i$  according to [Gruppen and Shwartz, 2008]

$$\mu = \frac{N_A}{A} \sum_{i=0}^n \sigma_i \quad , \quad (2.6)$$

where  $A$  is the atomic weight and  $N_A$  the Avogadro number. Due to the strong energy dependence of the three interaction processes, the mass attenuation coefficient is also strongly dependent on the energy of the incident photon. For photon energies below 100 keV, the dominant interaction process is the photoelectric effect where the photon is absorbed and its full energy is delivered to a target electron. For increasing energy the Compton effect becomes more relevant, where a part of the kinetic energy of the photon is delivered to a target electron while the photon is scattered. For energies larger than  $2m_e \approx 1 \text{ MeV}$  the pair production becomes relevant where the photon is able to create a positron/electron pair in the Coulomb field of a nucleus. For photon beam energies above 2 MeV the process of pair production is the dominant one [Kleinknecht, 1992].

Tab.2.1 summarizes some properties of Ar:CO<sub>2</sub> and Ne:CF<sub>4</sub> based gases at normal temperature and pressure (NTP: 20 °C, one atm), including relative energy loss of MIPs and created ionization charge.

gas	density [mg cm <sup>-3</sup> ]	$W_i$ [eV]	$dE/dx _{\min}$ [keV cm <sup>-1</sup> ]	$n_T$ [cm <sup>-1</sup> ]
Ar	1.66	26	2.53	97
CO <sub>2</sub>	1.84	34	3.35	100
Ne	0.839	37	1.45	40
CF <sub>4</sub>	3.78	54	6.38	120
Ar:CO <sub>2</sub> 93:7 vol.%	1.67	26.6	2.59	97
Ne:CF <sub>4</sub> 80:20 vol.%	1.43	40.4	2.44	56

Table 2.1: Properties of Ar:CO<sub>2</sub> and Ne:CF<sub>4</sub> based gases at NTP.  $W_i$ : average energy per ion pair,  $n_T$ : total number of created electron-ion pairs per cm per MIP. [Olive et al., 2014a].

## 2.2 Charge Carrier Drift and Amplification in Gaseous Detectors

If free charge carriers drift in the presence of an electric field, it is required that they do not recombine and are also not attached to atoms or molecules of the active gas volume. Then the mean drift velocity of ions in direction of the field lines is given by

$$v_d^+ = \mu^+ E \cdot \frac{p_0}{p}, \quad (2.7)$$

with the nominal pressure  $p_0 = 1013$  mbar, the *ion mobility*  $\mu^+$ , the applied electric field  $E$  and the gas pressure  $p$ . Tab. 2.2 shows some mobilities of ions used in possible detector gas mixtures Ar:CO<sub>2</sub> or Ne:CF<sub>4</sub> for Micromegas detectors.

gas	ion	mobility $\mu^+$ [cm <sup>2</sup> V <sup>-1</sup> s <sup>-1</sup> ]
Ar	Ar <sup>+</sup>	1.54
CO <sub>2</sub>	CO <sub>2</sub> <sup>+</sup>	1.09
Ar	CO <sub>2</sub> <sup>+</sup>	2.14
Ne	Ne <sup>+</sup>	4.7

Table 2.2: Ion mobility in various gases at 1013 mbar and 20° [Ellis et al., 1976].

The more than three times bigger mobility of Ar<sup>+</sup>-ions compared to Ne<sup>+</sup>-ions is clearly visible. In the case of Micromegas detectors, the signal duration depends on both electron and ion drift time in the gas. Thus this is one of the reasons to replace a typical Argon based gas mixture with Neon, when a faster signal processing in the detector is desired.

As electrons are at least by a factor of 1000 lighter than ions, their drift in the presence of an electric field is a more complex process. The energy gain per mean free path  $\lambda$  can get quite large such that quantum mechanical processes and elastic scattering become important [Kleinknecht, 1992]. Adding additional molecular quencher gases like carbon dioxide or tetrafluoromethan, reduces the elastic scattering of the electrons at the nuclei of the noble gas and therefore increase the effective electron drift velocity. Furthermore the quencher gas has a broader excitation energy spectrum than the noble gas partner and can thus absorb UV-photons created in the gas amplification process,

preventing streamer formation and thus discharges in the detector. Fig. 2.2 shows the behavior of the electron drift velocity with a varied electrical field of two detector gas mixtures computed with MAGBOLTZ [Biagi, 2012]. Mind the two working points at  $E_{\text{drift}}=200$  V/cm with a ratio of  $v_{d, \text{Ne}}/v_{d, \text{Ar}} \approx 3$  and at  $E_{\text{drift}}=500$  V/cm with a ratio of  $v_{d, \text{Ne}}/v_{d, \text{Ar}} \approx 2$ . The substantially bigger drift velocity for electrons in the Neon based gas mixture is clearly visible.

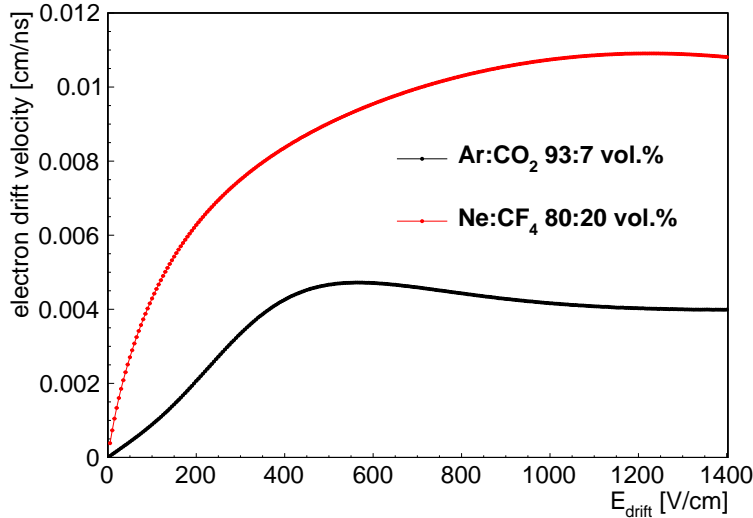


Figure 2.2: Calculated electron drift velocity versus electric field in the drift region. Two typical detector gas mixtures Ar:CO<sub>2</sub> 93:7 vol.% (black) and Ne:CF<sub>4</sub> 80:20 vol.% (red) have been simulated with MAGBOLTZ at 1013 mbar and 20°, respectively [Biagi, 2012].

The amount of charge carriers created during the ionization process of a minimum ionizing particle traversing the active volume of the detector is rather small. To get a decent, recordable signal on the readout electronics, an avalanche process must take place. This can be achieved by increasing the applied field drastically to higher values, such that the the electron reaches enough energy within its mean free path  $\lambda$  between two collisions with gas atoms to again ionize a gas atom.

In a sufficiently large electric field, the number of electrons  $n$  increases by

$$dn = \alpha n dx \quad (2.8)$$

per unit path length  $dx$  with the Townsend coefficient  $\alpha = \lambda^{-1}$ . In a homogeneous electric field, as it is the case for a planar chamber like Micromegas detectors,  $\alpha$  is not a function of  $x$ . Integration over  $x$  then yields

$$n(d) = n_0 \cdot \exp^{\alpha d} = n_0 \cdot A, \quad (2.9)$$

with  $A = \exp(\alpha d)$  describing the multiplication factor of charges or the *gas gain*, depending on the electric field, the parameters of the detector gas as the ionization cross-sections and density, and the amplification gap width  $d$  [Kleinknecht, 1992]. Fig. 2.3 shows calculated values of the Townsend coefficient as a function of the amplification field strength.

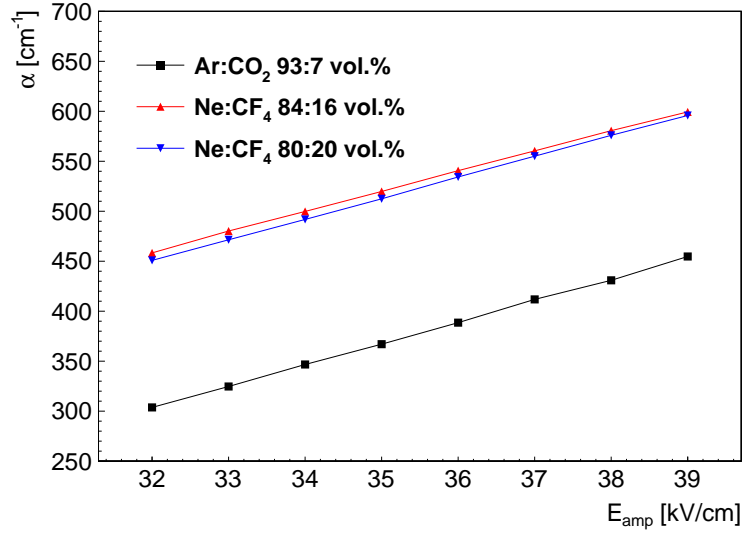


Figure 2.3: First Townsend coefficient versus electric field in the amplification region. Three detector gas mixtures Ar:CO<sub>2</sub> 93:7 vol.% (black), Ne:CF<sub>4</sub> 86:14 vol.% (red) and Ne:CF<sub>4</sub> 80:20 vol.% (blue) have been simulated with MAGBOLTZ at 1013 mbar and 20°C, respectively.

## 2.3 Multiple Scattering of Charged Particles

A charged particle passing through matter undergoes multiple small-angle scattering processes. An initially parallel particle beam therefore spreads after travelling through the absorbing material, which is typically unwanted in applications where the precise hit position of particles is measured. The width of the distribution of track inclinations  $\Theta$  can be calculated by [Gruppen and Shwartz, 2008]

$$\Theta = \frac{13.6 \text{ MeV}}{\beta c p} \cdot z \sqrt{\frac{x}{X_0}} (1 + 0.038 \ln(x/X_0)) , \quad (2.10)$$

where  $\beta c$  is the velocity,  $p$  the momentum in MeV/c and  $z$  the charge of the scattered particle.  $x/X_0$  describes the thickness of the absorbing material in units of the radiation length  $X_0$ , which is defined as the average decrease of an electron energy to a fraction of  $1/e$  from the initial energy via bremsstrahlung. For an admixture of elements or a compound it can be approximated by

$$X_0 = \frac{1}{\sum \eta_i / X_0^i} , \quad (2.11)$$

where  $\eta_i$  are the atomic mass fractions of an absorber element with radiation length  $X_0^i$ . Values for the radiation length can be found in [Olive et al., 2014b].

# Chapter 3

## The Floating Strip Micromegas Detector

In the following sections, the floating strip Micromegas detector is introduced. The internal structure and the signal formation within the detector, the mesh transparency and detection efficiency, as well as potential discharges between anode and mesh are explained. Furthermore, a two-dimensional floating strip readout anode as well as the front-end boards, used for data acquisition, are briefly explained.

### 3.1 Internal Structure

The functional principle of the floating strip Micromegas is demonstrated in Fig. 3.1: A charged particle traverses the detector and ionizes the gas. Created ionization electrons drift into the high-field region between mesh and anode strips, where they are amplified into Townsend avalanches.

The drift region of the floating strip Micromegas, formed by the cathode plane and the micro-mesh, is unchanged compared to standard Micromegas, see Fig. 1.1 and Fig. 3.1. The micro-mesh is held at a constant distance of  $150\ \mu\text{m}$  from the anode strips with a  $150\ \mu\text{m}$  thick pillar shaped spacer structure, which is photo-lithographically produced on the anode strips with  $0.5\ \text{mm}$  pitch and  $0.3\ \text{mm}$  width.

The anode strips are individually connected to high voltage via high ohmic resistors of above  $20\ \text{M}\Omega$ , signals are decoupled either by discrete pF capacitors connected to the anode strips, or by readout strips beneath the anode strips, separated by an insulating material such as FR4 or Kapton. The signal is then amplified by fast charge sensitive preamplifiers.

Two possible realizations, see Fig. 3.2, for decoupling the anode strip signals to charge sensitive preamplifiers have been developed by J.Bortfeldt [2014]:

A *discrete* version (see Fig. 3.2, left), with soldered  $15\ \text{pF}$  capacitors and  $22\ \text{M}\Omega$  resistors connected to the anode strips, enables the possibility to easily exchange the SMD components. Thus allowing for adjusting the detector parameters.

The *integrated* version (see Fig. 3.2, right) makes use of the screen printing technology: A resistive paste, consisting of a mixture of carbon and penolic resin with either  $100\ \text{k}\Omega/\square$  or  $1\ \text{M}\Omega/\square$ , is printed onto the PCB material. This allows for a smaller

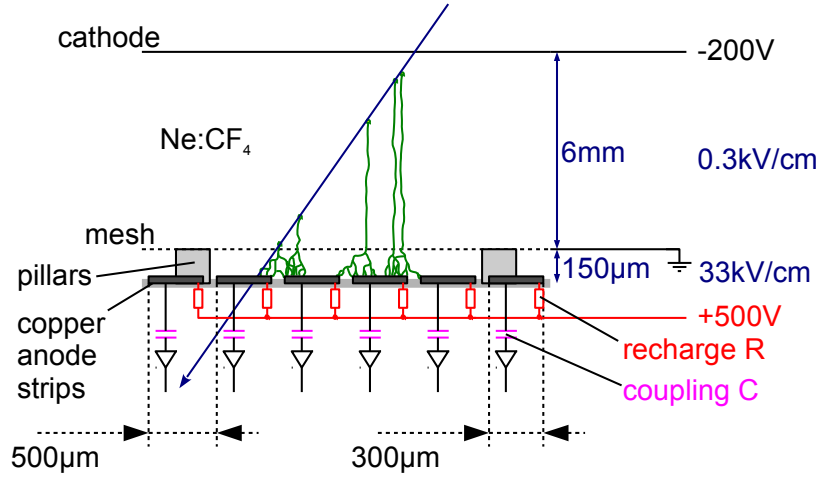


Figure 3.1: Schematic cut through a floating strip Micromegas: A charged particle traverses the detector (blue line). The ionization charge is collected within the drift region between cathode and mesh. Electrons drift towards the mesh and are able to reach the amplification region. After completed gas amplification, the signals on the individually to high voltage connected copper strips are decoupled via pF capacitors [J.Bortfeldt, 2014].

strip pitch and avoids the time consuming soldering process for the SMD components. The signal is decoupled via parallel copper readout strips, below the anode strips. They are separated by a thin layer of insulating FR4 material, each forming a high-voltage resistant capacitor. A combination between both realizations has been used for the measurements presented in this thesis: All floating strip Micromegas with one-dimensional strip readout are equipped with soldered SMD resistors and parallel copper readout strips beneath the floating strips. For the two-dimensional readout anode, the fully integrated realization is used. The setup is described in section 3.5.

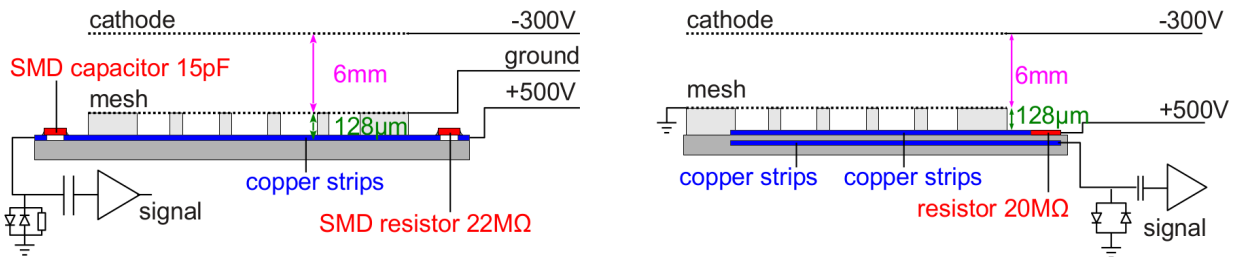


Figure 3.2: Two possible realizations for floating strip Micromegas: The *discrete* version (left) allows for easy exchangeability of the used SMD components. The *integrated* version (right) makes use of the screen printing technology for the resistors and exploits the capacitance between striplines, allowing for a smaller strip pitch [J.Bortfeldt, 2014].

## 3.2 Signal Formation

In the following only the main aspects of the signal formation is described, a detailed study can be found in [J. Bortfeldt, 2010].

A charged particle traverses the detector, creating electron-ion pairs in the drift gap, see Fig. 3.1. Due to the applied voltage between the typically 6 mm distant cathode and micro-mesh, charge carriers drift to their corresponding electrodes. The electrons, created in this process, thus drift into the high-field region between micro-mesh and anode strips, where they are amplified in Townsend avalanches with the process described in section 2.2. Due to the large mobility of the electrons in gas, the amplification process is finished in less than 1 ns. Nevertheless, the temporal signal evolution depends strongly on the ions drifting away from the anode strips, as most of the charge is being created in the last amplification steps close to the anode. All electrons created during the amplification process arrive nearly instantaneous ( $<1$  ns) at the anode (see Fig. 4.6 for the charge configuration after finished amplification process). However, the positive ion cloud, drifting away from the anode strips, is inducing localized, negative mirror charges on the anode strips as well, preventing the detection of the electron charges on the preamplifier. As the ions drift towards the mesh, the induced mirror charges vanish, thus releasing the negative electron signal for detection on the preamplifier. With the constant drift of the ions away from the anode strips, the negative charge signal on the anode evolves until the ions reach the mesh.

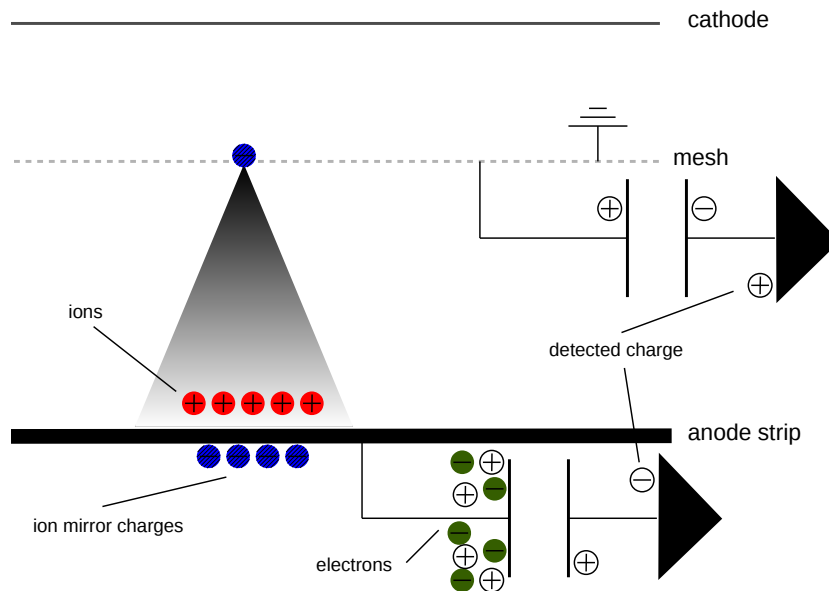


Figure 3.3: Charge configuration in a Micromegas detector after finished gas amplification. As the mesh was neutral before, a positive signal due to negative mirror charges of the positive ions can be observed. On the anode strips however, a negative charge signal due to the avalanche electrons is observed. Drift and amplification width not drawn to scale.

The drift time of ions from anode strips to mesh is approximately 100 ns, which thus corresponds to a typical signal rise time in Micromegas detectors with amplification gap width  $\mathcal{O}(100 \mu\text{m})$ . For a charged particle, that produces electrons also in the proximity of the cathode, the maximum signal duration is therefore defined by the drift of these electrons to the mesh - which is also in the order of 100 ns - plus the additional drift time  $\mathcal{O}(100 \text{ ns})$  of the positive ions created in the avalanche process away from the anode strips to the mesh. The overall signal duration can thus easily be reduced by increasing the electron drift velocity through adapting the drift field. The amplification

field and thus the ion drift velocity is determined by the desired gas gain. A significant reduction can thus only be achieved by replacing the used detector gas. In this thesis, the commonly used detector gas Ar:CO<sub>2</sub> is replaced by the significantly faster gas mixture Ne:CF<sub>4</sub>. For comparison of the electron drift velocity and ion mobility, see Tab. 2.2 and Fig. 2.2. For specific field configurations a three times bigger electron drift velocity and ion mobility can be reached with the new gas.

### 3.3 Mesh Transparency and Detection Efficiency

The ionization electrons created in the drift gap move along the field lines towards the amplification region. If the field lines end on the micro-mesh, the electrons are lost. This leads to a reduced reconstructed pulse height. It has been shown by Giomataris et al. [1996], that the electron transparency of the mesh i.e. the fraction of the electrons actually reaching the amplification region strongly depends on the ratio  $\xi = E_{\text{amp}}/E_{\text{drift}}$  of the amplification and drift field. For low values of  $\xi$  the field lines end on the micro mesh, resulting in a low transparency. However for high values of  $\xi$ , the field lines of the drift region bend through the holes of the mesh into the amplification region, allowing for electron transparencies close to 100%.

The transverse diffusion of the electrons also leads to a loss of a fraction of electrons on the mesh as electrons diffuse off the field lines, that would guide them into the amplification region. The diffusion depends both on field strength and composition of the used detector gas. Fig. 3.4 shows the simulated transverse electron diffusion after 1 mm drift and the mesh transparency for Ar:CO<sub>2</sub> 93:7 vol.% and Ne:CF<sub>4</sub> gas mixtures, as a function of the drift field. For the simulation [Lösel et al., 2015], a woven mesh with 18  $\mu\text{m}$  thick wires and 63  $\mu\text{m}$  pitch has been used. It can be seen that for drift fields above 175 V/cm, the diffusion of Ne:CF<sub>4</sub> 80:20 vol.% is considerably smaller than for Ar:CO<sub>2</sub>. For the mesh transparency, values above 94% can be reached for both gas mixtures for fields below 400 V/cm. Above 400 V/cm, Ne:CF<sub>4</sub> shows a better transparency.

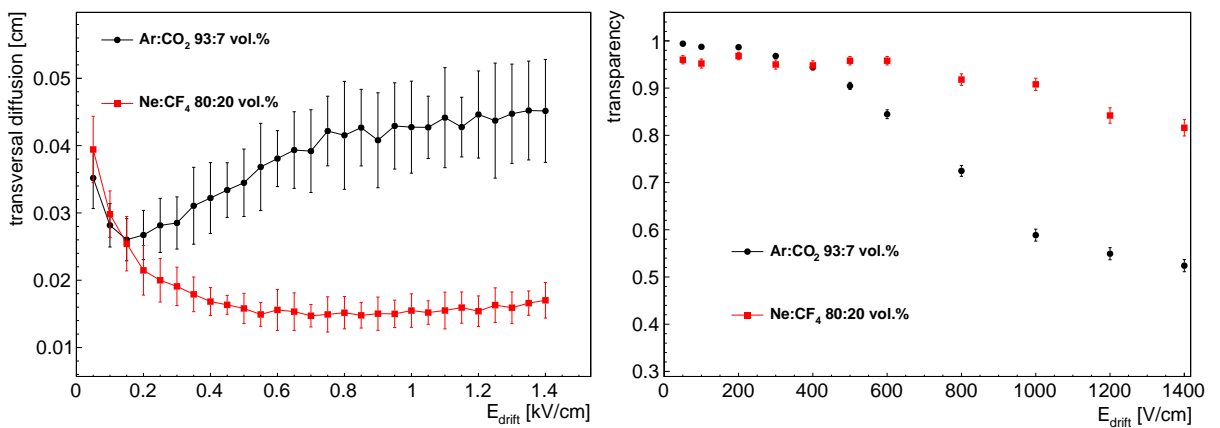


Figure 3.4: Transversal diffusion after 1 mm drift (left) and mesh transparency for electrons (right) as a function of the drift field for gas mixtures Ar:CO<sub>2</sub> 93:7 vol.% (black) and Ne:CF<sub>4</sub> 80:20 vol.% (red), simulated with GARFIELD [Veenhof, 2010] at 20°C and 1013 mbar.

### 3.4 Discharges

The major difficulty encountered in Micromegas is due to discharges between mesh and anode. A discharge may follow due to a traversing heavy ionizing particle or fragments e.g. from particle showers produced in the atmosphere or in the concrete ceiling [Zibell, 2010]. If the charge density during the amplification process, described by the previous processes, exceeds a critical value<sup>1</sup>, a conducting plasma channel between mesh and anode strips develops, which results in a discharge of the mesh onto the anode strips. This conducting channel, also called a streamer [Raether, 1964][Raizer, 1991], is localized and non-destructive for Micromegas. Nevertheless, the streamer equalizes the potential between the anode and the mesh. During this time, no charge amplification is possible and thus the detector is inefficient. The big advantage of floating strip Micromegas compared to standard Micromegas is that during a discharge only a group of strips is affected, as the streamer develops localized. For a floating strip Micromegas with high-voltage individually supplied on the anode strips, therefore only a few strips are affected by the discharge. However for a standard Micromegas with high-voltage supplied on the mesh, the whole mesh is affected and equalized to the anode potential, disabling the whole detector until the mesh is recharged. Calculating the inefficiency  $\epsilon$  of a floating strip Micromegas with [J.Bortfeldt, 2014]

$$\epsilon = \left(1 - \lambda \exp^{-\lambda}\right) c, \quad (3.1)$$

where  $c$  is the fraction of the active area affected by the discharge and  $\lambda = t_{\text{dead}} f_{\text{discharge}}$ , shows, that

$$\epsilon_{\text{floating}} < \epsilon_{\text{standard}}/1000 \quad (3.2)$$

i.e. the inefficiency of a floating strip Micromegas is more than three orders of magnitude lower than of a comparable standard Micromegas detector. The corresponding recharge time of the mesh of a standard Micromegas after a discharge is with  $t_{\text{dead}} = 75$  ms is about a factor of 50 bigger than the single strip dead time of a comparable floating strip Micromegas with  $t_{\text{dead}} = 1.5$  ms. All necessary variables needed for calculating the inefficiency or dead time can be found in [J.Bortfeldt, 2014].

### 3.5 Two-Dimensional Floating Strip Readout Anode

To enable reconstruction of a two-dimensional hit position within one detector, a floating strip Micromegas with two perpendicular layers of readout strips has been developed. The signal on the floating anode strips is decoupled onto the parallel  $x$  readout strips. To resolve the particle hit position in the  $y$  direction, an orthogonal  $y$  readout strip layer is placed below the  $x$  readout strips. The layers are separated by a  $25 \mu\text{m}$  thick insulating Kapton layer, see Fig. 3.5.

---

<sup>1</sup> $1.77 \times 10^6$  e/0.01 mm<sup>2</sup> for a standard Micromegas with 128  $\mu\text{m}$  amplification gap, operated with Ar:CO<sub>2</sub> 93:7 vol.%, [Moll, 2013].

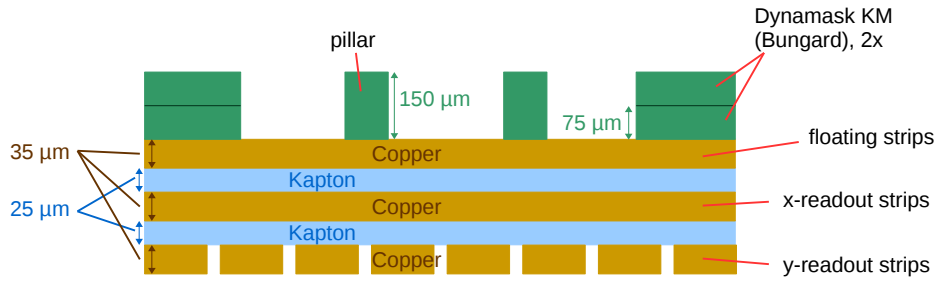


Figure 3.5: Configuration of a two-dimensional floating strip anode with two perpendicular layers of readout strips within the readout PCB [König, 2015].

The observed signal polarity on both readout layers is of opposite sign, see chapter 7 for signal shapes of the two strip layers and characterization measurements. The likely process of signal formation on the two readout layers is sketched in Fig. 3.6.

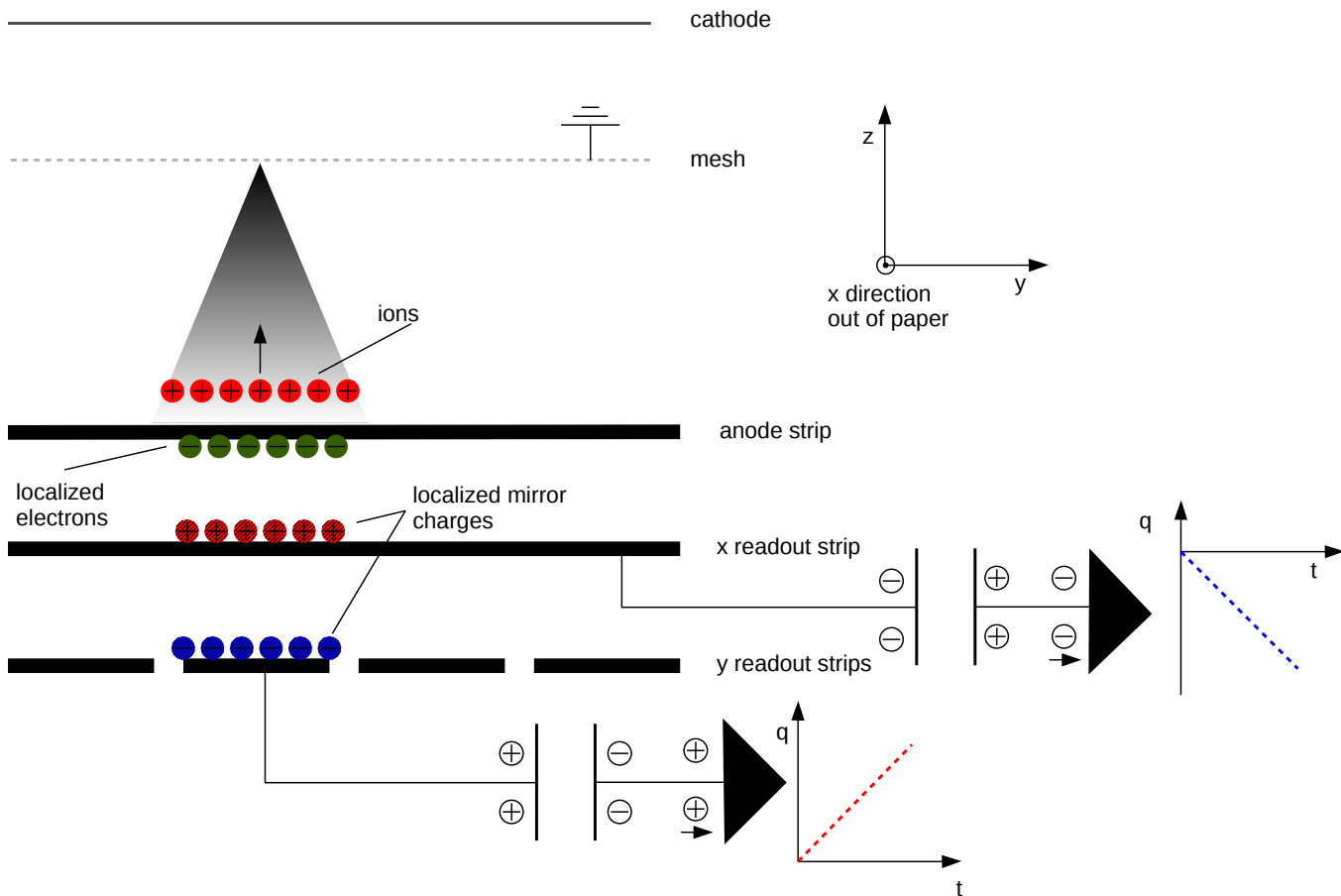


Figure 3.6: Possible charge configuration directly after completed gas amplification (not drawn to scale).

The localized negative surface charge on the anode strips is coupled to  $x$  readout strips, inducing localized positive surface charges. The signal detected on the preamplifier is therefore negative. For the  $y$  readout strips however, the signal is decoupled from the  $x$  readout strips, leading to a localized negative surface charge on the  $y$  readout strips.

The signal recorded on the preamplifier is therefore of opposite sign as for the  $x$  layer, leading to a positive observable signal on the  $y$  readout strips. Nevertheless, the signal formation in two-dimensional floating strip Micromegas anodes is a complex process and thus still a topic of current research.

### 3.6 High-density APV25 front-end electronics

The APV25 (Analogue Pipeline Voltage mode) is a 128-channel VLSI ASIC, developed for the readout of the CMS tracker at the CERN LHC [French et al., 2001]. In this thesis, it has been used for the readout of the floating strip Micromegas detectors. The chip contains 128 channels and for each channel a preamplifier and shaper, driving a 192 column analogue pipeline memory into which samples are written at 40 MHz [Jones, 2001]. This corresponds to the LHC bunch clock. When an event is triggered, the trigger signal is delivered synchronized to the clock. Accordingly, the chip outputs the following data set: a digital head (three bits), a digital address (eight bits), an error bit and an analogue data part (128 bit) containing the charge information of all 128 channels, see Fig. 3.7.

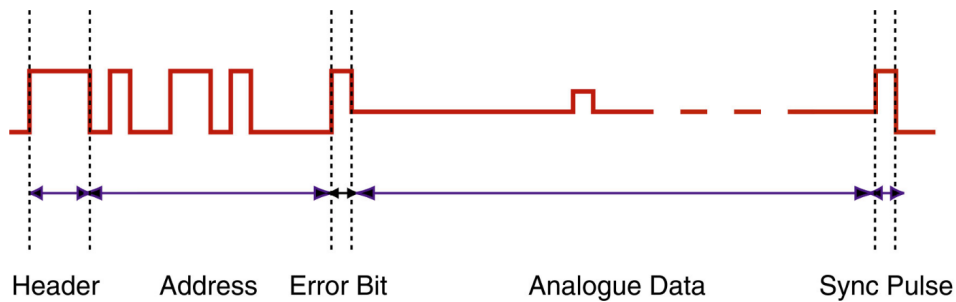


Figure 3.7: Analogue data output of the APV25 ASIC. To remain synchronized with the DAQ electronics when there is no data to read out, a sync pulse is output every 35 clock cycles. [Jones, 2001].

With a maximum analogue data length of 30 clock cycles after an accepted trigger, a maximum signal length of  $30 \times 25 \text{ ns} = 750 \text{ ns}$  can be recorded within the APV capturing window, more than enough for typical signal rise times on the order of 100 ns for Micromegas detectors. For an analogue pipeline length of 192 slots with 25 ns spacing, a maximum trigger delay of  $192 \times 25 \text{ ns} = 4.8 \mu\text{s}$  is possible. After receiving a trigger, the 140 values (128 chip channels + 12 header information) are consecutively output, allowing for a maximum input trigger frequency of 285.7 kHz per read out timebin<sup>2</sup> [Moll, 2013]. The raw data for an internal test pulse applied to the APV25 chip is shown in Fig 3.8, for 12 consecutive read out time bins.

The chip is carried by a front-end board and connected via HDMI cable to a front-end concentrator card (FEC), which digitizes the analogue APV signal with eight two-channel 12 bit analogue-to-digital-converter (ADC) units, operated at 40 MHz. The communication between the data acquisition computers and the FEC is realized via 1 GBit Ethernet, on the basis of UDP packets.

<sup>2</sup>one timebin is defined as a 25 ns clock cycle period

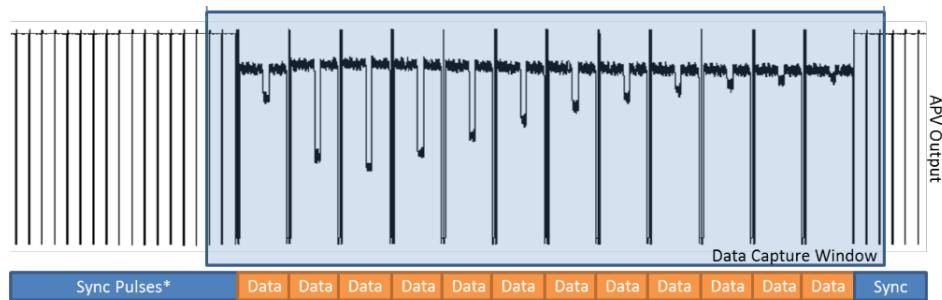


Figure 3.8: Capturing window of the APV25 for 12 read out clock cycles. A test pulse is applied to certain chip channels. The recorded charge evolving in time is visible.

Due to the scalability of this readout method from small to large detector systems, it is also called *Scalable Readout System* (SRS) [RD51, 2010].

As the trigger for the readout during our measurements is not synchronized to the 40 MHz clock, the trigger signal jitters with 25 ns, thus limiting the absolute time resolution of the Micromegas initially. To correct for the jitter, the trigger signal can be separately recorded via an APV-injection board<sup>3</sup> which is also connected to the FEC, allowing to subtract the jitter during the analysis on an event-to-event basis and thus to increase the time resolution.

---

<sup>3</sup>The APV-injection board has been developed by J. Bortfeldt at the LMU. It enables the possibility of recording the NIM trigger signal via an external APV25 front-end board after dedicated attenuation.

# Chapter 4

## Signal Analysis - Methods

In this chapter the analysis of Micromegas signals acquired with APV25 based front-end boards is discussed. Various methods to extract deposited charge, hit position, track inclination of the particle and spatial resolution of the detector are presented.

### 4.1 Signal Reconstruction: Pulse Height and Timing

A typical Micromegas raw signal, measured with protons and recorded with the APV25 based Scalable Readout System (SRS, c.f. 3.6), is shown in Fig 4.1. The internal channel offset is subtracted and the signal is corrected for common mode noise. With the knowledge of hit strip number, charge and timing of the strip pulse, all relevant information of the traversing particle can be reconstructed. In the following, the basics of the cluster reconstruction are introduced.

A cluster is defined as a group of adjacent hit strips, with typically one non-hit strip allowed within the cluster. A strip is marked as hit, if the maximum value  $q_{\max}$  of the strip pulse exceeds three times the standard deviation  $\sigma_{\text{noise}}$  of the strip. The sum of the maximum charge values  $q_{\max, i}$  of the strips  $i$  in the cluster i.e. the cluster charge is then defined as [J.Bortfeldt, 2014]

$$q_{\text{clust}} = \sum_{i \in \text{cluster}} q_{\max, i} \quad (4.1)$$

The maximum charge value can either be extracted by searching for the maximum value of the charge-time distribution or by fitting a skewed Gaussian function

$$q(t) = q_{\max} \exp \left( - \left( \frac{t^s - t_G}{t_w} \right)^2 \right) \quad (4.2)$$

to the strip pulse, where  $s \in ]0,1]$  defines the skewness,  $t_w$  describes the width and  $t_G$  shifts the function on the time axis.

The position of the maximum, i.e. the pulse timing, is then given by  $t_{\max} = t_G^{1/s}$ .

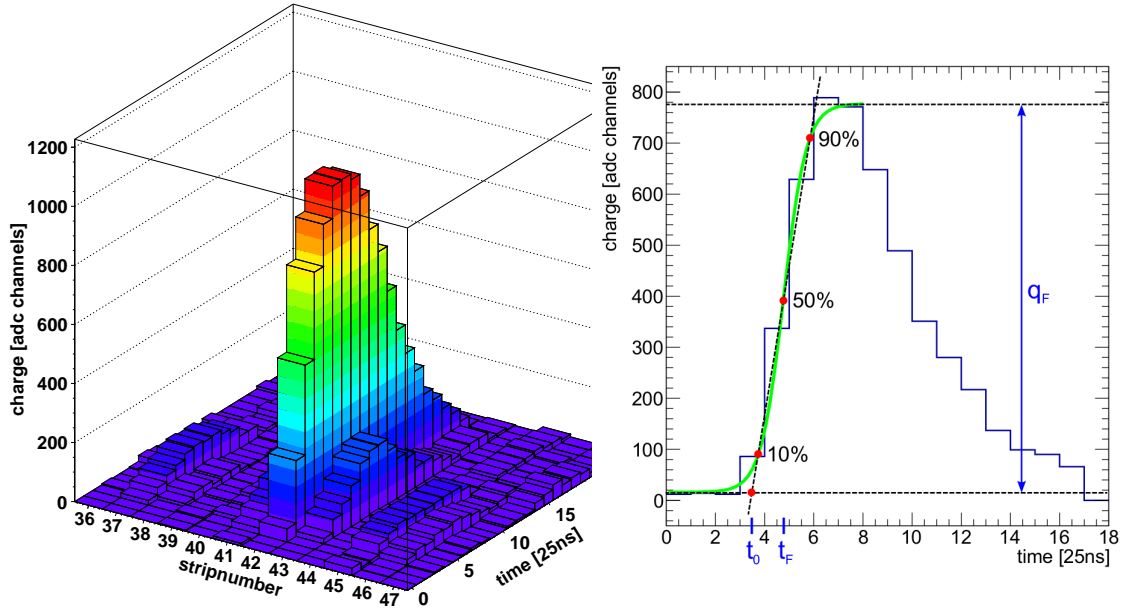


Figure 4.1: Evolution of a typical Micromegas charge signal as a function on the strip number of a proton traversing the detector. The right figure (taken from [J.Bortfeldt, 2014]) shows the signals on the strip with maximum deposited charge as a function of the time. All relevant information as timing and pulse height can be extracted by fitting e.g. an inverse Fermi function to the rising edge of the distribution.

In order to extract the strip pulse timing more precisely, an inverted Fermi function

$$q(t) = \frac{q_F}{1 + \exp((t_F - t)/t_{\text{rise}})} + q_{\text{offset}} \quad (4.3)$$

is fitted to the rising edge of the signal, with the pulse height  $q_F$ ,  $t_{\text{rise}}$  describing the width of the function and  $q_{\text{offset}}$  representing the baseline i.e. the dashed line in Fig. 4.1. That the position of the maximum of the strip pulse is influenced by the rise time of the pulse itself and therefore the actually measured pulse height brings additional uncertainties to the time resolution. To compensate this, a straight line is fitted through three points of the Fermi function: the 10%, 50% and 90% rise, see Fig. 4.1. The more precise timing can now be extracted by extrapolating the straight line onto the baseline [Lösel, 2013] and is given by

$$t_0 = t_F - \frac{10 \ln 9}{9} t_{\text{rise}}. \quad (4.4)$$

## 4.2 $\mu$ TPC Method

The  $\mu$ TPC method opens the possibility to measure the inclination angle of a particle crossing the detector in a single detector layer. It is inspired by the reconstruction in the time projection chamber invented by Nygren [1974].

The basic idea is based on measuring the signal timing of strips within a selected cluster, represented by the blue data points in Fig. 4.2.

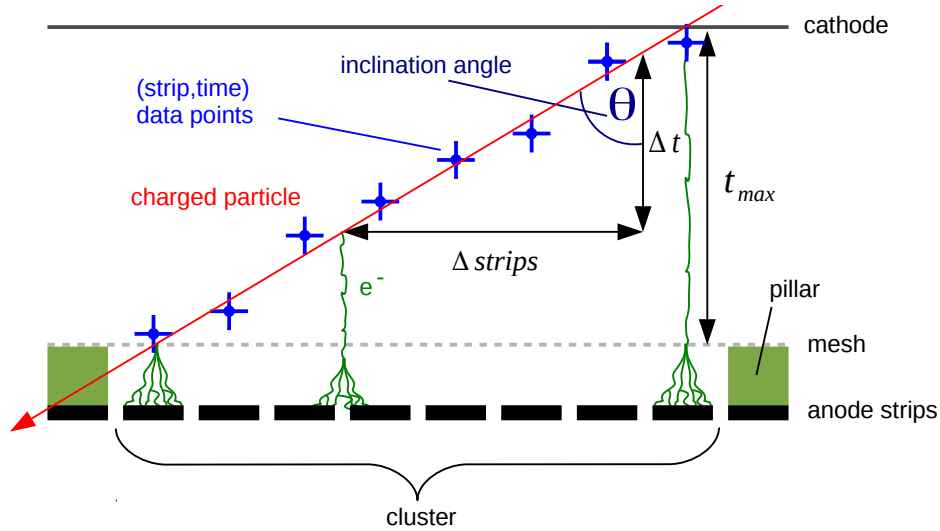


Figure 4.2: The basic principle of the  $\mu$ TPC method for a Micromegas: A charged particle (red line) traverses the detector and creates signals on various strips, depending on the inclination angle. The strips signal timing (blue data points) depends on the origin of the primary created electrons and can be used to reconstruct the inclination angle  $\Theta$ .

The timing of each strip can be determined individually by fitting an inverse Fermi function to the strip pulse as explained in the previous section. The strip-time dependence can be plotted, followed by  $\chi^2$ -minimization fit with a straight line (see section 4.5.1 for explanation of the  $\chi^2$ -minimization). The slope  $a$  of the line allows for calculating the inclination angle, if the drift velocity  $v_d$  of electrons in the used gas and strip pitch  $p_s$  is known:

$$\theta = \arctan \left( \frac{p_s}{a \cdot v_d \cdot 25ns} \right) \quad (4.5)$$

### 4.2.1 Selection of Data Points and Weighting

To improve the reconstruction quality, strip-time data points have been weighted individually depending on pulse height and signal rise time of the strip pulse, see Fig. 4.3, left, for a typical event. Initially all data points are assigned an uncertainty  $w_i=1$ . If the rise time of the signal  $t_r < 0.5$  or  $t_r > 1.5$ ,  $w_i=3$  is assigned [J.Bortfeldt, 2014]. Signals with maximum pulse height, deduced from a landau fit to strip pulse, below 10 times the standard deviation of the respective strip, i.e.  $ph < 10 \cdot \sigma_{noise}$ , are completely removed from the fit ( $w_i=1000$ ). Same holds for all signals with a maximum pulse height from the Fermi signal fit below 10 ADC channels, since then the fit has failed. Signal timings  $t_s < -2$  and rise times  $t_r < 0.2$  are also neglected. To account for capacitive coupling at the corner strips within a selected cluster, first and last strip data points are removed if the maximum pulse height is below 25% of the neighboring strip in the cluster, see Fig. 4.3 right.

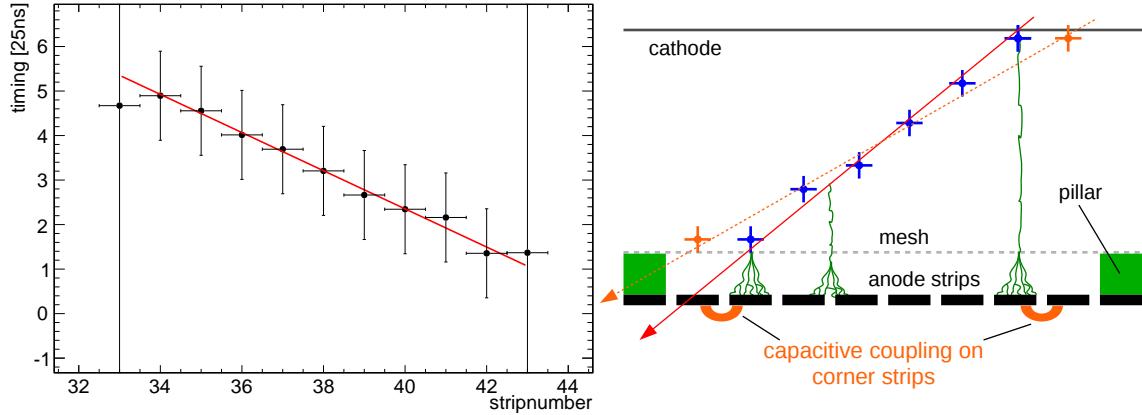


Figure 4.3: Time-strip diagram with assigned fit weights of a typical event of a  $30^\circ$  incident proton (left). First and last strip of the cluster are removed from the track fit (e.g.  $w_i=1000$ ) due to too small deposited charge, primarily due to capacitive coupling on corner strips of the cluster. This typically leads to a bigger reconstructed angles (right figure, orange dashed line).

If the residual of the fit to the data points is insufficient, i.e.  $\chi^2 > 2.5$ , a Hough transform based algorithm<sup>1</sup> has been used to identify points that are not compatible with a straight line.

## 4.2.2 Angle Reconstruction

Knowing the slope of the track, determined in the previous section, the angle can be reconstructed via Eq. (4.6). If the inclination angle is known, e.g. for a tilted detector, the  $\mu$ TPC reconstruction capabilities can be tested. Fig. 4.4 shows reconstructed track inclination for a true inclination of  $(35 \pm 1)^\circ$ , measured with 23 MeV protons.

The distribution typically possesses a tail to bigger reconstructed angles, due to capacitive coupling between neighboring strips and uncorrelated noise, misinterpreted as signals. This results in a smaller reconstructed slope and therefore a higher reconstructed angle.

To retrieve information about the angular resolution, the maximum of the distribution, being the most probable reconstructed angle  $\theta_{\max}$ , has been determined by fitting the upper part with a Gaussian function. For angles  $\theta < \theta_{\max}$  and  $\theta > \theta_{\max}$ , a piece wise Gaussian function has been fitted to extract the asymmetric standard deviation of the distribution [J.Bortfeldt, 2014].

Due to the non-linear transformation function between the reconstructed slope  $a$  and the resulting track inclination angle  $\Theta$  (Eq. (4.5)), histograms with variable bin width have to be used or alternatively unbinned distributions have to be analyzed. See [J.Bortfeldt, 2014] appendix B.3 for an exemplary shift of the mean value of a histogram due to a non-linear transformation.

<sup>1</sup>The used algorithm has been proposed by the framework of the Muon ATLAS Micromegas Activity collaboration (MAMMA) and implemented by Jonathan Bortfeldt.

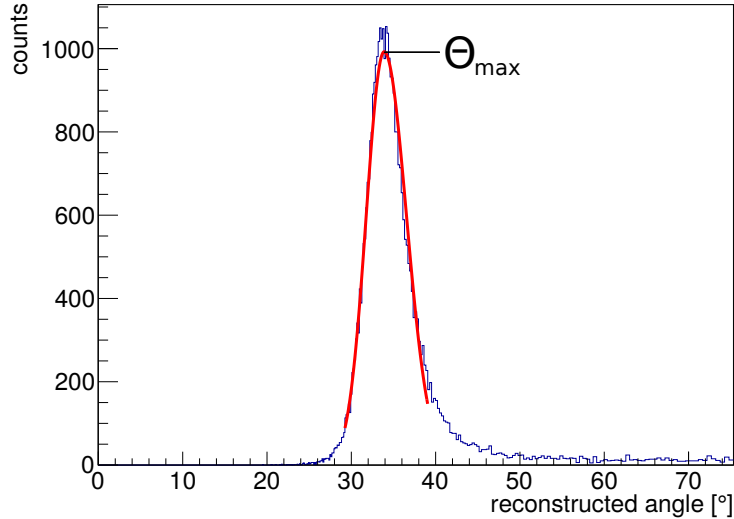


Figure 4.4: Distribution of the reconstructed angle from the  $\mu$ TPC method for a  $35^\circ$  incident 23 MeV proton beam. The maximum  $\theta_{\max}$  is determined by a fit with a Gaussian function to the upper part of the distribution. Two single Gaussian functions are fitted below and above  $\theta_{\max}$  to extract the asymmetric standard deviation of the distribution.

### 4.3 Determination of Drift Velocity

The electron drift velocity can be determined in two different ways as follows.

#### 4.3.1 Inverting the $\mu$ TPC Method

When determining the angle via the  $\mu$ TPC method, the drift velocity has to be known. If the inclination  $\Theta$  of the track is known, e.g. by tilting the detector with respect to the beam direction, the drift velocity can be determined by just inverting the formula from Eq. (4.5) and is therefore given by

$$v_d = \frac{p_s}{a \cdot \tan(\theta) \cdot 25 \text{ ns}} , \quad (4.6)$$

where  $a$  is the slope of the track and  $p_s$  the strip pitch.

#### 4.3.2 Signal Timing Distribution

As the drift velocity, weakly dependent on temperature and pressure, should be a constant for given drift field, another possibility is to measure the maximum drift time  $\Delta t$  of an electron from the cathode to the mesh. As the distance  $d$  is known, the drift velocity can easily be extracted by

$$v_{\text{drift}} = \frac{d}{\Delta t} . \quad (4.7)$$

As the individual timing of each strip is known, the drift velocity can thus be reconstructed via the timing distribution shown in Fig. 4.5, left. All timings described in

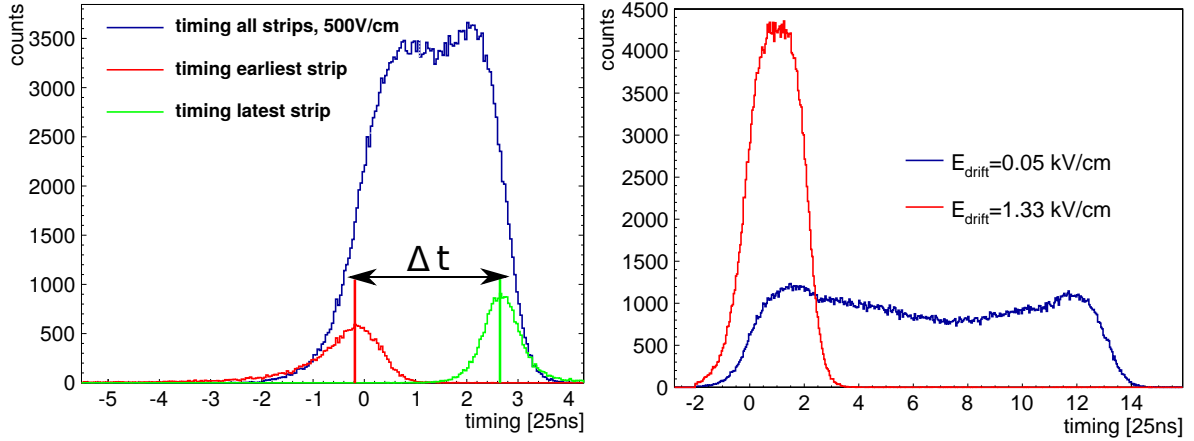


Figure 4.5: Signal timing distribution of all strips in a selected cluster, measured with a Ne:CF<sub>4</sub> 80:20 vol.% based gas mixture with 40k events of 23 MeV protons. The timing of earliest and latest strips have been superimposed (left). This leads to better results when extracting  $\Delta t$ , as it corresponds to the ionization processes directly at the cathode and mesh, respectively. It should be noted that in this figure earliest and latest timing are selected with slightly different selection criterias, explaining the different tails of the distributions. The strong drift field dependence of the timing distribution is shown in the figure on the right side.

this section have been determined via Eq. (4.4). Ideally one would expect a rectangular shape of this distribution, since the ionization process and therefore the energy loss should on average be constant. A typical timing distribution can be seen in Fig. 4.5, left. The width of the distribution depends on the electron drift velocity in the gas, which itself strongly depends on the drift field, see Fig. 4.5, right. Taking into account that the timing of most strip is being distorted towards earlier values because of the capacitive coupling of strips with earlier signals, the width of the distribution is in general too short. This has been observed by J. Bortfeldt [2014] for a Ar:CO<sub>2</sub> 93:7 vol.% gas mixture.

For Ne:CF<sub>4</sub> based gas mixtures however, the drift velocity is considerably larger, see Fig. 2.2. The timing of the signals of all strips within a cluster are therefore more difficult to distinguish. Accordingly the timing distribution of the first strip is considerably influenced by the timing distribution of the second strip as well as the last strip of the cluster is significantly influenced by the second to last, leading to a timing distribution which is in general too broad.

It could be shown that the problem of interfering strip timings can be solved best by considering only the timing of earliest and latest strip of the cluster, defining the ionization process directly at the cathode and the mesh, respectively. Both timings are determined by either taking the minimum or maximum of the timings, checked for fit quality to the strip pulse and timing plausibility. As the signal timing is known for each strip individually, it is possible to histogram both timings separately and extract the time difference between average timing of earliest and latest strip, see Fig. 4.5, left. The values are extracted by fitting a Gaussian function to each distribution. This difference defines the time an electron needs to travel from the cathode to the mesh and can be used to determine the drift velocity in the used gas. Of course this method also works for gases with smaller drift velocities and could possibly lead to better results.

## 4.4 Determination of Hit Position

### 4.4.1 Centroid Method

The centroid method, also called the charge weighted mean method, is a commonly used method to reconstruct a particle hit position on a segmented readout structure (being either strips or pixels). A particle traversing the detector, creates an approximately Gaussian distributed charge signal on the respective strips. Weighting the position of each strip  $x_{\text{strip}}$  with the deposited charge  $q_{\text{strip}}$  allows to calculate the charge weighted mean hit position

$$x_{\text{cen}} = \frac{\sum_{\text{cluster}} x_{\text{strip}} \cdot q_{\text{strip}}}{\sum_{\text{cluster}} q_{\text{strip}}} . \quad (4.8)$$

Due to a possible inclination of the track, the resulting reconstructed position of the particle therefore lies in a plane in the middle of the drift gap, which has to be taken into account when aligning detectors.

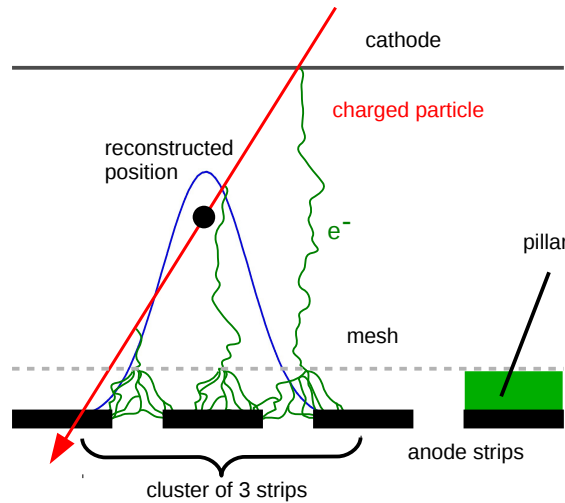


Figure 4.6: Schematic of a slightly inclined particle traversing the detector, where typically only a few strips are hit. The ionization charge created by the traversing particle creates an approximately Gaussian distributed charge signal (blue) on the corresponding strips.

The charge weighted mean hit position yields reliable and good results for close to perpendicularly incident particles. For inclination angles larger than  $10^\circ$  [J.Bortfeldt, 2014], the non-homogeneous ionization of the traversing particles leads to a jitter of the reconstructed position, thus worsening the spatial resolution. For inclined tracks, the  $\mu$ TPC method can provide an additional hit position, independent of the distribution of charge on the strips and thus more appropriate than the charge weighted mean.

### 4.4.2 $\mu$ TPC Method

For the reconstruction of the hit position of inclined particle tracks with angles larger than approximately  $10^\circ$ , the  $\mu$ TPC method can provide an additional hit position, independent of the charge distribution on the strips and thus not influenced by non-homogeneous clustering effects during the ionization process of the traversing particle. As explained in section 4.2, a straight line can be fitted to the (strip,time) data points, describing the particle trajectory in the strip-time plane by

$$t(s) = a \times s + b, \quad (4.9)$$

with  $t(s)$  being the signal time of a certain strip  $s$ ,  $a$  the slope of the track and  $b$  the intersection with the time axis. With both parameters  $a$  and  $b$  known, every point on the line can be reconstructed.

The maximum drift time  $t_{\max}$  an electron needs to travel from the cathode to the mesh can be extracted from the time distribution shown in Fig. 4.7, right, and explained in section 4.3.2. Accordingly the minimal recorded time  $t_{\min} \neq 0$  corresponds to the ionization process directly at the mesh. Hence the time  $t_{1/2} = (t_{\max} + t_{\min})/2$  can be determined, suitable for defining an additional hit position, see Fig. 4.7, left. It could be shown that an online calculation of  $t_{1/2}$  on an event-to-event basis leads to a minor degradation of the resulting spatial resolution, however, with the advantage of not running the analysis algorithm twice.

Using Eq. (4.9), the additional  $\mu$ TPC based hit position  $x_{\mu\text{TPC}}$  is then given by

$$x_{\mu\text{TPC}} = \frac{t_{1/2} - b}{a}. \quad (4.10)$$

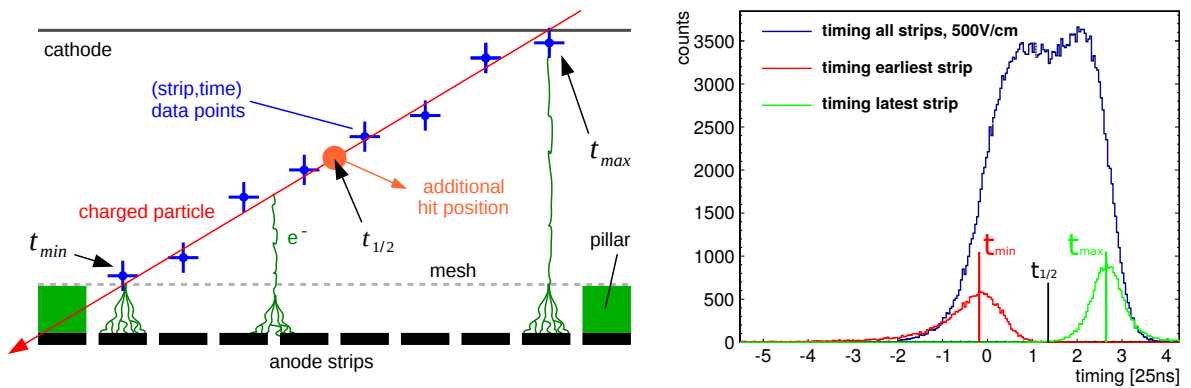


Figure 4.7: Using the  $\mu$ TPC method to reconstruct the slope of the track enables the possibility to extract an additional hit position: By determining the maximum drift time  $t_{\max}$  an electron needs to drift from the cathode to the mesh from the timing distribution (right), the time  $t_{1/2} = (t_{\max} + t_{\min})/2$  on half passage through the drift gap can be determined. This opens the possibility to reconstruct a charge independent hit position (left, orange) of the particle, suited for inclined particle tracks.

It is possible that the average reconstructed  $\mu$ TPC hit position  $\bar{x}_{\mu\text{TPC}}$  differs from the average centroid position  $\bar{x}_{\text{cen}}$ , due to the not optimally reconstructed time distributions or fits to the distribution, resulting in a slightly incorrect  $t_{1/2}$  value. Therefore an

effective time  $t_{1/2, \text{eff}}$  can be approximated: Comparing the mean reconstructed hit positions  $\bar{x}_{\text{cen}}$  and  $\bar{x}_{\mu\text{TPC}}$ , the effective time  $t_{1/2, \text{eff}}$  can be determined iteratively by varying  $t_{1/2}$  until  $\bar{x}_{\mu\text{TPC}} = \bar{x}_{\text{cen}}$ .

For unknown track inclination  $\Theta$  it is possible to use a combined version of both methods [Ntekas, 2013]. The combined hit position  $x_{\text{comb}}$  is then given by the sum of both hit positions  $x_{\text{cen}}$  and  $x_{\mu\text{TPC}}$ , each weighted with a factor depending on the registered number of hit strips  $n_{\text{strips}}$  within the cluster, following

$$x_{\text{comb}} = \frac{w_{\text{cen}} \cdot x_{\text{cen}} + w_{\mu\text{TPC}} \cdot x_{\mu\text{TPC}}}{w_{\text{cen}} + w_{\mu\text{TPC}}}, \quad (4.11)$$

with

$$w_{\text{cen}} = \left( \frac{n_{\text{strips cut}}}{n_{\text{strips}}} \right)^2 \quad \text{and} \quad w_{\mu\text{TPC}} = \left( \frac{n_{\text{strips}}}{n_{\text{strips cut}}} \right)^2. \quad (4.12)$$

The variable  $n_{\text{strips cut}}$  represents the cut value in units of strips, describing the maximum number of hit strips for perpendicular incident particles. For the used floating strip Micromegas detectors in this thesis, with a strip pitch of 0.5 mm and strip width of 0.3 mm, a perpendicularly incident particle typically creates signals on three strips. Comparing this with an incident particle with  $\Theta \approx 35^\circ$ , typically more than 9 strip hits are registered. Accordingly a discrimination value of  $n_{\text{strips cut}} = 4$  has been chosen. Let, for example, a particle, perpendicular incidenting, create a signal on three strips using the combined hit reconstruction, both weights can be calculated from Eq. (4.12):

$$w_{\text{cen}} = \left( \frac{n_{\text{strips cut}}}{n_{\text{strips}}} \right)^2 = \left( \frac{4}{3} \right)^2 = \frac{16}{9} \approx 1.78$$

and

$$w_{\mu\text{TPC}} = \left( \frac{n_{\text{strips}}}{n_{\text{strips cut}}} \right)^2 = \left( \frac{3}{4} \right)^2 = \frac{9}{16} = 0.563.$$

A particle, incidenting at an angle of  $\Theta \approx 35^\circ$ , creating a signal on 9 strips, yields following weights:

$$w_{\text{cen}} = \left( \frac{4}{9} \right)^2 = \frac{16}{81} \approx 0.198 \quad \text{and} \quad w_{\mu\text{TPC}} = \left( \frac{9}{4} \right)^2 = \frac{81}{16} \approx 5.06.$$

The reconstructed combined hit position, for the perpendicularly incident case, thus consists to

$$\frac{w_{\text{cen}}}{w_{\text{cen}} + w_{\mu\text{TPC}}} \times 100\% = \frac{1.78}{1.78 + 0.563} \times 100\% \approx 76\%$$

and for the non-perpendicularly case to

$$\frac{0.198}{0.198 + 5.06} \times 100\% \approx 3.8\%$$

of the charge weighted mean hit position, respectively. The weighting is chosen such that the combined hit depends mainly on the  $\mu\text{TPC}$  hit for inclined tracks with  $\Theta > 20^\circ$ . However its being dynamically supported by the charge weighted mean position for smaller angles, if the  $\mu\text{TPC}$  line fit fails.

For a perpendicularly incident particle beam, the charge weighted hit reconstruction is always chosen, as it yields excellent results.

## 4.5 Track Fitting

For a detector system consisting of more than two detectors, a straight line can be fitted through the registered hit positions. An analytical  $\chi^2$ -minimization (for analysis results computed in chapter 5) and a combinatorial Kalman-filter based method (for chapter 6) has been used to reconstruct the track parameters, described in the following two sections.

### 4.5.1 Track Reconstruction via Analytic $\chi^2$ -Minimization

The fit of a two parameter function, such as a straight line  $x(z) = az + b$ , to a set of data points  $(z_i, x_i)$ ,  $i = 1, \dots, n$  can be performed analytically [Horvat, 2005]. This can either be used for track reconstruction in a detector system with registered hit  $x_i$  of detector layer  $i$ , or for the single layer  $\mu$ TPC tracklet reconstruction described in section 4.2. An overview of the main steps within the  $\chi^2$ -minimization can be found in appendix A.1.

### 4.5.2 Combinatorial Kalman Filter Based Track Reconstruction

For a detector layer which registered more than one hit, resulting from i.e. simultaneous passage of multiple particles, it is important to identify the true hit position belonging to each observed particle. When reconstructing multiple tracks per event, the maximum number of tracks per event is defined by the layer with the smallest number of clusters. The used Kalman filter performs a least-squares fit of the data in a track candidate and is based on a matrix multiplication in the three dimensional space. The algorithm has been implemented by J. Bortfeldt, based on a non-combinatorial exemplary Kalman filter from Tobias Schlüter<sup>2</sup>. The basic principle is explained in a flow diagram, see Fig. 4.8, illustrating the individual steps of the algorithm. A detailed description of the used Kalman filter algorithm can be found in appendix A.2.

## 4.6 Detector Alignment

In order to reconstruct tracks in a detector system, the detectors have to be aligned with respect to their position in space. In the following sections the methods to align the Micromegas with respect to their three space dimensions  $x, y$  and  $z$ , including relative rotations about the axes, are briefly explained. A more detailed discussion can be found in [J.Bortfeldt, 2014].

---

<sup>2</sup>LMU Munich, Excellence Cluster Universe

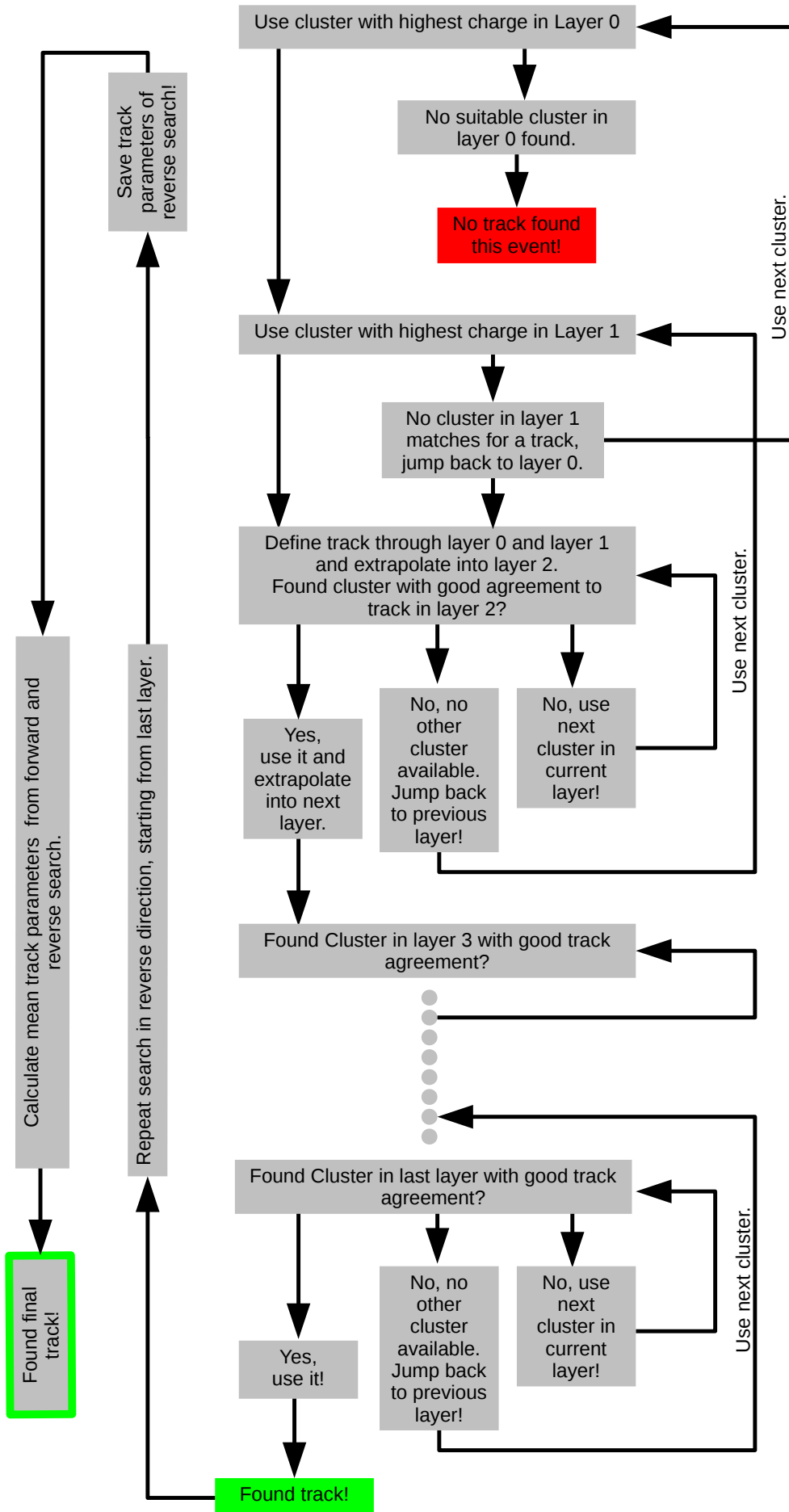


Figure 4.8: Kalman filter based track finding algorithm.

### 4.6.1 High Precision Coordinate $x$ and $y$

Tracking can be used for the alignment of a detector system, e.g. under irradiation with a perpendicular incident particle beam, with respect to the measured high precision coordinate  $x_i$  ( $y_i$ ). Consider a detector system consisting of  $n$  detectors. In a first step, the residual  $\Delta x_{0,n}$  between the measured hit position of the first and last detector layer is determined for many similar tracks, yielding a Gaussian distribution. The mean  $\overline{\Delta x_{0,n}}$  of the distribution can be used to align both layers in the sub-mm region. In the next step, a track is defined only by hits in both layers, excluding the other  $n-2$  layers from the fit, allowing alignment of the rest of the system with respect to the constrained straight line. The correction for the high precision coordinate  $\Delta_{\text{pos } x,y}$  is then given by the mean  $\overline{\Delta x}$  of the residual distribution of the track predicted hit and the measured hit in the investigated layer,

$$\Delta_{\text{pos } x} = \overline{\Delta x} . \quad (4.13)$$

### 4.6.2 Distance $z$ Between Detector Layers

The slope  $a$  of the track, defined by the hits in the detector system, can be used for the determination of the distance between the detectors. A shift in the distance  $z$  of detector layer  $i$  leads to a linear dependence of its measured track residual  $\Delta x_i$  on the measured slope  $a$  of the track:

$$\Delta x_i(a) = m \cdot a + t , \quad (4.14)$$

where the slope  $m$  can be directly used to correct for a shift of the  $z$  position

$$\Delta_{\text{pos } z} = -m \quad (4.15)$$

and the intersect  $t$  allows again for the correction of a shift in the  $x$ -direction.

### 4.6.3 Relative Rotations Around $y$ -Axis and $z$ -Axis

A linear dependence between the measured residual  $\Delta x_i$  and the measured hit position  $x_i$  of layer  $i$  allows for a correction of a rotation  $\Theta$  around the  $y$ -axis. Alternatively, the rotation  $\Theta$  can also be precisely determined by comparing hits of two detectors with only a small relative distance  $z$ . It is described in section 5.5 for a titled floating strip Micromegas doublet with respect to the  $z$ -axis.

For the correction of a rotation  $\Phi$  around the  $z$ -axis, hit information in the two dimensions  $x$  and  $y$  need to be known. A rotation around  $\Phi$  in layer  $i$  then leads to a linear dependence of its measured residual  $\Delta x_i$  on the measured (or track predicted) hit position  $y_i$

$$\Delta x_i(y_i) = m \cdot y_i + t , \quad (4.16)$$

allowing for a correction of  $\Phi$  with

$$\Delta\Phi = \arctan(m) . \quad (4.17)$$

## 4.7 Determination of Spatial Resolution

### 4.7.1 Residual Distribution for Two Layers

The spatial resolution of a detector system consisting of two detectors can only be calculated by directly comparing the measured hit positions. Assume a perpendicularly incident beam traversing detector layer 0 and layer 1, measuring hit position  $x_0$  and  $x_1$ , respectively. The difference of the measured hit positions  $\Delta x = x_0 - x_1$  can be calculated for many similar straight tracks, yielding a distribution of residuals as shown in Fig. 4.9, right.

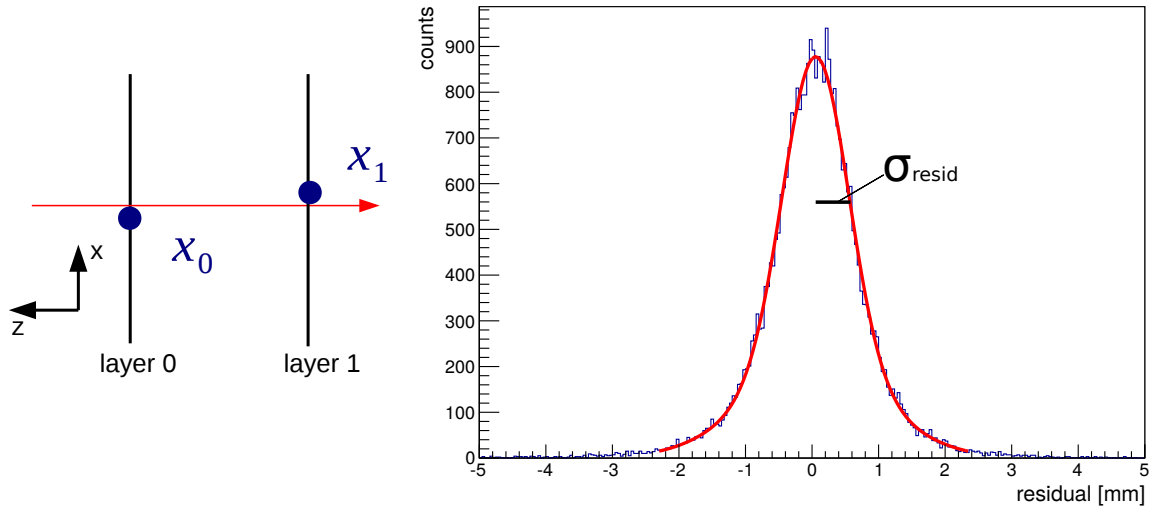


Figure 4.9: The difference of the measured hit position of layer 0 and layer 1 for a perpendicularly incident particle (left figure, red line) can be calculated for many similar tracks and yields a distribution of residuals, shown in the right figure. It has been recorded with 40000 events of 23 MeV protons traversing the detectors. The width of the distribution  $\sigma_{\text{resid}}$ , determined by a fit with a Gaussian function, allows directly for the calculation of the spatial resolution of the involved detectors.

Assuming that all tracks are parallel, the width of the distribution  $\sigma_{\text{resid}}$  includes the spatial resolution of both involved detectors,  $\sigma_0$  and  $\sigma_1$ . Thus, assuming Gaussian distributed contributions

$$\sigma_{\text{resid}}^2 = \sigma_0^2 + \sigma_1^2 . \quad (4.18)$$

Using equal operational parameters for both layers, their spatial resolutions are assumed to be equal, i.e.  $\sigma_0 = \sigma_1 =: \sigma_{\text{SR}}$ . Inserting into equation (4.18) yields

$$\sigma_{\text{SR}} = \sigma_{\text{resid}} / \sqrt{2} . \quad (4.19)$$

As the operational parameters of a detector are often varied to investigate its behavior on the varied parameter, in a first step, the spatial resolution for equal parameters can be calculated by Eq. (4.19). This allows to calculate the spatial resolution of layer  $i \in 0,1$  with varied operational parameters via Eq. (4.18), yielding

$$\sigma_{\text{SR}, i} = \sqrt{\sigma_{\text{resid}}^2 - \sigma_{\text{SR}}^2} . \quad (4.20)$$

As this method assumes a perpendicularly incident beam with parallel tracks, the resulting spatial resolution is rather an upper limit of the true spatial resolution, as a possible divergence of the beam and multiple scattering of the particles in the detector readout structure broadens the residual distribution. Therefore it applies generally that

$$\sigma_{\text{SR}} \leq \sigma_{\text{resid}}/\sqrt{2} . \quad (4.21)$$

### 4.7.2 Track-Based Geometric Mean Method

For a detector system consisting of at least three detectors, a track can be fitted through the measured hit positions as described in section 4.5. The spatial resolution, determined from the residual distribution of measured and track predicted hit, can then be calculated using the geometric mean method, including ( $\sigma_{\text{in}}$ ) and excluding ( $\sigma_{\text{ex}}$ ) the detector under study [R. K. Carnegie, 2005]. The geometric mean, given by

$$\sigma_{\text{SR}} \approx \sqrt{\sigma_{\text{in}} \cdot \sigma_{\text{ex}}} \quad (4.22)$$

provides an estimation of the detector intrinsic resolution, independently of the distance of the detectors used for track fitting [Alexopoulos et al., 2014]. Nevertheless, for reliable results of the spatial resolution determined with the described method, the detectors must have same characteristics and thus equal spatial resolutions.

### 4.7.3 Track Interpolation Method

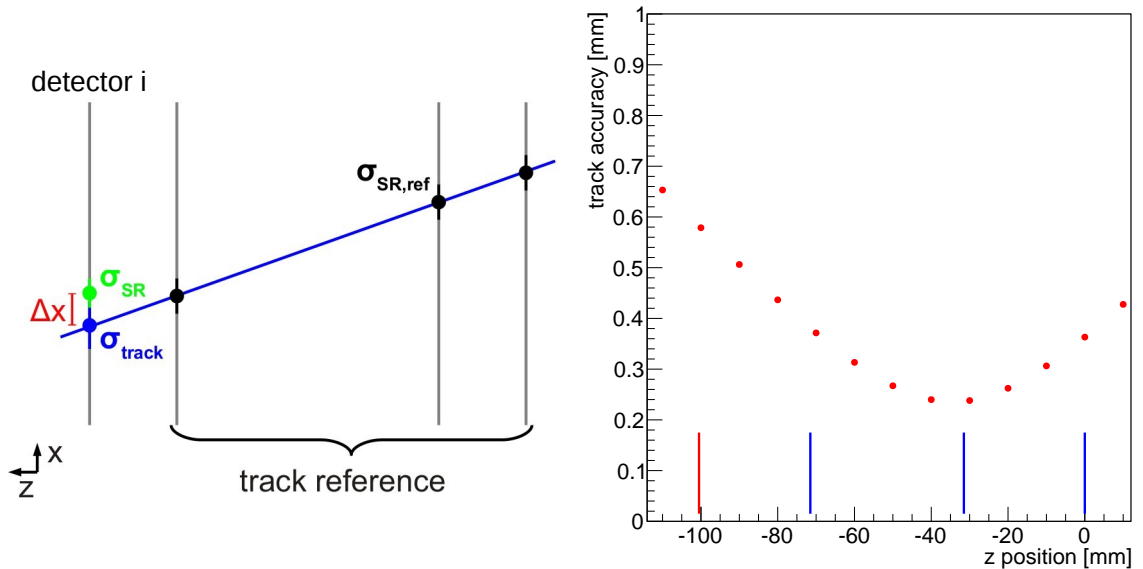


Figure 4.10: The track interpolation method allows calculation of the spatial resolution of a detector under study. The operational parameters of the detector under test can be varied, as the track is defined through a set of reference detectors (left, taken from [J.Bortfeldt, 2014]). The residual of predicted and measured hit is afflicted with the track uncertainty at the position of the detector under test. Determining the track accuracy of the reference system (right; blue lines represent the reference detectors) thus allows for the calculation of the spatial resolution of the studied detector.

When determining the spatial resolution of a detector under test while varying its operational parameters, a set of reference detectors can be used to extrapolate the track into the detector under study. Therefore the resolution of the reference detectors has to be known, e.g. previously determined with the geometric mean method. The residual  $\Delta x$  of predicted and measured hit includes the spatial resolution of the detector under test and the track uncertainty at the position of the detector under test, see Fig. 4.10, left.

Determining the track accuracy  $\sigma_{\text{track}}$  of the reference system (see appendix A.1), allows to calculate the spatial resolution  $\sigma_{\text{SR}}$  of the studied detector, following

$$\sigma_{\text{SR}} = \sqrt{\Delta x^2 - \sigma_{\text{track}}^2} \quad (4.23)$$

Fig. 4.10, right, shows the dependence of the reference track accuracy on the position of the detector under test. It can be seen, that the best track accuracy i.e. minimal track uncertainty is observed near the middle of the reference system, following a parabolic dependence.

# Chapter 5

## Investigation of a Ne:CF<sub>4</sub> 80:20 vol.% Gas Mixture at the Tandem Accelerator

In the following chapter, measurements with four one-dimensional floating strip Micromegas under irradiation with a continuous 23 MeV proton beam at a particle rate of  $(180 \pm 20)$  Hz, acquired at the Max Planck tandem Van de Graaff linear accelerator in Garching, are presented. A new gas mixture Ne:CF<sub>4</sub> 80:20 vol.%, a considerable faster drift gas compared to commonly used Ar:CO<sub>2</sub> based gas mixtures, has been tested and the signal reconstruction capabilities of the Micromegas have been studied. Angle reconstruction capabilities have been tested for inclined detectors at  $(25.5 \pm 1.0)^\circ$ ,  $(30 \pm 1)^\circ$  and  $(35 \pm 1)^\circ$  with respect to the beam axis. Pulse height dependencies on amplification and drift field, spatial resolution for inclined detectors, electron drift velocity measurements and hit efficiencies are presented. In the last section, two of four Micromegas were rotated by  $90^\circ$  around the beam axis, such that the detectors yield hit information in  $x$ - and  $y$ -direction. The tracking system combined with a particle range telescope has then been used to reconstruct images of phantoms positioned in front and behind the tracking system.

### 5.1 Testbeam Setup

The setup during the test beam is shown schematically in Fig. 5.1. Four floating strip Micromegas, always pair-wise mounted back to back forming doublets, represent a tracking telescope of four detectors. All Micromegas have an active area of  $6.4 \times 6.4$  cm<sup>2</sup> with 128 strips of 0.5 mm pitch and 0.3 mm width, an amplification gap of 150  $\mu$ m and drift gap width of 6 mm. The woven micro-mesh consists of 25  $\mu$ m thick wires. For all measurements, despite the ones described in section 5.7, the strips were oriented in  $y$ -direction and thus measuring particle hit position in  $x$ -direction. Micromegas doublet 2, as sketched in the upper left corner of Fig. 5.1, had recently been assembled and thus the operational parameters have been crosschecked. A particle range telescope [Bortfeldt et al., 2016] is placed behind the Micromegas tracking system, consisting of six layers of 1 mm thick plastic scintillators, each equipped with a pair of wave-length-shifting fibers for the readout.

Charge signals of the Micromegas are recorded with APV25 front-end boards (as described in section 3.6) and read out with the Scalable Readout System [RD51, 2010]. The 12 fibers of the particle range telescope are fed into a 64-channel Hamamatsu H7546B-300 multianode photomultiplier [Hamamatsu H7546B-300, 2007] connected to a 4-channel Timing Shaping Amplifier<sup>1</sup> (TSA) with a negative timing output, used for triggering signals with NIM electronics and a positive output to record the signal amplitude via a 16-channel CAEN VME 785N Peak Sensing ADC. For the remaining eight fibers, a 12-channel Le Croy Amplifier with the output fed into a six Ortec 452 Spectroscopy Amplifiers was used to record the pulse height information with the PS ADC. The negative timing signals are fed into a 16-Channel CAEN Low Threshold Discriminator (LTD), whereas the trigger signal for the readout is created by the coincidence (CAEN N455) of both fibers of the first scintillator layer. The timing of all 12 fibers are then recorded by a 16-channel CAEN VME 775N Time To Digital Converter (TDC). In order to avoid missed trigger, the internal busy logic of the VME and a CAEN N93B  $\infty$  Timer was used to create a global busy signal, vetoing the coincidence AND used for generating the trigger. After the VME components finished processing the signals, the CAEN VME 977 I/O resets the  $\infty$  Timer, thus allowing new trigger signals. The VME data communication with the DAQ computer is managed via a CES R102 embedded Power PC. To enable a reliable offline merging of the SRS and VME data streams, impeded by missed triggers especially by the SRS readout system, the trigger signal is separately recorded by the so called Triggerbox [J.Bortfeldt, 2014], a 12 bit scaler. It emits the current counter reading on 12 parallel logic signal outputs, recorded by a TDC for the VME based readout and, after appropriate attenuation, with a dedicated APV25 front-end board (APV injection board) for the SRS system. This also allows for the correction of the 25 ns time jitter in the SRS readout system, see section 3.6. During the measurements, the Micromegas were constantly flushed with a Ne:CF<sub>4</sub> 80:20 vol.% gas mixture with 1.5 ln/h, leading to a slight over pressure in the active region of about 2 mbar with respect to the normal pressure of around 989 mbar and normal temperature of approximately 20°C in Garching. The detectors were supplied with high-voltage via a CAEN SY5527 Universal Multichannel Power Supply System. To avoid further misunderstanding, the Micromegas are named mm0, mm1, mm2 and mm3 with respect to their position in the beam, i.e. the first detector hit by the beam would be mm0 and the last one mm3.

## 5.2 Pulse Height Behavior

In this section, the pulse height behavior for a perpendicularly incident 23 MeV proton beam is discussed as a function of the amplification and drift field for the recently assembled Micromegas mm2 and mm3. A pulse height spectrum of mm2 is displayed in Fig. 5.2, left, fitted with a Gaussian convoluted with a Landau function to extract the most probable pulse height. The spectrum of 40000 events is acquired with an amplification field of  $E_{\text{amp}}=32$  kV/cm and drift field of  $E_{\text{drift}}=500$  V/cm. It is, as described in section 2.1.1, of asymmetric shape, indicating a particle loss of energy typical for a thin - gaseous - detector. The distribution shows a dominant peak at around 2150 ADC

---

<sup>1</sup>developed by Jonathan Bortfeldt at the LMU in Munich

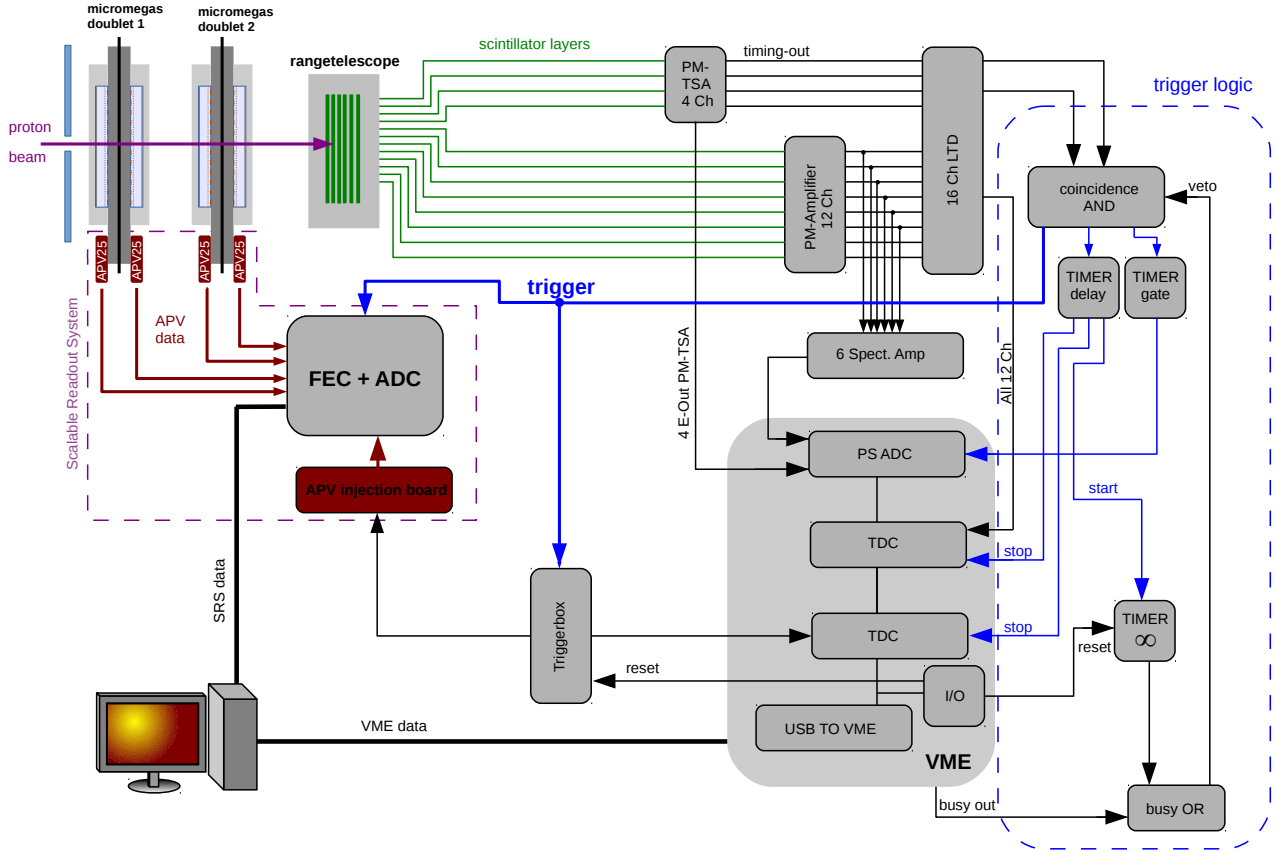


Figure 5.1: Schematic setup for the measurements with 23 MeV protons at the tandem accelerator Garching. Two Micromegas doublets with  $6.4 \times 6.4 \text{ cm}^2$  active area and 128 strips per detector are read out via APV25 front-end boards, using the Scalable Readout System. Traversing protons are stopped within the particle range telescope, consisting of six scintillator layers. The trigger signal for the readout is provided by the coincidence of the two fibers of the first scintillator layer. The range telescope signals are acquired by a VME based readout, providing timing and pulse height information for each layer. The trigger signal is recorded via a 12 bit logic counter unit ('Triggerbox' [J.Bortfeldt, 2014]), allowing to align the SRS and VME data streams and correct for the 25 ns jitter of the SRS system via an additionally used APV25 front-end board ('APV injection board').

channels, corresponding to the most probable energy loss of the protons, and a peak at smaller values around 200 ADC channels, due to insufficient discrimination of noise. The number of hit strips corresponding to the selected charge cluster is displayed in Fig. 5.2, right. With a strip pitch of 0.5 mm, around four hit strips typically correspond to a perpendicularly incident particle.

The extracted most probable pulse height as a function of drift and amplification field is shown in Fig. 5.3. The fit parameter accuracy is used as a vertical error in the following figures. If no error bars are visible, the corresponding marker is bigger than the error.

Typical Micromegas behavior can be observed: A maximum value of the pulse height is achieved for  $E_{\text{drift}} \approx 200 \text{ V/cm}$ . For  $E_{\text{drift}} < 200 \text{ V/cm}$ , the probability of attachment of the ionization electrons to gas atoms and molecules increases. Also the recombination of the created electron-ion pairs is possible for very small drift fields. As these elec-

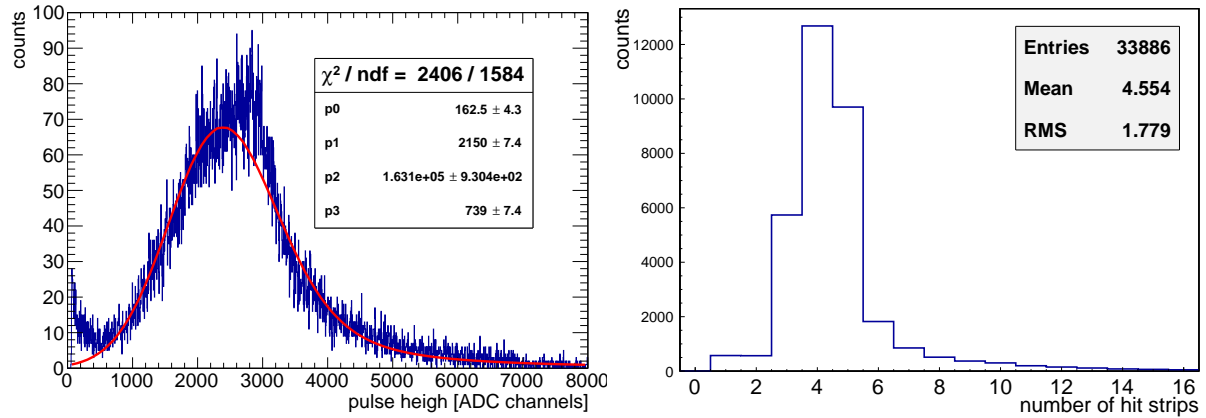


Figure 5.2: Pulse height distribution of Micromegas 2 (left), measured with 23 MeV protons at  $E_{\text{amp}}=32$  kV/cm and  $E_{\text{drift}}=500$  V/cm. The pulse height is filled only if all Micromegas registered a hit, explaining the about 34000 events in the spectrum. A Gaussian convoluted Landau function has been fitted to extract the most probable pulse height of 2150 adc channels. The right figure shows the corresponding number of strips hit within the selected charge cluster, with a maximum at around four strips hit.

trons are lost for the amplification process, the resulting pulse height decreases with further decreasing drift field. For  $E_{\text{drift}} > 200$  V/cm, the pulse height decreases again, due to the dependence of the electron transparency of the micro-mesh on the ratio of amplification and drift field, as explained in section 3.3.

The pulse height dependence on the amplification field shows the expected exponential rise with increasing  $E_{\text{amp}}$ , due to the linear dependence of the Townsend coefficient  $\alpha$  on the amplification field (c.f. Fig. 2.3). For  $E_{\text{amp}} > 32$  kV/cm saturation of both detectors is visible due to a decrease of the measured pulse height.

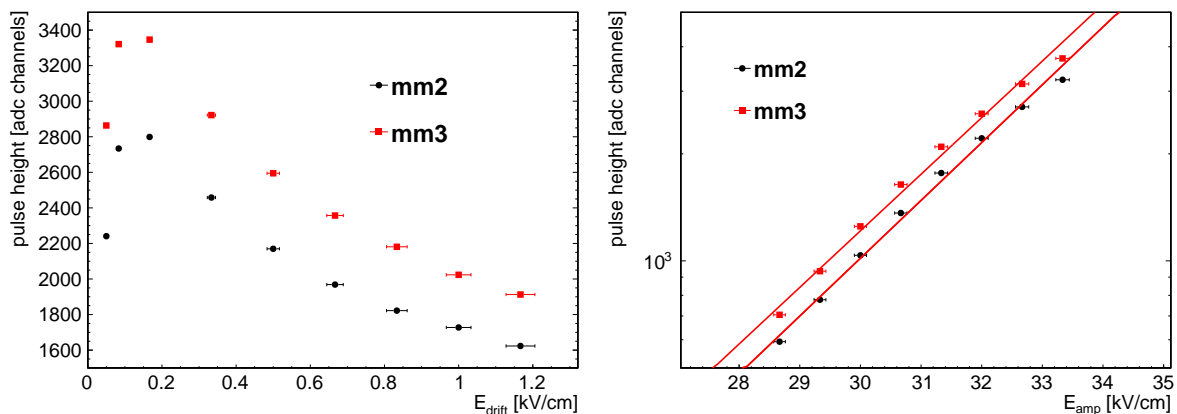


Figure 5.3: The most probable pulse height of mm2 and mm3 as a function of  $E_{\text{drift}}$  (left) with  $E_{\text{amp}}=32$  keV/cm and  $E_{\text{amp}}$  (right) with  $E_{\text{drift}}=500$  V/cm. The typical Micromegas behavior can be observed for both figures, with a higher measured pulse height for mm3 due the lower proton energy after the passage of mm2.

The observed pulse height of mm2 is about 15% smaller than the observed pulse

height of mm3. As protons of 23 MeV energy with  $\beta\gamma \approx 0.25$  are not minimum ionizing particles (see Fig. 2.1), their energy loss  $dE/dx$  per unit path length depends strongly on the energy of the particle. Since 23 MeV protons lose several MeV in the anode PCBs, a loss of energy during the passage of the readout structure of mm2 and mm3 leads to an increase of the energy loss in mm3, resulting in a higher observed pulse height. Fig. 5.4 shows the results of a TRIM based SRIM calculation [Ziegler et al., 2010], for a perpendicularly incident 23 MeV proton beam traversing the detector system consisting of the four Micromegas. The approximately 10 mm thick layer of air between the two doublets has been neglected. The energy loss is thus calculated for transversing the 50  $\mu\text{m}$  Kapton (Polyimid) beam window, the entrance window of 10  $\mu\text{m}$  Kapton, the 10  $\mu\text{m}$  Kapton cathode (Aluminum metalized), the gas filled 6 mm drift gap as well as the readout structures consisting of 35  $\mu\text{m}$  thick copper strips, 125  $\mu\text{m}$  thick FR4 PCB (Epoxy) and the 30  $\mu\text{m}$  thick aluminum shielding foil in between two detectors of one doublet. The 25  $\mu\text{m}$  thick stainless steel micro-mesh has been neglected in the simulation, as it is a woven structure with not well defined thickness and particles are also able to pass through the holes without interacting with the mesh.

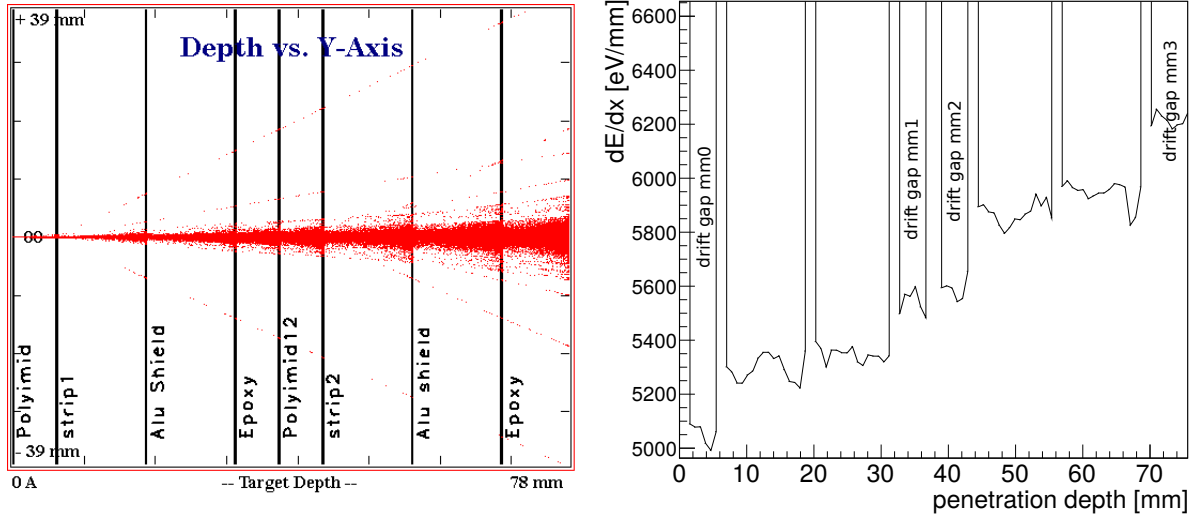


Figure 5.4: TRIM based SRIM simulation for a perpendicularly incident 23 MeV proton beam, traversing the detector system. The left figure shows the particle trajectories (red dots) simulated for approximately 16000 events. The readout structure as well as the gas filled volume in all detectors has been simulated. A broadening of the initially pencil-like beam (0,0 at  $x$ - and  $y$ -axis) up to approximately a FWHM of 8 mm at 78 mm depth due to multiple scattering in the readout material is clearly visible. The right figure shows the calculated energy loss per unit length as a function of the penetration depth, revealing the immense energy loss at the high  $Z$  materials and the increase of energy loss for deeper penetrating beam into the system.

Knowing the energy loss as a function of the position in the detector system, the deposited energy in mm2 and mm3 can be approximated by averaging over the respective energy loss in the drift gaps with thickness  $d = (6.0 \pm 0.2)$  mm. Thus

$$\Delta E|_{mm2} = \left. \frac{dE}{dx} \right|_{mm2} \cdot \Delta x = 5577 \text{ eV/mm} \cdot 6 \text{ mm} = (33.5 \pm 1.2) \text{ keV} \quad (5.1)$$

and

$$\Delta E|_{mm3} = \left. \frac{dE}{dx} \right|_{mm3} \cdot \Delta x = 6220 \text{ eV/mm} \cdot 6 \text{ mm} = (37.3 \pm 1.3) \text{ keV} \quad . \quad (5.2)$$

With an average ionization energy for a Ne:CF<sub>4</sub> 80:20 vol.% gas mixture of  $I=40.4 \text{ eV/ion}$  (c.f. Tab.2.1), the total amount of ionization electrons  $q_0$  created when traversing both drift gaps can be calculated:

$$q_{0,mm2} = \frac{33.45 \text{ keV}}{40.4 \text{ eV/ion}} = (828 \pm 28) \text{ e} \quad (5.3)$$

and

$$q_{0,mm3} = \frac{37.32 \text{ keV}}{40.4 \text{ eV/ion}} \approx (924 \pm 31) \text{ e} \quad . \quad (5.4)$$

Assuming identical detector geometry for both detectors, the ratio of the measured pulse heights  $ph_i$  can be approximated, following

$$ph_{mm2}/ph_{mm3} \approx q_{0,mm2}/q_{0,mm3} = (0.90 \pm 0.06) \quad . \quad (5.5)$$

Thus the observed pulse height difference of approximately 15% is in agreement with the simulation within the errors. Additional deviations could also be due to possible deformations in the amplification gaps on the order of several  $\mathcal{O}(\mu\text{m})$ , leading to deviations of the amplification field and thus slightly different gas gains. This could be determined in a gas gain measurement with a <sup>55</sup>Fe X-ray source, where the recorded pulse height e.g. the current on the anode strips is not sensitive to drift gap deformations, as the 5.9 keV photo-electrons deposit the complete energy within a few millimeters in the drift region.

### 5.3 Efficiency

In this section, the efficiency of the second doublet, i.e. mm2 and mm3, is discussed as a function of the amplification field  $E_{\text{amp}}$  and the drift field  $E_{\text{drift}}$  for a perpendicularly incident beam. Typically the efficiency  $\epsilon$  of a detector is determined by counting the events  $n_{\text{good}}$ , for which the detector registered a hit, divided by the total number of particles  $n_{\text{tot}}$  traversing the detector, e.g. the sum of  $n_{\text{good}}$  and  $n_{\text{bad}}$ , where  $n_{\text{bad}}$  corresponds to the number of events where the detector failed to register a particle hit. Thus

$$\epsilon = \frac{n_{\text{good}}}{n_{\text{tot}}} = \frac{n_{\text{good}}}{n_{\text{good}} + n_{\text{bad}}} \quad . \quad (5.6)$$

As this is a counting experiment for two independent variables  $n_{\text{good}}$  and  $n_{\text{bad}}$ , the error  $\Delta\epsilon$  for the efficiency  $\epsilon$  can be calculated via Gaussian error propagation, following [J.Bortfeldt, 2014]

$$\Delta\epsilon = \sqrt{\left(\frac{d\epsilon}{dn_{\text{good}}} \cdot \Delta n_{\text{good}}\right)^2 + \left(\frac{d\epsilon}{dn_{\text{bad}}} \cdot \Delta n_{\text{bad}}\right)^2} = \sqrt{\frac{\epsilon \cdot (1 - \epsilon)}{n_{\text{tot}}}} \quad . \quad (5.7)$$

For the Micromegas system consisting of four detectors, the efficiency of detector  $i$  can then be calculated by defining the good events  $n_{\text{good}}$  as the number of events where

all detectors registered a signal  $n_{\text{all hit}}$ . The events  $n_{\text{bad}}$  for which detector  $i$  failed to identify a hit, even though all other detectors in the reference system registered a signal, are counted as bad events for detector  $i$ , e.g.  $n_{i \text{ not hit}}$ . Therefore follows for the efficiency  $\epsilon_i$  of detector  $i$

$$\epsilon_i = \frac{n_{\text{good}}}{n_{\text{good}} + n_{\text{bad}}} = \frac{n_{\text{all hit}}}{n_{\text{all hit}} + n_{i \text{ not hit}}} . \quad (5.8)$$

Fig. 5.5 shows the observed efficiency for mm2 and mm3, calculated via equation (5.8), as a function of the drift and amplification field. If no errors in vertical direction are visible, the markers are bigger the corresponding error bars. For the errors in horizontal direction, an uncertainty of the drift gap width  $\Delta d_{\text{drift}}=0.2 \text{ mm}$  leads to a relative error for the drift field of  $\Delta E_{\text{drift}}/E \approx 0.033$ . An assumed amplification gap uncertainty  $\Delta d_{\text{amp}}=3 \mu\text{m}$  leads to a relative error of the amplification field  $\Delta E_{\text{amp}}/E \approx 0.02$ . It should be noted that e.g. an increased amplification gap of  $3 \mu\text{m}$  leads to an effective smaller field but also to additional avalanche steps due to a longer path length, which slightly compensates the smaller field. Nevertheless, a deviation on the order of 2% of the amplification field seems plausible.

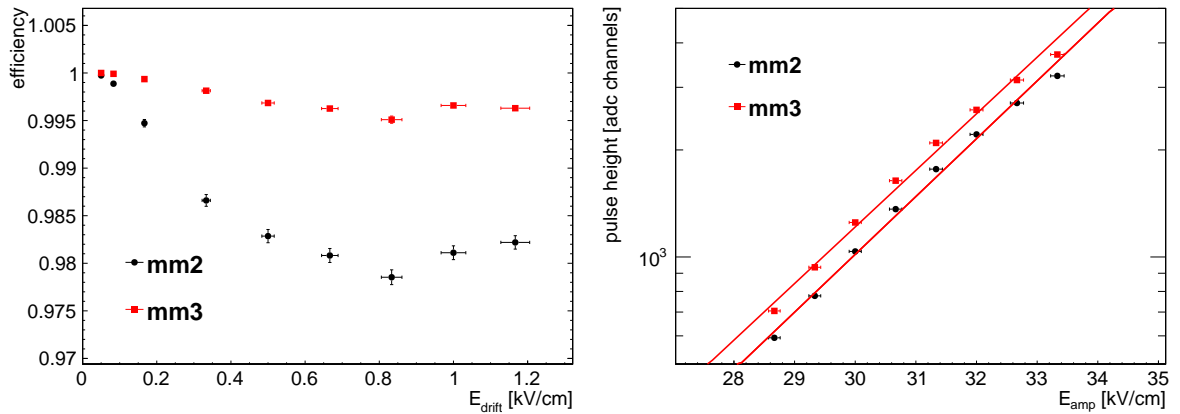


Figure 5.5: The efficiency of mm2 and mm3 as a function of  $E_{\text{drift}}$  (left) with  $E_{\text{amp}}=32 \text{ keV/cm}$  and  $E_{\text{amp}}$  (right) with  $E_{\text{drift}}=500 \text{ V/cm}$ . It should be noted that for typical chosen amplification  $\mathcal{O}(32 \text{ keV/cm})$  and drift field strengths  $\mathcal{O}(300 \text{ to } 500 \text{ V/cm})$ , all efficiencies of the detectors are well above 98%.

The observed efficiency drop in both detectors for increasing  $E_{\text{drift}}$  can be explained by the decreasing mesh transparency, explained in section 3.3. For  $E_{\text{drift}} \approx 800 \text{ V/cm}$ , the efficiency reaches a minimum value of approximately 0.995 for mm3 and approximately 0.978 for mm2, leveling off for  $E_{\text{drift}} > 800 \text{ V/cm}$ . The rise for  $E_{\text{drift}} > 800 \text{ V/cm}$  is somehow unexpected. An explanation may be a variation of the beam shape, which before has hit inefficient parts of the detectors.

The increase of efficiency in both detectors with increasing  $E_{\text{amp}}$  can be explained by the exponential increase of pulse height, thus also allowing for the recovery of small signals at high amplification fields.

For all configurations of  $E_{\text{drift}}$  and  $E_{\text{amp}}$ , the observed efficiency of mm2 is smaller than for mm3. This is on one hand due to the fact mm2 has a pair of dead strips in the beam spot region, ultimately reducing the detection efficiency in this region. Fig. 5.6 shows the hit distribution in  $x$ -direction for mm2 (black) with superimposed mm3 (red). The two dead strips in the mm2 hit distribution can be identified in the region around

$x \approx 45$  mm and have also been observed under a microscope during detector assembly. Some copper strips on the anode structure were interconnected which had to be cut with a scalpel. On the other hand, mm2 generally reconstructs a smaller pulse height than mm3, as described in the previous section, therefore small signals are lost due to the  $3\sigma$  requirement for the strip pulse height during the cluster building.

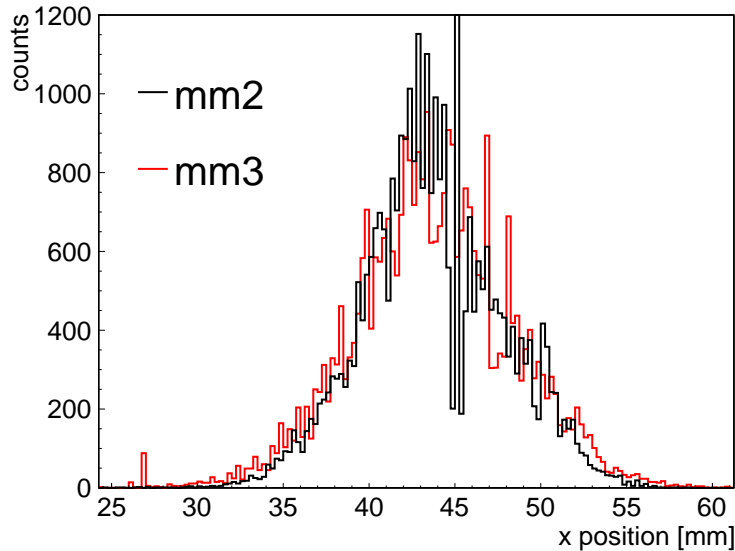


Figure 5.6: Hit distribution in  $x$  direction for mm2 (black) and mm3 (red), recorded with 40000 events of perpendicularly incident 23 MeV protons, at  $E_{\text{drift}} = 500$  V/cm and  $E_{\text{amp}} = 32$  kV/cm. The two dead strips in the beam spot region of mm2 at  $x \approx 45$  mm are visible.

## 5.4 Drift Velocity

The drift velocity of electrons depends strongly on the detector gas composition and the electric field, see section 2.2. To investigate whether the gas of a detector under test is contaminated, it is possible to determine the drift velocity indirectly via the  $\mu$ TPC method or by explicitly measuring the time that ionization electrons need to pass through the drift gap.

Fig. 5.7, left, shows the determined electron drift velocity as a function of  $E_{\text{drift}}$  in mm0. The first doublet has been tilted by  $(35 \pm 1)^\circ$  with respect to the beam axis, such that particles traverse the detector at  $(35 \pm 1)^\circ$ . The drift velocity has been determined with two different methods, measuring the drift time  $\Delta t$  between the cathode and the mesh, as described in section 4.3. The simulated electron drift velocity for a Ne:CF<sub>4</sub> 80:20 vol.% gas mixture has been superimposed. It can be seen that the determined drift velocity via the earliest and latest strip in the cluster yields better results than the determination via the timing distribution of all strips. This is due to the Neon based gas mixture with a higher drift velocity, as compared to the Argon based gases (see Fig. 2.2). The difference of the measured strip timings becomes smaller for higher  $E_{\text{drift}}$ . Thus the strip timing is heavily influenced by neighboring strips in the cluster and thus the edges of the timing distribution are washed out, which ultimately leads to a smaller reconstructed drift velocity. Fig. 5.7, right, shows the timing distribution

of all strips at  $E_{\text{drift}}=1.33$  keV/cm, the timing of the earliest and latest strip has been superimposed. It can be seen that the timing of the falling edge for all strips defined by its point of inflection is larger than the average timing of the latest strip, thus leading to a smaller reconstructed drift velocity.

It has also been tested to take the difference in time of the two inflection points of rising and falling edge of the distribution of the timings with all strips, fitted with two Fermi functions. However, the acquired results were not as good as with earliest and latest timing. It can also be seen that the reconstruction of the earliest timing yields a worse time resolution than for the latest timing, as the fit to the strip pulse is more likely to fail for very early signals not completely recorded within the APV capturing window.

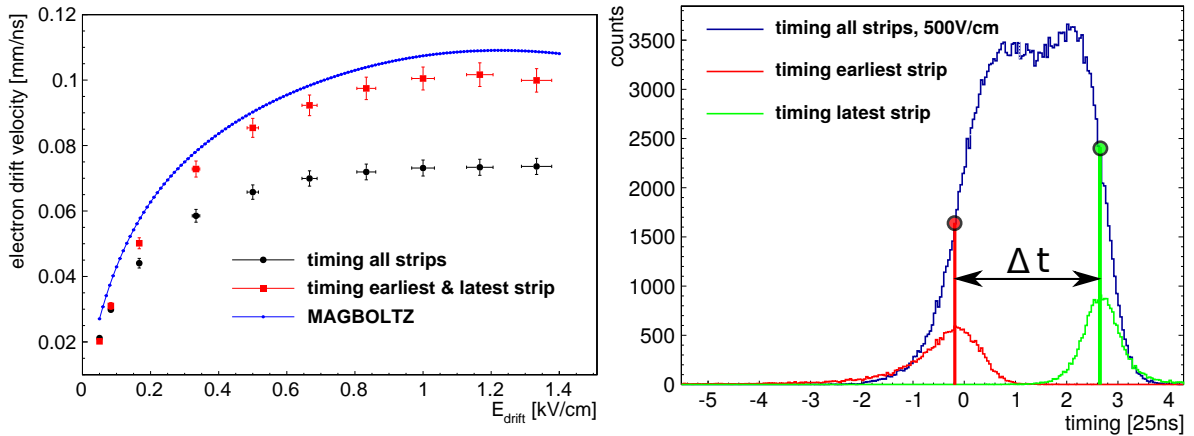


Figure 5.7: Reconstructed electron drift velocity for mm0 via the timing of all strips, as a function on  $E_{\text{drift}}$ , measured with a  $35^\circ$  incident proton beam (left). The drift velocity, determined via earliest and latest strip (red) and a MAGBOLTZ simulation (blue) is superimposed. The slightly broader distribution of all strip timings is visible in the right figure (blue) for  $E_{\text{drift}}=500$  V/cm.

Fig. 5.8, left, shows the drift velocity for particle inclination angles  $(25.5 \pm 1.0)^\circ$ ,  $(30 \pm 1)^\circ$  and  $(35 \pm 1)^\circ$ , determined via measuring the earliest and latest timing of the cluster. The MAGBOLTZ [Biagi, 2012] simulated electron drift velocity for a Ne:CF<sub>4</sub> 80:20 vol.% gas mixture has been superimposed. The reconstructed drift velocity for  $30^\circ$  and  $35^\circ$  are very similar but smaller compared to the simulation, whereas for  $25.5^\circ$  a higher drift velocity has been determined. Fig. 5.8, right, shows the cluster length, e.g. the number of hit strips in the detector, for  $25.5^\circ$  and  $35^\circ$ , respectively. The decrease in cluster length for smaller inclination angles leads to a false reconstruction of the earliest and latest timing, as they are more biased by neighboring strips: For  $35^\circ$  around nine strips are typically hit, whereas for  $25.5^\circ$  only around six strips are usually hit. As time difference between cathode and mesh must be the same for both angles, the timing distribution on the strips begin to smear out, leading to a worse reconstruction. Additionally, capacitive coupling of neighboring strips leads for smaller inclination angles to smaller timings, thus increasing the measured drift velocity.

The drift velocity has also been determined via the  $\mu$ TPC method, as the inclination angle of the particle track is known. This can then be compared to the drift velocity based on drift time measurements, see Fig. 5.9 for a particle incident at an angle of  $35^\circ$ . Comparing both determined drift velocities with the simulation, shows that the

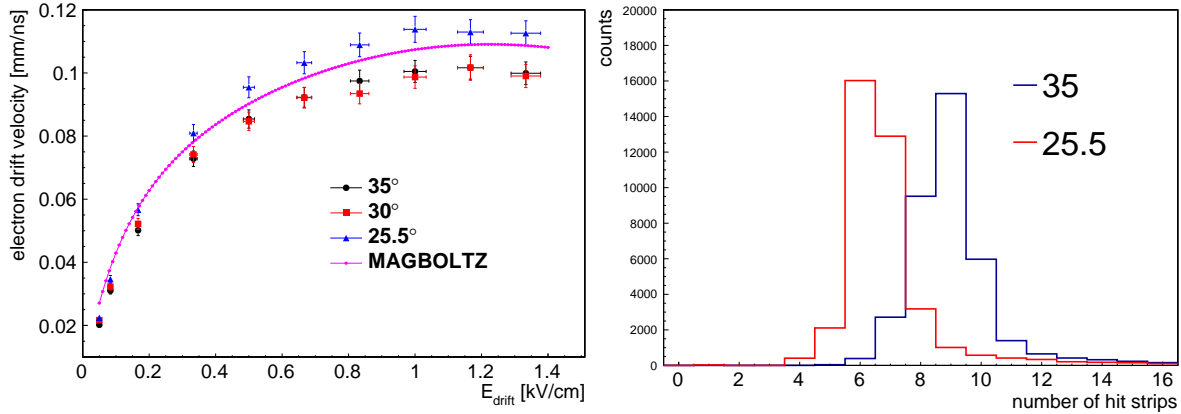


Figure 5.8: Reconstructed electron drift velocity for mm0 as a function on  $E_{\text{drift}}$  (left) for a by 35° (black), 30° (red) and 25.5° (blue) inclined particle track. The reconstruction for 25.5° yields higher values for the drift velocity as for 35° and 30° due to less hit strips (right) for the smaller angle.

measured drift velocity in the gas seems to be systematically smaller than expected. For this reason two simulated drift velocities with an additional admixture of 0.1 and 0.08 vol.% H<sub>2</sub>O gas have been superimposed, respectively, representing left-over humidity in the detector. For  $E_{\text{drift}} \leq 500$  V/cm the better agreement with the data is visible, indicating left over humidity in the detector. For an estimated saturation for H<sub>2</sub>O gas in a Ne:CF<sub>4</sub> 80:20 vol.% at around 2.5 vol.%<sup>2</sup>, an additional admixture of below 0.1 vol.% H<sub>2</sub>O seems plausible. For  $E_{\text{drift}} > 500$  V/cm the difference between simulation and data increases due to the misreconstruction of the correct signal timings at high drift velocities for high values for  $E_{\text{drift}}$ , also limited by the time resolution of the readout system.

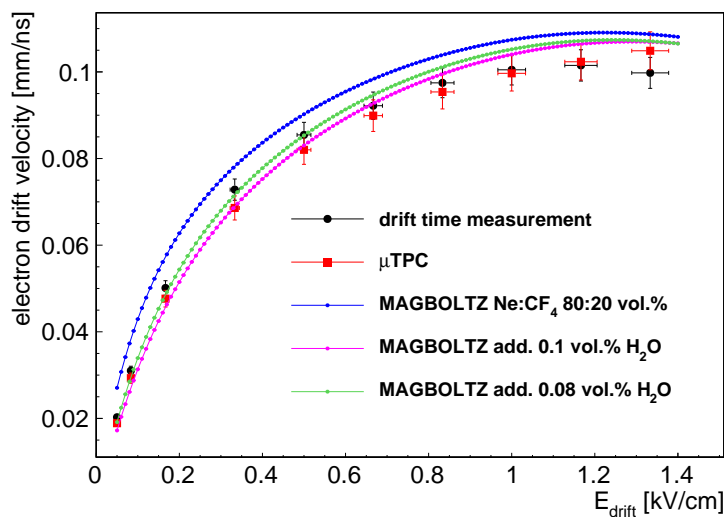


Figure 5.9: Reconstructed and simulated electron drift velocities for mm0 with a particle beam incident at an angle of 35°. Simulations with additional humidity of 0.1 and 0.08 vol.% H<sub>2</sub>O gas are superimposed.

<sup>2</sup>J. Bortfeldt, private communication

## 5.5 Track Angle Reconstruction and Angular Resolution

In this section, the angular reconstruction capabilities of the detectors are tested with the Ne:CF<sub>4</sub> based gas mixture. The first doublet, consisting of mm0 and mm1, has thus been inclined to  $(25.5 \pm 1.0)^\circ$ ,  $(30 \pm 1)^\circ$  and  $(35 \pm 1)^\circ$  with respect to the beam axis. Besides the angle reconstruction via the  $\mu$ TPC method, the incident angle can also be reliably reconstructed by the shift of the beam spot measured in mm0 and mm1, independent of the detector gas composition. The idea is explained in Fig. 5.10, left.

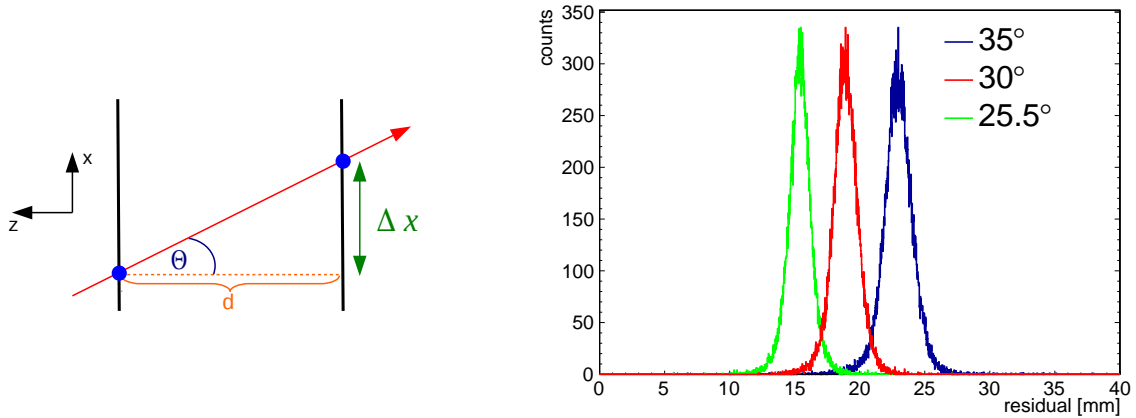


Figure 5.10: Determined hit positions (blue points, left figure) in two different detector layers (vertical black lines) differ by a certain distance  $\Delta x$  for a particle traversing the system at an inclination angle  $\Theta$ . With known distance  $d$ , the inclination angle can be reconstructed due to a shift of the measured residual distribution (right) between both layers.

Assume a particle incident at an angle  $\Theta$  traversing mm0 and mm1 which measure hit positions  $x_0$  and  $x_1$ , respectively. Determining the residual between hit positions of both detectors for many similar tracks yields a distribution with the mean value shifted with respect to the non-inclined case by  $\Delta \bar{x} \neq 0$ , see Fig. 5.10, right. By fitting the upper part of the distribution with a Gaussian function, the relative shift of the beam spot  $\Delta x$  of mm0 and mm1 can thus be determined. The inclination angle  $\Theta$  can then be calculated, following

$$\Theta = \arctan \left( \frac{\Delta x}{d} \right) , \quad (5.9)$$

where  $d=(31.9 \pm 0.5)$  mm is the distance between mm0 and mm1. Tab. 5.1 summarizes the determined angles  $\Theta$  for the three different inclination angles.

The reconstructed angles, listed in Tab. 5.1, are all slightly bigger but very close to the assumed angles for the tilted doublet. The systematically too big reconstructed angle may be due to a minimally underestimated distance between the detectors.

angle [°]	$\Delta x$ [mm]	reconstructed $\Theta$ [°]
25.5	15.40	$25.8 \pm 0.4$
30	18.91	$30.7 \pm 0.4$
35	22.98	$35.8 \pm 0.5$

Table 5.1: Determined inclination angle  $\Theta$  via the shift of the beam spot in mm0 and mm1.

The  $\mu$ TPC method represents a possibility to reconstruct the inclination angle of a particle in a single plane, see section 4.2. Fig. 5.11 shows the distribution of the reconstructed  $\mu$ TPC angle for mm0 with an inclination angle  $\Theta=35^\circ$ , recorded with 40000 events, for  $E_{\text{drift}}=50$  V/cm (black) and  $E_{\text{drift}}=1300$  V/cm (red). The strong dependence of the angular resolution, i.e. the width of the distribution, on the drift field is clearly visible. This is due to the smaller pulse height and larger electron drift velocity for higher drift fields, as the quality of the reconstructed slope suffers from fast signals.

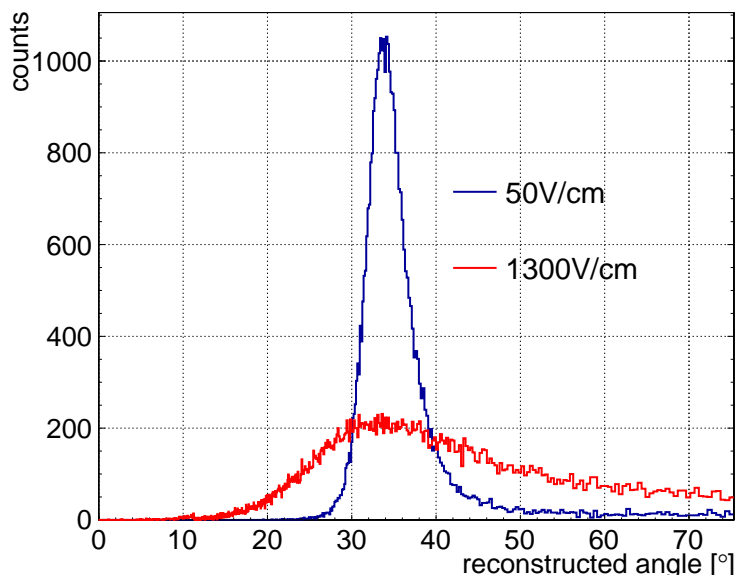


Figure 5.11: Reconstructed angle in mm0 via the  $\mu$ TPC method with 40000 recorded events of  $35^\circ$  incident 23 MeV protons and a Ne:CF<sub>4</sub> 80:20 vol.% gas mixture. The strong dependence of the angular resolution on  $E_{\text{drift}}$  is visible, yielding a distinctly narrower distribution for  $E_{\text{drift}}=50$  V/cm (black) than for  $E_{\text{drift}}=1.3$  kV/cm (red).

Furthermore the reconstructed most probable angle is for both drift fields smaller than the assumed  $35^\circ$  incident angle. This needs some investigation, as the reconstructed angle via the shift of the beam spot is slightly larger but still in good agreement with the actually rotated angle. As described in the previous section, the reconstructed drift velocity is also smaller than expected. Assuming a detector gas contamination of approximately 0.1 vol.% humidity leads to a smaller effective drift velocity, resulting in a larger reconstructed angle. Fig. 5.12 shows the most probable reconstructed angle and the angular resolution as a function of the drift field for mm1 with an assumed humidity of 0.08 vol.%. The red dashed bar in the figures illustrate the true inclination angles of the doublet,  $(25.5 \pm 1.0)^\circ$ ,  $(30 \pm 1)^\circ$  and  $(35 \pm 1)^\circ$ .

The reconstruction with the slightly modified drift velocity yields good results, as for nearly all drift field configurations the reconstructed angles agree with the expectation within the errors. For  $E_{\text{drift}} > 300 \text{ V/cm}$  the angular resolution steadily increases with increasing  $E_{\text{drift}}$ . As the signal formation thus takes less time, it leads to smaller difference between the timings of adjacent strips within the cluster and therefore the quality of the line fit to the (strip,time)-data points suffers, also limited by the finite time resolution of the readout electronics. In general one has to say, that the angle reconstruction via the  $\mu\text{TPC}$  method depends strongly on the drift velocity of the used gas. Thus for an optimal angular reconstruction, a slow drift gas is in most cases the preferred choice. Nevertheless, the most probable reconstructed angle also reveals excellent results for the used fast gas mixture. Taking a closer look at the reconstructed angle for small values of  $E_{\text{drift}} < 300 \text{ V/cm}$  reveals, that for all inclination angles the reconstructed value is bigger than expected. As explained in section 4.2, the  $\mu\text{TPC}$  method tends to reconstruct larger angles due to the capacitive coupling of adjacent strips. A LTSpice based detector simulation of the used floating strip Micromegas detectors has been implemented by J.Bortfeldt [2014], explaining the systematic shift of the signal timings for all strips towards earlier values. Even for non hit strips in the cluster, a pulse height of 25 % of the neighboring strips could be detected.

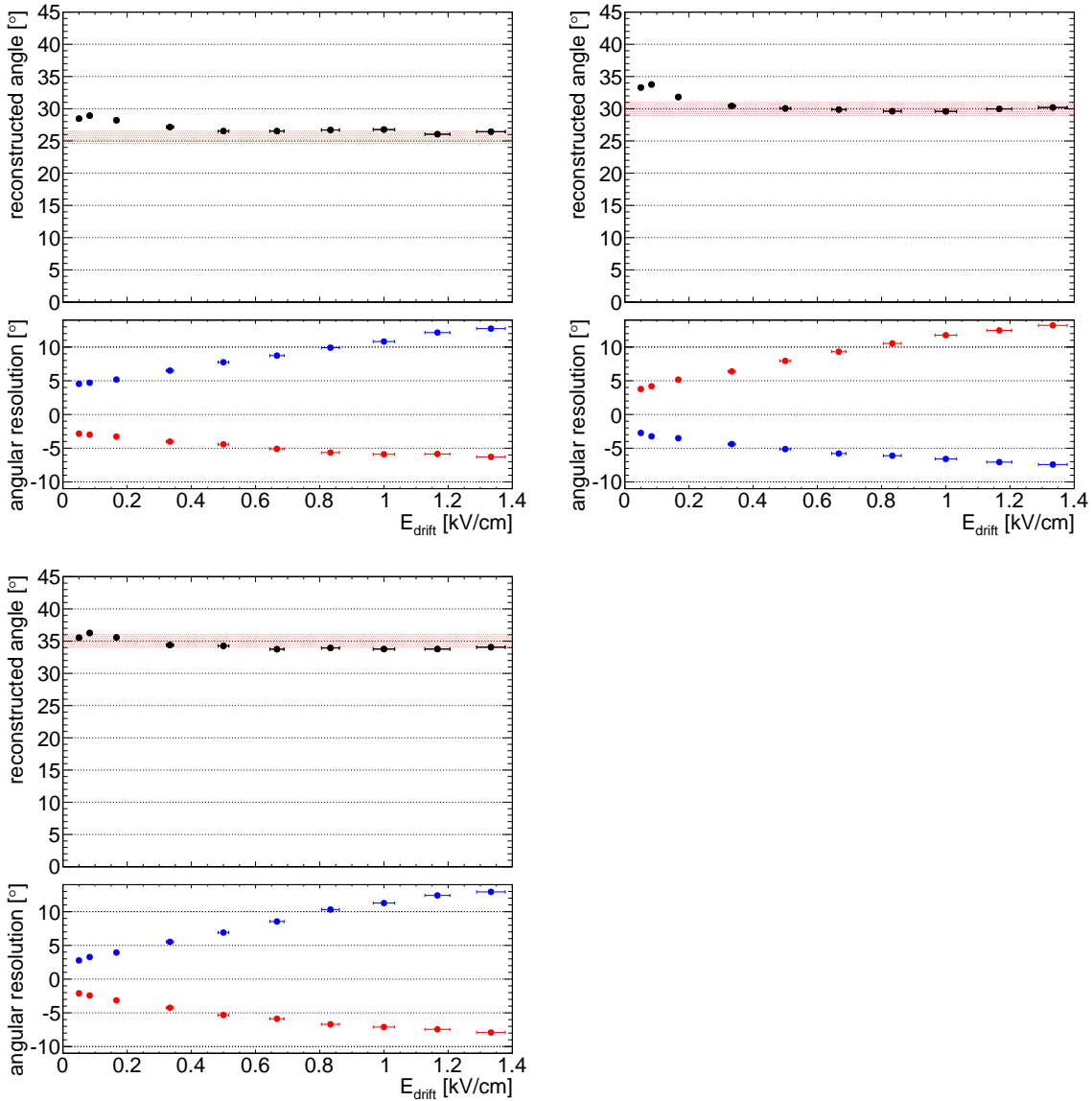


Figure 5.12: Reconstructed most probable angle and angular resolution for mm1, acquired with the  $\mu$ TPC method for an inclination angle of  $(25.5 \pm 1.0)^\circ$  (top left),  $(30 \pm 1)^\circ$  (top right) and  $(35 \pm 1)^\circ$  (bottom), as a function on  $E_{\text{drift}}$  at  $E_{\text{amp}} = 32$  kV/cm.

To compensate the coupling on corner strips of the cluster, they have been explicitly removed from the line fit, if their pulse height is smaller than 25% of the neighbors pulse height. Fig. 5.13 shows the fit quality as a function of the hit strip in a selected cluster used for the  $\mu$ TPC reconstruction for mm0 at  $35^\circ$  with  $E_{\text{drift}} = 500$  V/cm. After checking the corner strips for a reasonable pulse height, it could be observed, that the first and last strip of the cluster, being the 0th and 8th to 10th respectively, could often be identified with a too small pulse height primarily due to capacitive coupling of the adjacent strip and not due to charge deposition.

For  $E_{\text{drift}} < 500$  V/cm, the difference between reconstructed most probable angle and true track inclination is for  $25^\circ$  larger as compared to  $35^\circ$ , as it is more affected by capacitive coupling. Due to only around six strips typically hit, a wrongly measured timing at  $25^\circ$  has a greater impact on the determined slope than for a measurement at

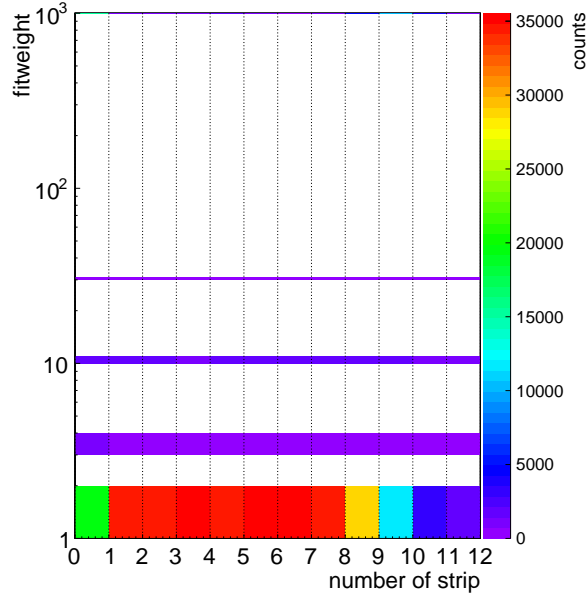


Figure 5.13: Assigned fit weight (as described in section 4.2) as a function of the strip in a selected cluster, used for reconstructing the  $\mu$ TPC slope for a  $35^\circ$  incident beam traversing mm0 at  $E_{\text{drift}} = 500 \text{ V/cm}$  and  $E_{\text{amp}} = 32 \text{ kV/cm}$ . In this context, strip 0 corresponds to the first strip in the cluster, with a small value for the fit weight describing a good signal on the strip, whereas a fit weight of 1000 completely removes the strip from the further analysis. In this figure, strip 0 and strip 9 are often excluded from the fit (fit weight = 1000), as a too small pulse height could be identified, which are not due to charge deposition but due to capacitive coupling of the adjacent strip.

$35^\circ$ , where more than nine strips are usually hit, see Fig. 5.8, right. Referring to small drift fields at e.g.  $E_{\text{drift}} = 50 \text{ V/cm}$ , also the angular resolution shows better results for a larger track inclination at  $35^\circ$  with  $\Delta\Theta \approx_{-2}^{+3^\circ}$  as compared to  $25.5^\circ$  with  $\Delta\Theta \approx_{-3}^{+5^\circ}$ . With increasing  $E_{\text{drift}}$ , measurements at all three inclination angles share the same feature: The reconstructed most probable angle decreases, leveling off around the expected value. This is due to the fact that for small drift fields, the electron drift velocity (including left-over humidity in the detector) is assumed i.e. simulated slightly too small, leading to a bigger reconstructed most probable angle. This is indeed observed for the electron drift velocity at  $E_{\text{drift}} < 500 \text{ V/cm}$  in Fig. 5.9, when comparing drift time measurement and MAGBOLTZ simulation with additional 0.08 vol.% humidity - which has been used for the  $\mu$ TPC angle reconstruction.

## 5.6 Spatial Resolution

In the following section the spatial resolution of mm2 and mm3 for perpendicularly incident beam as well as for mm0 and mm1 for inclined tracks at  $(25.5 \pm 1.0)^\circ$ ,  $(30 \pm 1)^\circ$  and  $(35 \pm 1)^\circ$  is discussed.

The spatial resolution in a detector system consisting of more than two detectors can be determined by extrapolating a track, defined by a reference tracking system, in the detector under test and determine the residual between predicted and measured hit, as described in section 4.7.3. Fig. 5.14 shows the spatial resolution of mm2 and

mm3 for a perpendicularly incident beam, determined with the track interpolation method as a function on  $E_{\text{drift}}$  (left) and  $E_{\text{amp}}$  (right). The corresponding spatial resolution  $\sigma_{\text{mm}_0} = (0.454 \pm 0.04)$  mm at  $E_{\text{drift}} = 500$  V/cm and  $E_{\text{amp}} = 32.67$  kV/cm and  $\sigma_{\text{mm}_1} = (0.346 \pm 0.09)$  mm at  $E_{\text{drift}} = 500$  V/cm and  $E_{\text{amp}} = 31.25$  kV/cm, have been previously determined via the geometric mean method described in section 4.7.2.

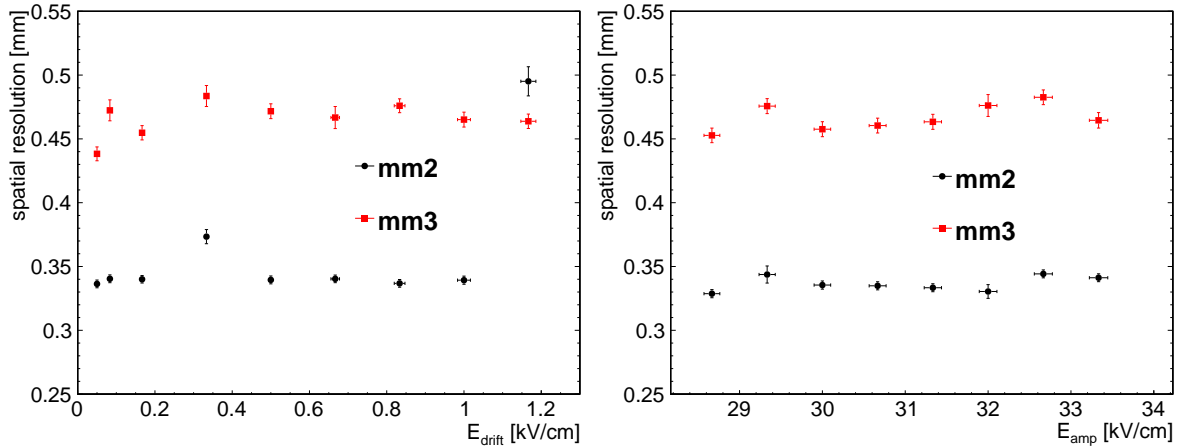


Figure 5.14: Reconstructed spatial resolution of mm2 and mm3 for a perpendicularly incident 23 MeV proton beam as a function on  $E_{\text{drift}}$  (left) and  $E_{\text{amp}}$  (right), determined by the difference of predicted and measured hit in the detector under test. For the drift field variation (left)  $E_{\text{amp}} = 32$  keV/cm has been chosen, where as for the amplification scan (right)  $E_{\text{drift}} = 500$  V/cm was set for both detector layers.

The determined spatial resolution in both layers mm2 and mm3 show no dependence on varied  $E_{\text{drift}}$  and  $E_{\text{amp}}$ . The two points in the left figure for mm2 at  $E_{\text{drift}} = 333$  V/cm and  $E_{\text{drift}} = 1167$  V/cm are misreconstructed due to a reconfiguration of the Scalable Readout System, leading to a variation of the APV25 internal offset and thus a loss of signals. It is observed, that the determined spatial resolution is larger for the outer layers of the tracking system, being mm0 and mm3, and smaller for the inner layers mm1 and mm2. Nevertheless, the determined track accuracy as a function of the detector position, as described in section 4.7.3, should compensate for the bigger measured residuals of the outer layers, due to an increased track uncertainty. As this is not the case, the outer layers are dominated by multiple scattering of the low energy protons at the readout structures between mm0/mm1 and mm2/mm3, respectively. The constant spatial resolution as a function of both drift and amplification field indicates as well that it is dominated by scattering, as a dependence is expected. Also see Fig. 5.4, right, as the energy loss of the protons drastically increases after passing the readout structures for the both doublets, where they lose several MeV and thus scatter accordingly. The measured residual distribution of the first and last compared to first and second detector, for a perpendicular incident beam, see Fig. 5.15, shows the immense broadening of the original beam. It is a combination of beam divergence and scattering of the protons. The width of the residual distribution between mm0 and mm3, acquired with a Gaussian fit, is with  $\sigma_{0,3} = (2.8 \pm 0.2)$  mm more than four times larger than for mm0 and mm1 with  $\sigma_{0,1} = (0.65 \pm 0.09)$  mm.

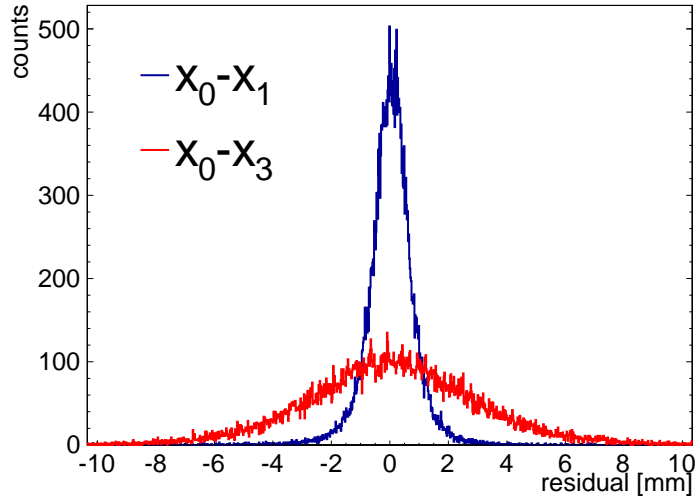


Figure 5.15: Determined residual between measured hits in the first and second detector (blue) for a perpendicular incident 23 MeV proton beam. The residual distribution between first and last detector is superimposed (red). The immense broadening of the beam spot due to multiple scattering of the low energy protons, combined with a beam divergence, is clearly visible.

For the determination of the spatial resolution for inclined tracks, the first doublet consisting of mm0 and mm1 has been tilted to angles  $(25.5 \pm 1.0)^\circ$ ,  $(30 \pm 1)^\circ$  and  $(35 \pm 1)^\circ$ . It has been tried to reconstruct the spatial resolution via the track interpolation method, which can compensate the beam divergence. However, the determination of the spatial resolution with the track reference system yielded implausible high residuals. This is particularly due to two main reasons: First, the track is always constrained via both detectors of the second doublet. Thus the uncertainty of the track increases, as the protons already traversed the first doublet i.e. lost a significant amount of energy via several scattering processes. Second, the first doublet is tilted at an angle  $\Theta$  with respect to the beam axis. This means straightaway that the effective path length of the protons increases proportional to  $1/\cos(\Theta)$ , which additionally increases the energy loss. Furthermore, it is known for Micromegas detectors, that for inclined particle tracks, the charge weighted mean spatial resolution degrades with increasing track inclination. As always one detector of the first doublet is included in the track fit, this additional position uncertainty worsens the track prediction at the other detector. To still be able to reconstruct an accurate estimate of the spatial resolution as a function on the inclination angle, it has been determined directly from the residual distribution of mm0 and mm1 as described in section 4.7.1 and is shown in Fig. 5.16. The hits in both layers have been reconstructed with the charge weighted mean.

For the determination of the spatial resolution, the residual distribution has been fitted with the sum of two Gaussian functions (Fig. 5.16, left). The resulting spatial resolution  $\sigma_{\text{SR}}$  is thus a weighted sum of the determined widths  $\sigma_1$  and  $\sigma_2$  of both Gaussian functions, normalized with the respective integrals, following

$$\sigma_{\text{SR}} = \frac{\text{integral1} \cdot \sigma_1 + \text{integral2} \cdot \sigma_2}{\text{integral1} + \text{integral2}}, \quad (5.10)$$

where the color coding is the same as in Fig. 5.16, left. The resulting spatial resolu-

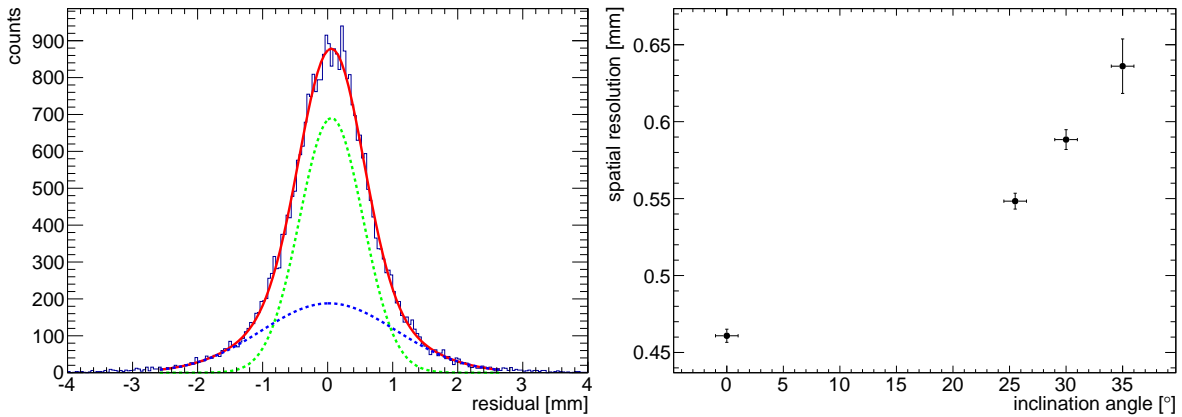


Figure 5.16: Spatial resolution of mm0/mm1 as a function on the inclination angle (right) for angles  $(0 \pm 1)^\circ$ ,  $(25.5 \pm 1.0)^\circ$ ,  $(30 \pm 1)^\circ$  and  $(35 \pm 1)^\circ$ , determined via a fit with two Gaussian functions to the residual distribution (left) of the measured charge weighted mean hits in mm0 and mm1, respectively.

tions for the different angles are shown in Fig. 5.16, right, using the errors resulting from the fit parameters. The operational parameters for both detectors are equal with  $E_{\text{drift}}=500$  V/cm and  $E_{\text{amp}}=32$  kV/cm. The observed dependence on the inclination angle is understandable, as clustering of the traversing particle increasingly affects the charge weighted mean hit position for an increasing track inclination.

For particle tracks with an inclination angle  $> 10^\circ$ , the  $\mu$ TPC method yields an alternative hit position, independent of the charge deposition on the strips (see section 4.4.2). The spatial resolution, determined via the residual distribution of mm0 and mm1, acquired with the charge weighted mean and the  $\mu$ TPC method as a function on  $E_{\text{drift}}$ , at  $E_{\text{amp}}=32$  keV/cm for both detectors, is shown in Fig. 5.17.

The spatial resolution, reconstructed via the charge weighted mean, is for all angles nearly constant over the varied drift field spectrum, c.f. Fig 5.14. However, the spatial resolution acquired with the  $\mu$ TPC method is increasing for increasing  $E_{\text{drift}}$ . This is understandable, as the quality of the  $\mu$ TPC (strip,time) line fit suffers from fast and small signals at high values of  $E_{\text{drift}}$ . Nevertheless, the determined spatial resolution via the  $\mu$ TPC alternative hit reconstruction yields better results than the centroid method for  $E_{\text{drift}} < 500$  V/cm at all inclination angles. For  $E_{\text{drift}}=0.18$  kV/cm and  $35^\circ$ , the spatial resolution acquired with the  $\mu$ TPC method is approximately 16% better than the charge weighted mean, showing only a small dependence on the inclination angle.

## 5.7 2D-Imaging

For the measurements presented in this section, the second Micromegas doublet (mm2 and mm3) has been rotated by  $90^\circ$  around the  $z$ -axis, enabling hit information in  $y$ -direction. The residual range in the particle range telescope, consisting of six layers of 1 mm thick plastic scintillators each equipped with two wavelength shifting fibers, thus yields information about the particle energy, after passing a small PLA step phantom. The conceptual setup for the measurements is schematically shown in Fig 5.18.

The penetration depth in the rangetelescope is determined from binary hit information,

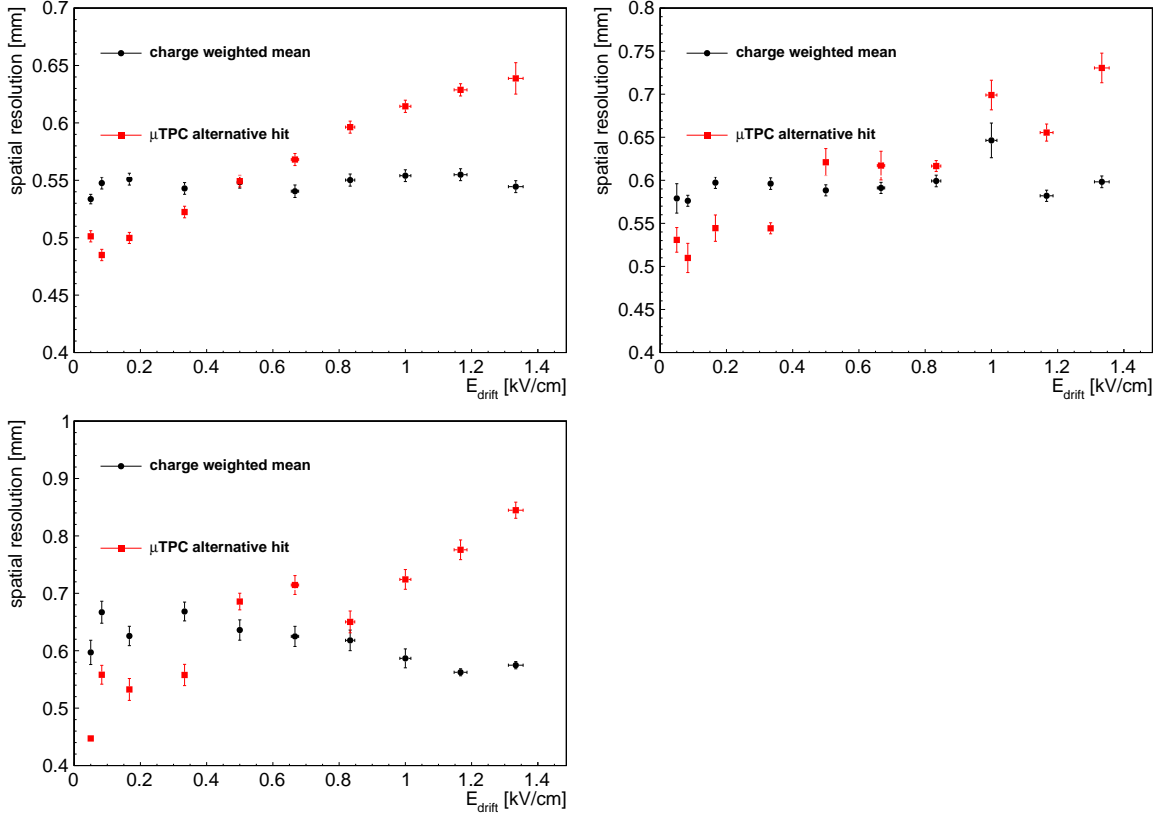


Figure 5.17: Reconstructed spatial resolution of mm1 as a function on  $E_{\text{drift}}$ , acquired with the charge weighted mean (black) and the  $\mu$ TPC alternative hit (red) for an inclination angle of  $(25.5 \pm 1.0)^\circ$  (top left),  $(30 \pm 1)^\circ$  (top right) and  $(35 \pm 1)^\circ$  (bottom), determined via the residual distribution of mm0 and mm1.

i.e. whether a layer is hit, or not. Due to the low proton energy, only the first four layers are hit. The recorded pulse height correlation between two fibers of these four scintillator layers is shown in Fig. 5.19, with a step phantom in the beam positioned 60 mm in front of mm0. It can be seen that for layers 3 and 4, often no signal could be identified, leading to the accumulation of points in the origin, whereas fiber 0 and fiber 1 of layer 0 always register a signal as they were used for triggering. The recorded pulse height for both fibers of layer 0 indicate that fiber 1 reconstructs about a factor of two higher pulse height than fiber 0. For layer 2, the reconstructed pulse height in both fibers are similar. However for layer 1 and layer 3, fiber 1 reconstructs a higher pulse height. The fact that two fibers of one layer reconstruct different pulse heights is on one hand due to the not optimally centered position of the beam, thus preferring a specific fibers geometric position. On the other hand a not immaculate condition of the respective photomultiplier tube ( $\pm 30\%$  amplification for each pixel of the photomultiplier tube as specified by the manufacturer) could as well lead to a decrease of the recorded pulse height. Also the endings of each fiber may be polished differently, leading to a loss of photons.

As different amplifier electronics has been used for layer 0 and 1 (TSA) and layer 2 to 5 (Ortec) no direct comparison of the pulse height between layers is possible. However, from the pulse height and hit distribution over the first four scintillator layers it can be assumed that most of the protons get stopped within the first 3 layers.

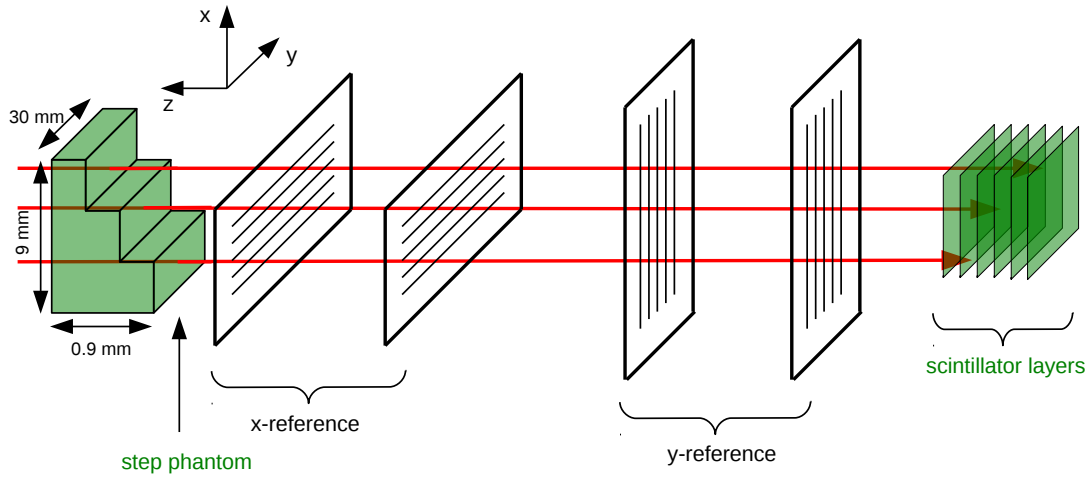


Figure 5.18: Setup for the radiography of a step phantom, acquired with the Micromegas tracking system. The second doublet has been tilted by  $90^\circ$  around the beam axis, enabling the hit information in  $y$ -direction. The step phantom is positioned in front and behind the tracking system, with the particle range telescope used to retrieve an energy loss information of every single particle via the penetration depth into the scintillator layers.

Fig. 5.20 shows the number of registered hits as a function of the penetration depth in the range telescope, in units of scintillator layers with and without the step phantom in the beam. The coincidence signal of both fibers of layer  $i$  marks the respective layer as hit. Layer  $i + 1$  is only allowed to register a hit, if the previous layer  $i$  already registered a signal. The distribution shows that most of the protons get stopped within the first three layers. Without the phantom in the beam, more hits are registered in the third and fourth layer. For the step phantom in the beam, more protons get stopped within the first two layers, as they do not have sufficient energy to penetrate further into the following layers. The pulse height distribution of Fig. 5.19 indicates the same behavior.

For every triggered event, the penetration depth into the range telescope is then filled into a histogram as a function of the hit position predicted by the Micromegas tracking system. A 'dynamic' bin width of 0.6 mm has been chosen, consisting of nine  $0.2 \text{ mm}$  bins with different weights  $w$ , allowing two bins to overlap and build a combined bin content. The principle is sketched in Fig. 5.21, left. The central bin, corresponding to the predicted particle hit position, is initialized with a weight  $w=1$ , whereas all surrounding eight bins are also filled with the same content, but with  $w=0.5$ . This corresponds to an uncertainty of 50% to the predicted position within a  $0.2 \times 0.2 \text{ mm}^2$  bin, due to the scattering of the low energy protons, but with a combined bin width of 0.6 mm in the same order as the determined spatial resolution of  $\mathcal{O}(0.5 \text{ mm})$ .

The acquired radiography of the step phantom, positioned behind the tracking system, is shown in Fig 5.21, right. The horizontal axis represents the reconstructed particle hit position in  $y$ -direction, acquired by mm2 and mm3, whereas the vertical axis yields the hit information in  $x$ -direction, measured by mm0 and mm1. The bin content corresponds to the measured particle range in the telescope, averaged over all events. The phantom can be identified within the geometric region for  $x \lesssim 54 \text{ mm}$  and  $30 \lesssim y \lesssim 60 \text{ mm}$ . The actual width of the phantom with  $d_y = 30 \text{ mm}$  in  $y$ -direction could thus be reconstructed very well via the relatively sharp edges of the image at  $y=29 \text{ mm}$  and

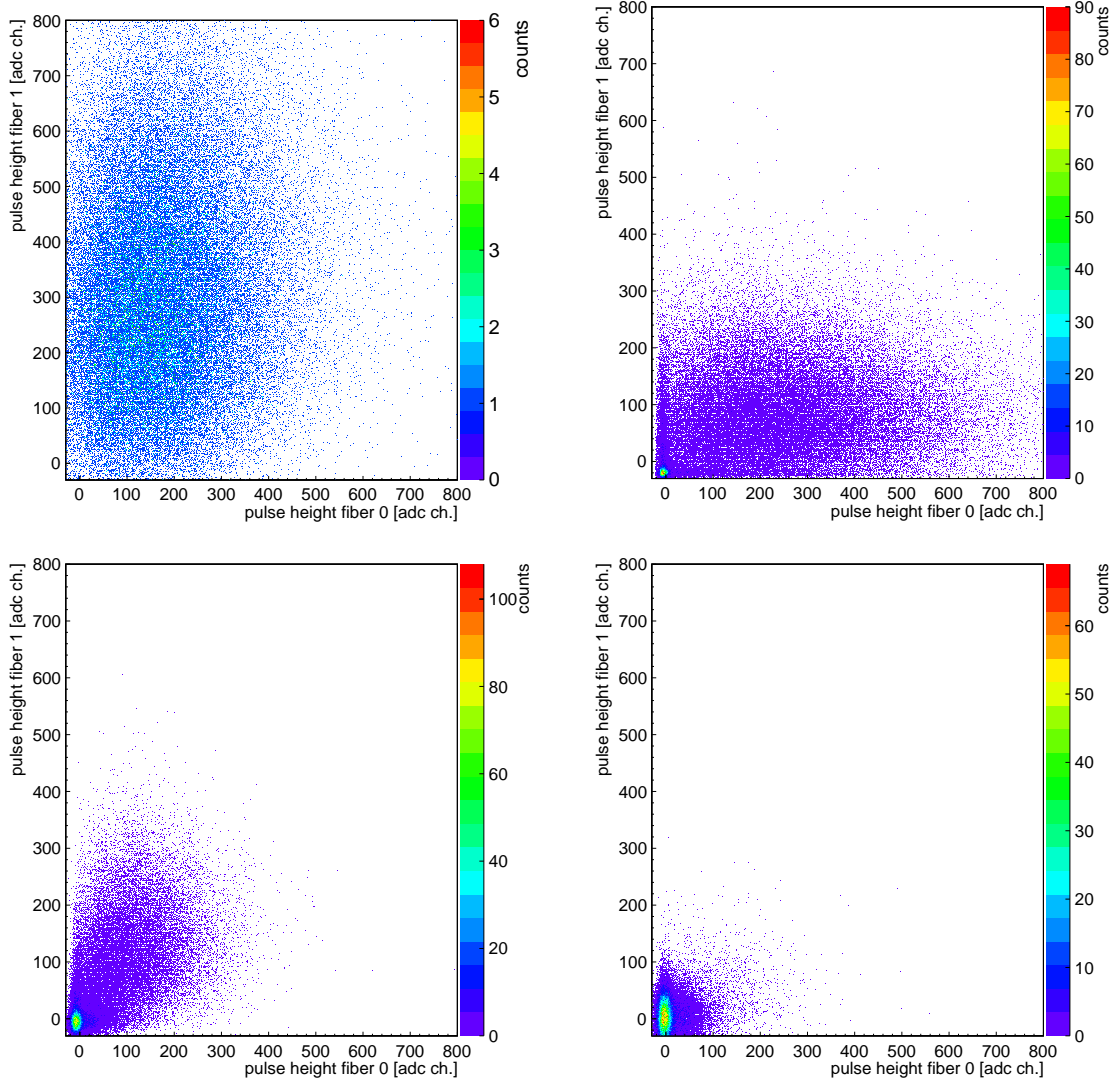


Figure 5.19: Correlation between the recorded pulse heights of the two fibers belonging to scintillator layer 0 (top left), layer 1 (top right), layer 2 (bottom left) and layer 3 (bottom right).

$y=60$  mm. For the  $x$ -direction however, no sharp borders are observed. A continuous decrease of the average range is observed for  $x \lesssim 54$  mm. This is understandable, as the thickness of one scintillator layer with 1 mm is larger than the difference in thickness between two adjacent steps of the phantom with 0.3 mm. Due to the scattering of the protons and the considerable extrapolation error of the track in  $x$ -direction, the reconstruction of the edges is not optimal. Note also that the track in  $x$ -direction is only constrained via the two hits measured in mm0 and mm1. This yields a big uncertainty for the predicted hit at the position of the phantom, as the relative distance of the  $z$ -coordinate between mm0 and mm1 is much smaller than the distance between mm1 and the phantom. This is not observed for the  $y$ -direction, as the position of the phantom is right behind the second Micromegas doublet, largely reducing the error for the predicted track.

The reconstructed slope of the track in  $x$ -direction is shown in Fig. 5.22 for the step phantom positioned in front (blue) and behind (red) the Micromegas tracking system.

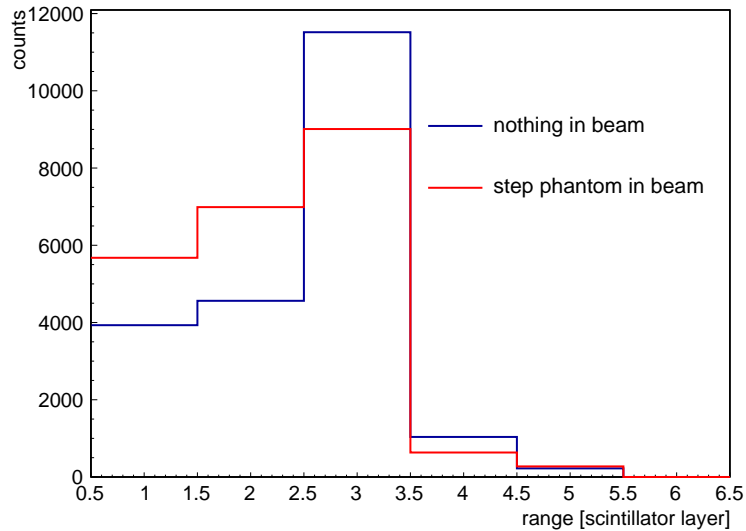


Figure 5.20: Particle range in the range telescope in units of scintillator layers. The coincidence signal of both fibers of one layer marks it as hit. Without a phantom in the beam (blue), most protons get stopped in the third layer of the telescope. With the step phantom in the beam (red), positioned about 60 mm in front of mm0, more protons get stopped within the first two layers.

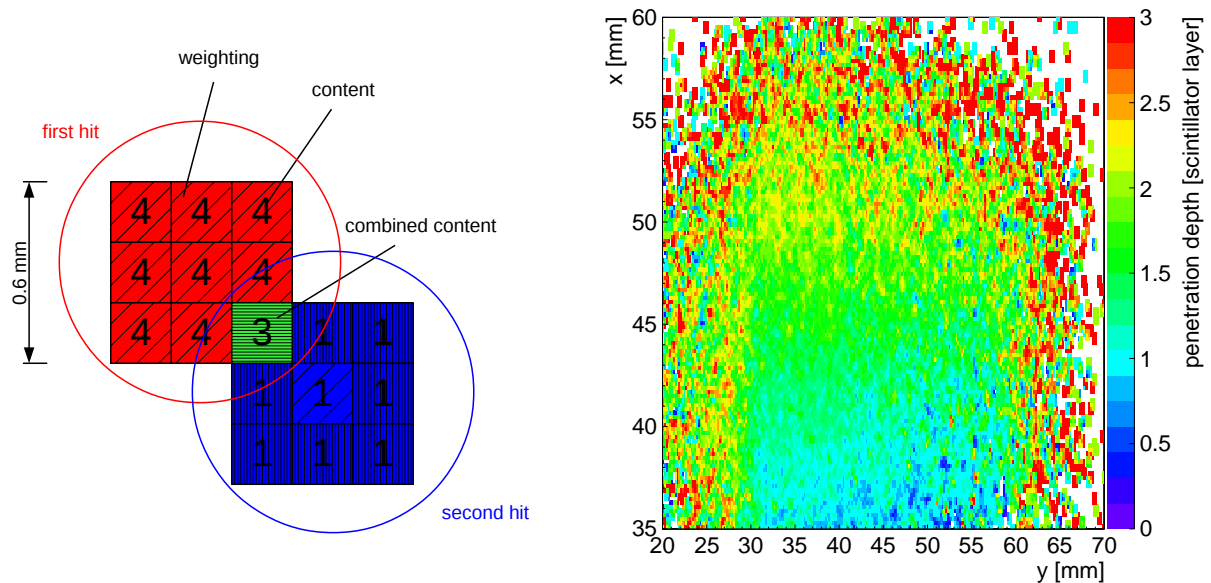


Figure 5.21: Radiography of the step phantom (right), positioned behind the tracking system and recorded with 100k events of 23 MeV protons traversing the system. When filling the histogram, a 'dynamic' bin width is created (left), consisting of nine bins with different weights and allowing for two neighboring bins of different events to overlap, building a combined bin content.

The distribution of the slope acquired with the step phantom in front of the system is broadened, caused by multiple scattering of the protons within the phantom.

The radiographies acquired with the phantom in front (left) and behind (right) the tracking system are shown in Fig. 5.23. A better contrast at the borders of the step

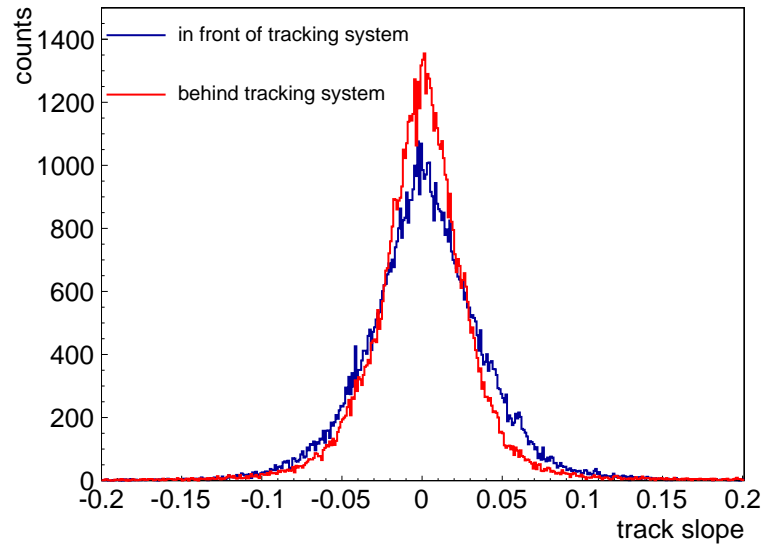


Figure 5.22: Reconstructed slope of the track in  $x$ -direction for a step phantom positioned in front (blue) and behind (red) the Micromegas tracking system.

phantom is observed for the radiography acquired with the step phantom positioned behind the tracking system. No improvement of the step resolution is observed if the phantom is positioned in front of the system, although this reduces the track error in  $x$ -direction. It is probably due to the increased scattering after traversing the phantom and the fact that the step phantom was not perfectly illuminated by the beam. As the dynamic range of the particle range telescope only encompasses three layers due to the low energy protons, the depth resolution is limited. Additionally only two tracking detectors within one dimension generally limits the reconstructed resolution of the radiography.

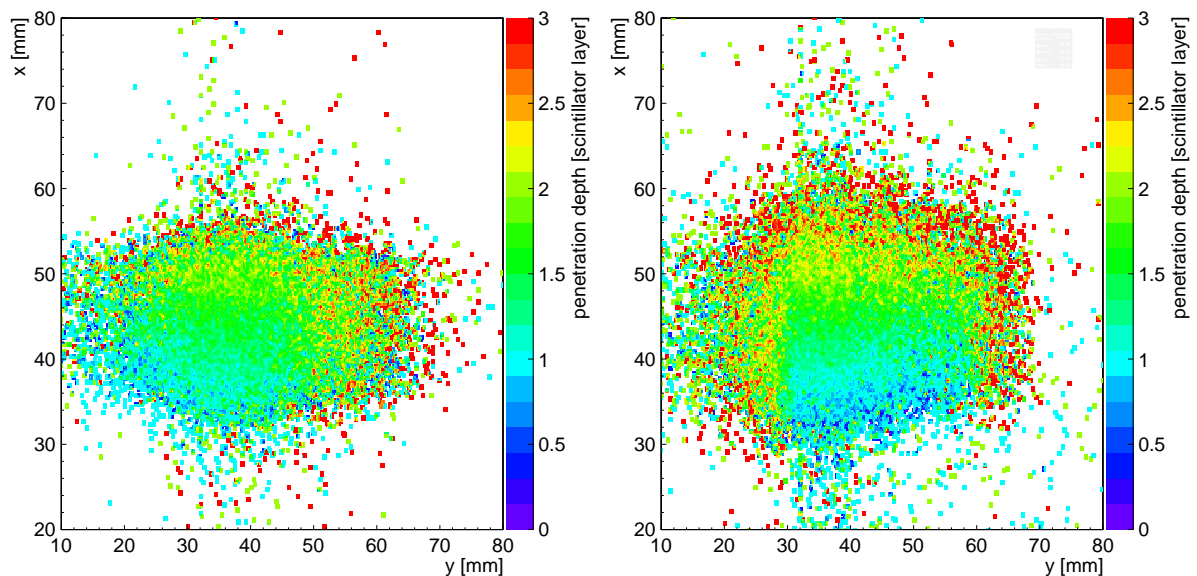


Figure 5.23: Acquired radiography of the step phantom positioned in front (left) and behind (right) the tracking system, recorded with 100k events of 23 MeV protons traversing the system.

## 5.8 Summary

Two floating strip Micromegas doublets with low material budget, combined with a scintillator based particle range telescope, have been tested with 23 MeV protons at the tandem accelerator in Garching. A new, faster Ne:CF<sub>4</sub> based drift gas has been tested, increasing the electron drift velocity up to a factor of three for a chosen working point at  $E_{\text{drift}} = 200 \text{ V/cm}$ . A recently assembled floating strip Micromegas doublet has been tested with respect to pulse height behavior and detection efficiency.

The pulse height behavior on amplification and drift field of is observed as expected. The measured pulse height of mm2 is about 15 % smaller than for mm3. A TRIM based SRIM simulation of 23 MeV protons traversing the main components of the whole detector system showed that the increased energy loss of the protons at outer layers of the detector system explains the observed difference.

The efficiency of the recently assembled Micromegas doublet is for all drift and amplification field configurations above 96 % and for optimized electric fields above 98 %. The observed efficiency of mm2 is at most 4 % smaller than for mm3, due to two dead strips in the beam spot region and a smaller pulse height.

Drift velocity measurements for inclined tracks at  $(25.5 \pm 1.0)^\circ$ ,  $(30 \pm 1)^\circ$  and  $(35 \pm 1)^\circ$  showed that the measured electron drift velocity is smaller than expected, explained by left over humidity in the gas below 0.1 vol.%.

Angle reconstruction capabilities for the new drift gas via the  $\mu$ TPC method have been investigated for different drift fields of the first doublet. The most probable angle agrees for nearly all measurements with the expectation. The observed angular resolution depends strongly on the drift field, whereas an optimum resolution of  $(\begin{smallmatrix} +3 \\ -2 \end{smallmatrix})^\circ$  was reconstructed for a track inclination of  $35^\circ$  for small drift fields.

The reconstructed spatial resolution of the detector system is strongly limited by multiple scattering of the low energy protons especially at high  $Z$  materials of the readout structure. For a perpendicularly incident beam, an optimum resolutions of  $(346 \pm 90) \mu\text{m}$  could be reconstructed for an inner layer of the four tracking detectors. For all three track inclinations, the  $\mu$ TPC reconstructed alternative hit position yields better results than the charge weighted mean at drift fields below  $E_{\text{drift}} < 500 \text{ V/cm}$ .

First radiographic measurements of a step phantom in the beam have been performed successfully. The depth resolution of the acquired image is limited by the a dynamic range of only three hit scintillator layers in the particle range telescope, resulting from the low proton energy. It was observed, that the the acquired image quality depends on the step phantom position in the beam, as for a position behind the tracking system a better contrast was observed than for a step phantom position in front of the system. The reconstructed slope for both scenarios confirmed the observed behavior.

# Chapter 6

## High-Rate Tracking and Imaging at the Heidelberg Ion Therapy Center with Carbon Beams

In the following chapter, measurements with three low material budget floating strip Micromegas doublets, a GEM detector<sup>1</sup> and a scintillator based particle range telescope at the Heidelberg Ion Therapy Center (HIT) are presented. As the Micromegas were operated without external drift voltage, a GEM was included for performance measurements of the Micromegas at a first set of measurements with carbon ion beams between 88 MeV/u and 430 MeV/u beam energy at a particle rate of 2 MHz. The single strip readout of a two dimensional floating strip Micromegas anode has been tested for the first time. For acquisition of radiographies with the Micromegas tracking system combined with the range telescope, the GEM has been replaced by suitable phantoms. As the GEM is no primary point of study in this thesis, no analysis of the GEM data is presented here.

### 6.1 Setup

The measurement setup for performance studies of the Micromegas and GEM detectors is schematically drawn in Fig. 6.1: Two one-dimensional thin floating strip Micromegas doublets, a two-dimensional readout GEM detector and a two-dimensional readout thin floating strip Micromegas doublet with integrated setup - as described in section 3.5. The three Micromegas doublets, each consisting of two back-to-back floating strip Micromegas, have an active area of  $6.4 \times 6.4 \text{ cm}^2$ , formed by 128 copper anode strips of 0.5 mm pitch and 0.3 mm width. The strips were oriented in horizontal  $y$ -direction, yielding precise particle hit information in  $x$ -direction. The two dimensional Micromegas provided hit information in  $x$ - and  $y$ -direction. The GEM detector with an active area of  $9 \times 9 \text{ cm}^2$  and two perpendicular layers of 250 readout strips with 0.4 mm pitch and 0.3 mm width also yielded hit information in  $x$ - and  $y$ -direction. All detectors were read out using APV25 based front-end boards, interfaced by the Scalable Readout System [RD51, 2010]. Charge signals are recorded after following a

---

<sup>1</sup>operated by Bernhard Flierl

trigger from the coincident signals of scattered particles in two scintillators placed off the beam axis. High-voltage for the gas detectors was supplied via a CAEN SY5527 Universal Multichannel Power Supply System [CAEN SY5527, 2015], equipped with three 12-channel CAEN A1821 [CAEN A1821, 2015] modules with positive and negative polarity and a 12-channel CAEN A1535dn [CAEN A1535dn, 2015] module to supply the scintillators with appropriate power.

The Micromegas detectors were continuously flushed with a premixed Ne:CF<sub>4</sub> 84:16 vol.% gas with an overall flux of around 2 ln/h. The GEM detector was flushed with a premixed Ar:CO<sub>2</sub> 93:7 vol.% gas mixture. All detectors were operated at normal pressure and temperature.

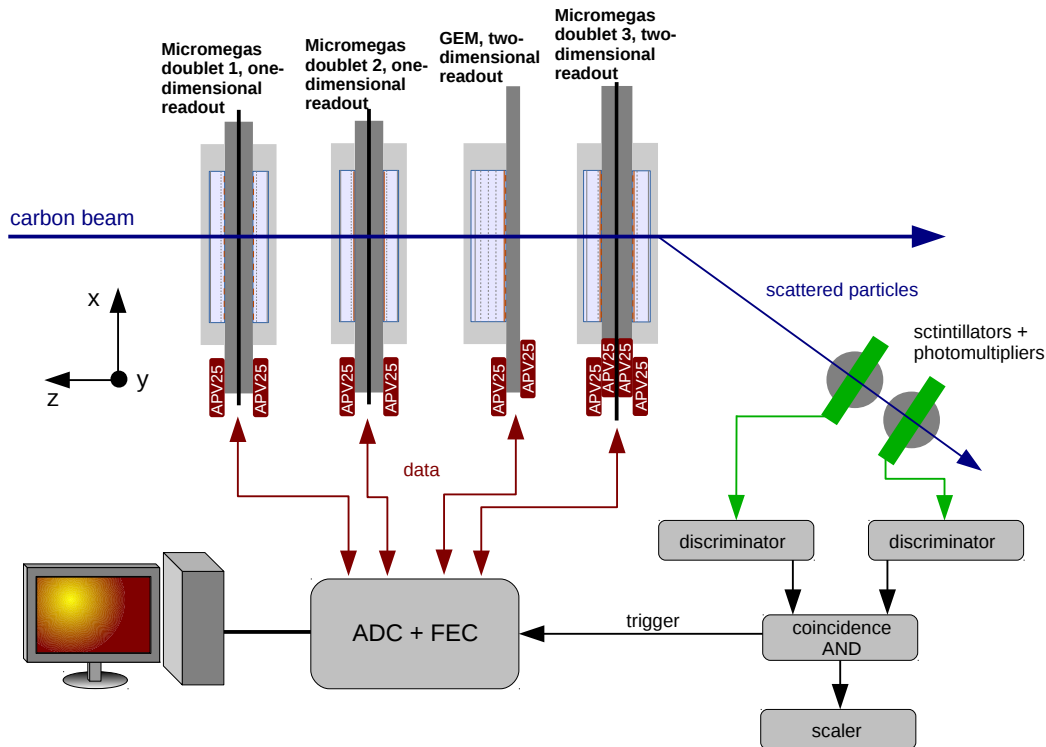


Figure 6.1: Setup for the measurements at the Heidelberg Ion Therapy center (HIT) with carbon beams. The SRS based readout of all detectors is triggered with the coincidence signal of scattered particles in two off-axis scintillators. As no drift voltage has been applied to the Micromegas, a two-dimensional GEM is included for measurements of the working performance of the Micromegas.

For radiographies acquired with the Micromegas tracking system, the GEM detector has been replaced by suitable phantoms and a scintillator based particle range telescope was placed behind the tracking system, see Fig. 6.2. The range telescope consists of 18 1 mm thick plastic scintillator layers, each equipped with two wave length shifting fibers to acquire the photon signal. After amplification with photomultipliers, a Timing Shaping Amplifier<sup>2</sup> (TSA) and dedicated attenuation, all charge signals are recorded with a separate APV25 front-end board, connected to the SRS [RD51, 2010]. The beam energy is adjusted such that the particles are stopped within the range telescope,

<sup>2</sup>developed by Jonathan Bortfeldt at the LMU in Munich

with the trigger generated from the coincidence signals of two fibers of the first two scintillator layers.

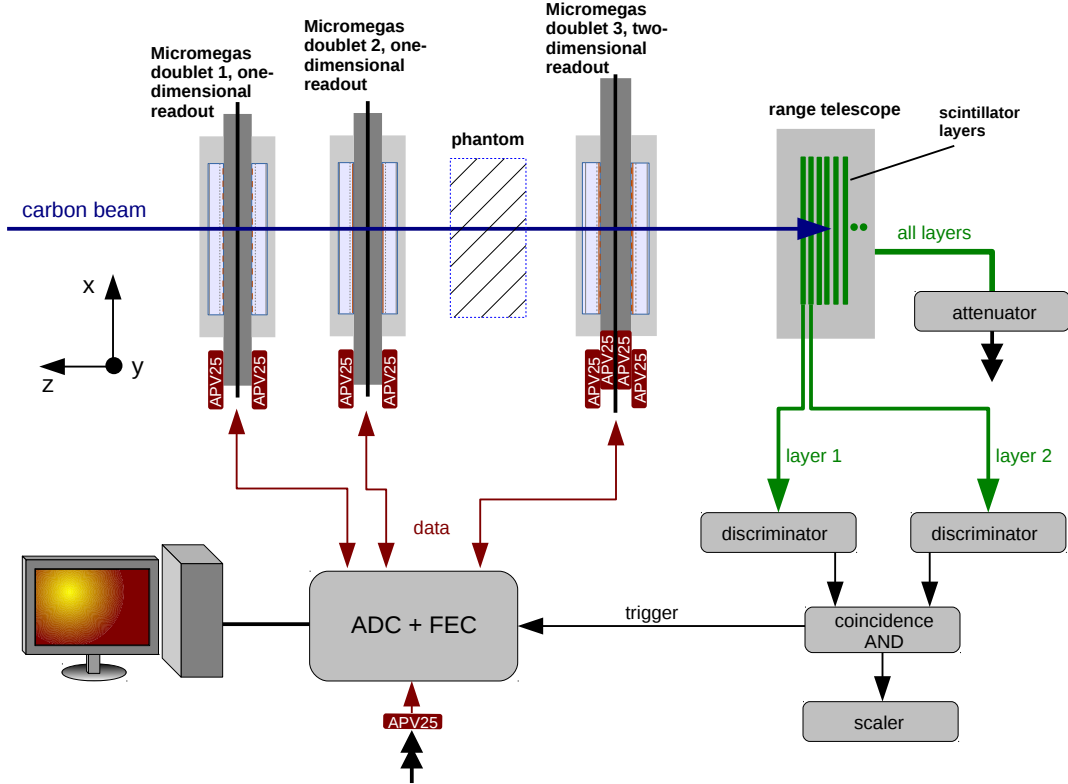


Figure 6.2: Setup for the radiographic measurements at the Heidelberg Ion Therapy center (HIT). The GEM is replaced by suitable phantoms and a scintillator based range telescope connected to the SRS readout system is placed behind the tracking system. The readout of all detectors is triggered with the coincidence signal of two fibers of the first two scintillator layers of the particle range telescope.

Following naming for each detector layer has been chosen: the first Micromegas doublet will be denoted by mm0 and mm1, the second by mm4 and mm5. As Micromegas of the third doublet each consists of two perpendicular layers of readout strips, the strip layers of a single Micromegas are treated separately, thus naming the readout strips yielding hit information in  $x$ -direction mm2 and mm3, whereas mm6 and mm7 describe the strips yielding hit information in  $y$ -direction.

## 6.2 Pulse Height Behavior and Hit Efficiency

As the Micromegas were operated without external drift voltage, the following section will cover pulse height and hit efficiency discussions based on this special case. As only charge created in the close proximity of the micro-mesh will contribute to the recorded signal of each Micromegas, the observed pulse height is considerably smaller as compared to Micromegas working under normal operational conditions. For that reason, the required signal amplitude for marking a strip as hit during the analysis in the cluster building was optimized, to accept small signals while rejecting most of the electronic noise at the same time. Also no strips without charge signal are allowed

within a selected cluster, as only a few strips will be hit. After the cluster building processes is finished, an algorithm searches for neighboring strips of the found cluster, adding them to the cluster if a charge signal was found that amplitude exceeds the standard deviation of the respective strip. Fig. 6.3 shows the pulse height distribution and the number of hit strips per cluster of 40000 recorded events of 88.83 MeV/u carbon ions for mm0 and mm2, before and after applied correction. Only clusters that could be matched to a track are considered. The considerable improvement due to including small signals is obvious. The shape of both pulse height distributions after the correction, follows the expected Landau-shaped distribution for thin detectors. The number of hit strips per cluster after the correction also confirms the recovery of small signals, leading in the case of mm2 to a distinctly larger pulse height, as well as shifting the most probable number of hit strips from 1 to 2. Comparing the maximum probable pulse height of mm0 and mm2 also shows that the overall recorded pulse height for the  $x$ -layer of the two-dimensional floating strip Micromegas (mm2) is about a factor of three smaller than the recorded pulse height of mm0, with a one-dimensional strip readout. Nevertheless it shows that the principle of signal generation in a two-dimensional floating strip Micromegas anode works, although with a smaller recorded pulse height for the bottom layer of the readout PCB.

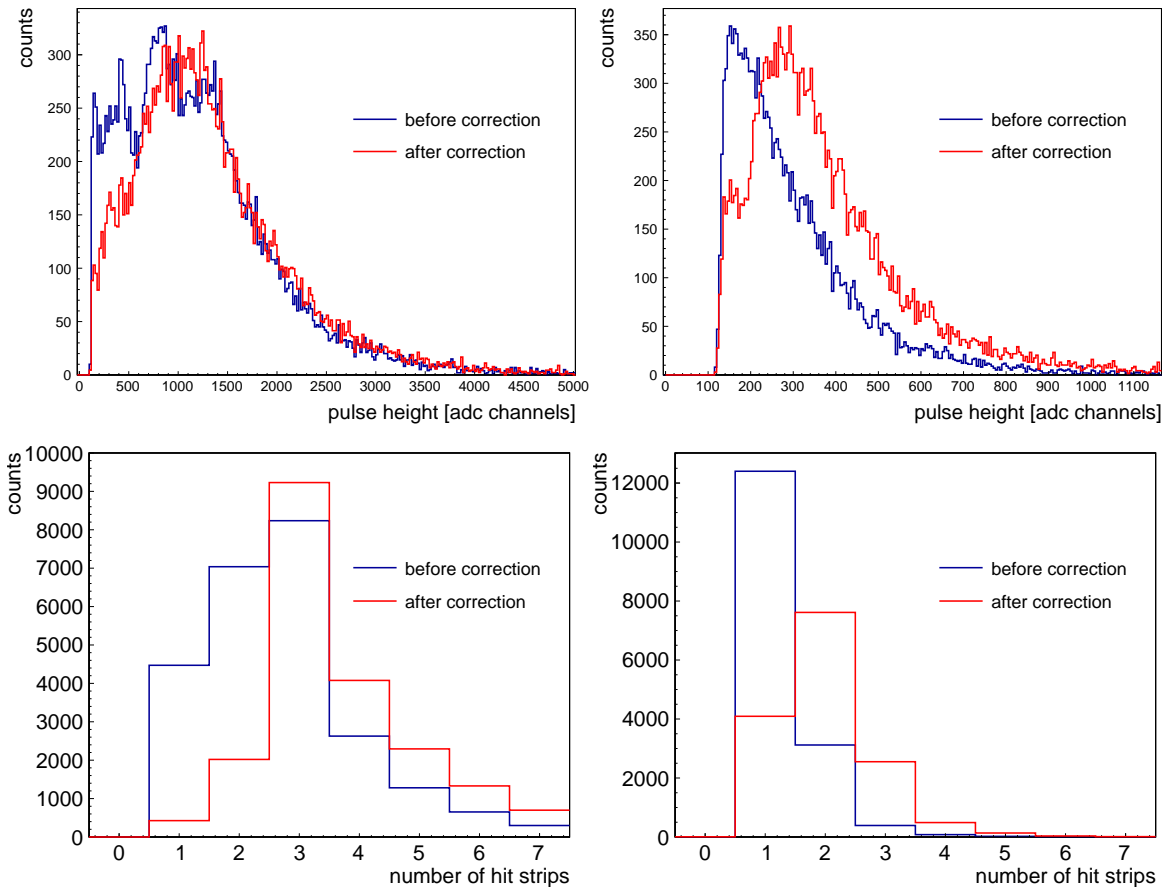


Figure 6.3: Reconstructed cluster pulse height (top) and number of hit strips per cluster (bottom) for mm0 (left) and mm2 (right) with 40000 recorded events of 88.83 MeV/u carbon ions for optimized amplification fields  $E_{amp,0}=32$  kV/cm and  $E_{amp,2}=34$  kV/cm.

Characterization measurements of the two dimensional readout anode can be found in chapter 7, where pulse height dependencies of both PCB layers are investigated. Nev-

ertheless it should be noted, that the signal polarity of the  $x$ -layers are positive. As the polarity of the APV for these layers has not been inverted for the measurements presented in this chapter, the signals have been inverted in the analysis program. As the signals are very small, no loss of pulse height is observed despite the limited dynamic range of the APV for inverted ADC values. Fig. 6.4 and 6.5 show the pulse height distributions and number of hit strips for all Micromegas in the tracking system. The amplification fields for each detector have been optimized, such that the highest possible pulse height was reconstructed but simultaneously keeping the average current, measured between mesh and anode, below 300 nA. This yields the following amplification fields for all detectors:  $E_{\text{amp},0} = 32 \text{ kV/cm}$ ,  $E_{\text{amp},1} = 30.3 \text{ kV/cm}$ ,  $E_{\text{amp},2} = E_{\text{amp},6} = 34 \text{ kV/cm}$ ,  $E_{\text{amp},3} = E_{\text{amp},7} = 32 \text{ kV/cm}$ ,  $E_{\text{amp},4} = 32 \text{ kV/cm}$  and  $E_{\text{amp},5} = 31.3 \text{ kV/cm}$ . The correlation between well shaped pulse height distribution, with higher values for the most probable pulse height, and number of hit strips is visible. Furthermore, the reconstructed pulse height distribution of all layers of the two-dimensional readout anode (being in this case mm2, mm3, mm6 and mm7) is less smooth than the pulse height of the detectors with one-dimensional strip readout structure. This is mainly due to the generally smaller recorded pulse height, which leads to a loss of small signals on adjacent strips in a cluster and therefore to a smaller number of reconstructed hit strips.

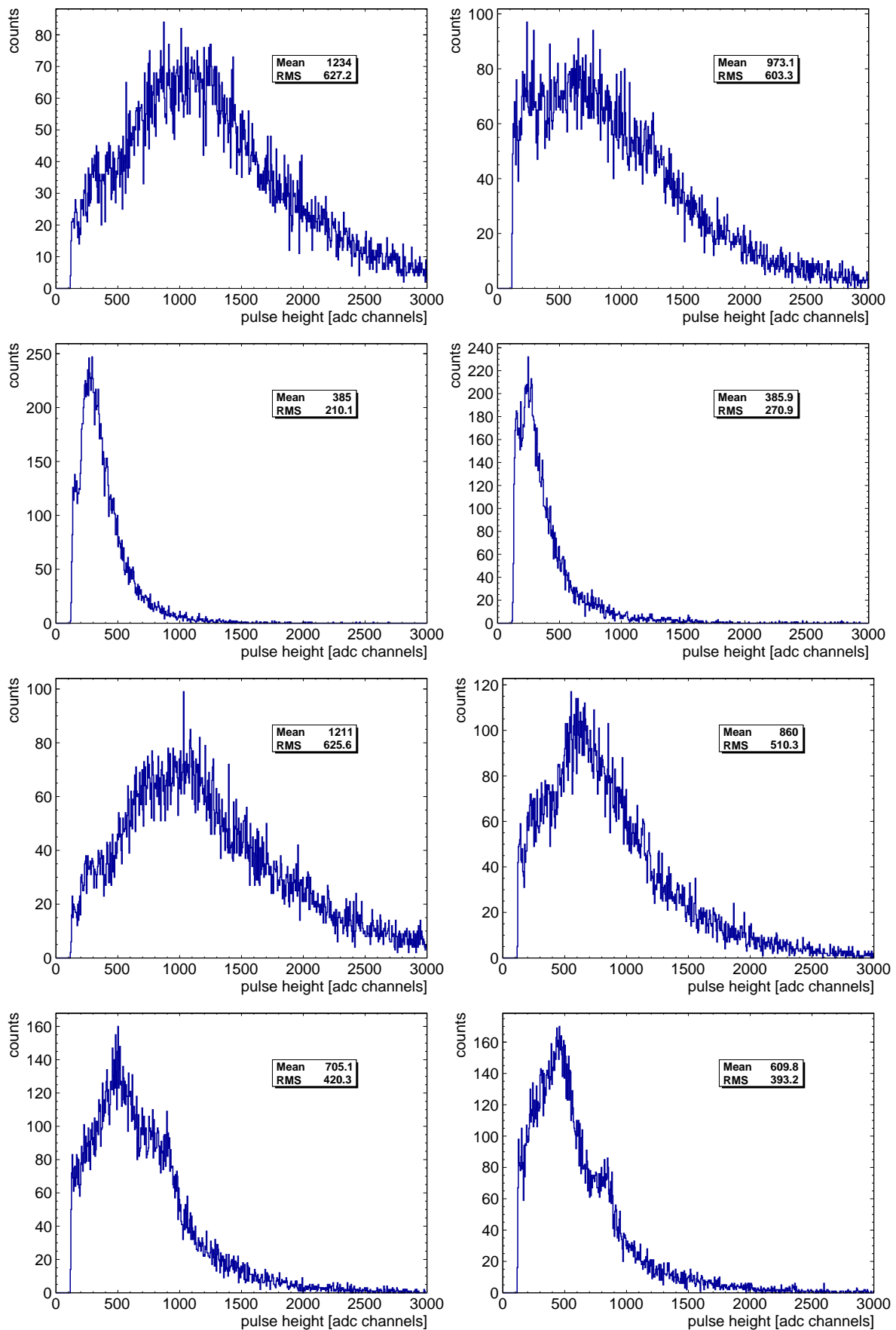


Figure 6.4: Corrected pulse height distribution of the Micromegas in the tracking system, recorded with 40000 events of 88.83 MeV/u carbon ions traversing the system. The figures are ordered the following way: mm0 (first row, left), mm1 (first row, right), mm2 (second row, left), mm3 (second row, right), mm4 (third row, left), mm5 (third row, right), mm6 (fourth row, left) and mm7 (fourth row, right). As no drift voltage is applied to the detectors, the measured pulse height is rather small.

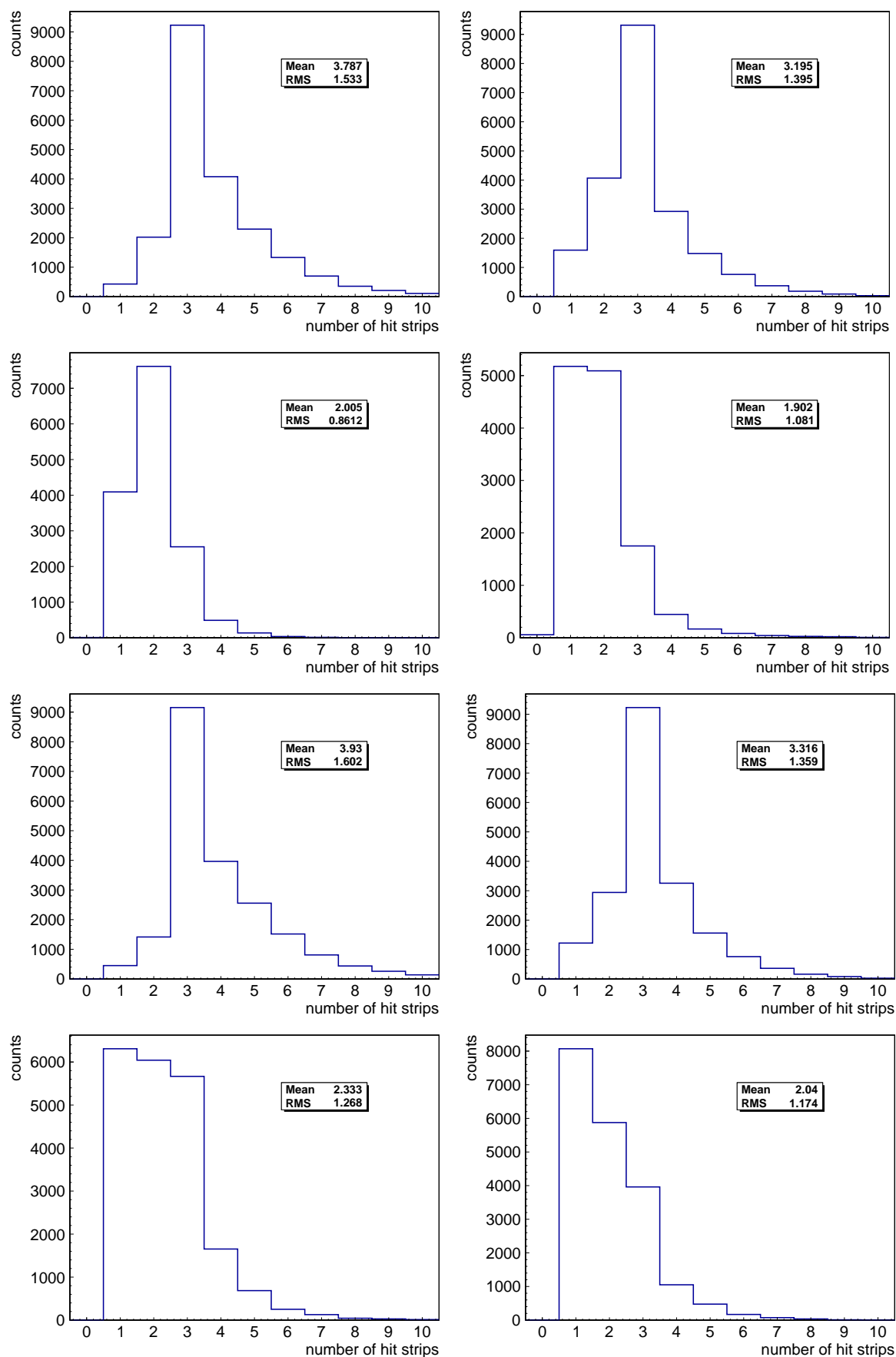


Figure 6.5: Corrected number of hit strips within a selected cluster of the Micromegas in the tracking system, recorded with 40000 events of 88.83 MeV/u carbon ions traversing the system. The figures are ordered in the following way: mm0 (first row, left), mm1 (first row, right), mm2 (second row, left), mm3 (second row, right), mm4 (third row, left), mm5 (third row, right), mm6 (fourth row, left) and mm7 (fourth row, right). As no drift voltage is applied to the detectors, typically less than 4 strips are hit.

Due to the small observed signals, the hit efficiencies of the detectors are an important criterion to estimate the performance under the special condition without applied drift voltage. For this reason, the hit based efficiency  $\epsilon_i$  for each detector layer  $i$  can be calculated, following Eq. (5.8):

$$\epsilon_i = \frac{n_{\text{good}}}{n_{\text{good}} + n_{\text{bad}}} = \frac{n_{\text{all hit}}}{n_{\text{all hit}} + n_{\text{i not hit}}} . \quad (6.1)$$

For the calculation of the hit efficiency during the measurements with the GEM detector,  $n_{\text{all hit}}$  defines an event where at least both layers of the GEM detector registered a signal, as it has been operated under normal conditions. Bad events for detector  $i$  are counted if it failed to reconstruct the hit. Following efficiencies for all tracking Micromegas have been calculated for a measurement of 40000 carbon ions with 88.83 MeV/u beam energy:

$$\begin{aligned} \text{mm0} : \epsilon_0 &= 0.975 \pm 0.001 \\ \text{mm1} : \epsilon_1 &= 0.959 \pm 0.002 \\ \text{mm2} : \epsilon_2 &= 0.727 \pm 0.003 \\ \text{mm3} : \epsilon_3 &= 0.623 \pm 0.003 \\ \text{mm4} : \epsilon_4 &= 0.974 \pm 0.001 \\ \text{mm5} : \epsilon_5 &= 0.937 \pm 0.002 \\ \text{mm6} : \epsilon_6 &= 0.877 \pm 0.002 \\ \text{mm7} : \epsilon_7 &= 0.900 \pm 0.002 \end{aligned} \quad (6.2)$$

An efficiency above 93% can be reached for all Micromegas with one-dimensional strip readout, where as for the two-dimensional Micromegas smaller efficiencies are observed. The efficiency of mm5 with  $(93.7 \pm 0.2)\%$  is about 3.7% smaller than the efficiency of mm4 with  $(97.4 \pm 0.1)\%$  due to three dead strips in the beam spot region, see Fig. 6.10. As the reconstructed pulse height for both  $y$ -layers (mm6 and mm7) of the two-dimensional anode are by a factor of approximately 1.8 larger than for both  $x$ -layers (mm2 and mm3), the resulting smaller hit efficiency is understandable. Still an optimum of  $(97.5 \pm 0.1)\%$  can be reached for mm0 with also the highest reconstructed pulse height. This is comparable to hit efficiencies under normal conditions with about 98%, see section 5.3.

Fig. 6.6 shows the hit efficiency for a carbon beam as a function of the beam energy in a range from 88 MeV/u to 430 MeV/u. The amplification fields were slightly reduced for these measurements to  $E_{\text{amp},2,6} = 32.7$  kV/cm. This explains the considerable efficiency drop of mm2 by about 20% at the smallest beam energy of 88.83 MeV/u compared to the efficiency listed in Tab. 6.2. Due to a smaller energy loss of the particles with increasing beam energy, the recorded pulse height for each detector decreases, which leads to a loss of small signals and therefore a decrease of the hit efficiencies.

The generally smaller reconstructed efficiency for the two-dimensional Micromegas doublet is also due to a bigger mesh-supporting pillar diameter with 0.8 mm instead of 0.4 mm for the one-dimensional readout PCB layout. In the case of the two-dimensional readout anode, the mesh, spanned over the active area of  $64 \times 64 \text{ mm}^2$ , is supported by 625 pillars with an area of  $\pi \cdot 0.4^2 \text{ mm}^2 = 0.503 \text{ mm}^2$ . For the one-dimensional readout PCB, 650 pillars with an area of  $\pi \cdot 0.2^2 \text{ mm}^2 = 0.126 \text{ mm}^2$  are distributed over the

active area. Thus the covered fraction of the two-dimensional readout structure is with

$$\eta_{2d} = \frac{625 \cdot 0.503 \text{ mm}^2}{64 \cdot 64 \text{ mm}^2} \approx 0.077 \quad (6.3)$$

larger than the fraction

$$\eta_{1d} = \frac{650 \cdot 0.126 \text{ mm}^2}{64 \cdot 64 \text{ mm}^2} \approx 0.020 \quad (6.4)$$

for the one-dimensional readout structure. Thus an efficiency drop of about 5.7% can be explained due to a 'loss' of active area for the two different PCB designs, as for particles traversing the pillars, the signals are lost. As this does not completely cover the difference for the efficiencies calculated for both designs, also the different methods of decoupling the signal from floating strips to readout strips may lead to a loss of signals. Furthermore, the smaller recorded pulse height for the two dimensional Micromegas leads to a loss of signals.

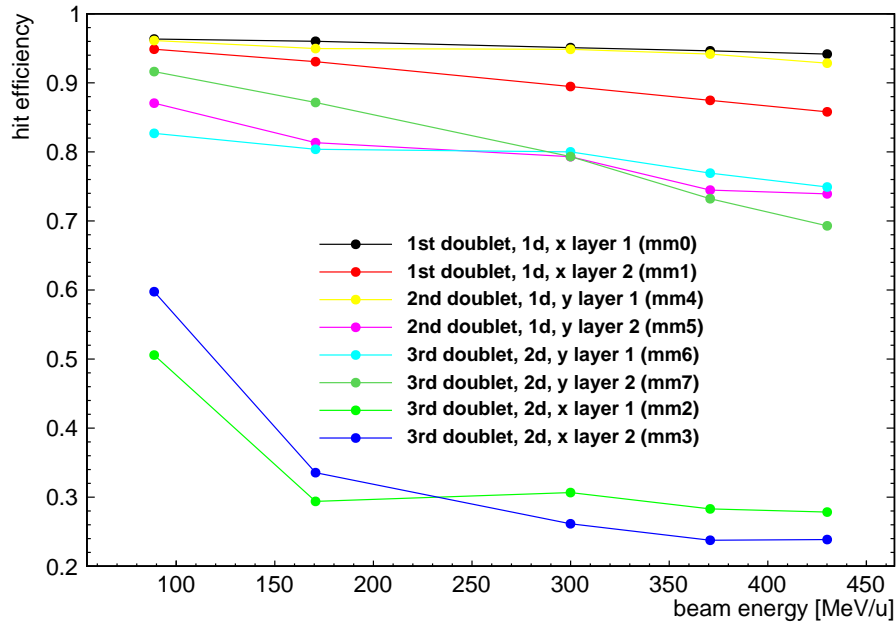


Figure 6.6: Calculated hit efficiencies for all Micromegas as a function of the beam energy for carbon ions. The efficiency of the  $x$ -layers (mm2 and mm3) of the two-dimensional Micromegas doublet is significantly smaller than all other measured efficiencies, primarily due to the smaller recorded pulse height.

## 6.3 Signal Timing

Due to operation without drift voltage, the timing behavior of the Micromegas differs from the nominal case. As no significant charge is collected from the ionization process in the drift gap, the signal is only created in the amplification region and in the close proximity of the micro mesh in the drift region. The signal shape is thus not influenced by later arriving ionization charge, created at different points in the drift gap. This is a similar behavior as compared to inclined particle tracks with applied drift voltage,

where charge created in the proximity of the mesh arrives on a different strip than charge created e.g. near the cathode. Thus timing studies without drift voltage applied are worth investigating.

All timings discussed in this section are determined from an inverse Fermi fit to the strip pulse, extrapolating the rising edge onto the baseline to acquire a timing information independent of the signal amplitude (see section 4.1 Eq. (4.4)). For every triggered event, the cluster with highest charge of each detector is searched for the smallest reconstructed timing, which is used for further analysis. Fig. 6.7 shows the correlation between measured timings of mm0 and the measured timings in the second layer mm1 (left) and between mm0 and the last layer mm7 (right). A correlation between later and/or earlier arriving signals can be observed: If a, in particular, later (earlier) arriving signal is measured in the first detector, also a later (earlier) timing is measured in the second and the last detector.

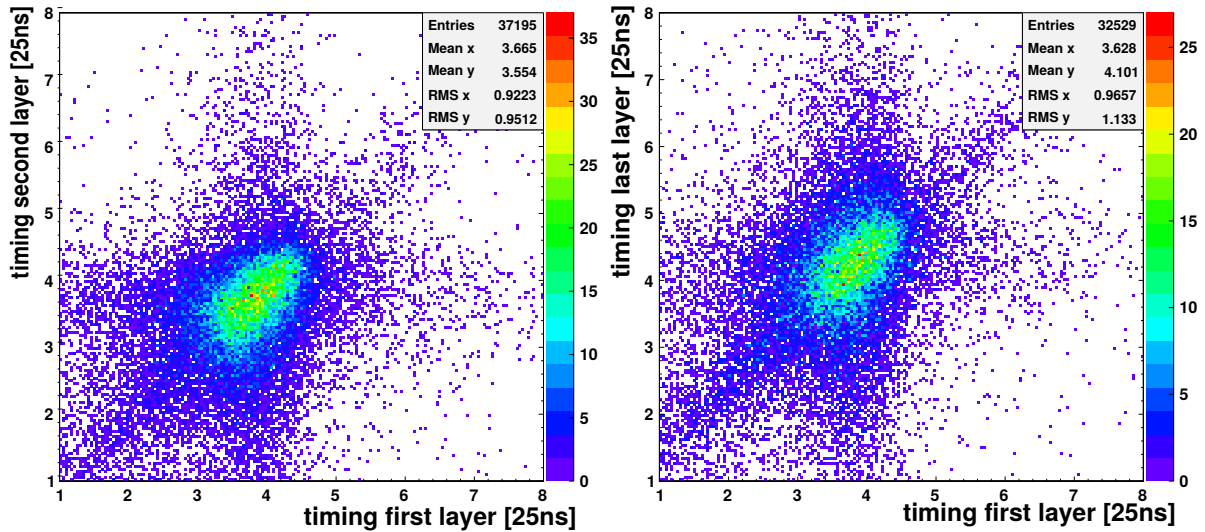


Figure 6.7: Correlation between signal timings measured in the first (mm0) and second layer (mm1, left) and in the first and the last layer (mm7, right), recorded with 40000 carbon ions of 88.83 MeV/u perpendicularly traversing the detector system.

Furthermore, the signal measured in the last detector is delayed with respect to the second layer. This is observed accordingly for the other detector layers. It was thus tested to calculate the mean velocity of the carbon ions, via a 'time-of-flight' measurement between layer 0 and layer 7, as the distance between the detectors is known.

The difference between the measured most probable timing between mm0 and mm7 can be determined with a fit with a Gaussian function to the upper part of both distributions. A difference of  $\Delta t = (0.41 \pm 0.03) \times 25 \text{ ns} = (10.3 \pm 0.8) \text{ ns}$  is determined. The relative distance  $\Delta z$  in beam direction is known with  $\Delta z = (383 \pm 5) \text{ mm}$ . Thus the measured velocity  $v_{C^{12}, \text{ meas.}}$  of the carbon ions can be determined, following

$$v_{C^{12}, \text{ meas.}} = \frac{\Delta z}{\Delta t} = (0.12 \pm 0.02) c \quad . \quad (6.5)$$

This is not in agreement though with the expected velocity of 88.83 MeV/u carbon ions with  $v_{C^{12}, \text{ expe.}} = 0.41 c$ . However, particles with a speed of 0.41 c need approximately 3 ns to cover the distance between the first and last layer. Hence, the time resolution

of the detectors is being investigated in the following.

The correlation between the timings (Fig. 6.7) is only visible due to the good time resolution of the detectors, which visualizes the 25 ns jitter of the trigger signal (see section 3.6). It allows correction of the jitter directly, described in the following:

In a first step, the detector internal time offset is determined, defined by the mean value of the distribution derived by a fit with two Fermi functions, see Fig. 6.8. The asymmetric shape e.g. the tail towards smaller time values arises from misreconstruction and failed strip pulse fits for very early signals. The determined mean value for each Micromegas is then used as an offset correction within each detector, such that all measured timings jitter around zero. On an event-to-event basis, every offset corrected signal timing with an absolute value below 12.5 ns is marked as a good timing - previously checked for suitable fit quality and pulse height. The jitter can then be approximated by the average of all measured good signal timings in all detectors for every event. If only one or zero good signal is found, then no jitter is being calculated for this event. In this case about 10% of all events did not allow for a jitter calculation. The measured timing of every detector is then being corrected with the determined value of the jitter.

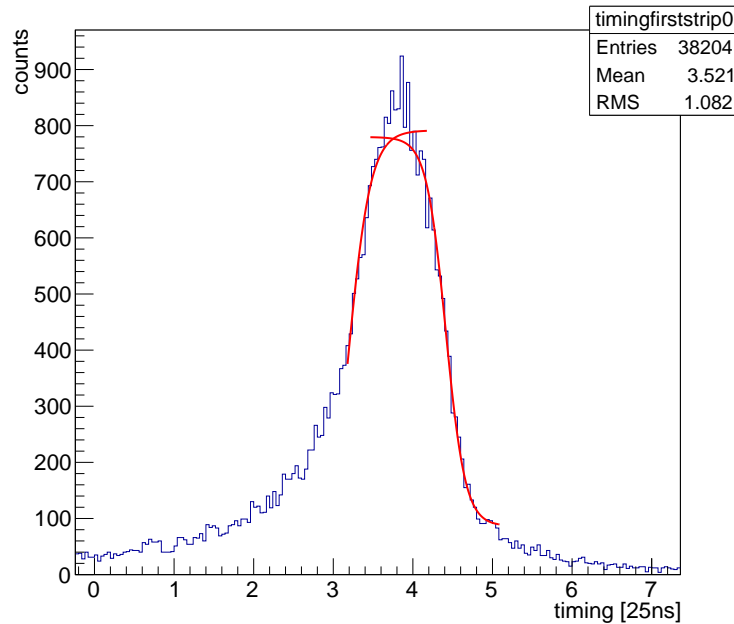


Figure 6.8: Signal timing distribution of mm0, measured with a 88.83 MeV/u perpendicularly incident carbon beam. The signal timing jitters around its expectation value. A fit with two Fermi functions (red) is used to determine the mean value of the distribution, which is then further used for timing offset correction in each detector separately.

Fig. 6.9 shows the offset corrected signal timing distribution for mm0 (top left), the jitter corrected distribution (top right) and the jitter correction in the 'wrong' direction, meaning not subtracting but adding the determined jitter value (bottom). A Gaussian function has been fit to the upper part of each distribution to get an estimate of the width. It is clearly visible that the correction works, when applying the correction in the right direction. The resulting width decreases from  $\sigma = 0.50 \times 25$  ns to  $\sigma = 0.34 \times 25$  ns

by about a factor of 1.47, whereas the time resolution worsens for the cross-check of the correction in the other direction, with increasing width from  $\sigma = 0.50 \times 25$  ns to  $\sigma = 0.94 \times 25$  ns. The width after the correction with  $\sigma = 0.34 \times 25$  ns corresponds to a single layer time resolution of  $(8.53 \pm 0.07)$  ns.

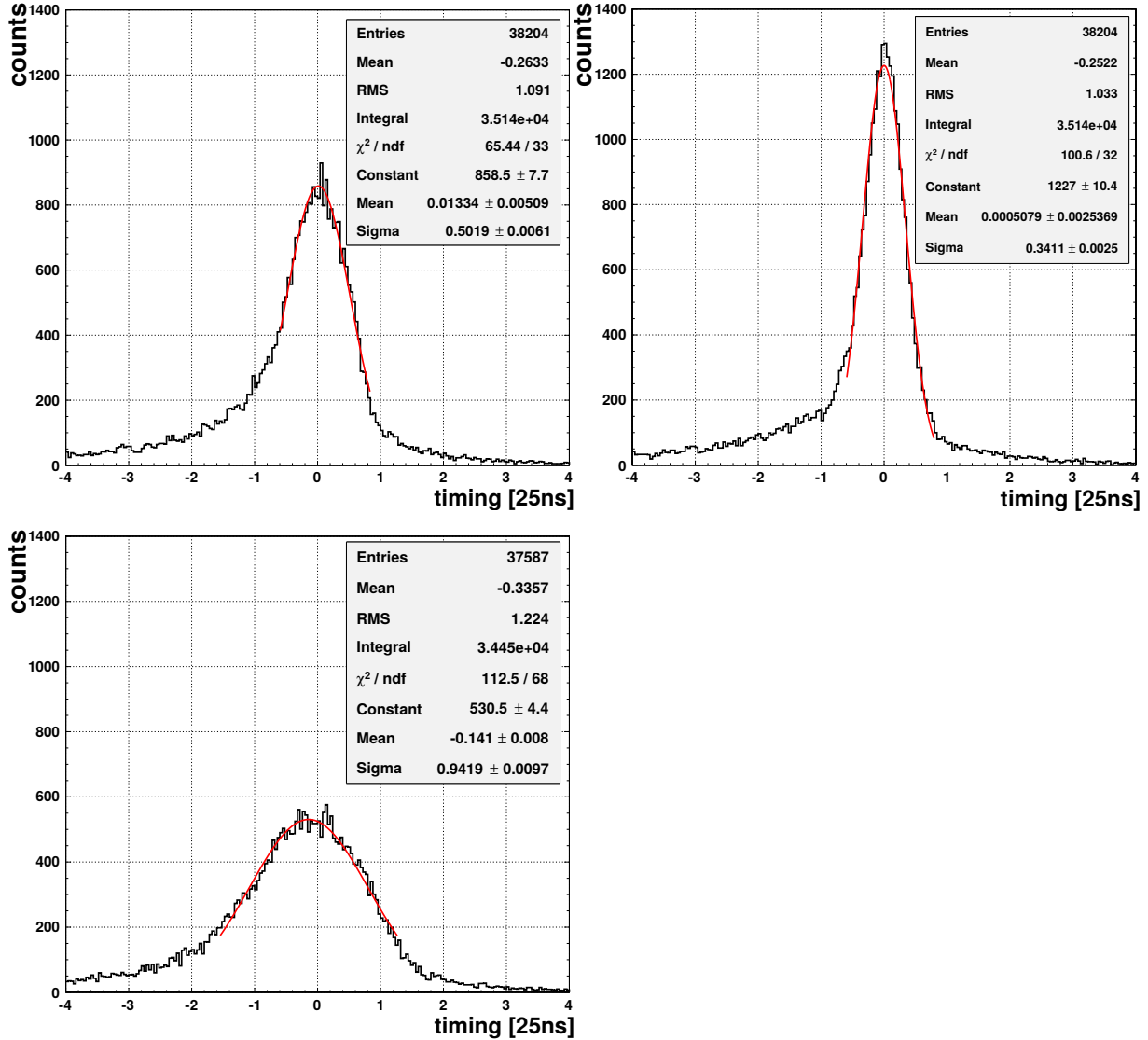


Figure 6.9: Offset corrected (top left), offset + jitter corrected (top right) and offset + incorrectly jitter corrected (jitter added) timing distribution of mm0 (bottom). The determined widths after fitting the upper part with a Gaussian function are:  $\sigma = 0.50 \times 25$  ns (top left),  $\sigma = 0.34 \times 25$  ns (top right) and  $\sigma = 0.94 \times 25$  ns. The improvement of the time resolution is obvious when applying the jitter correction.

During the tandem measurements described in chapter 5, no correlation between signal timings could be found. It leads to conclusion that the time resolution of the detectors with applied drift voltage is not sufficient to allow for the jitter correction within the detector system. Of course the jitter has been corrected for this measurements, but using a separate APV recording the trigger signal.

The similarly shaped strip pulses in all detectors lead to the possibility for a correction of the jitter with no applied drift voltage, as the reconstructed timing is not disturbed by uncontrollable effects as e.g. diffusion, scattering or clustering within the drift gap.

The jitter correction has also been checked with taking the cluster timing as the signal timing - defined by the average position of the maximum of each strip pulse within the selected cluster - instead of the timing of the earliest strip. The correlations could as well be observed and thus the jitter corrected. No significant difference was observed between the two methods.

## 6.4 Track Reconstruction and Spatial Resolution

The particle hits in the detectors are acquired by combining position and charge information of neighboring strips, forming a cluster. In a first step, it is checked that a predefined subset of detectors for which highest hit efficiency is expected has been hit in an event, marking this event as good. For results presented in this section, the following detectors are required to have registered a hit: mm0, mm1, mm4, mm6 and both layers of the GEM detector. If the listed detectors are hit, the Kalman-based track finding algorithm searches combinatorically in every detector layer for a registered hit, that matches to the track prediction. After the track finding algorithm is finished, the track parameters of the found track are saved, so that they can be used later in the analysis. Only if a track is found in an event, pulse height, hit and timing of all tracking detectors included in the track fit as well as the range information from the particle range telescope are considered and stored. Fig. 6.10 shows the reconstructed hit position in all layers of the tracking Micromegas system, where mm0 to mm3 measure the particle hit position in  $x$ -direction and mm4 to mm7 in  $y$ -direction. It has been recorded with 40000 events of 88.83 MeV/u carbon ions traversing the tracking system, with a beam width of 13.1 mm FWHM as given by the accelerator control system. The amplification fields for all Micromegas are:  $E_{\text{amp},0} = 32$  kV/cm,  $E_{\text{amp},1} = 30.3$  kV/cm,  $E_{\text{amp},2} = E_{\text{amp},6} = 34$  kV/cm,  $E_{\text{amp},3} = E_{\text{amp},7} = 32$  kV/cm,  $E_{\text{amp},4} = 32$  kV/cm and  $E_{\text{amp},5} = 31.3$  kV/cm. Groups of dead strips can be identified within mm1 at  $x \approx 32$  mm and within mm5 at  $y \approx 40$  mm, also explaining the smaller observed hit efficiency of both layers. mm2 and mm3 are also able to reconstruct the beam spot, demonstrating that the position resolution works in floating strip Micromegas with two-dimensional strip readout. The Root Mean Square (RMS) of both hit distributions from mm0 and mm1 with  $\text{RMS} \approx 5.7$  mm yields a reconstructed beam width of  $\text{FWHM} = 2.3 \times 5.7 \text{ mm} = 13.11$  mm and is therefore in good agreement with the expected value.

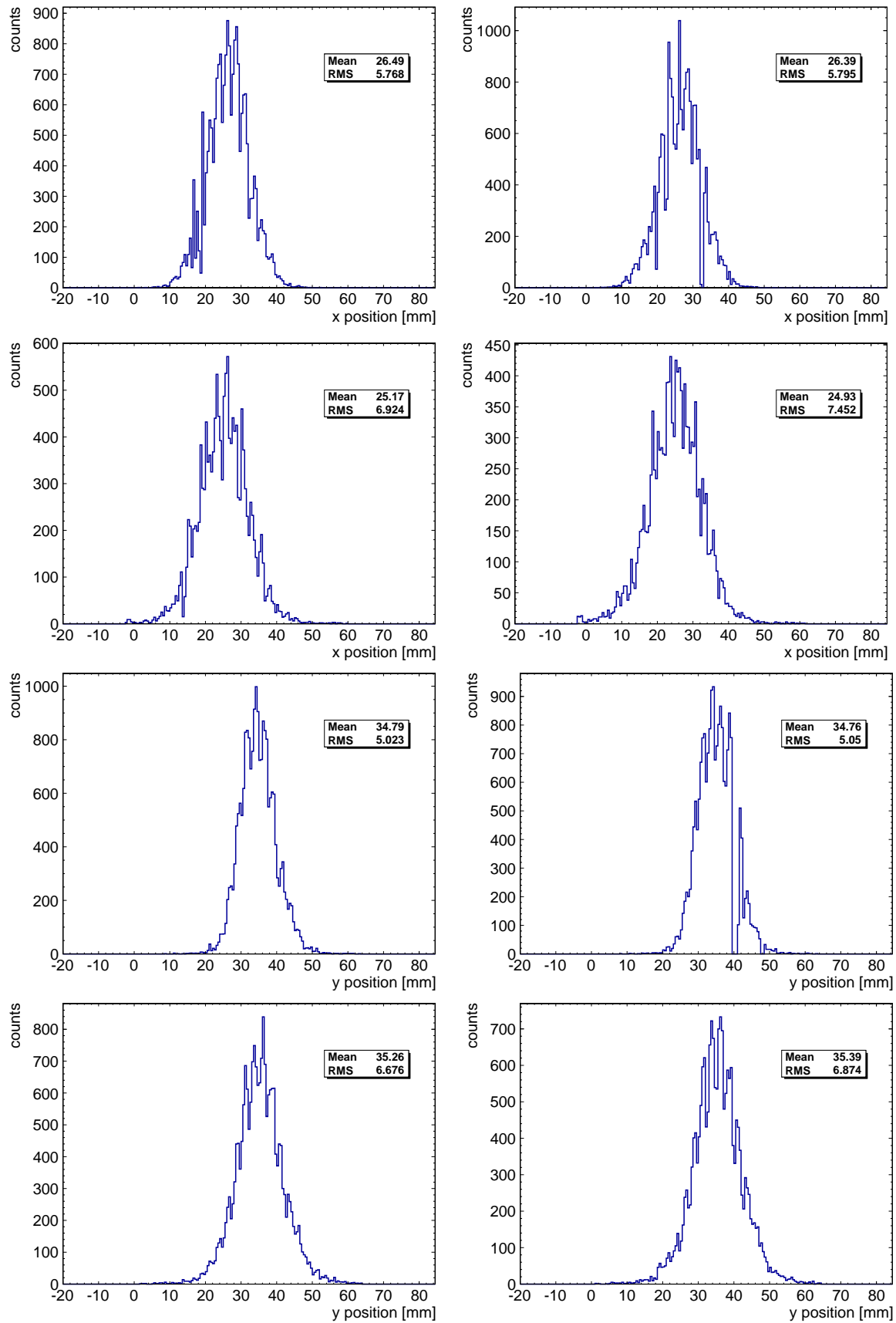


Figure 6.10: Reconstructed hit position i.e. the beam spot in all Micromegas of the tracking system, recorded with 40000 triggered events of 88.83 MeV/u carbon ions traversing the system at a particle rate of 2 MHz. The nominal beam width is 13.1 mm FWHM, given by the accelerator control system. The figures are ordered in the following way: mm0 (first row, left), mm1 (first row, right), mm2 (second row, left), mm3 (second row, right), mm4 (third row, left), mm5 (third row, right), mm6 (fourth row, left) and mm7 (fourth row, right). Note that mm0 to mm3 are tracking detectors in  $x$ -direction, whereas mm4 to mm7 measure the hit position in  $y$ -direction.

The continuous increase of the RMS for the following layers due to the expected beam divergence and various small angle scatterings within the readout structures of the tracking system and is reasonable.

The maximum number of tracks allowed per event is defined by the detector of the subset of detectors used to decide whether the event was good or not with the smallest number of clusters. Fig. 6.11 shows the number of reconstructed tracks per event and the determined  $\chi^2/\text{ndf}$  of the track fit.

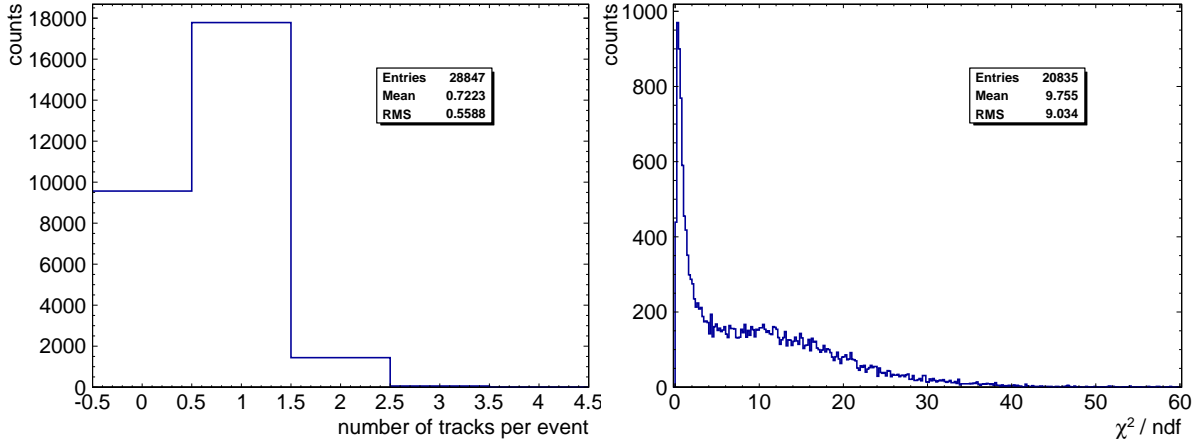


Figure 6.11: Number of reconstructed tracks per event (left) and track  $\chi^2/\text{ndf}$  (right) for a measurement with 88.83 MeV/u carbon ions at a rate of 2 MHz with a beam width of 13.1 mm FWHM.

The fraction of events, where at least one track was found, with respect to events where no track could be reconstructed, although the requested subset of detectors have registered a signal, allows for an estimate of the efficiency of the detector system and the used tracking algorithm to find a track. This yields a track finding efficiency on the order of  $\epsilon_{\text{track}} \approx 72\%$ .

The spatial resolution of a detector can then be determined via measuring the residual between track predicted and detector measured hit. Doing this for many similar tracks yields a distribution of residuals as shown in Fig. 6.12, with mm0 being included (left) and excluded (right) in the track fit.

The residual distributions can be subdivided into three areas corresponding to different physical processes, depending on which a suitable fit is used:

1. A constant background of uncorrelated noise or fragments created during the passage of the carbon ions within the readout structure of the detectors, which are emitted in any direction and are misinterpreted as signal,
2. a wide Gaussian distributed signal component due to too few hit strips (two or less) in the cluster, correlated with too small recorded pulse height,
3. a narrow Gaussian distributed signal component describing correct reconstructed hit position with more than two strips hit per cluster and appropriate pulse height.

The fit-function  $f(x)$  is defined as follows:

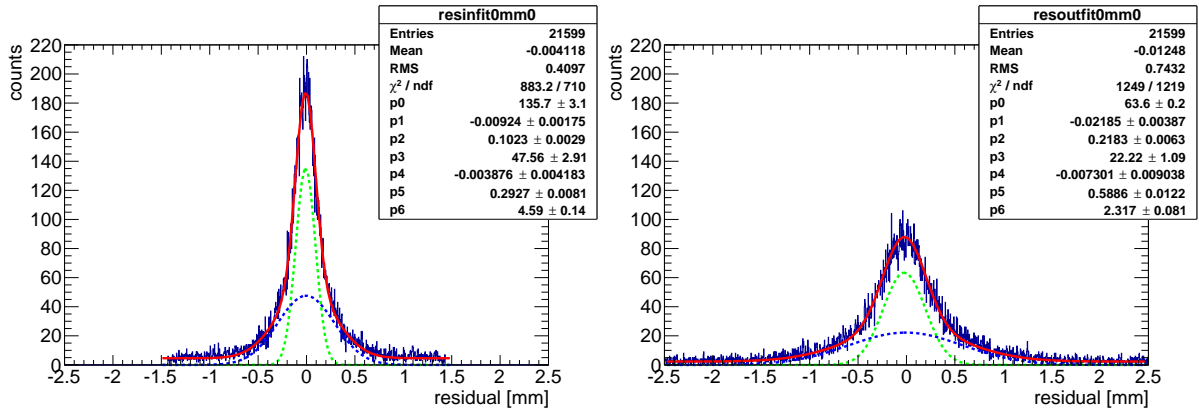


Figure 6.12: Residual distribution between predicted and measured hit position in mm0. In the left figure mm0 is included and in the right figure explicitly excluded from the track fit during a measurement with 88.83 MeV/u carbon ions at a particle rate of 2 MHz with a beam width of 13.1 mm FWHM. To determine the spatial resolution, both distributions can be fitted (red line) with the sum of two Gaussian functions (green and blue dashed line) plus an offset (p6 in the info box).

$$f(x) = p_0 \cdot \exp\left(-0.5\left(\frac{x - p_1}{p_2}\right)^2\right) + p_3 \cdot \exp\left(-0.5\left(\frac{x - p_4}{p_5}\right)^2\right) + p_6 \quad . \quad (6.6)$$

The fit compensates (1.) with a constant  $p_6$ . The calculated  $\chi^2/\text{ndf}$  value, see Fig. 6.11, right, with values  $\chi^2/\text{ndf} \geq 5$  corresponds to the same physical process (1.), where at least one detector measured such uncorrelated signals. The sum of two Gaussian functions describes the physical processes (2.) and (3.), where the narrow Gaussian function (green dashed line,  $p_0$  to  $p_2$ ) describes (3.) and the wide (blue dashed line,  $p_3$  to  $p_5$ ) compensates (2.). The resulting fit  $\chi^2/\text{ndf} \approx 1$  (see Fig. 6.12 info box) of the combined fit describe the good agreement to the measured residual data. Small values for the track  $\chi^2/\text{ndf} \leq 5$  (Fig. 6.11, right) describe situation (2.) and (3.), where a reasonably good track could be reconstructed due to enough hit strips in all detectors and no misinterpreted signals in the detector system.

The geometric mean method thus allows for the calculation of the spatial resolution of each detector in the tracking system, as described in section 4.7.2. Therefore both residual distributions for all detectors, included and excluded in the track fit, are fitted with the defined fit function from Eq. (6.6). As both physical effects of (2.) and (3.) describe the intrinsic spatial resolution of each detector without applied drift voltage, a combined spatial resolution  $\sigma_{\text{comb}}$  has thus been determined by weighting the width of each Gaussian function ( $p_2$  and  $p_5$ ) with the corresponding integral below the function, neglecting the contributions of the background estimated by  $p_6$ . However, the spatial resolution  $\sigma_{\text{narrow}}$  computed only via the narrow Gaussian part of the distribution has also been determined, as it describes the spatial resolution in events with good pulse height and a reasonable number of strips being hit in most detectors. For all determined spatial resolutions, the Kalman-based track finding algorithm correctly treats scattering of the incident particle within the readout structures of the detectors. The multiple scattering at each detector layer can be calculated via Eq. (2.10). Corresponding effective thickness in units of radiation length are for the one-dimensional floating

strip Micromegas  $0.0088 X_0$  and  $0.0106 X_0$  for the two-dimensional Micromegas. The method of how the scattering data is included in the track is described in appendix A.2. It follows, that also 'kinks' in the track are allowed. Fig. 6.13, left shows the included residual distribution of mm0 with and without allowed scattering in the tracking algorithm. A small improvement of the acquired spatial resolution on the order of 5 % is observed. The right figure shows the excluded residual distribution of mm0 with allowed scattering and superimposed (red) requiring a track fit  $\chi^2/\text{ndf} < 5$ . The elimination of constant background that was due to uncorrelated background signals is clearly visible. However, only a fraction of about 39 % of the initially as good considered events are left. An interesting fact is that the resulting spatial resolution after requiring a hard cut of  $\chi^2/\text{ndf} < 5$  only minimally improves by about 3.3 %, which justifies neglecting the background estimated by  $p6$  in the determination of the spatial resolution.

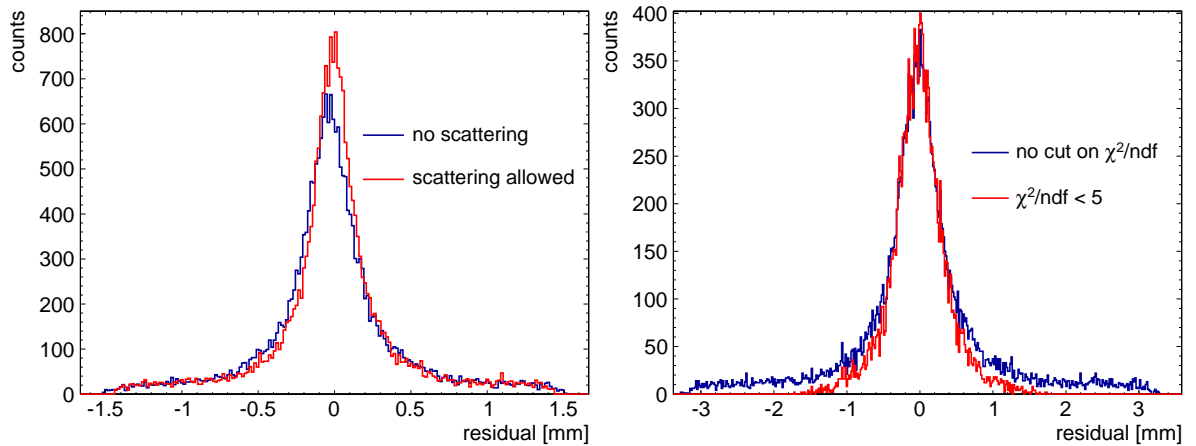


Figure 6.13: Inclusive residual distribution (left) of mm0 with scattering in the readout structures not allowed (blue) and allowed (red). Exclusive residual distribution (right) with superimposed final track fit required for  $\chi^2/\text{ndf} < 5$  (red, scaled).

Both determined spatial resolution  $\sigma_{\text{comb.}}$  and  $\sigma_{\text{narrow}}$  are tabulated in Tab. 6.1 for all Micromegas in the tracking system, measured with 88.83 MeV/u carbon ions at 2 MHz. A tracking efficiency  $\epsilon_{\text{comb.}}$  and  $\epsilon_{\text{narrow}}$  has been calculated for both spatial resolutions, where the events covered by the fit with the Gaussian functions are divided by the total number of good events. It yields an information about the fraction of events where not only a hit was registered within the detector under test - which also incorporates faked signals due to noisy strips or fragments in a detector, but also if the measured signal could be matched to a particle track through the tracking system. The residual distributions for the determined spatial resolutions of all detectors can be found in Fig. 6.14 for the inclusive and in Fig. 6.15 for the exclusive residuals.

Best values for the combined spatial resolution are found for mm0 with  $\sigma_{\text{comb.}} = (280 \pm 29) \mu\text{m}$  with an tracking efficiency of  $\epsilon_{\text{comb.}} = (57.4 \pm 6.0) \%$  and for mm7 with  $\sigma_{\text{comb.}} = (257 \pm 29) \mu\text{m}$  and  $\epsilon_{\text{comb.}} = (46.7 \pm 5.3) \%$ . The smaller observed efficiency is primarily due to a smaller reconstructed pulse height in mm7 and therefore a loss of signals. This leads in the case of mm1 to an increase of the observed spatial resolution of about  $100 \mu\text{m}$  compared to mm0 due to the limitation from too few strips being hit. The smallest efficiencies are observed for mm2 and mm3 with 41 % and 33 %, respectively. As also the reconstructed pulse height for both layers are considerably

# mm	$\sigma_{\text{comb.}}$ [mm]	$\epsilon_{\text{comb.}}$	$\sigma_{\text{narrow}}$ [mm]	$\epsilon_{\text{narrow.}}$	residual fit $\chi^2/\text{ndf}$
0	$0.280 \pm 0.029$	0.574	$0.149 \pm 0.009$	0.291	1.13
1	$0.371 \pm 0.030$	0.609	$0.154 \pm 0.006$	0.317	1.08
2	$0.308 \pm 0.035$	0.412	$0.121 \pm 0.008$	0.200	1.09
3	$0.298 \pm 0.036$	0.328	$0.136 \pm 0.010$	0.147	1.01
4	$0.433 \pm 0.054$	0.594	$0.173 \pm 0.010$	0.259	1.12
5	$0.359 \pm 0.054$	0.521	$0.172 \pm 0.008$	0.300	1.04
6	$0.284 \pm 0.030$	0.525	$0.144 \pm 0.007$	0.275	1.12
7	$0.257 \pm 0.029$	0.467	$0.180 \pm 0.008$	0.308	1.12

Table 6.1: Spatial resolution and tracking efficiency for all Micromegas, determined via the geometric mean method with a weighted double Gaussian plus offset fit for a 88.83 MeV/u carbon beam at 2 MHz.  $\sigma_{\text{comb.}}$  refers to a combined spatial resolution via weighting both Gaussian function distributions with the integral below the found functions.  $\sigma_{\text{narrow}}$  describes the spatial resolution calculated only via the narrow Gaussian. Same holds for the efficiency  $\epsilon_{\text{comb.}}$  and  $\epsilon_{\text{narrow}}$ , describing the relative fraction of events covered by either both or only the narrow Gaussian function. The values for  $\chi^2/\text{ndf}$  around 1 show the good agreement between fit and data.

smaller than for all other detectors, this is understandable. Nevertheless, both detectors exhibit a spatial resolution of  $\sigma_{\text{comb.}} = (308 \pm 35) \mu\text{m}$  and  $\sigma_{\text{comb.}} = (298 \pm 36) \mu\text{m}$ . The fact that mm4 shows the worst spatial resolution with  $\sigma_{\text{comb.}} = (433 \pm 54) \mu\text{m}$  is not yet fully understood, as it reconstructs a comparatively high pulse height with a reasonable number of hit strips within the selected cluster.

The observed spatial resolution only for the narrow part of the residual distribution is for all detectors below  $180 \mu\text{m}$  with describing on average 26.2% of the events. The best results are observed for mm0 with  $\sigma_{\text{narrow}} = (149 \pm 9) \mu\text{m}$  and  $\epsilon_{\text{narrow}} = (29.1 \pm 1.8) \%$  and for mm2 with  $\sigma_{\text{narrow}} = (121 \pm 8) \mu\text{m}$  and  $\epsilon_{\text{narrow}} = (20.0 \pm 1.3) \%$ .

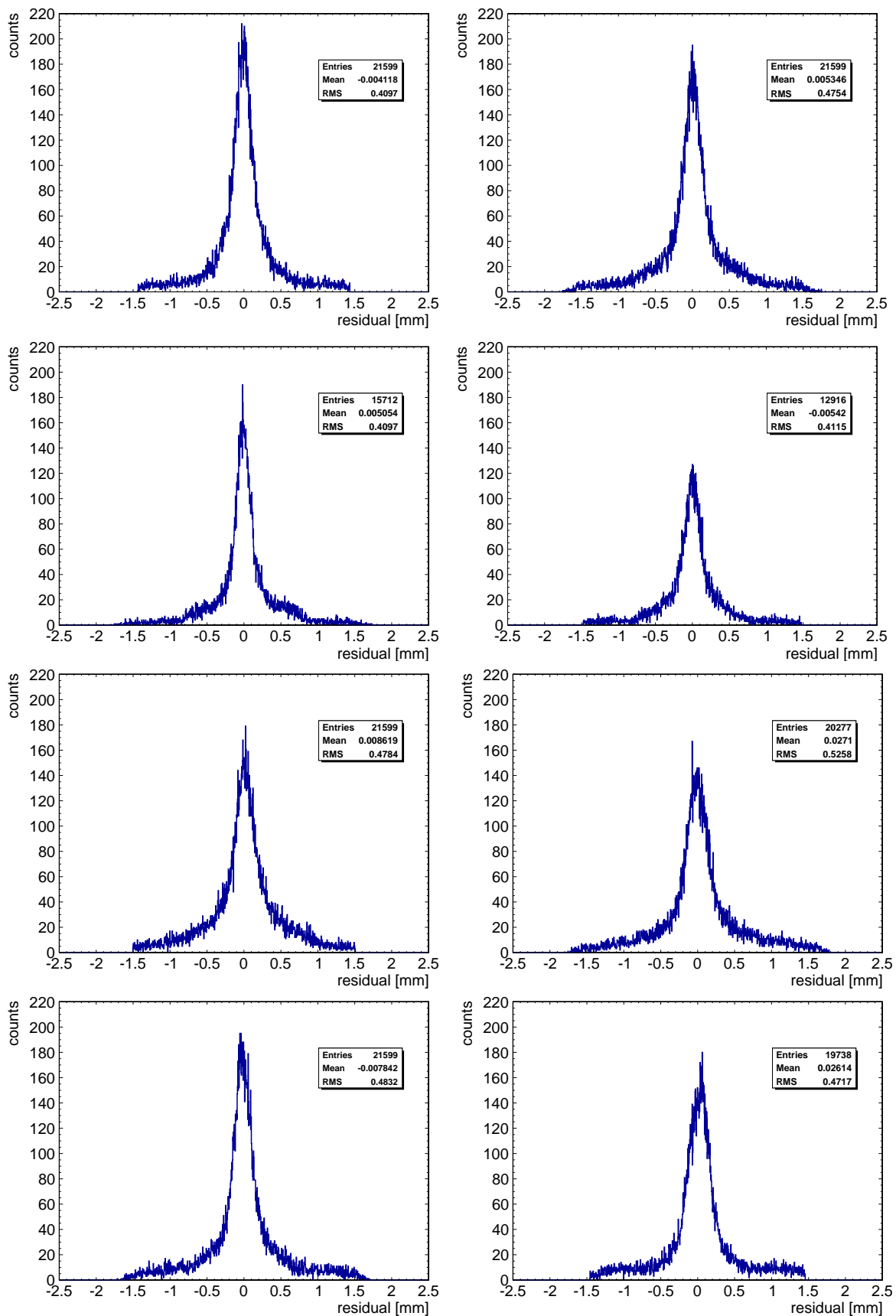


Figure 6.14: Inclusive residual distribution of all Micromegas, measured with 88.83 MeV/u carbon ions at a beam width of 13.1 mm FWHM and a rate of 2 MHz. The figures are ordered the following way: mm0 (first row, left), mm1 (first row, right), mm2 (second row, left), mm3 (second row, right), mm4 (third row, left), mm5 (third row, right), mm6 (fourth row, left) and mm7 (fourth row, right). Note that mm0 to mm3 are tracking detectors in  $x$ -direction, whereas mm4 to mm7 measure the hit position in  $y$ -direction.

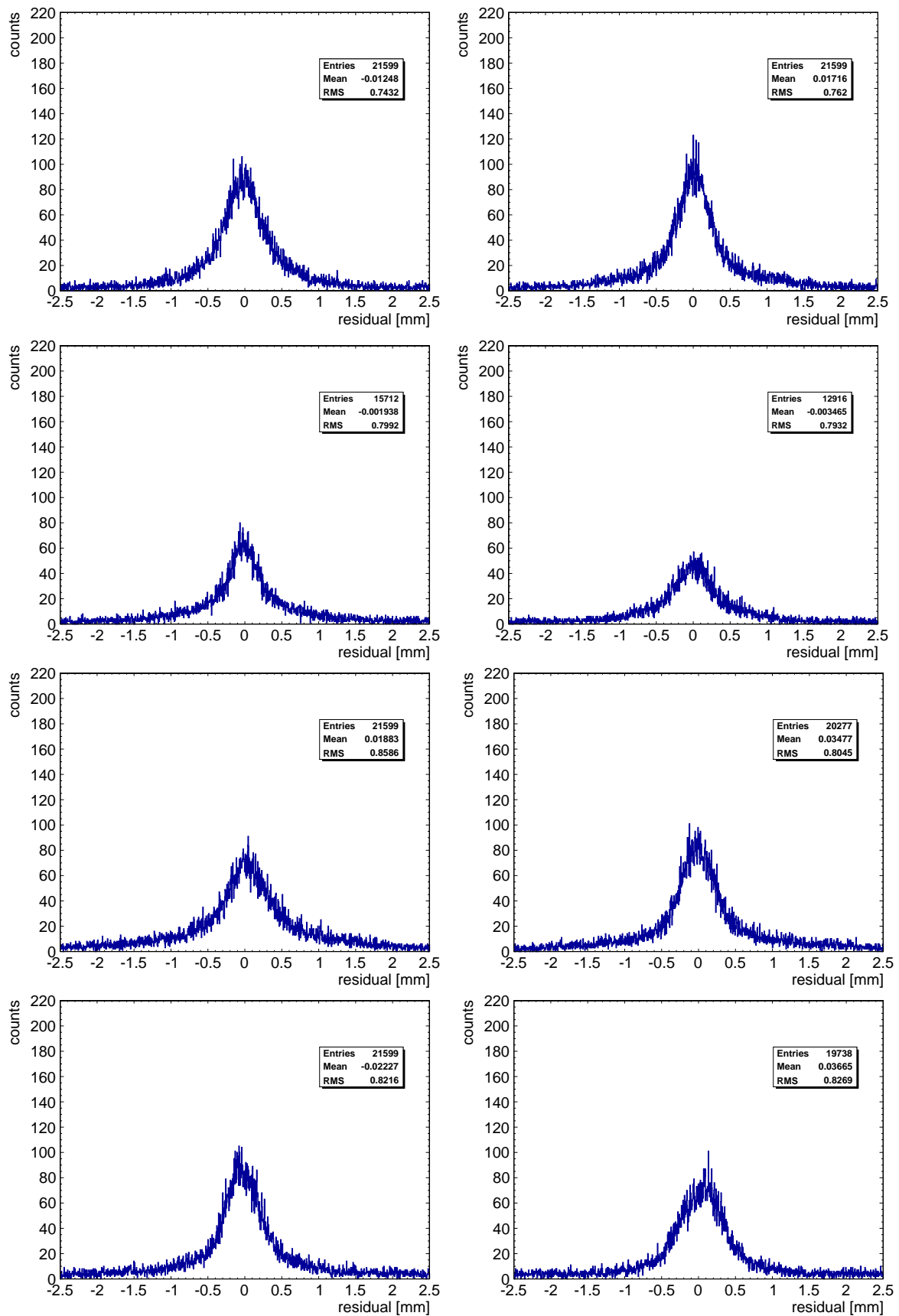


Figure 6.15: Exclusive residual distribution of all Micromegas, measured with 88.83 MeV/u carbon ions at a beam width of 13.1 mm FWHM and a rate of 2 MHz. The figures are ordered the following way: mm0 (first row, left), mm1 (first row, right), mm2 (second row, left), mm3 (second row, right), mm4 (third row, left), mm5 (third row, right), mm6 (fourth row, left) and mm7 (fourth row, right). Note that mm0 to mm3 are tracking detectors in  $x$ -direction, whereas mm4 to mm7 measure the hit position in  $y$ -direction.

Fig. 6.16 shows the inclusive residual distribution of mm0 for a carbon beam with 88.83 MeV/u beam energy and superimposed the distribution with a significantly higher beam energy of 270.55 MeV/u after scaling both histograms to the same number of entries. First it can be seen that for increasing beam energy, the fraction of background signals increases. This is due to the increased fragmentation with increasing beam energy, after inelastic scattering of carbon ions and the decreasing signal to noise ratio. Second, the Gaussian distributed part of the residual distribution changes in two ways: On the one hand, the narrow part gets more narrow, as due to a higher beam energy the carbon ions are less affected by multiple scattering in the detectors. On the other hand, the wide part of the distribution gets more wide, as the lower energy loss of the carbon ions lead to a smaller reconstructed pulse height, thus limiting the hit reconstruction capabilities due to too few hit strips.

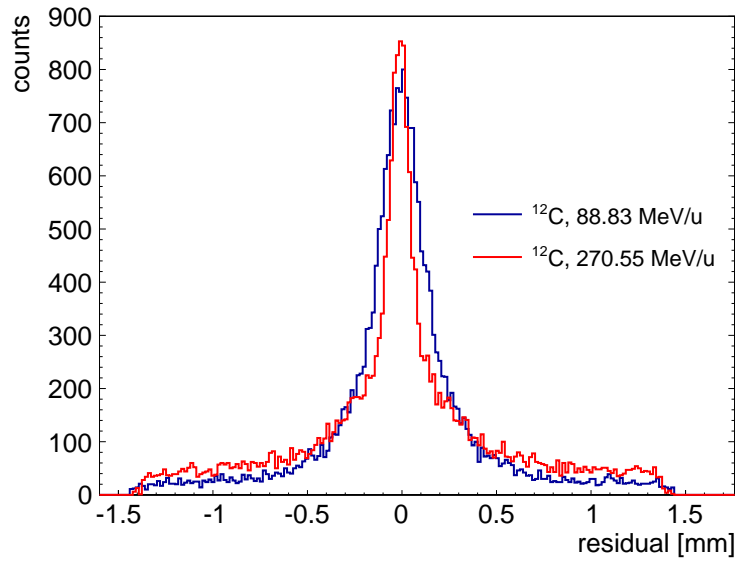


Figure 6.16: Inclusive residual distribution of mm0 for a 88.83 MeV/u carbon beam (blue) and superimposed the distribution with 270.55 MeV/u beam energy (red). The distributions are scaled to the same number of tracks for a better comparison.

The acquired spatial resolution and tracking efficiency of all Micromegas in the tracking system for the increased beam energy are listed in Tab. 6.2, also determined by the fit defined in Eq. (6.6) to the residual distributions. A track finding efficiency of about 63 % is determined. All resulting combined spatial resolution get worse as compared to results at lower beam energy, c.f. Tab. 6.1. As the pulse height decreases considerably, a large fraction of the reconstructed hit positions is afflicted with the systematic error due to too few hit strips, thus broadening the residual distribution of each detector in the flat part of the Gaussian distribution.

As the computed hit efficiency for 270.55 MeV/u is already significantly lower than for the 88.83 MeV/u beam energy (see Fig. 6.6), the resulting tracking efficiency is decreasing as well.

The determined spatial resolution for the two-dimensional floating strip Micromegas doublet are either suffering from very low statistics (mm2 and mm3) or the residual distribution becomes highly asymmetric due to only one hit strip (mm6 and mm7; also denoted with a star in Tab. 6.2). In Fig. 6.17 the number of hit strips in mm7 is shown as a function of the residual. It is clearly visible that for the majority of events,

# mm	$\sigma_{\text{comb.}}$ [mm]	$\epsilon_{\text{comb.}}$	$\sigma_{\text{narrow}}$ [mm]	$\epsilon_{\text{narrow.}}$	$\chi^2/\text{ndf}$
0	$0.362 \pm 0.041$	0.429	$0.087 \pm 0.004$	0.167	1.66
1	$0.465 \pm 0.048$	0.479	$0.096 \pm 0.005$	0.162	1.47
2*	$0.440 \pm 0.093$	0.134	$0.125 \pm 0.011$	0.054	1.21
3*	$0.388 \pm 0.059$	0.088	$0.134 \pm 0.007$	0.036	1.14
4	$0.460 \pm 0.045$	0.497	$0.115 \pm 0.006$	0.183	1.25
5	$0.528 \pm 0.066$	0.438	$0.152 \pm 0.007$	0.193	1.23
6*	$0.397 \pm 0.042$	0.463	$0.158 \pm 0.006$	0.232	1.70
7*	$0.267 \pm 0.023$	0.293	$0.090 \pm 0.004$	0.134	1.99

Table 6.2: Spatial resolution and tracking efficiency for all Micromegas, determined via the geometric mean method with a weighted double Gaussian plus offset fit for a 270.55 MeV/u carbon beam at I=2 MHz.  $\sigma_{\text{comb.}}$  refers to a combined spatial resolution from weighting the standard deviation of both Gaussian functions with the respective integral.  $\sigma_{\text{narrow}}$  describes the spatial resolution calculated only via the narrow Gaussian. Same holds for the tracking efficiency  $\epsilon_{\text{comb.}}$  and  $\epsilon_{\text{narrow.}}$ , describing the relative fraction of events covered by either both or only the narrow Gaussian function. The remaining events are either due to uncorrelated noise signals or fragments originating from inelastic scattering processes of carbon ions within the detector structures. The values for  $\chi^2/\text{ndf}$  are on average bigger than for the measurements at lower energy, as the distributions get more asymmetric due to fewer hit strips. The 'star' symbol\* denotes that the determined spatial resolution has to be taken with a grain of salt, due to low statistics combined with noise (mm2 and mm3) or reconstruction of double peaks in the residual distribution (mm6 and mm7) due to only one hit strip.

where only one hit strip is reconstructed, the residual distribution gets split into two separate, approximately Gaussian distributed parts. They correspond to the position of two different hit strips that should intrinsically belong to the same cluster, but have been reconstructed as only one hit strip, as the pulse height on the other strip was too small to overcome the noise threshold. For the less frequent case of more than one hit strip, the true hit position between the two adjacent strips is reconstructed (in the middle of both peaks). The larger  $\chi^2/\text{ndf}$  values of the fit in Tab. 6.2 confirm the inaccuracy of fit.

Also for the lower beam energy the same effect also limits the reconstructed spatial resolution, but with a smaller impact, as the majority of events yield more than one hit strip per detector layer, see Fig. 6.5.

The asymmetric shape of the residual distributions can be suppressed by requiring more than one hit strip for the cluster building, but leading to a loss of statistics. As low statistics already is a problem due to the smaller recorded pulse height resulting in rather low tracking efficiencies of mm2 and mm3 with  $\epsilon_{\text{comb.}}=13.4\%$  and  $\epsilon_{\text{comb.}}=8.8\%$ , this is not feasible. To improve the tracking quality with higher pulse height in all detectors, higher amplification fields are advantageous in this case, as they have not been pushed to the limits for the presented measurements at 270.55 MeV/u carbon beam energy with:  $E_{\text{amp},0}=32.7\text{ kV/cm}$ ,  $E_{\text{amp},1}=30.9\text{ kV/cm}$ ,  $E_{\text{amp},2}=E_{\text{amp},6}=33.3\text{ kV/cm}$ ,  $E_{\text{amp},3}=E_{\text{amp},7}=31.3\text{ kV/cm}$ ,  $E_{\text{amp},4}=32.7\text{ kV/cm}$  and  $E_{\text{amp},5}=31.3\text{ kV/cm}$ .

Nevertheless, the best combined spatial resolution is observed for mm0 with  $\sigma_{\text{comb.}} = (362 \pm 41)\ \mu\text{m}$  at a tracking efficiency of  $\epsilon_{\text{comb.}} = (42.9 \pm 4.9)\%$ . The significantly better

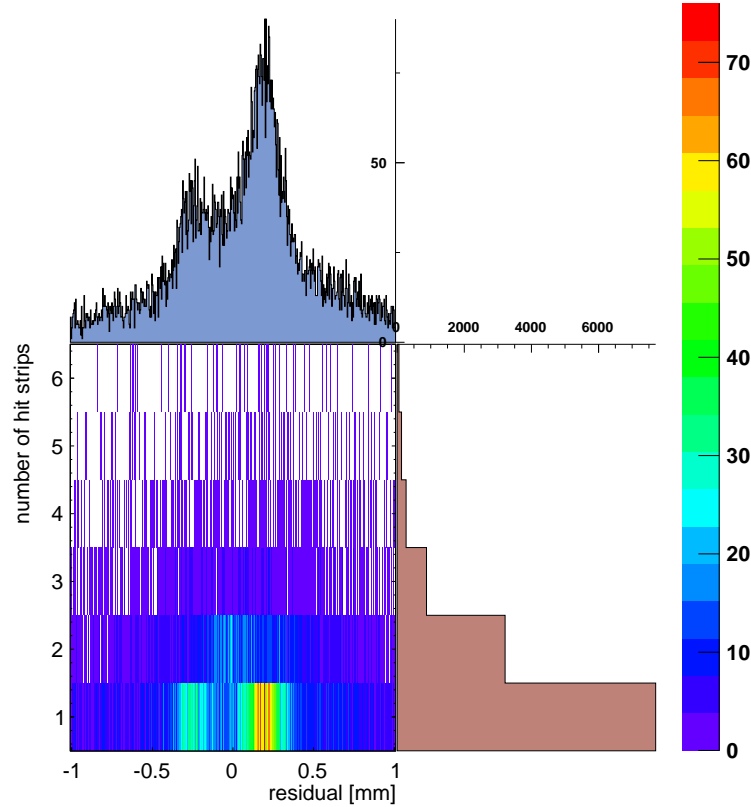


Figure 6.17: Reconstructed number of hit strips as a function of the measured exclusive residual in mm7 for a 270.55 MeV/u carbon beam at 2 MHz with  $E_{\text{amp},7} = 31.3$  kV/cm. The asymmetric shape of the residual distribution due to only one hit strip is visible in the upper projection.

spatial resolution for the narrow part of the distribution with  $\sigma_{\text{narrow}} = (87 \pm 4) \mu\text{m}$  promises excellent track reconstruction capabilities if the signals amplitude is large enough and more than two strips are hit. However, in this case only about  $(16.7 \pm 0.8)\%$  of all good events fulfill these requirements.

In the following, the first, one-dimensional readout floating strip Micromegas doublet, consisting of mm0 and mm1, has been tilted by  $(15.0 \pm 0.5)^\circ$ ,  $(25.3 \pm 0.5)^\circ$  and  $(35.0 \pm 0.5)^\circ$  with respect to the beam axis. The spatial resolution is now being discussed as a function of the track inclination.

As the charge weighted mean hit reconstruction usually suffers from clustering during the ionization process in the drift gap, the resulting spatial resolution typically worsens for increasing track inclination above  $10^\circ$  in Micromegas detectors, see section 5.6. However, in the case of Micromegas without drift voltage, the reconstructed hit position does not lie in a plane in the middle of the drift gap, but in close proximity to the micro-mesh: For known track inclination  $\Theta$  of the traversing particles, the distance between two virtual sensitive planes in the two detectors mm0 and mm1 can be calculated via the shift of the beam spot  $\Delta x$ , as already explained in section 5.5. A track inclination of  $(25.3 \pm 0.5)^\circ$  yields a shift  $\Delta x = (12.76 \pm 0.06)$  mm. Thus the distance  $d$  between both reconstructed hit positions can be calculated by

$$d = \frac{\Delta x}{\tan(\Theta)} = \frac{(12.76 \pm 0.06) \text{ mm}}{\tan(25.3^\circ \mp 0.5^\circ)} = (27.0 \pm 0.8) \text{ mm} . \quad (6.7)$$

Since the distance between both readout PCB's within the doublet is  $d_0=(25.9\pm 0.5)$  mm, the position  $z_0$  of the reconstructed charge weighted mean hit position above the anode plane can be estimated for both detectors, following

$$z_0 = \frac{d - d_0}{2} = \frac{(27.0 - 25.9) \text{ mm}}{2} = (0.55 \pm 0.63) \text{ mm} . \quad (6.8)$$

As the error with 0.63 mm is larger than the value for  $z_0$  with 0.55 mm, unfortunately no accurate statement about the reconstruction plane in the detectors can be made. It is due to the uncertainty of the determined track inclination with  $0.5^\circ$  which was not possible to be measured more accurately. Also the uncertainty of the distance between both readout PCBs is with  $500 \mu\text{m}$  a limiting factor. Nevertheless, the value is not compatible with a sensitive plane in the middle of the drift gap, as it is obviously considerably closer to the mesh.

The exclusive residual distribution of mm0 and mm1 is shown in Fig. 6.18, superimposed for all investigated inclination angles. It is clearly visible that the width of the distribution, describing the spatial resolution of the detectors, does not change much for increasing track inclination.

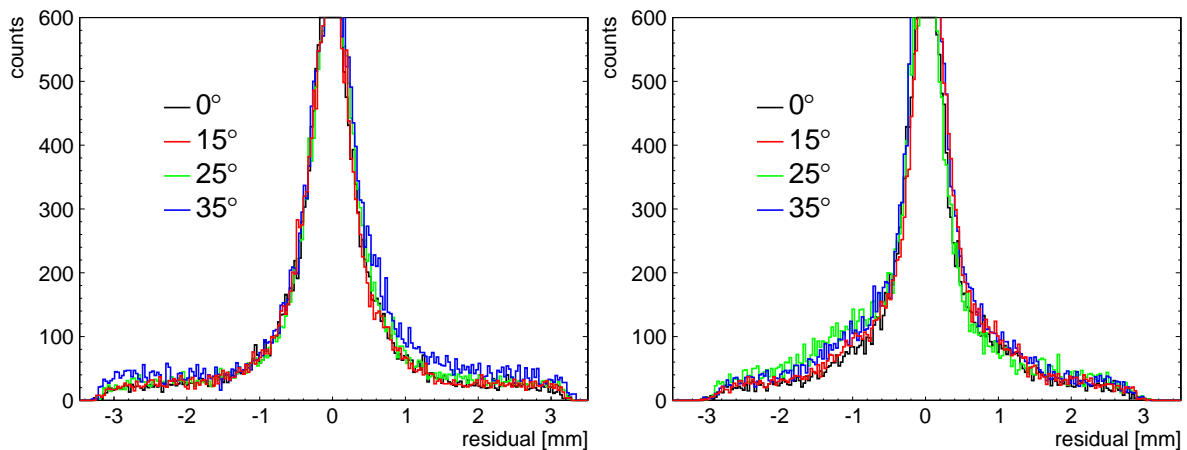


Figure 6.18: Exclusive residual distribution of mm0 (left) and mm1 (right) for different inclination angles  $(0.0 \pm 0.5)^\circ$  (black),  $(15.0 \pm 0.5)^\circ$  (red),  $(25.3 \pm 0.5)^\circ$  (green) and  $(35.0 \pm 0.5)^\circ$  (blue), measured with 88.83 MeV/u carbon ions.

In the case of mm0, the narrow part of the distribution is unchanged for all inclination angles. Only for a track inclination of  $35^\circ$ , the positive part of the wide Gaussian distributed region increases (blue line). The asymmetric increase can be explained by the scattering of the ions around the expected hit position: Positive values of the residual describe the case of a scattering process against the orientation of the track inclination. This leads to a reduced effective path length of the traversing particle within the region of the amplification gap. A smaller path length ultimately leads to a reduction of the pulse height and number of hit strips in the detector, which again, degrades the spatial resolution of the detector.

The distribution of mm1 looks similar, however, the asymmetric tail of the distribution, in this case for negative values of the residual as expected, increases for all track inclinations. As mm1 reconstructs a smaller pulse height than mm0, an increase of the inclination angle of already  $15^\circ$  leads to a degradation of the wide part of the distribution. For angles  $25.3^\circ$  (green) and  $35^\circ$  (blue) the effect becomes more dominant.

The residual distributions of both detectors are then fitted with the function defined in Eq. (6.6) and the spatial resolution is determined with the geometric mean ( $\sigma_{\text{geo}}$ ), as well as with the track interpolation ( $\sigma_{\text{tr. int.}}$ ) method, both explained in section 4.7. The calculated spatial resolution is the combined resolution of wide and narrow part of the distribution, as already explained and used in Tab. 6.1 and Tab. 6.2.

Fig. 6.19 shows the determined spatial resolution of mm0 and mm1 as a function of the track inclination ( $0.0 \pm 0.5$ ) $^\circ$  (black), ( $15.0 \pm 0.5$ ) $^\circ$ , ( $25.3 \pm 0.5$ ) $^\circ$  and ( $35.0 \pm 0.5$ ) $^\circ$ . The track uncertainty at both detector positions, needed for the calculation of the track interpolation spatial resolution, is deduced from the acquired spatial resolutions listed in Tab. 6.1, explicitly only for tracking detectors in  $x$ -direction, as the first doublet consisting of mm0 and mm1 is oriented in  $x$ -direction. For the analytical determination of the track uncertainty at each detector position, see appendix A.1. The vertical errors are calculated from the accuracy of the fit to the residual distributions for the geometric mean method and for the track interpolation method also from the error of the track uncertainty determination. The determined spatial resolution from the two different methods are constant within their respective errors for increasing track inclination, as the similar shaped residual distribution already indicated.

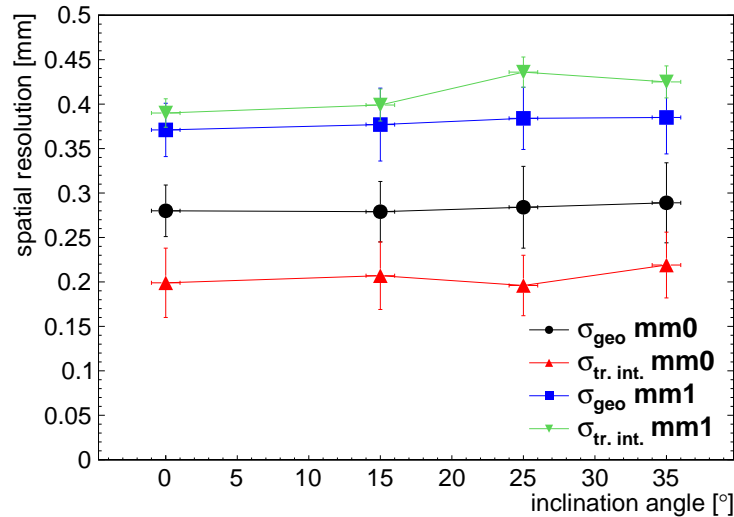


Figure 6.19: Spatial resolution of mm0 and mm1 as a function of the track inclination, calculated via two different methods for a 88.83 MeV/u carbon beam at 2 MHz.

The spatial resolution of mm0 for a perpendicularly incident beam ( $0^\circ$ ) determined via the track interpolation method is with  $\sigma_{\text{tr. int.}} = (199 \pm 39) \mu\text{m}$  by 81  $\mu\text{m}$  better than the geometric mean spatial resolution with  $\sigma_{\text{geo}} = (280 \pm 29) \mu\text{m}$ . In the case of mm1, the geometric mean reconstructs a 19  $\mu\text{m}$  better spatial resolution with  $\sigma_{\text{geo}} = (371 \pm 30) \mu\text{m}$  as compared to  $\sigma_{\text{tr. int.}} = (390 \pm 16) \mu\text{m}$ . This different behavior of both methods is understandable, as the geometric mean method tends to equalize all spatial resolutions in a system, therefore pulling values for mm0 to higher and for mm1 to lower values. Reliable results can in this case only be obtained with the track interpolation method. The spatial resolutions of mm0 and mm1 determined via the track interpolation method differ by 191  $\mu\text{m}$ . This reveals the immense impact of the lower gas gain of mm1, resulting in a significantly lower reconstructed pulse height.

As already mentioned, for increasing track inclination, the spatial resolution is nearly constant within the calculated errors for both used methods. For  $35^\circ$  the spatial res-

olution of mm0 with  $\sigma_{\text{tr. int.}} = (219 \pm 37) \mu\text{m}$  increases only by  $20 \mu\text{m}$  compared to the perpendicular case. In the case of mm1, the resolution degrades by  $35 \mu\text{m}$  to  $\sigma_{\text{tr. int.}} = (425 \pm 18) \mu\text{m}$  at  $35^\circ$ .

## 6.5 Ion Transmission Radiography

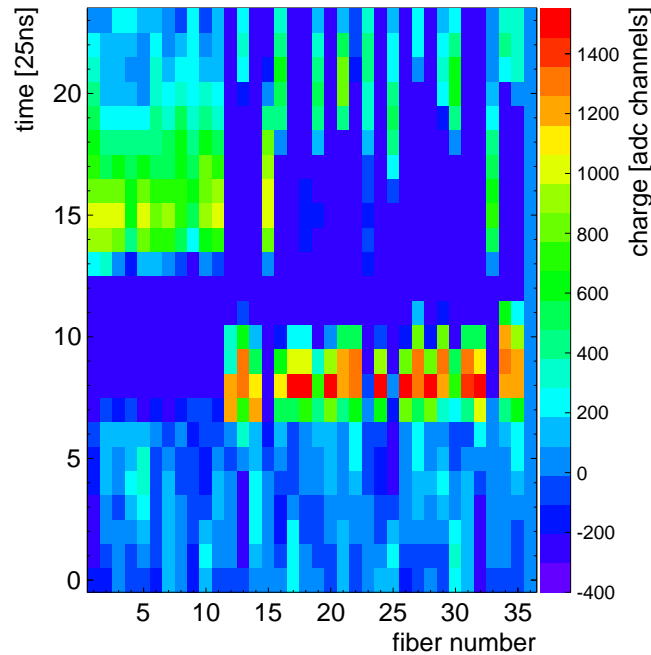


Figure 6.20: Typical event of the range telescope APV25 raw data, measured with 126.11 MeV/u carbon ions with a 15 mm PMMA plate in front of the range telescope. As the 18 scintillator layers are each equipped with two fibers, a total of 36 fibers are connected to APV-channels. The beam enters from the right, therefore fibers 35 and 34 represent scintillator layer 1. Thus the carbon ion penetrating into the range telescope can be identified by the red peaks (time  $\approx 8 \times 25$  ns) and stops at fiber 12 - corresponding to a penetration depth of a total of 12 scintillator layers.

For acquiring radiographies, the GEM detector has been removed from the tracking system and the particle range telescope, described in section 6.1, is placed behind the tracking system. A carbon beam with energies 126.11 MeV/u and 248.91 MeV/u has been used to acquire radiographies of a PMMA step phantom (section 6.5.1) and a slab phantom (section 6.5.2), respectively. A treatment plan has been used, where the carbon beam scanned an area of  $5 \times 5 \text{ cm}^2$  in steps of 5 mm, at a particle rate of 2 MHz. This corresponds to  $8 \times 10^6$  particles per raster point. The readout electronics for the tracking and range telescope has been triggered by a coincident signal of two fibers of the first two scintillator layers. As the range telescope is not able to trigger at the full rate of the treatment plan due to saturation of the photomultiplier, an approximately 20% smaller trigger frequency is observed. As the SRS based readout system [RD51, 2010] allowed only for a maximum acquisition rate of about 1.5 kHz, a  $5 \times 5 \text{ cm}^2$  radio-

graphy usually required more than one scan. The data acquisition rate is limited by the data transfer of the nine APVs from the FEC via Ethernet to the DAQ computer and then to disk.

A 15 mm PMMA plate is placed in front of the range telescope, to modify the position of the Bragg peak in the range telescope. As the range telescope consists of 18 1 mm thick plastic scintillator layers, each read out with two wave length shifting fibers, a total of 36 signals are recorded with the external APV after amplification by photomultipliers, shaping and amplification and dedicated attenuation. Fig. 6.20 shows the APV25 raw data of a typical event in the particle range telescope, recorded with 126.11 MeV/u carbon ions. No phantom is in the beam. The horizontal axis denotes the fiber id from 0 to 35, where fiber 34 and 35 correspond to the first scintillator layer in the beam direction. After an accepted trigger, a temporal capturing window of 600 ns is recorded on disc, corresponding to 24 timebins of each 25 ns length on the vertical axis. The carbon ion penetrating into the range telescope can be identified by the recorded fiber pulses between fiber 35 and 12 with a timing of the maximum at around 8 timebins. The fast scintillator signal is clearly visible, as the APV time resolution of 25 ns barely allows to resolve the full shape of the pulse with only about 3 to 4 timebins of pulse duration. It is visible as well, that most of the fibers drive the respective APV channels into saturation with a maximum recorded ADC value of about 1400. Signals recorded for fibers 0 to 11 are not from the triggered carbon ion but correspond to the base-line shift of the APV and the following negative shaper response of the TSA. Thus signals in the range telescope are accepted only for timings smaller than 11 timebins and with a maximum pulse height exceeding 400 ADC channels, corresponding to signals created by the initially triggering carbon ion.

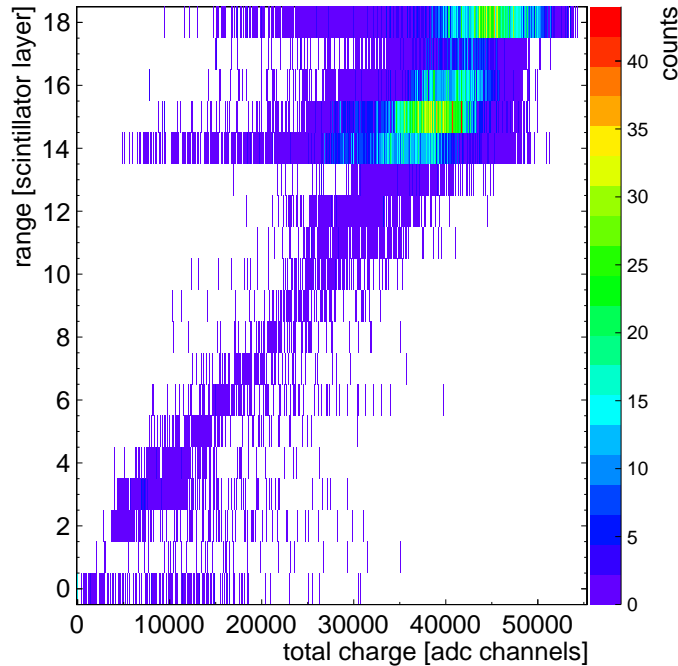


Figure 6.21: Correlation between penetration depth and measured total charge in the particle range telescope of 80k recorded events with 126.11 MeV/u carbon ions and a 15 mm PMMA plate in front of the telescope. The position of the Bragg-peak is visible.

Fig 6.21 shows the correlation between the measured penetration depth into the range telescope and the total recorded pulse height, represented by the sum of all signals in the range telescope. If one out of two fibers per scintillator layer registered a hit, the corresponding layer is treated as hit. It is measured with 80k carbon ions with an energy of 126.11 MeV/u and a 15 mm PMMA plate in front of the telescope. It can be seen that the majority of ions get stop within layers 14 to 17, with a maximum recorded charge of about 38k ADC channels. The systematic, nearly linear increase of the measured total charge for increasing penetration depth is due to the saturation of each APV channel per fiber. However, a fraction of approximately 26 % of the ions show a maximum range of 18 scintillator layers. This corresponds to events where the ions got stopped in a previous layer but a fragment is emitted in flight direction and creates signals on adjacent layers or the range was misreconstructed due to noise in the APV.

However, the range straggling of the carbon ions can be calculated. Therefore, a Gaussian function is fitted to the range distribution between layers 13 and 17, representing the Bragg-peak. The resulting width  $\sigma_{\text{range}} = (0.810 \pm 0.003)$  mm gives an approximation about the range straggling of the carbon ions in the telescope. The thickness of each scintillator layer is with 1 mm in the same order as the straggling of the ions. Thus a finer segmentation below 0.8 mm is not beneficial for the particular case of 126.11 MeV/u carbon ions. Comparing the events used for the calculation of the straggling i.e. the events within the Bragg peak with all events registered in the telescope, yields an approximation of the fragmentation of ions and also the noise performance of the range telescope. A value of approximately 70 % is determined. Signals with recorded penetration depths smaller than 13 layers are due the misreconstruction caused by layer inefficiency. Accordingly the inefficiency of the range telescope can be calculated by counting these events, dividing it by the total number of events registered. An inefficiency  $\epsilon \approx 3.6$  % is determined.

### 6.5.1 Radiography: Step Phantom

In this section, radiographies of a PMMA step phantom acquired with the Micromegas tracking system and the scintillator range telescope are presented. The setup for this measurement is sketched in Fig. 6.22. The step phantom is positioned between the second one-dimensional and the two-dimensional floating strip Micromegas doublet. PMMA blocks of suitable thickness in front of the range telescope allow to adjust the particle energy such that the Bragg peak of the carbon beam lies within the 18 layers of the telescope.

The step phantom consists of PMMA with 3 mm long steps of 1 mm thickness. An effective thickness of  $d_{\text{step}} = 0.1 \cdot X_0$  has been calculated for the phantom, assuming an average thickness (in beam direction) of 35 mm with  $X_0 = 340.8$  mm for PMMA. It is used for multiple scattering approximations in the tracking algorithm, see appendix A.2.

A 126.11 MeV/u carbon beam at a rate of 2 MHz has been used, scanning an area of  $5 \times 5 \text{ cm}^2$  in steps of 5 mm. The Micromegas were supplied with following amplification fields for all measurements with the step phantom:  $E_{\text{amp},0} = 32 \text{ kV/cm}$ ,  $E_{\text{amp},1} = 30.3 \text{ kV/cm}$ ,  $E_{\text{amp},2} = E_{\text{amp},6} = 34 \text{ kV/cm}$ ,  $E_{\text{amp},3} = E_{\text{amp},7} = 33.3 \text{ kV/cm}$ ,  $E_{\text{amp},4} = 32 \text{ kV/cm}$  and  $E_{\text{amp},5} = 32.6 \text{ kV/cm}$ . The tracking algorithm searches for tracks only

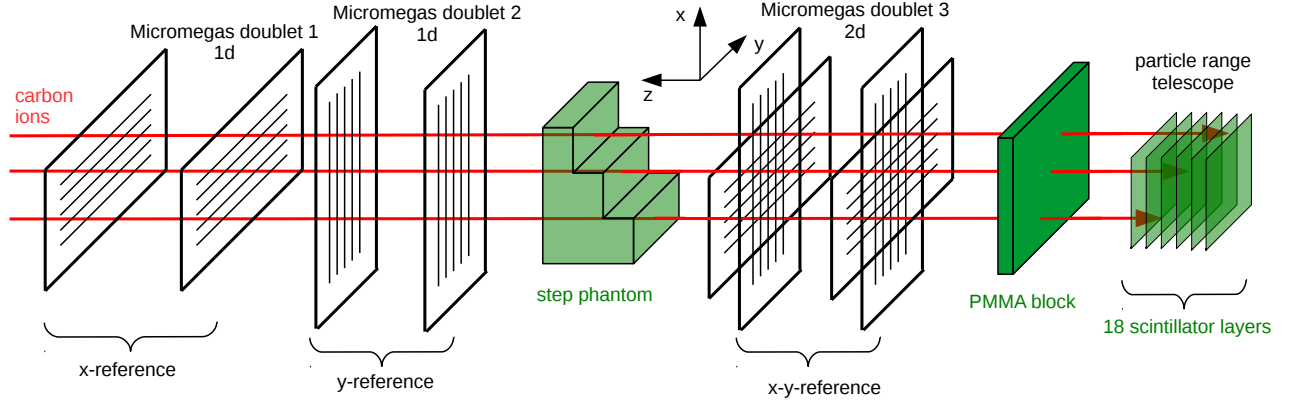


Figure 6.22: Setup for acquiring radiographies of a PMMA step phantom. A PMMA block of suitable thickness is placed in front of the particle range telescope to adjust the carbon ion energy such that they stop within the range telescope.

if mm1 and mm4 simultaneously have registered a signal, then using all additionally available hits registered in the other detectors.

Fig. 6.23, left, shows the reconstructed track inclination in the  $z$ - $y$ -plane after the last detector in the tracking system, with (red) and without (blue) the step phantom in the beam. A fit with a Gaussian function to the upper part of both distributions yields an estimate of the beam divergence for both cases with  $\sigma_{\text{with}} = (7.14 \pm 0.03)$  mrad and  $\sigma_{\text{without}} = (6.50 \pm 0.03)$  mrad, respectively. The inclination is only minimally influenced by scattering of the carbon ions within the thin PMMA material of the step phantom. The scattering angle  $\Theta$  in the step phantom can be approximated via Eq. (2.10), using the effective phantom thickness of  $0.1 \cdot X_0$  and  $\beta cp/z = 474.36$  MeV for 126.11 MeV/u carbon ions. A value of  $\Theta = 2.6$  mrad is determined, which is in the same order as the observed inclination difference and thus in good agreement with the measurement.

Fig. 6.23, right, shows the radiography of the step phantom i.e. the range of the carbon ions as a function of the extrapolated hit position in the step phantom, rotated by  $90^\circ$  around the  $z$ -axis. A sharper contrast of the steps, oriented in  $y$ -direction, is observed, when comparing it to Fig. 6.24, left, although the number of recorded events for the rotated measurement is about 20k events smaller. The better contrast is due to the higher efficiency of the  $y$ -tracking detectors: As the tracking detectors in  $x$ -direction after the phantom are the two bottom layers of the two-dimensional Micromegas doublet, which show a considerable smaller efficiency (see section 6.4), the track in  $x$ -direction is often only defined by the hits measured in Micromegas doublet 1 in front of the phantom. This leads to a larger error for the extrapolated  $x$  hit position of the phantom and thus to a degradation of the image resolution in  $x$ -direction.

Fig. 6.24, left, shows the radiography of the step phantom (rotated  $90^\circ$  back around  $z$ -axis to the initial position, as shown in Fig. 6.22) with 30 mm PMMA placed in front of the range telescope. Steps can be identified in  $x$  direction for  $x \geq 20$  mm, where the range changes from 2 layers (blue) to about 9 layers (green) for  $x \geq 40$  mm. An inefficient region at around  $x \approx 55$  mm can be identified which is due to 10 dead strips at the borders of the active region of mm0. For  $x \leq 20$  mm the track prediction has been

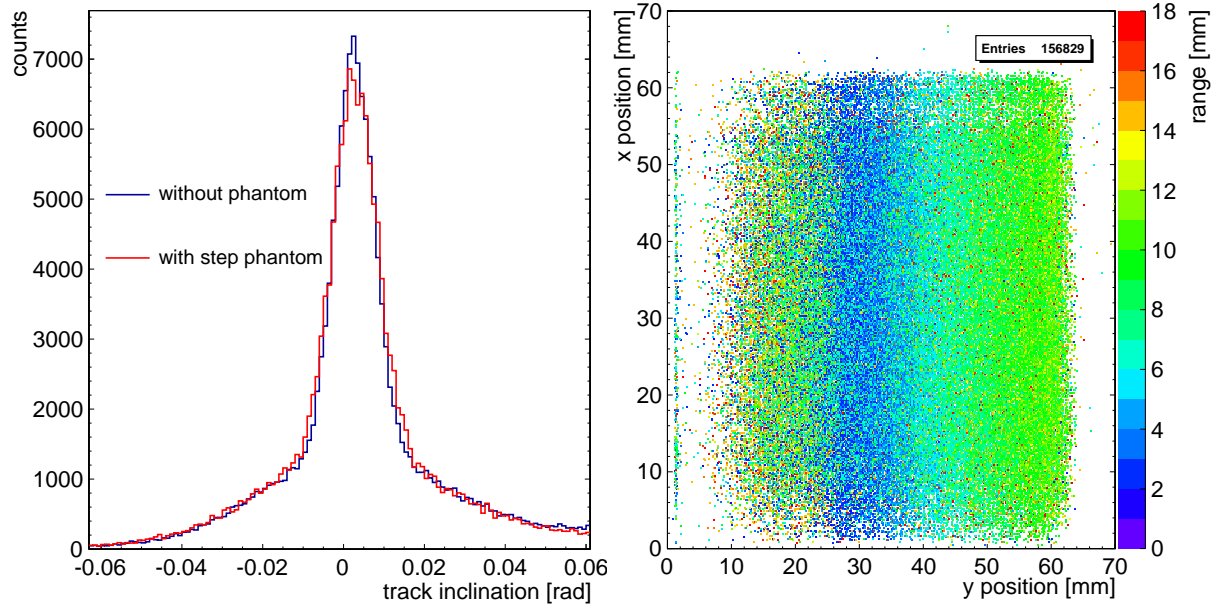


Figure 6.23: Reconstructed track inclination in the  $z$ - $x$ -plane of the carbon ions after the tracking system (left), with (red) and without (blue) the step phantom in the beam. Reconstructed range of the ions in the particle range telescope as a function of the hit position in the step phantom (right), rotated by  $90^\circ$  around the  $z$ -axis with a total of 30 mm PMMA in front of the range telescope.

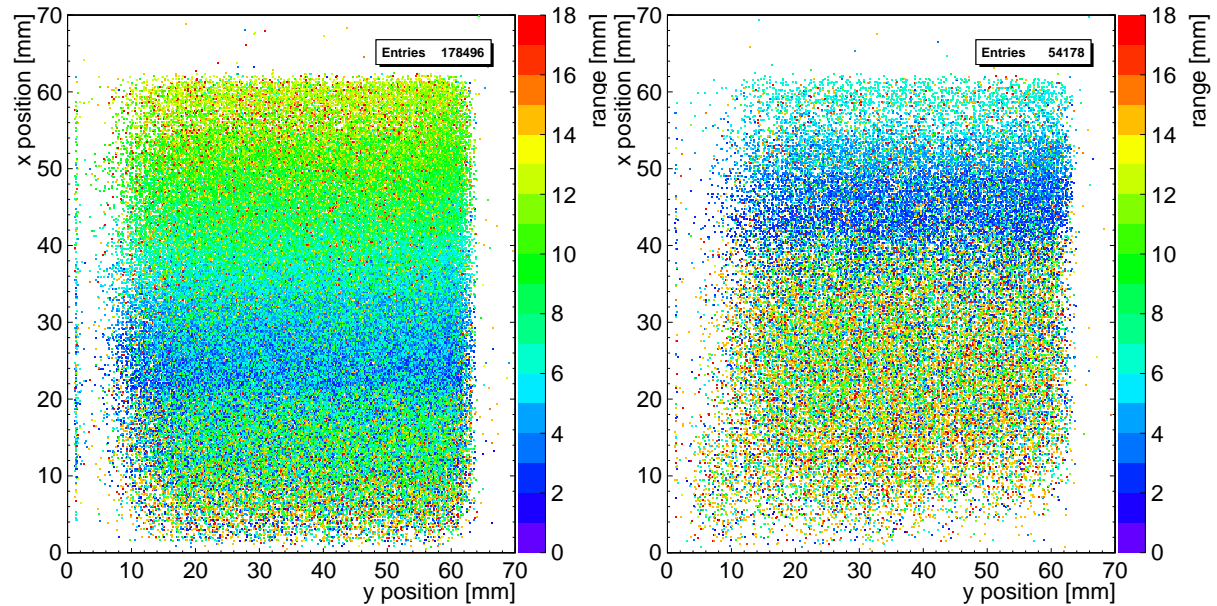


Figure 6.24: Reconstructed range of the ions in the particle range telescope (left) as a function of the extrapolated hit position in the step phantom, with a total of 30 mm PMMA in front of the range telescope. In the right figure a total of 35 mm PMMA is placed in front of the range telescope.

matched to range telescope signals from fragments, as the next step of the phantom stops the initially trigger carbon ion. The created fragments have a smaller atomic number than the carbon ion, resulting in a smaller energy loss. This leads to a larger

range in the telescope. It is even better visible in Fig. 6.23, right, where 5 mm additional PMMA is placed in front of the telescope. The increased range of the fragments is clearly visible for  $x \leq 40$  mm. Not visible in this figure is, that these events are not very frequent.

Fig. 6.25 shows the radiography of the step phantom with a total of 25 mm PMMA in front of the range telescope (left) and the projection of the range onto the measured  $x$ -position (right). The dynamic range of the range telescope is more efficiently used due to less additional PMMA. The projection when requiring a track quality with  $\chi^2/\text{ndf} < 5$  (red) has been superimposed. The 3 mm wide steps with a thickness of 1 mm can be identified in the projection of the range onto the  $x$  position. To guide the eye, a green line has been drawn, representing the average range of the projection with  $\chi^2/\text{ndf} < 5$ .

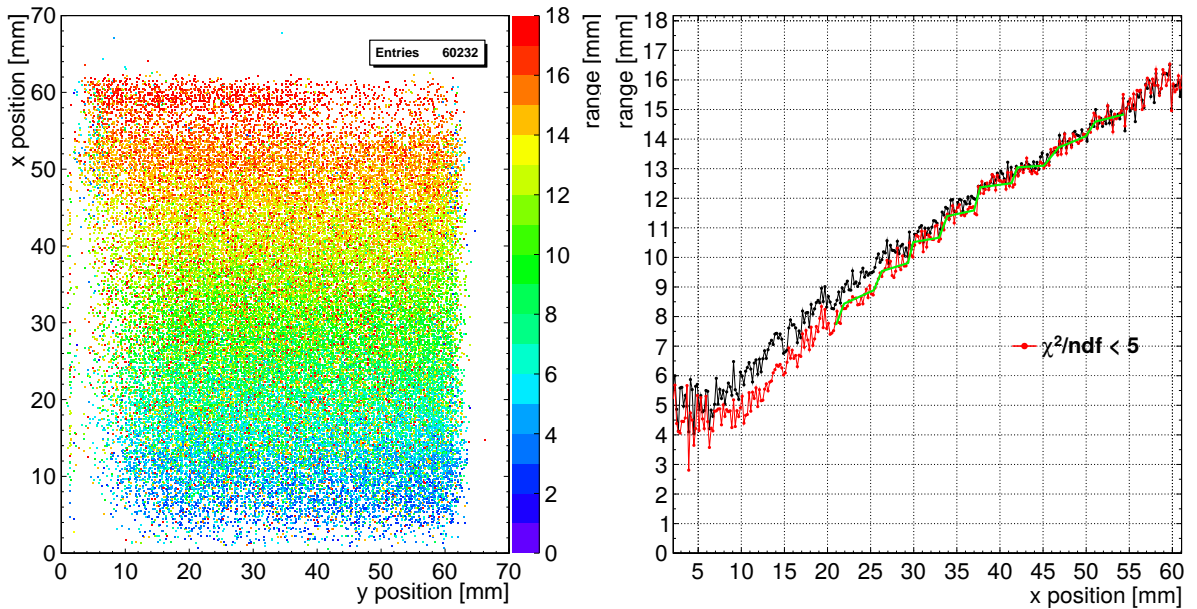


Figure 6.25: Reconstructed range of the ions in the particle range telescope as a function of the hit position in the step phantom, with a total of 25 mm additional PMMA placed in front of the range telescope (left). Projection of the range onto the measured  $x$  position in the phantom, in the region between  $1 < x < 61$  mm (right). The projection with requiring  $\chi^2/\text{ndf} < 5$  for the track quality has been superimposed (red).

## 6.5.2 Radiography: Slab Phantom

For measurements with a tissue equivalent slab phantom, carbon ions with 248.91 MeV/u beam energy at a rate of 2 MHz have been used, scanning an active area of  $5 \times 5$  cm<sup>2</sup> in steps of 5 mm. Due to the higher energy of the particles and thus a smaller energy loss in the Micromegas, the amplification voltages for all Micromegas have been increased to:  $E_{\text{amp},0} = 34.67$  kV/cm,  $E_{\text{amp},1} = 33.33$  kV/cm,  $E_{\text{amp},2} = E_{\text{amp},6} = 36$  kV/cm,  $E_{\text{amp},3} = E_{\text{amp},7} = 36$  kV/cm,  $E_{\text{amp},4} = 34.67$  kV/cm and  $E_{\text{amp},5} = 34.67$  kV/cm. Carbon ion tracks in the tracking system are searched if mm1 and mm4 simultaneously registered a signal.

The slab phantom, positioned between the second and third doublet as sketched in Fig. 6.26, consists of four tissue equivalent layers. The four different regions, with the corresponding thickness in beam direction and the density in brackets, ordered by increasing  $y$ -position, are:

- Skeletal Muscle (97.45 mm,  $\rho = 1.049 \text{ g/cm}^3$ )
- Inner Bone (top: 96.8 mm, bottom: 97.4 mm,  $\rho = 1.93 \text{ g/cm}^3$ )
- Adipose (97.8 mm,  $\rho = 0.92 \text{ g/cm}^3$ )
- Skeletal Muscle (99.9 mm,  $\rho = 1.049 \text{ g/cm}^3$ )

An average thickness of the phantom with  $d_{\text{slab}} = 0.5 \cdot X_0$  has been assumed, which is used for multiple scattering calculations in the Kalman tracker, see appendix A.2.

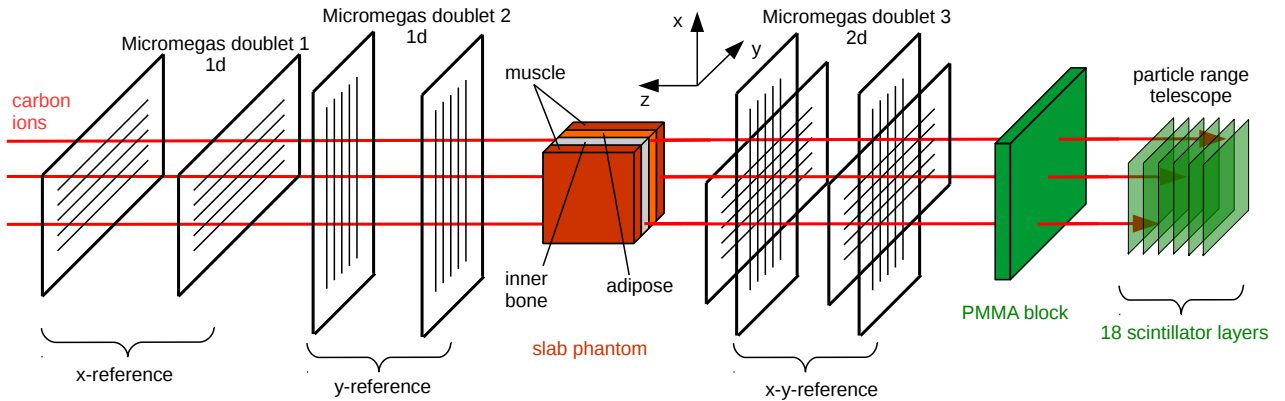


Figure 6.26: Setup for acquiring radiographies of a slab phantom. A PMMA block of suitable thickness is placed in front of the particle range telescope to adjust the carbon ions energy such that they stop within the range telescope.

For the radiography, the beam scanned the active area of  $5 \times 5 \text{ cm}^2$  four times, leading to a total number of 111572 accepted triggers for the SRS readout. From that number, 99206 events were found where mm1 and mm4 simultaneously registered a signal, resulting in a total of 81710 reconstructed single particle tracks.

Fig. 6.27 shows the reconstructed slope of the track in the  $z$ - $x$ -plane (left) and in the  $z$ - $y$ -plane (right), with (red) and without (blue) the slab phantom in the beam.

Fitting the upper part of each distribution with a Gaussian function gives an estimate of the track divergence with and without the slab phantom in the beam: For the  $z$ - $x$ -plane the corresponding widths are  $\sigma_{\text{without}} = (6.46 \pm 0.04) \text{ mrad}$  and  $\sigma_{\text{with}} = (8.99 \pm 0.05) \text{ mrad}$  and for the  $z$ - $y$ -plane  $\sigma_{\text{without}} = (6.69 \pm 0.03) \text{ mrad}$  and  $\sigma_{\text{with}} = (10.58 \pm 0.05) \text{ mrad}$ , respectively. Thus the observation is that particles get scattered more in the  $y$ -direction, as the difference of the track inclinations is bigger with  $\Delta\sigma_y = 3.89$ , than for the  $x$ -direction with  $\Delta\sigma_x = 2.53$ . An explanation may be due to the scattering in the different layers of the slab phantom, as they are oriented in  $y$ -direction. A small offset of the  $y$ -track can be identified with a mean value from the Gaussian fit of  $\bar{m}_y = -0.01215 \text{ rad}$  which is due to a slightly inclined detector setup in the  $z$ - $y$ -plane on the measurement table, with respect to the beam direction.

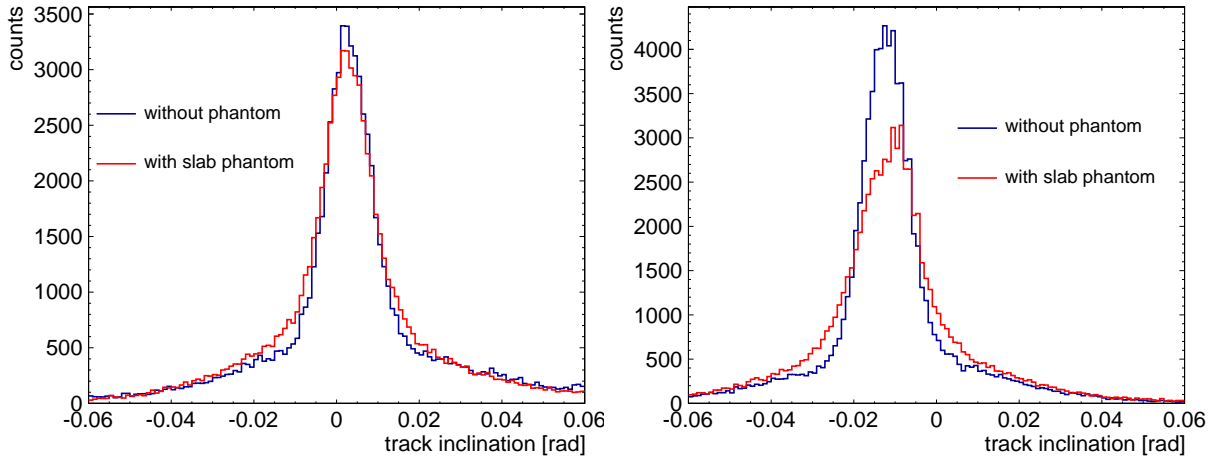


Figure 6.27: Reconstructed track inclination of 81k carbon ions in the  $z$ - $x$ -plane (left) and the  $z$ - $y$ -plane (right) after the tracking system, with (red) and without (blue) the slab phantom in the beam.

As the Kalman-based tracking algorithm extrapolates the particle track step wise to each detector (see appendix A.2 for a detailed description of the tracking algorithm), it is possible to compare particle tracklets before (with a track interpolation in the forward direction) and after (with a track interpolation in the reverse direction) the slab phantom.

Fig. 6.28, left, illustrates the principle of ion scattering within the phantom, resulting in different slopes  $m$  and  $m'$  before and after the phantom, respectively. The intersection point between both tracklets before and after the phantom is determined. In Fig. 6.28, right, the reconstructed  $z$  position of the intersection point in the  $x$ - $z$ -plane is shown. Assuming that the difference of the two tracklets is due to ion scattering in the phantom, the intersection point should then on average agree with the position of the phantom. The center of the 100 mm long slab phantom is expected to be at  $z = -235$  mm.

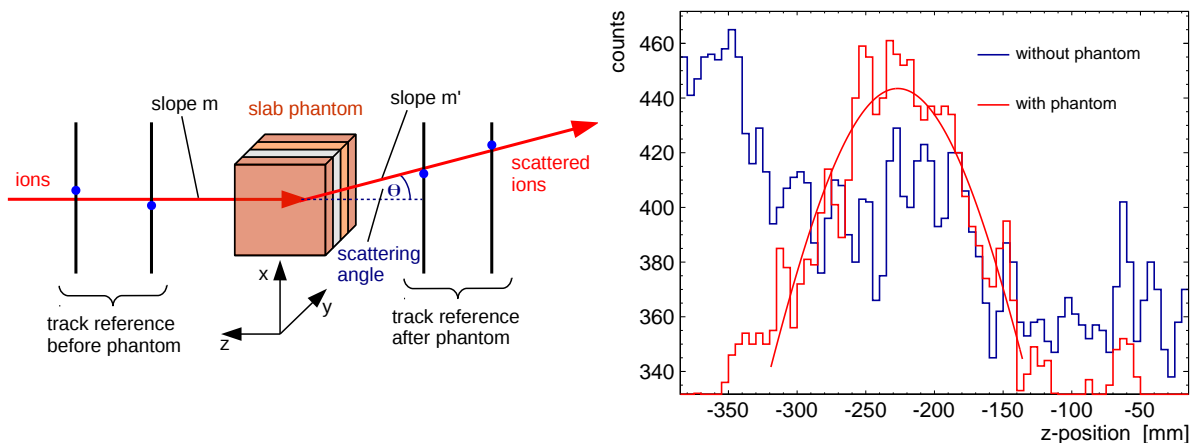


Figure 6.28: Schematic of scattering of ions in the slab phantom, resulting in different track slopes  $m$  and  $m'$  measured by the tracking system before and after the phantom. The right figure shows the reconstructed  $z$ -coordinate of the intersection point of both tracklets in the  $x$ - $z$ -plane, without (blue) and with (red) the slab phantom in the beam. A Gaussian function has been fitted to the upper part of the red distribution.

Comparing both scenarios, with and without the phantom in the beam, shows that it is possible to reconstruct the  $z$ -position of the phantom in the beam (red line Fig. 6.28, right). A Gaussian function has been fitted to the upper part of the red distribution, yielding a most probable value of  $(-227 \pm 3)$  mm, which represents an excellent estimate of the phantom position. Without the phantom in the beam, the distribution shows no real accumulation point despite the most probable value around a  $z$ -position of  $-360$  mm, which corresponds to scattering in the third doublet.

Knowing both track inclinations  $m$  and  $m'$  before and after the phantom on an event-to-event basis, the scattering angle  $\Theta$  in the phantom can be calculated via

$$\Theta = |\arctan(m) - \arctan(m')| . \quad (6.9)$$

Fig. 6.29 shows the reconstructed track inclination  $\Theta$  as a function of the extrapolated hit position in the slab phantom, checking the tracks for a sufficiently good quality e.g. a small uncertainty, before.

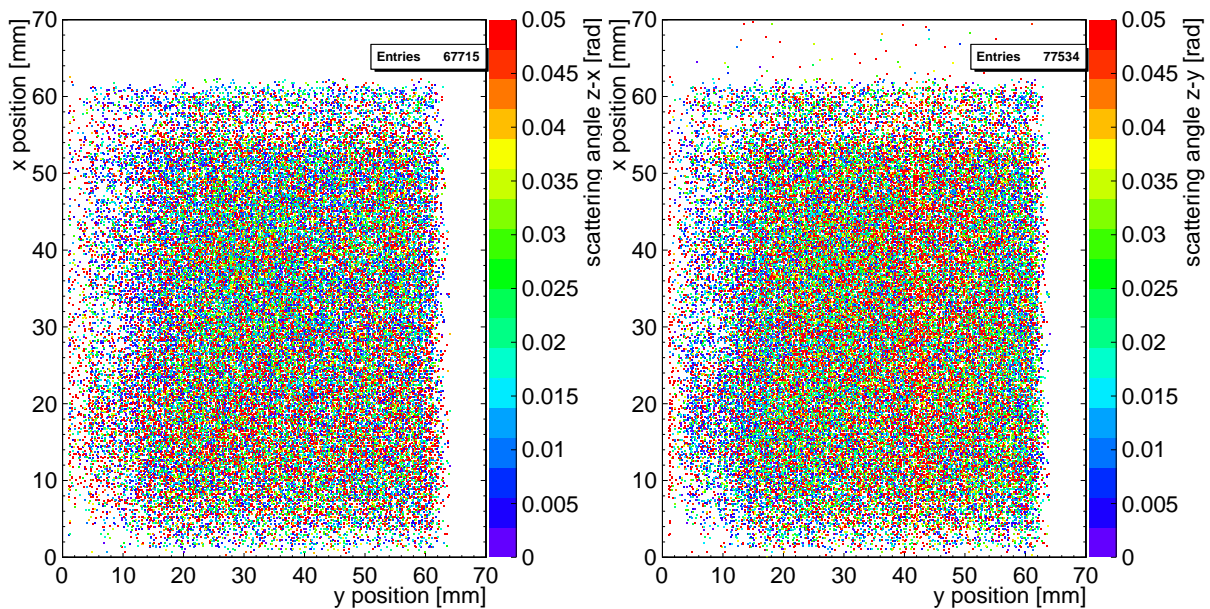


Figure 6.29: Calculated scattering angle  $\Theta$  for the  $z$ - $x$ -plane (left) and the  $z$ - $y$ -plane (right), as a function of the extrapolated hit position in the slab phantom.

No difference of the scattering angle between different tissue equivalent layers can be identified. As already observed for the track inclination in the  $z$ - $y$ -plane, the average value of the scattered angle in the  $z$ - $x$ -plane with  $\bar{\Theta}_x = (36.7 \pm 0.3)$  mrad is slightly smaller than in the  $z$ - $y$ -plane with  $\bar{\Theta}_y = (38.4 \pm 0.4)$  mrad. In the region  $y \approx 41$  mm, the  $y$ -tracking detector mm5 has a group of dead strips. Thus no straight track is expected in this region. This leads to a locally increased scattering angle in the  $z$ - $y$ -plane, as only scattered particles are able to hit the phantom at this position. The same is observed for the scattering angle in the  $z$ - $x$ -plane for the region  $x \approx 55$  mm, with around then 10 dead strips of the  $x$ -tracking detector mm0. However, this is only visible in the projection of the range on to the  $x$  position, which is not shown here. It is also observed that the scattering angle  $\Theta$  is about a factor of five bigger than the the average track inclinations in both planes  $x$ - $z$  and  $y$ - $z$ , with and without the slab phantom in the beam (Fig. 6.27). This is probably due to difference of comparing a

track fully constrained from all detectors with the two tracklets only defined by the set of detectors before and after the phantom, respectively. The track inclination of the fully constrained track tends to be smaller than the inclination of the two tracklets, where both tracks are less constrained. This effect could be reduced by placing another two-dimensional tracking detector in front of and also behind the phantom, significantly increasing the track quality due to three instead of two measurements in  $x$ - and  $y$ -direction.

Fig. 6.30, top left, shows the radiography of the slab phantom i.e. the range of the carbon ions in the particle range telescope with a total of 35 mm PMMA in front of the range telescope, as a function of the track extrapolated hit position in the phantom. The top, right figure shows the radiography while requiring a track quality of  $\chi^2/\text{ndf} < 5$ . The bottom figure shows the projection of the range onto the  $y$  position (black) and superimposed, requiring a track quality of  $\chi^2/\text{ndf} < 5$  (red). The different tissue equivalent layers are clearly visible in all figures. Due to the track quality requirement, around 50% of the found tracks are discarded, with 42k tracks remaining. An improvement of the image quality is visible, as the reconstructed average ranges for the denser materials decreases.

The four tissue equivalent layers can be identified within the following four regions:

- $(17.9 \leq y \leq 28.5)$  mm: muscle, average range: 13.4 layers [mm]
- $(28.5 \leq y \leq 38.0)$  mm: inner bone, average range: 10.6 layers [mm]
- $(38.0 \leq y \leq 48.8)$  mm: adipose, average range: 15.8 layers [mm]
- $(48.8 \leq y \leq 57.7)$  mm: muscle, average range: 12.7 layers [mm]

As one scintillator layer consists of 1 mm thick plastic (polyvinyltoluen,  $\rho = 1.03 \text{ g/cm}^3$ ), the range in units layers can also be translated into a plastic equivalent range in mm, as indicated in the brackets above. However, it should be noted that the scintillator layers were also covered light tight by a  $30 \mu\text{m}$  Aluminum foil.

The average range has been determined by a fit with a polynomial of 0th order within the given ranges for the  $y$  position. This results in an average layer thickness of  $(10 \pm 1)$  mm, which is in agreement with the 10 mm thick layers of the phantom in  $y$ -direction. As only the first muscle equivalent layer in the region  $(17.9 \leq y \leq 28.5)$  mm shows range-position dependence within the layer, this could be due to a possible inclined surface of the phantom i.e. a low quality saw cut of the piece. For regions with  $y \leq 17.9$  mm and  $y \geq 57.7$  mm, the  $5 \times 5 \text{ cm}^2$  irradiated area exceeds the slab phantom. A range difference of 0.7 mm of the two muscle equivalent layers is observed. However, a thickness difference of 2.45 mm for both muscle layers in beam direction was measured, which corresponds to a fraction of 3% more material in the beam direction. With the additional 35 mm PMMA in the beam, a range difference of approximately 2.5 mm is expected. A possible explanation is due to the inclined edge of the phantom, thus allowing not to measure the distance in beam direction accurately. Nevertheless, the biggest difference is expected and observed between adipose ( $\rho = 0.92 \text{ g/cm}^3$ ) and inner bone equivalent layer ( $\rho = 1.93 \text{ g/cm}^3$ ) with 5.2 mm. It should be noted that the range of the carbon ions in adipose is in this case equivalent to the range in air.

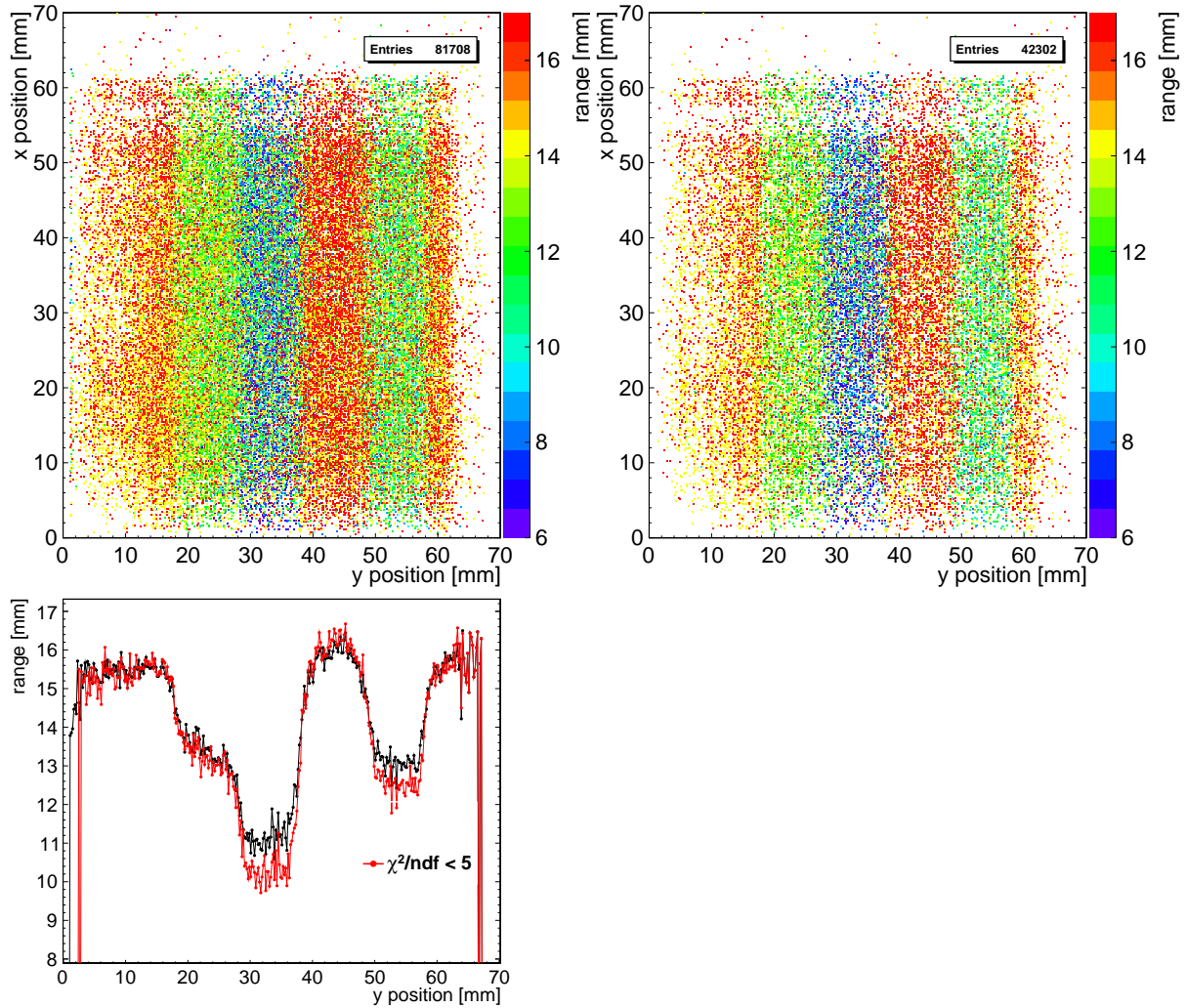


Figure 6.30: Measured range of the carbon ions in the particle range telescope as a function of the track extrapolated hit position in the slab phantom (top, left) and with requiring a track quality of  $\chi^2/\text{ndf} < 5$  (top, right). The range projected onto the y position is shown in the bottom figure (black line) with superimposed requiring a track quality of  $\chi^2/\text{ndf} < 5$  (red line). A total of 35 mm PMMA has been placed in front of the particle range telescope.

From the range projection on the y position in Fig. 6.30, bottom, the image quality can be estimated. It yields a spatial resolution  $\mathcal{O}(1 \text{ mm})$  and range resolution  $\mathcal{O}(0.2 \text{ mm})$ , with only a around 40k single particle tracks.

## 6.6 Summary

A tracking system consisting of three floating strip Micromegas doublets without applied drift voltage, a GEM detector under normal operational conditions and a scintillator layer based particle range telescope has been successfully tested in high rate carbon ion beams at the Heidelberg Ion Therapy center. A two-dimensional floating strip Micromegas has been tested for the first time and yields promising results. A readout rate of  $\mathcal{O}(1 \text{ kHz})$  has been recorded, limited by the transfer time of the non

zero-suppressed SRS data to the acquisition computer.

For a carbon beam energy of 88.83 MeV/u, all one-dimensional floating strip Micromegas showed hit efficiencies still above 93 %, with an optimum value of  $(97.5 \pm 0.1)$  %. The two-dimensional anode showed efficiencies above 87 % for the  $y$ -readout layer and above 62 % for the  $x$ -readout layer limited by a small recorded pulse height. However with applied drift field, a factor of 10 larger pulse height is expected, yielding efficiencies close 100 %.

Signal timing measurements showed the unique feature of correlations between signal timings in all layers with no applied drift voltage, allowing for a correction of the 25 ns APV time jitter within the seven detector tracking system.

An optimum spatial resolution of  $(199 \pm 39)$   $\mu\text{m}$  has been determined for a perpendicularly incident 88.83 MeV/u carbon beam. As no drift voltage was applied, the spatial resolution for inclined particle tracks showed optimum values better than 220  $\mu\text{m}$  for all investigated inclination angles up to  $35^\circ$ . For increasing beam energy, the spatial resolution suffers from decreasing particle energy loss leading to small recorded pulse height.

For measurements with the particle range telescope and the floating strip Micromegas tracking system, the GEM detector has been replaced by phantoms: Radiographies of a small PMMA step phantom with 1 mm thick and 3 mm wide steps and a slab phantom with four tissue equivalent layers have been successfully acquired with 125.11 MeV/u and 248.91 MeV/u carbon beams. The steps of the step phantom as well as the different tissue equivalent layers of the slab phantom could be reconstructed. Spatial resolution  $\mathcal{O}(1 \text{ mm})$  and range resolution  $\mathcal{O}(0.2 \text{ mm})$  for the acquired images are determined, with only around 40k single particle tracks.

To sum up, the principle of ion radiography with Micromegas as a tracking system combined with a scintillator layer based particle range telescope is working very well. For future radiographies, the efficiency of all detector layers and especially for the  $x$ -layers of the two-dimensional floating strip Micromegas, can be considerably increased by applied drift voltage. This also leads to an improvement of the spatial resolution of each detector and thus to a better image quality. Three tracking two-dimensional floating strip Micromegas in front of and behind the phantom could additionally improve the image quality. As the used detectors are low material budget, gaseous detectors with  $\mathcal{O}(0.01 \cdot X_0)$ , only small contributions from multiple scattering of the ions are expected. Furthermore, the particle range telescope can be upgraded to more scintillator layers to improve the dynamic range. The thickness of the scintillator layers is already in the same range as the particle range straggling, such that the use of thinner scintillator material is not necessary.

# Chapter 7

## Characterization of a Two-Dimensional Floating Strip Micromegas at the Tandem Accelerator

In this chapter a floating strip Micromegas with two-dimensional is investigated under irradiation with a 20 MeV proton beam at a particle rate of  $(280\pm 30)$  kHz. The measurement setup consists of the two-dimensional and a one-dimensional floating strip Micromegas doublet. The performance of the latter is not discussed in this chapter. Charge signals of the Micromegas have been recorded with the APV25 based Scalable Readout System. For pulse height studies with perpendicularly incident beam, an adapter has been developed which interconnects a number of readout strips to a single electronics channel of the APV25 front-end board. Studies of the  $\mu$ TPC reconstruction capabilities with both readout layers of the two-dimensional floating strip Micromegas doublet, tilted simultaneously with respect to two different axes, are presented.

### 7.1 Setup

The setup for a perpendicularly incident beam is shown schematically in Fig. 7.1. Each of the two back-to-back mounted Micromegas has an active area of  $6.4\times 6.4$  cm<sup>2</sup> with 128 copper anode (floating) strips of 0.5 mm pitch and 0.3 mm width per layer. The 128 readout strips, parallel to the floating strips, of 80  $\mu$ m width are separated by a 25  $\mu$ m thin insulating Kapton layer from the floating strips. The 128 readout strips, perpendicular to the floating strips, with a width of 0.4 mm are placed on the bottom of the PCB, separated by a 25  $\mu$ m thin Kapton layer from the parallel readout strips (see section 3.5 for a sketch of the anode PCB). The doublet is positioned in such a way that the perpendicular readout strips are oriented in  $y$ -direction (in the following always referred as  $y$ -layer), where as the parallel strips ran in  $x$ -direction (referred to as  $x$ -layer). For  $\mu$ TPC measurements the doublet has been tilted by  $(30.2\pm 1.0)^\circ$  around the  $y$ -axis and by  $(31.5\pm 0.1)^\circ$  around the  $x$ -axis. All charge signals are recorded with the APV25 based Scalable Readout System (SRS, [RD51, 2010]). The readout is triggered by a signal of a single  $9\times 10$  cm<sup>2</sup> scintillator, placed behind the Micromegas

system. Light signals of the scintillator are read out with a Hamamatsu R4124 photomultiplier [Hamamatsu R4124, 2007]. To correct for the 25 ns time jitter within the SRS, the trigger signal is recorded with a separate APV25 front-end board, which receives the trigger signal on a maximum of 12 channels from a 12 bit counter, called Triggerbox. Scintillator and trigger rate have been recorded with a custom 80 MHz scaler [J.Bortfeldt, 2014].

The Micromegas were constantly flushed with a Ne:CF<sub>4</sub> 80:20 vol.% gas mixture (Flexible System for Gas Mixing and Pressure Control [J. Bortfeldt, 2010]) at a flux of 1.5 ln/h. This corresponds to a slight over pressure of 2 mbar in both active areas of the gas detectors with respect to the normal atmospheric pressure and temperature in Garching. The detectors and scintillator were supplied with high voltage via a CAEN SY5527 Universal Multichannel Power Supply System [CAEN SY5527, 2015].

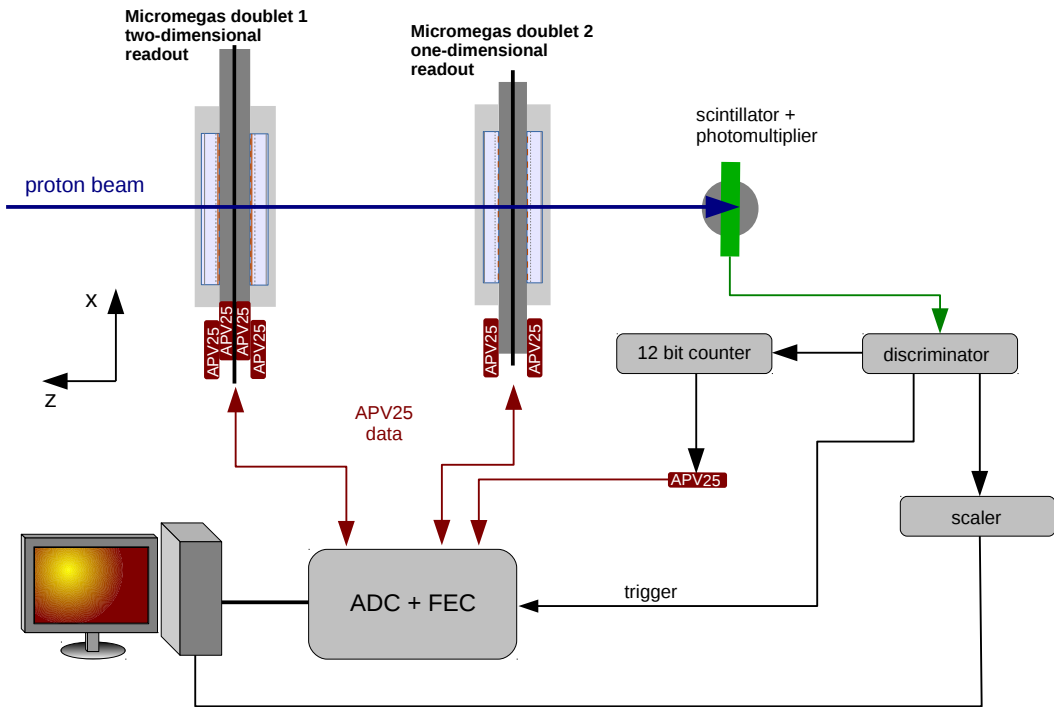


Figure 7.1: Setup for the measurements at the Tandem accelerator in Garching with 20 MeV protons at a rate of  $(280 \pm 30)$  kHz. The beam gets stopped in a single scintillator, generating the trigger signal for the SRS based readout. The performance of the two dimensional anode floating strip Micromegas doublet (doublet 1) is tested.

## 7.2 Signal Characteristics

A typical APV25 raw data event can be seen in Fig. 7.3. As the observed signal of the  $y$ -layer (right) is positive, the APV25 polarity has been inverted, using the unity gain amplifier between preamplifier and shaper. The signal on neighboring readout strips for 18 time steps of 25 ns length is shown in Fig. 7.2. The signals in both readout layers differ considerably: The recorded charge in the  $x$ -layer of the strip with maximum charge is with 1800 ADC channels already limited by the dynamic range of the

APV. The signal in the  $y$ -layer is with an amplitude of 900 ADC channels significantly smaller. Additionally the width of the cluster in the  $x$ -layer is four strips as compared to two strips for the  $y$ -layer (Fig. 7.3, bottom). The signal length in the  $x$ -layer is with a FWHM of around seven to eight time steps, corresponding to 275 ns to 200 ns significantly larger than for the  $y$ -layer with around three to four time steps, corresponding to 75 ns to 100 ns (Fig. 7.3, top). A similar signal shape in the perpendicular readout layer - with a negative charge contribution - was observed in measurements with a two-dimensional resistive strip Micromegas [Lin et al., 2014].

However, the observed signal polarity on the perpendicular strip layer is of opposite sign as for the parallel layer, which is not observed for resistive strip Micromegas. The signal on the  $y$ -strips is a superposition of signals due to couplings between floating strips with  $y$ -strips (negative polarity) and  $x$ -strips with  $y$ -strips (positive polarity). A LTSpice based simulation [LTSpice, 2014] of the three strip layers could not explain the observed opposite signs in  $x$ - and  $y$ -strips of the detector, as LTSpice considers only capacitive couplings. We assume, that the signal on the  $y$ -strips is dominantly produced as mirror charge of the localized charge on the  $x$ -strips.

Additionally, recent ANSYS based simulations [ANSYS, 2016] showed that the positive ion charge in close proximity of the floating strips leads to an observed positive recordable charge signal on the  $y$ -strips<sup>1</sup>.

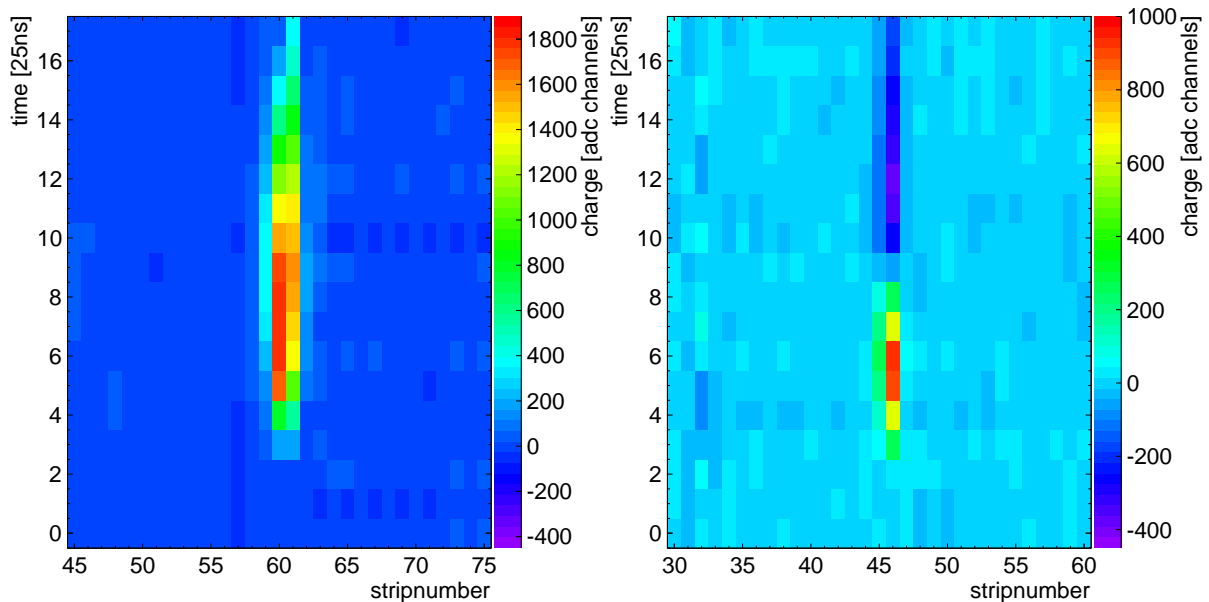


Figure 7.2: Typical event on the  $x$ -strips (left) and  $y$ -strips (right) of a perpendicularly incident 20 MeV proton, with  $E_{\text{amp}} = 35.3 \text{ keV/cm}$  and  $E_{\text{drift}} = 0.33 \text{ keV/cm}$ .

<sup>1</sup>simulated by Maximilian Hermann

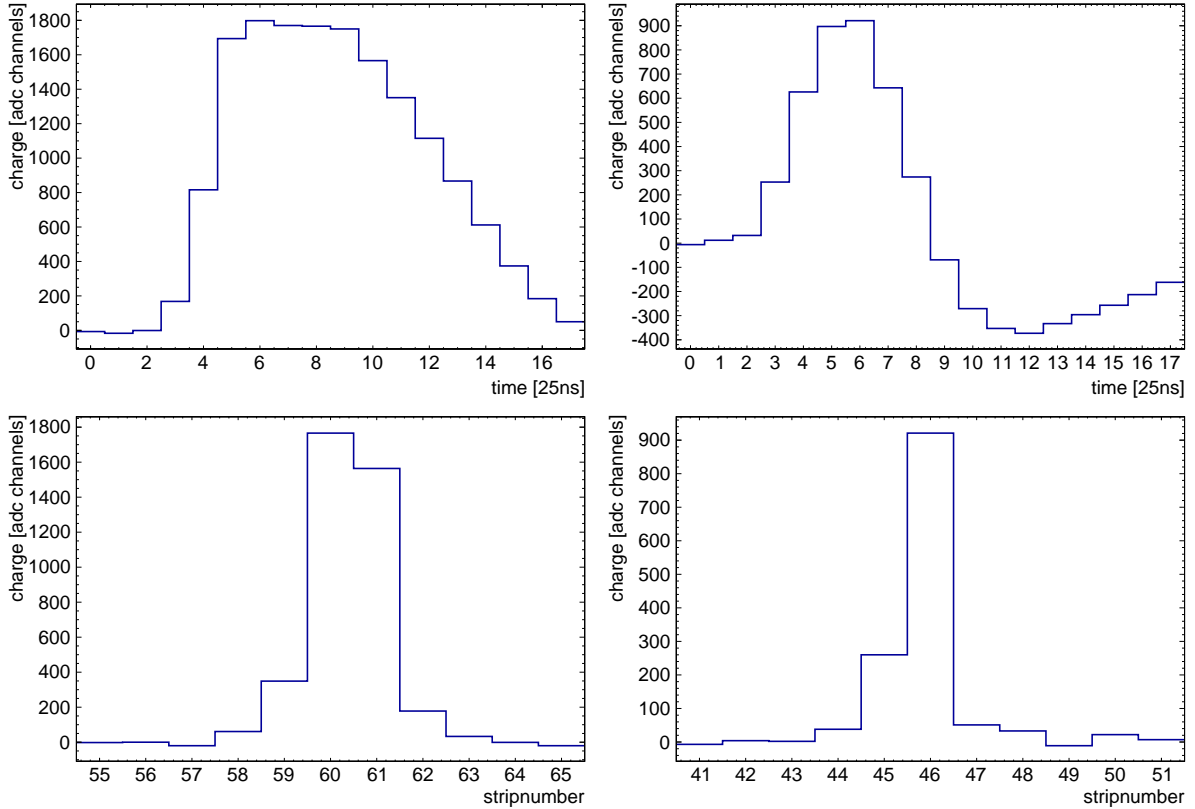


Figure 7.3: Typical event on the  $x$ -strips (left) and  $y$ -strips (right) of a perpendicularly incident 20 MeV proton, with  $E_{\text{amp}} = 35.3 \text{ keV/cm}$  and  $E_{\text{drift}} = 0.33 \text{ keV/cm}$ . The signal on the strip with maximum charge is shown in the top figures. The charge distribution over neighboring strips, at the time of the signal maximum, is shown in the bottom figures.

In the following, the pulse height of the two different readout layers is investigated. The pulse height is defined as the total charge of all strips in the cluster with maximum charge. Fig. 7.4 shows the recorded pulse height distribution of the second detector in the doublet of the  $x$ -layer (left) and  $y$ -layer (right) as a function of the amplification field  $E_{\text{amp}}$ . The significantly smaller recorded pulse height for the  $y$ -layer is clearly visible.

For a given amplification field, the most probable value of the pulse height can be extracted by a fit with a Landau function to the upper part of the distribution. This yields for the smallest amplification field of  $E_{\text{amp}} = 32 \text{ kV/cm}$  a value of  $(2394 \pm 4)$  ADC channels for the  $x$ -layer and  $(273 \pm 1)$  ADC channels for the  $y$ -layer. For the highest amplification of  $E_{\text{amp}} = 35.33 \text{ kV/cm}$  values of  $(4494 \pm 7)$  ADC channels and  $(1044 \pm 4)$  ADC channels are observed, respectively. The ratio between the two layers of the most probable pulse heights for both field configurations with  $(0.1140 \pm 0.0007)$  for  $E_{\text{amp}} = 32 \text{ kV/cm}$  and  $(0.232 \pm 0.002)$  for  $E_{\text{amp}} = 35.33 \text{ kV/cm}$  is thus not constant for increasing amplification fields. This is understandable, as the recorded single strip pulse height for the  $x$ -strips is limited by the dynamic range of the APV25, as can be seen in Fig. 7.3. However, the total pulse height in the  $y$ -layer increases with the expected exponential behavior. This leads to an increase of the ratio between the measured pulse heights in both readout layers for increasing amplification fields.

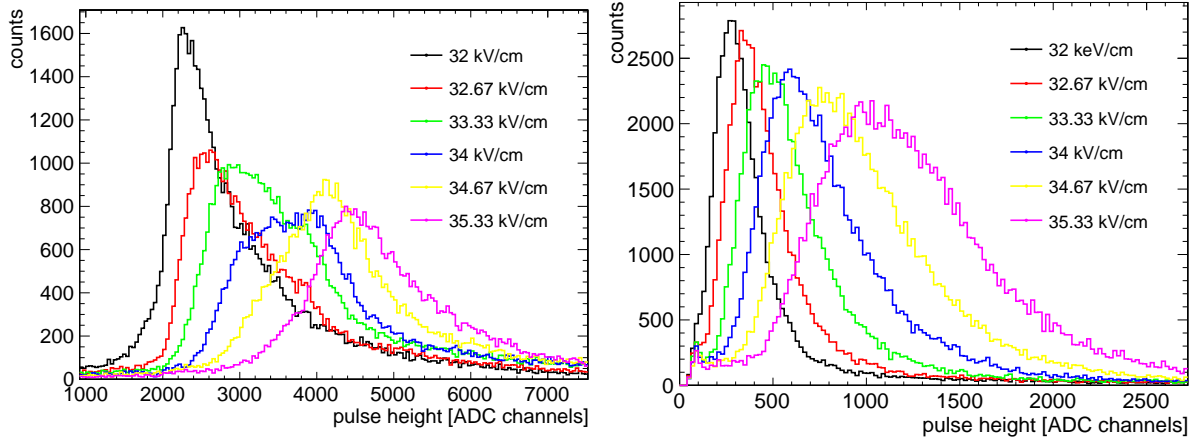


Figure 7.4: Pulse height distribution of the parallel readout layer (left) and the perpendicular readout layer (right) of the second detector as a function of the amplification field  $E_{\text{amp}}$  at  $E_{\text{drift}} = 0.333 \text{ kV/cm}$  for a perpendicularly incident 20 MeV proton beam.

To further study the pulse height behavior, a so called 'strip-merge-adapter' has been developed. It consists of a  $21 \times 44.5 \text{ mm}^2$  two-layer PCB with a 130 pin panasonic AXK5SA3277 socket and header [Panasonic, 2015] on top and bottom, respectively. The adapter can be inserted between detector and APV25 front-end board. It merges neighboring readout strips of the detector in four groups of two, one, five and three strips into a single electronics channel, see Fig. 7.5, left, for a simplified model.

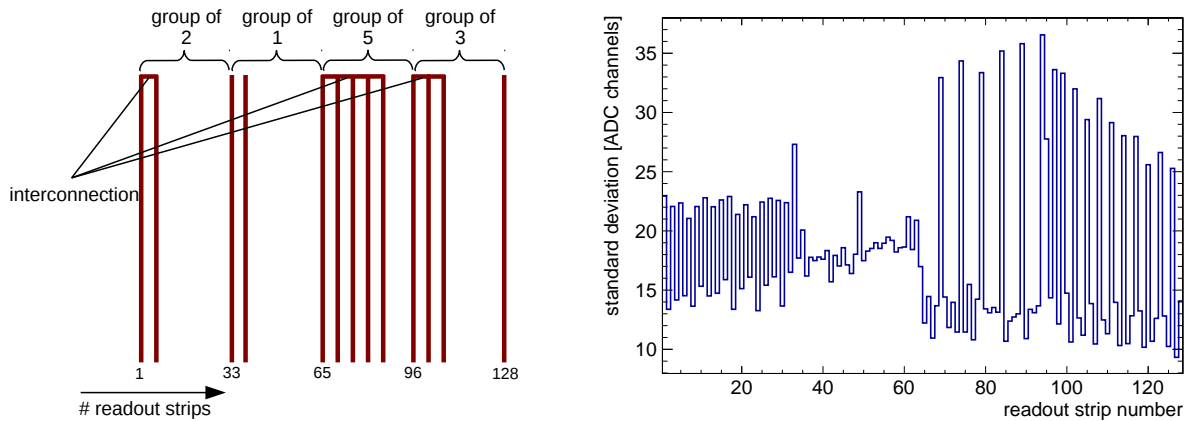


Figure 7.5: Schematic of the 'strip-merge-adapter' (left): The 128 readout strips can be interconnected into four groups of two, one, five and three consecutive strips. An interconnected group is then connected to a single electronics channel of the APV25 front-end board. The right figure shows the measured noise standard deviation for each readout channel of the perpendicular readout layer, equipped with the adapter. The different strip groups of the adapter are visible.

Accordingly channels of the APV are consequently not connected with the detector. They are explicitly not grounded, as it reduces the electronic noise for these channels considerably<sup>2</sup>. Fig. 7.5, right, shows the noise standard deviation of each readout strip of the  $y$ -layer in the second detector, equipped with the adapter. It has been measured with reduced amplification fields in the order of  $13.3 \text{ kV/cm}$  and typical drift fields of

<sup>2</sup>J. Bortfeldt, private communication

0.33 kV/cm with 500 triggered events for the SRS readout. The interconnection pattern is clearly visible. The largest noise standard deviation is observed for the group of five interconnected strips. As the interconnection of readout strips increases the capacity due to a bigger effective strip area, this behavior is expected.

For the following measurements, the strip-merge-adapter has been plugged onto the  $y$ -strips of the second detector in the doublet. The measured pulse height as function of the amplification field for different groups of interconnected strips is being investigated. As the  $y$ -strips are oriented in  $y$ -direction, the  $x$ -position of the detector has been varied so that the beam spot of 16.5 mm FWHM centrally hits each strip group. Only clusters are considered where the cluster position lies in the expected region. Fig. 7.6, left, shows the most probable pulse height of the  $y$ -layer as a function on the amplification field and number of interconnected strips.

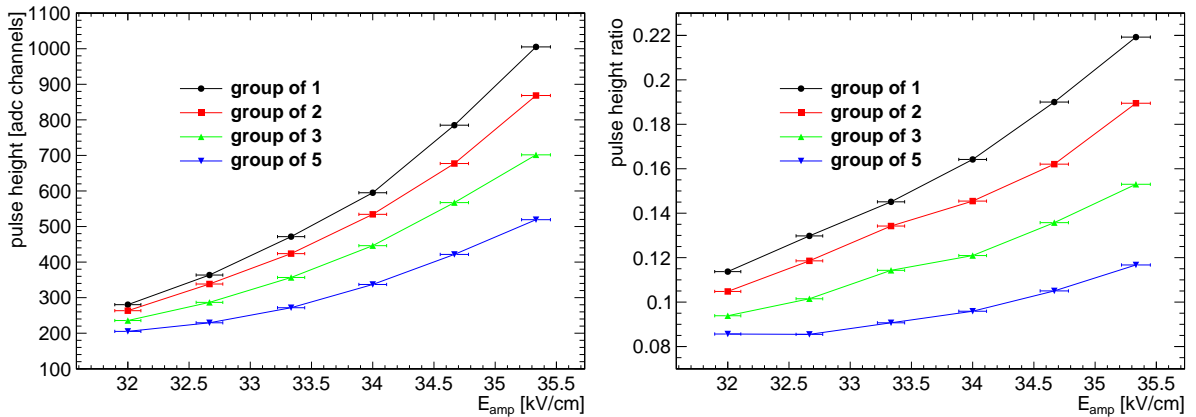


Figure 7.6: Most probable pulse height on the perpendicular readout layer, as a function of the interconnected readout strip groups and the amplification field (left). The right figure shows the measured pulse height ratio between perpendicular and parallel readout layer.

Two features can be extracted from the figure. First, the most probable pulse height rises exponentially as a function of the amplification field, as expected. Second, the pulse height decreases for increasing number of interconnected strips. This behavior has already been observed by [J. Bortfeldt, 2010]. It can be explained by the increasing readout strip capacity with increasing number of interconnected strips. The amount of charge recordable by the charge sensitive preamplifier in the APV25-front-end board depends on the capacities of detector strip and the coupling capacitor on the front-end board. As the strip capacity increases for interconnected strips, more charge is trapped within the detector. Thus less charge is detected on the preamplifier. This leads to a decrease of the measured pulse height for increasing number of interconnected strips.

Fig. 7.6, right, shows the calculated ratios between most probable pulse heights on  $y$ - and  $x$ -strips as a function on amplification field and number of interconnected strips. As previously calculated, the ratio between the pulse heights is not constant. The smallest recorded ratio is observed for the interconnection of five strips with  $(0.085 \pm 0.001)$  for  $E_{amp} \leq 32$  kV/cm. However, the variation of the ratio  $d(\text{ratio})/d(E_{amp})$  reduces for smaller amplification fields, as the  $x$ -layer comes out of saturation. To determine the

effective coupling between the two readout layers, the ratio needs to be determined at an amplification field where the  $x$ -layer is not in saturation. Unfortunately no measurements below  $E_{\text{amp}}=32\text{ kV/cm}$  have been recorded, as the cluster charge on the  $y$ -layer was with  $(273\pm 1)$  ADC channels already very small. It is thus assumed that the effective coupling onto the  $y$ -strips is equally or smaller than 11.4% of the charge recorded on the  $x$ -strips. It corresponds to the ratio that is observed for the smallest amplification field at  $E_{\text{amp}}=32\text{ kV/cm}$  with no interconnection of readout strips.

Measurements with the strip-merge-adapter plugged onto the  $x$ -layer, scanned through all four groups, showed no dependence on the recorded pulse height in the  $y$ -layer. Only small deviations due to the scan along the  $y$ -strips are observed.

As the temporal behavior of the signal in  $x$ - and  $y$ -layer differs considerably, the strip pulse width of both layers has been investigated. The doublet has therefore been tilted by  $(30.2\pm 1.0)^\circ$  around the  $x$ -axis and  $(31.5\pm 0.6)^\circ$  around the  $y$ -axis. Fig. 7.7 shows the pulse width of all strips in the cluster with highest charge of the  $x$ -layer in the second detector of the doublet.

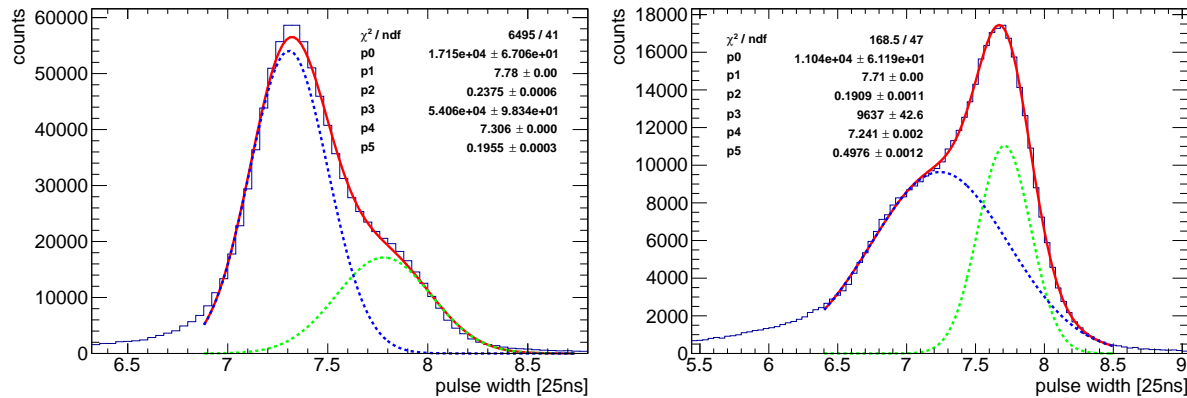


Figure 7.7: FWHM of a skew Gaussian fit (i.e. the temporal pulse duration) to each strip pulse in the cluster with highest charge of the  $x$ -layer at  $E_{\text{amp}}=33.33\text{ kV/cm}$  (left) and at  $E_{\text{amp}}=36.67\text{ kV/cm}$  (right). Each distribution has been fitted with a double Gaussian function. The increasing saturation of the strip pulse with increasing amplification field is visible (green dashed line).

It is fitted with a double Gaussian function, representing two different processes: The green dashed line represents signals in saturation with a larger duration. The blue dashed line represents non saturated strip pulses. The increasing saturation of the strips for the two different amplification fields of  $E_{\text{amp}}=33.33\text{ kV/cm}$  (left) and  $E_{\text{amp}}=33.67\text{ kV/cm}$  (right) is clearly visible.

For the determination of the strip pulse width in the  $y$ -layer a fit with a single Gaussian function is sufficient, as the signals are significantly smaller and thus no contribution from saturation is observed. The most probable pulse width of the  $y$ -layer as a function of the amplification field is shown in Fig. 7.8. The (non saturated i.e. blue dashed line in Fig. 7.7) pulse width of the  $x$ -layer has been superimposed (red). A small decrease in the order of  $0.1 \times 25\text{ ns}$  of the pulse width for increasing amplification field is observed for both layers. Nevertheless, the large difference between both layers is clearly visible:

The  $x$ -layer pulse width is with on average  $7.34 \times 25$  ns by a factor of 2.63 larger than the pulse width of the  $y$ -layer with on average  $2.79 \times 25$  ns.

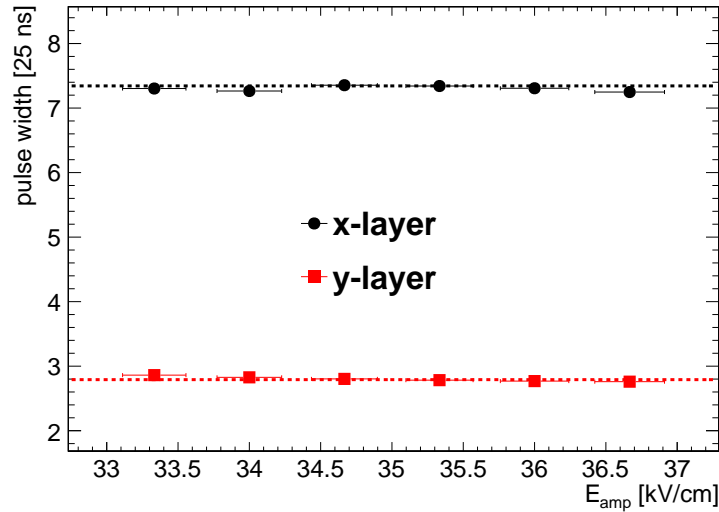


Figure 7.8: Most probable, non saturated strip pulse width of the  $x$ -layer (black) and the  $y$ -layer (red) of the second detector as a function on the amplification field.

As the principle of signal formation in the  $y$ -layer is not yet fully understood, the reason why the temporal shape differs in both layers is still under investigation. As the fall-off of the strip pulse is not an effect in the signal formation, but a feature of the pulse shaping network in the APV25, the obvious explanation is the smaller capacity of the  $y$ -strips with respect to the  $x$ -strips. As the APV25 internal pulse shaping depends on the detector (strip) capacity, a smaller value leads to a steeper fall-off of the strip pulse in the  $y$ -layer. An alternative explanation would be a bipolar signal on the perpendicular strips, which would actively pull the APV shaper signal to negative values.

### 7.3 3D Track Reconstruction in a Single Layer

To investigate the  $\mu$ TPC reconstruction (c.f. section 4.2) for both layers of the two-dimensional floating strip anode, the doublet has been tilted by  $(30.2 \pm 1.0)^\circ$  around the  $x$ -axis and  $(31.5 \pm 0.6)^\circ$  around the  $y$ -axis. The latter has been determined by the shift of the beam spot in the two parallel readout layers (c.f. section 5.5), as the actual rotation was not precisely determined during the measurements. Due to the different signal shapes in both readout layers, better signal timing results were obtained by fitting the strip pulses of the perpendicular layer with a skew Gaussian- instead of a Fermi-function to the rising edge of the pulse, see Fig. 7.9. The timing of the maximum is used for the  $\mu$ TPC reconstruction in the  $y$ -layer. For the  $x$ -layer, the timing is still determined by a fit with an inverse Fermi function. The fit weights for the (strip,time)-data points in the  $\mu$ TPC line fit are assigned as described in section 4.2. The determined skew Gaussian rise time of the  $y$ -layer strip pulse has additionally been checked for a reasonable value, assuring that the fit converged. All timings used for the  $\mu$ TPC reconstruction are explicitly corrected for the 25 ns time jitter of the SRS system. The

jitter is determined on an event-to-event basis from the average signal timings recorded by the external APV25 front-end board connected to the Triggerbox.

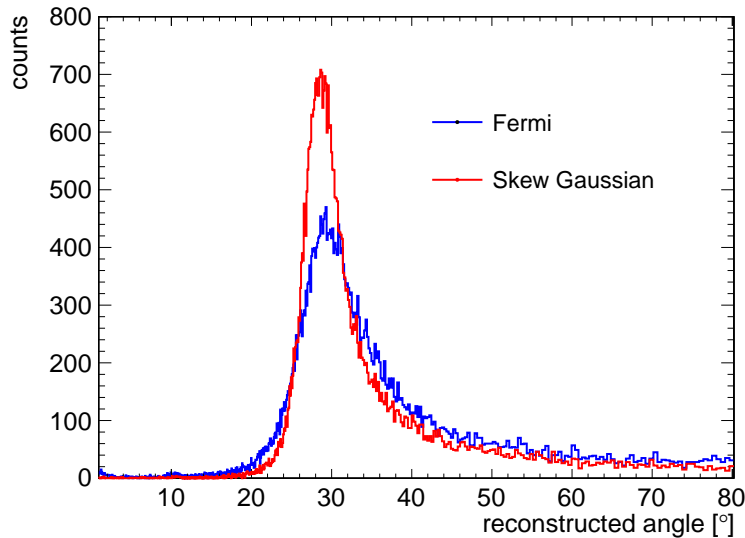


Figure 7.9: Reconstructed track angle using the  $\mu$ TPC method for the  $y$ -layer in the first detector, based on a signal fit with a Fermi-function to the rising edge of the strip pulse (blue) and a skew Gaussian-function to the entire strip pulse (red) at  $E_{\text{amp}}=37.67$  kV/cm and  $E_{\text{drift}}=0.333$  kV/cm, respectively. The detector has been tilted by  $(30.2\pm 1.0)^\circ$  with respect to the beam. The improvement of the resolution with the skew Gaussian fit is obvious.

The reconstructed most probable angle and the angular resolution of the first and the second detector is shown in Figs. 7.10 and 7.11 for the  $x$ - and the  $y$ -layer as a function of the amplification and drift field. The errors of the true inclination angle are indicated as red horizontal bars. Several trends are visible and need further explanation. First of all, the  $\mu$ TPC angle reconstruction works for both layers of the two-dimensional floating strip Micromegas despite of the small coupling of the signal onto the  $y$ -layer, which was observed for the perpendicularly incident beam in the measurements discussed in the previous section.

Second, the reconstruction works slightly better for both layers of the second detector in the doublet. This can be explained by the difference of the recorded pulse height i.e. the gas gain in both detectors: For the highest amplification field of  $E_{\text{amp}}=37.67$  kV/cm in the first detector, a most probable pulse height of  $(11683\pm 15)$  ADC channels with on average  $(9.8\pm 1.6)$  strips hit is observed in the  $x$ -layer. In the second detector with a maximum amplification field of  $E_{\text{amp}}=36.67$  kV/cm, a considerably larger pulse height of  $(15035\pm 11)$  ADC channels and  $(10.6\pm 1.6)$  hit strips is observed. This is probably due to a slight difference of the amplification gap. Of course the higher energy loss per unit path length  $dE/dx$  increases the recorded pulse height in the second detector. Nevertheless, comparable simulations for 23 MeV protons traversing the third and fourth Micromegas of the four detector system described in chapter 5 showed, that this only leads to a pulse height variation on the order of 10 %.

With the significantly smaller recorded pulse height in the first detector, the different behaviors of the two detectors for the field variations is understandable. It is also visible for the  $y$ -layer of the first detector in Fig. 7.10, top left. The scan of the amplification field reveals the strong dependence of the angular resolution on the pulse

height: For the smallest field configuration an unreasonably high angular resolution of  $\left(\begin{smallmatrix} +25 \\ -10 \end{smallmatrix}\right)^\circ$  is observed, since the angle reconstruction is barely working. However, for the highest amplification field of  $E_{\text{amp}}=37.67 \text{ kV/cm}$ , an optimum resolution of  $\left(\begin{smallmatrix} +3 \\ -2 \end{smallmatrix}\right)^\circ$  can be reached.

The increasing reconstructed most probable angle for smaller amplification fields in the  $y$ -layer of the first detector is due to a failed fit to the upper part of the angle distribution and not a physical reason.

For all other detector layers the dependence of the most probable reconstructed angle on the amplification field shows similar behavior: For increasing amplification field, the reconstructed angle increases slightly by about  $2^\circ$ . As the reconstructed angle should in principle be independent of the recorded strip pulse height, this is primarily due to capacitive coupling onto neighboring strips of the cluster. The pulse height on the strips registering only small signals increases due to capacitively coupled signals leading to larger reconstructed angles, see Fig 4.3.

Note that the corner strips of the cluster are explicitly checked for a charge larger than 25 % of the respective neighboring strip. If this is not the case, they are excluded from the reconstruction, as this is then typically a charge signal only originating from capacitive coupling. This is already included in the figures shown and led to a reduction of the reconstructed angle of about  $1^\circ$  for the  $x$ -layer of the first detector and about  $2^\circ$  for the  $x$ -layer of the second detector. It is due to saturation of nearly every strip in the cluster of the  $x$ -layer thus also considerably coupling to neighboring strips of the cluster. No reduction of the reconstructed angle was observed by applying the 25 % requirement for both  $y$ -layers of the doublet, as the signals are very small and thus also the capacitively coupled charge to the corner strips.

The angular resolution of all detectors improves as expected for increasing amplification field, as the signal to noise ratio increases. For the highest amplification field, all detectors converge to a similar optimum angular resolution of  $\left(\begin{smallmatrix} +3 \\ -2 \end{smallmatrix}\right)^\circ$  at a drift field of  $E_{\text{drift}}=0.333 \text{ kV/cm}$ .

The smaller gain in the first detector leads to a visible worsening of the angular resolution of the  $y$ -layer for increasing drift field. For the  $x$ -layers of both detectors and the  $y$ -layer of the second detector, the recorded pulse height is sufficiently high to allow precise angle reconstruction with a resolution smaller than  $\left(\begin{smallmatrix} +4 \\ -3 \end{smallmatrix}\right)^\circ$  up to drift fields of  $1.33 \text{ kV/cm}$ . This corresponds to maximum electron drift velocities up to  $0.109 \text{ mm/ns}$ , which is about a factor of three higher than compared to typical Argon based gas mixtures at similar drift fields.

Typically the reconstructed angle via the  $\mu\text{TPC}$  method is expected to be larger than the true track inclination due to capacitive coupling of neighboring strips. This is only observed for the  $x$ -layer of the second detector. Note however, that in this layer the capacitive coupling on the corner strips is also contributing most, leading to a bigger reconstructed angle. All other layers reconstruct a slightly smaller angle than expected. A possible explanation are small deviations from the expected drift velocity, due to a slightly different detector gas mixture. The deviation from the true drift velocity from the one, calculated with MAGBOLTZ [Biagi, 2012] and used in the  $\mu\text{TPC}$

reconstruction is also visible in the drift scan. The decrease of the reconstructed angle for  $E_{\text{drift}} < 0.2 \text{ kV/cm}$  is as well due to a not optimally simulated drift velocity for small drift fields.

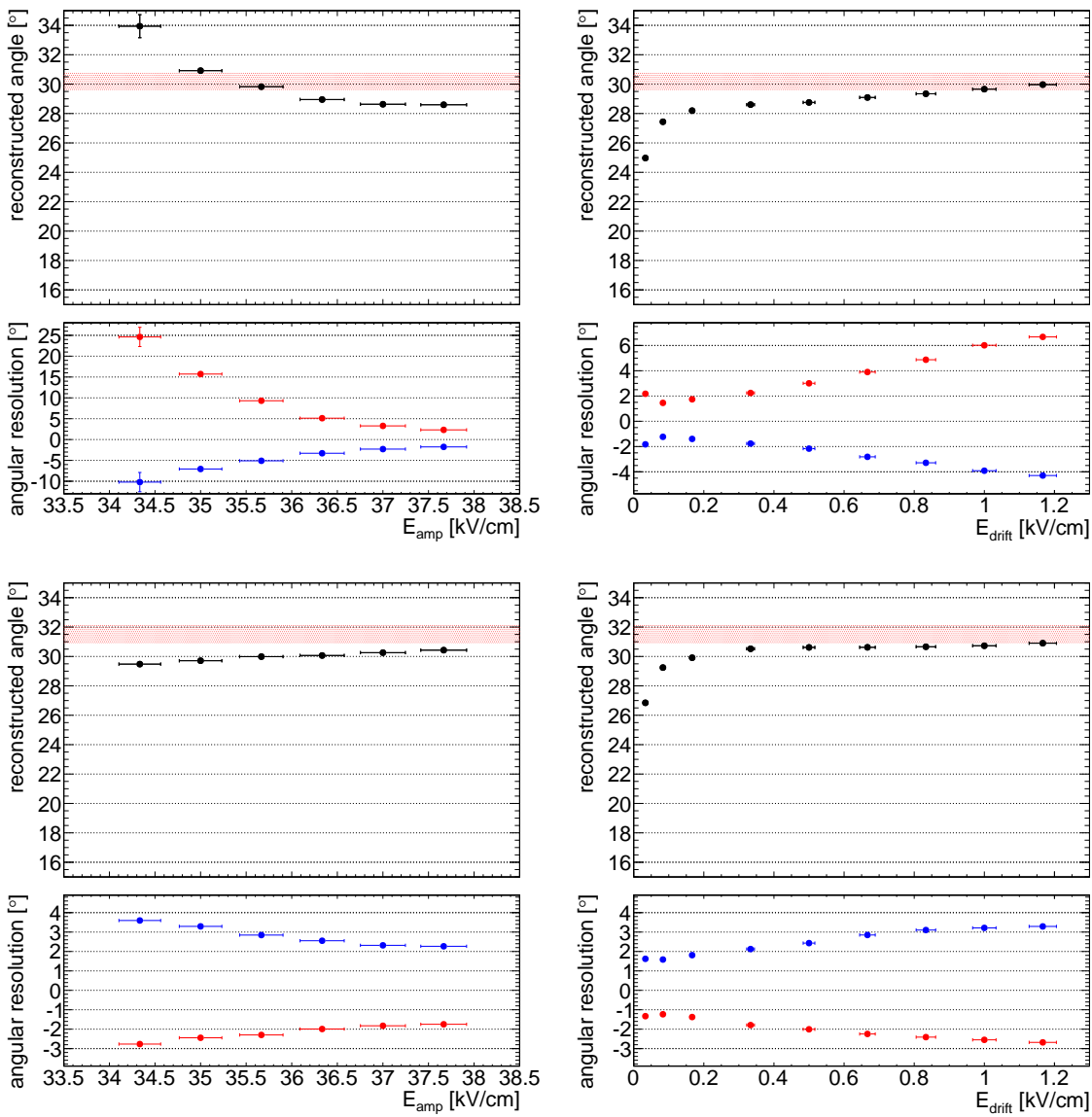


Figure 7.10: Reconstructed angle and angular resolution of the perpendicular  $y$ -layer (top) and the parallel  $x$ -layer (bottom) in the first detector, as a function of the amplification field  $E_{\text{amp}}$  at  $E_{\text{drift}}=0.333 \text{ kV/cm}$  (left) and as a function of the drift field  $E_{\text{drift}}$  at  $E_{\text{amp}}=37.67 \text{ kV/cm}$  (right).

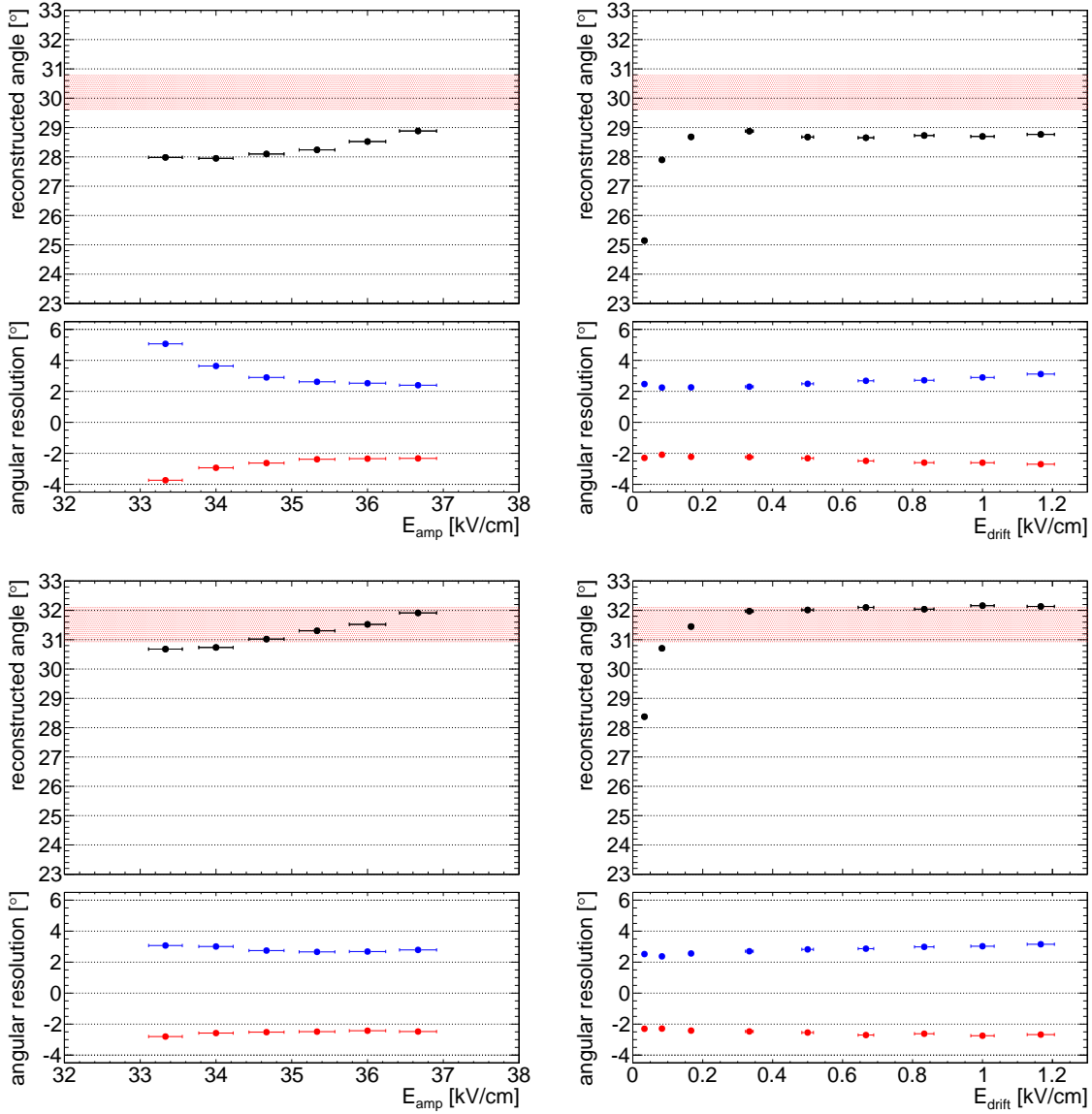


Figure 7.11: Reconstructed angle and angular resolution of the perpendicular  $y$ -layer (top) and the parallel  $x$ -layer (bottom) in the second detector, as a function of the amplification field  $E_{\text{amp}}$  at  $E_{\text{drift}} = 0.333$  kV/cm (left) and as a function of the drift field  $E_{\text{drift}}$  at  $E_{\text{amp}} = 36.67$  kV/cm (right).

Finally, Fig. 7.12 shows the correlation of the reconstructed angle in the  $y$ -layer and the  $x$ -layer for a measurement with 44k events at  $E_{\text{drift}} = 0.333$  kV/cm and  $E_{\text{amp}} = 36.67$  kV/cm. It shows the capability of the 3d-track reconstruction within a single layer of the doublet. Hence, it motivates the further study of two-dimensional floating strip Micromegas detectors, as the principle of signal generation works for both dimensions. This allows for constructing thin gaseous detectors with a small effective thickness  $\mathcal{O}(0.01X_0)$ . It reduces the unwanted multiple scattering in the detector material and lowers the detector budget at the same time.

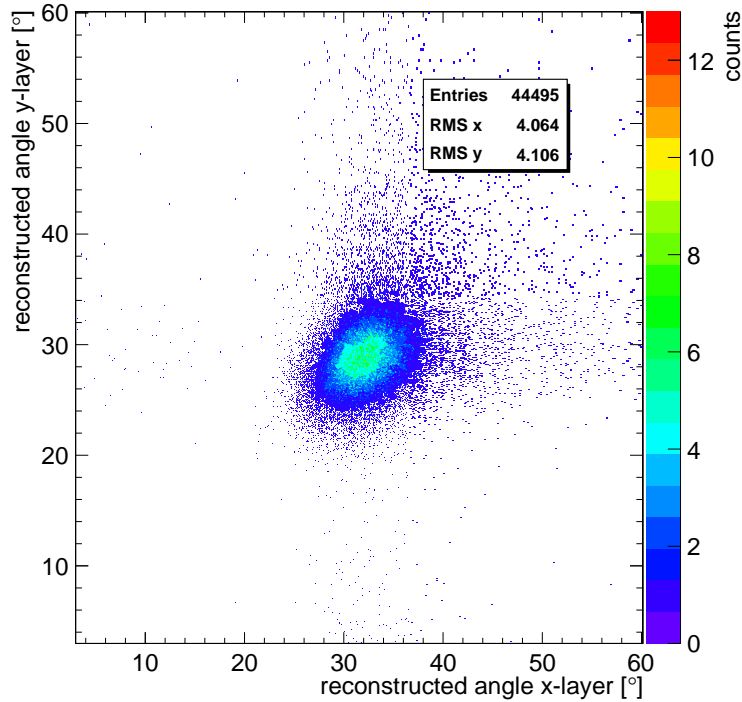


Figure 7.12: Reconstructed track angle in the  $y$ -layer and in the  $x$ -layer for  $E_{\text{drift}}=0.333$  kV/cm and  $E_{\text{amp}}=36.67$  kV/cm in the second detector. The expected inclination for the  $x$ -layer is  $(30.2\pm 1.0)^\circ$  and for the  $y$ -layer  $(31.5\pm 0.6)^\circ$ .

## 7.4 Conclusions

A floating strip Micromegas with a two-dimensional readout anode has been successfully tested in a 20 MeV proton beam. A Ne:CF<sub>4</sub> 80:20 vol.% gas mixture has been used, significantly increasing the electron drift velocity and the ion mobility. Signals are decoupled from the anode strips onto parallelly oriented  $x$ -readout strips within the PCB with a width of 80  $\mu\text{m}$  and onto perpendicularly oriented  $y$ -readout strips on the bottom of the PCB with a width of 400  $\mu\text{m}$ . Signals obtained on both readout strip layers have opposite polarity. Negative for the parallel layer and positive for the perpendicular layer.

For a perpendicularly incident beam, the pulse height of the  $y$ -layer is estimated to be smaller than 11.4% of the  $x$ -layer pulse height. Nevertheless, for amplification fields above 33.33 kV/cm, the gas gain is sufficiently high to obtain good signals on both layers of the PCB.

Measurements with inclined detector setup confirmed that  $\mu\text{TPC}$  reconstruction works for both readout-layers independently. For inclination angles  $(30.2\pm 1.0)^\circ$  and  $(31.5\pm 0.6)^\circ$ , optimum angular resolutions for the  $x$ -layer with  $(^{+1.6}_{-1.2})^\circ$  and for the  $y$ -layer  $(^{+1.5}_{-1.2})^\circ$  are determined, respectively. An optimum angular resolution smaller than  $(^{+4}_{-3})^\circ$  is obtained with all drift fields up to 1.33 kV/cm, corresponding to electron drift velocities up to 0.109 mm/ns.

---

The signal formation on the bottom, perpendicular layer with a significantly smaller pulse height is not yet fully understood. It is plausible that the signal on the  $y$ -strips is a superposition of signals due to couplings between floating strips with  $y$ -strips (negative polarity) and  $x$ -strips with  $y$ -strips (positive polarity). LTSpice simulations could not explain for the opposite signs in both layers only via capacitive coupling. Thus the signal on the  $y$ -strips is dominantly produced as mirror charge of the localized charge on the  $x$ -strips. Recent ANSYS-based simulations confirmed that the positive charge of the ion-cloud in the amplification region leads to positive signals on the  $y$ -strips.

# Chapter 8

## Summary and Outlook

In this thesis, novel discharge tolerant floating strip Micromegas detectors are studied in detail in proton and carbon beams. Micromegas detectors are planar gaseous detectors, with individual ionization and amplification region, separated by a thin metallic micro-mesh. The micro-mesh is held at a constant distance of  $150\ \mu\text{m}$  above the anode. Ionization charge is collected in the typically  $6\ \text{mm}$  wide drift region between cathode and mesh. The signal electrons are amplified in Townsend avalanches in the amplification region between mesh and segmented anode. In the case of floating strip Micromegas, the anode consists of copper strips, individually connected to high voltage via high ohmic resistors. Signals are decoupled via pF capacitors to charge sensitive pre-amplifiers. This combination enables a powerful protection against discharges between micro-mesh and anode, allowing highly efficient single particle tracking at highest rates with only low material budget detectors. A Ne:CF<sub>4</sub> based gas mixture has been used as detector gas for all measurements to further increase the already excellent high-rate capabilities of this detector. This increases the electron drift velocity as well as the ion mobility in the amplification region by a factor of three compared to typical Ar:CO<sub>2</sub> based detector gases.

Four one-dimensional floating strip Micromegas, operated with the new gas mixture are tested with  $23\ \text{MeV}$  protons at the tandem accelerator in Garching. Hit efficiencies above  $98\ \%$  are observed for optimized field configurations. A TPC-like track angle reconstruction allows to measure the particle track inclination in a single detector using the time of arrival information of ionization electrons on the strips. Optimum angular resolutions of  $(^{+3}_{-2}^{\circ})$  are observed.  $\mu\text{TPC}$  based alternative hit positions improve the spatial resolution for particle tracks above  $10^{\circ}$  inclination at drift fields below  $500\ \text{V/cm}$ . For a chosen working point at  $E_{\text{drift}}=0.18\ \text{kV/cm}$  and  $35^{\circ}$ , the  $\mu\text{TPC}$  spatial resolution yields approximately  $16\ \%$  better results than the charge weighted mean method and showed only a weak dependence on the inclination angle. MAGBOLTZ simulations show that the detector gas is contaminated by  $\mathcal{O}(0.1\ \text{vol.}\%)$  water during the measurements, leading to variations in the electron drift velocity and thus also in the most probable reconstructed angle. For perpendicularly incident particles, an optimum spatial resolution of  $(346\pm 90)\ \mu\text{m}$  is determined. TRIM based SRIM simulations confirm that the determined spatial resolution is dominated by multiple scattering of the low energy protons in the high  $Z$  materials of the readout structures.

Measurements are carried out at the Heidelberg Ion Therapy center in carbon beams with energy between 88 MeV/u and 430 MeV/u at a particle rate of 2 MHz. A two-dimensional floating strip Micromegas is successfully tested for the first time. The Micromegas detectors have been operated without applied drift voltage. An optimum hit efficiency of  $(97.5 \pm 0.1)\%$  is determined. A single layer time resolution of  $(8.53 \pm 0.07)$  ns is observed. As no drift voltage is applied, optimum values for the spatial resolution better than 220  $\mu\text{m}$  are determined for all investigated inclination angles up to  $35^\circ$ . Radiographies of a PMMA step phantom and a slab phantom with four tissue equivalent layers have been successfully acquired with a floating strip Micromegas tracking system and a scintillator layer based particle range telescope. The linear range behavior of the ions in the range telescope as a function of linearly increasing phantom thickness is observed as expected. The acquired images with only around 40k single particle tracks show a spatial resolution  $\mathcal{O}(\text{mm})$  and a range resolution  $\mathcal{O}(0.2 \text{ mm})$ . It is shown, that floating strip Micromegas as a tracking system are suitable for future medical imaging applications, with low material budget detectors and a small effective thickness  $\mathcal{O}(0.01X_0)$ .

Floating strip Micromegas with two-dimensional strip readout structure are successfully tested at the tandem accelerator with 20 MeV protons. The  $x$ -readout strips, parallel to the floating strips, of 80  $\mu\text{m}$  width are separated by a 25  $\mu\text{m}$  thin insulating Kapton layer from the floating strips. The  $y$ -readout strips, perpendicular to the floating strips, have a width of 0.4 mm and are placed on the bottom of the PCB, separated by a 25  $\mu\text{m}$  thin Kapton layer from the  $x$ -layer. The pulse height of the perpendicular readout strip layer is estimated to be smaller than 11.4% of the parallel readout strip layer. Measurements with inclined detector with respect to the beam allow for independent angle reconstruction with optimum resolution in the parallel  $x$ -layer of  $\left(\begin{smallmatrix} +1.6^\circ \\ -1.2^\circ \end{smallmatrix}\right)$  and in the  $y$ -layer of  $\left(\begin{smallmatrix} +1.5^\circ \\ -1.2^\circ \end{smallmatrix}\right)$ . The angular resolution is better than  $\left(\begin{smallmatrix} +4^\circ \\ -3^\circ \end{smallmatrix}\right)$  for both readout layers for drift fields up to 1.33 kV/cm with corresponding electron drift velocities up to 0.109 mm/ns.

It was shown that two-dimensional floating strip Micromegas can be realized. The observed signal on both readout layers is of opposite polarity. It is plausible that the opposite signal polarity of both readout layers is due to a superposition of signals coupling from floating strips to  $y$ -strips (negative polarity) and from  $x$ -strips to  $y$ -strips (positive polarity). To increase the signal amplitude on the bottom layer of the readout PCB, new designs with optimized strip width are currently under development.

# Bibliography

- [Alexopoulos et al.(2014)] T. Alexopoulos, G. Iakovidis, S. Leontsinis, K. Ntekas, and V. Polychronakos. Examining the geometric mean method for the extraction of spatial resolution. *Journal of Instrumentation*, 9, January 2014.
- [ANSYS(2016)] ANSYS. ANSYS - Structural Simulations. <http://www.ansys.com>, 2016. [Online; accessed 2016-02-20].
- [Biagi(2012)] S. Biagi. Magboltz - transport of electrons in gas mixtures. <http://consult.cern.ch/writeup/magboltz/>, Mai 2012.
- [Bichsel(1988)] H. Bichsel. Stragglings in thin silicon detectors. *Rev. Mod. Phys.*, 60:663–699, Jul 1988.
- [Bortfeldt et al.(2016)] J. Bortfeldt, O. Biebel, B. M. Flierl, R. Hertenberger, F. Klitzner, P. J. Lösel, L. Magallanes, R. Müller, K. Parodi, T. Schlüter, B. Voss, and A. Zibell. Low material budgeted floating strip Micromegas for ion transmission radiography. *The 14th Vienne Conference on Instrumentation*, 2016.
- [CAEN A1535dn(2015)] CAEN A1535dn. CAEN - Tools for Discovery - A1535dn 12/24 Channel 3.5 kV/3 mA (8 W) Common Floating Return Boards. <http://www.caen.it/>, 2015.
- [CAEN A1821(2015)] CAEN A1821. CAEN - Tools for Discovery - A1821 12 Channel 3 kV, 200/20 A Common Ground Dual Range Board. <http://www.caen.it/>, 2015.
- [CAEN SY5527(2015)] CAEN SY5527. CAEN - Tools for Discovery - SY5527 Universal Multichannel Power Supply System . <http://www.caen.it/>, 2015.
- [Ellis et al.(1976)] H.W. Ellis, R.Y. Pai, and E.W. McDaniel. Transport properties of gaseous ions over a wide energy range. *Atomic Data and Nuclear Data Tables*, 17:177–210, 1976.
- [French et al.(2001)] M. J. French, L. L. Jones, Q. R. Morrissey, A. Neviani, R. Turchetta, J. R. Fulcher, G. Hall, E. Noah, M. Raymond, G. Cervelli, P. Moreira, and G. Marseguerra. Design and results from the APV25, a deep sub-micron CMOS front-end chip for the CMS tracker. *Nucl. Instrum. Methods Phys. Res., A*, 466(2): 359–65, 2001.
- [Giomataris et al.(1996)] Y. Giomataris, Ph. Rebourgeard, J. P. Robert, and G. Charpak. Micromegas: a high-granularity position-sensitive gaseous detector for high particle-flux environments. *Nucl. Instrum. Methods Phys. Res., A*, 376(1046):29–35, 6 1996.

- [Groom(1993)] Don Groom. Energy loss in matter by heavy particles. [http://www.usc.es/gir/docencia\\_files/dosimetria/notas\\_pdg.pdf](http://www.usc.es/gir/docencia_files/dosimetria/notas_pdg.pdf), 1993.
- [Gruppen and Shwartz(2008)] C. Gruppen and B. Shwartz. Particle Detectors. *Cambridge University Press*, 2008.
- [Hamamatsu H7546B-300(2007)] Hamamatsu H7546B-300. Multianode Photomultiplier Tube H7546B-300. <http://www.hamamatsu.com>, 2007.
- [Hamamatsu R4124(2007)] Hamamatsu R4124. Photomultiplier Tube R4124. <http://www.hamamatsu.com>, 2007.
- [Horvat(2005)] S. Horvat. *Study of the Higgs Discovery Potential in the Process  $pp \rightarrow H \rightarrow 4\mu$* . PhD thesis, University of Zagreb, 2005.
- [J. Bortfeldt(2010)] J. Bortfeldt. Development of Micro - Pattern Gaseous Detectors - Micromegas. Diploma thesis, Ludwig-Maximilians-Universität München, 2010.
- [J.Bortfeldt(2014)] J.Bortfeldt. *Development of Floating Strip Micromegas Detectors*. PhD thesis, Ludwig-Maximilians-Universität München, 2014.
- [Jones(2001)] L. Jones. *APV25-S1 User Guide*, September 2001.
- [Kleinknecht(1992)] K. Kleinknecht. Detektoren für Teilchenstrahlung. *Teubner Stuttgart*, 1992.
- [König(2015)] V. König. Zusammenbau und Inbetriebnahme von dünnen Floating Strip Micromegas mit zweidimensionaler Auslesestruktur. Bachelor's thesis, Ludwig-Maximilians-Universität München, 2015.
- [Lin et al.(2014)] Tai-Hua Lin, Andreas Döder, Matthias Schott, Chrysostomos Valderanis, Laura Wehner, and Robert Westenberger. Signal characteristics of a resistive-strip micromegas detector with an integrated two-dimensional readout. *Nuclear Instruments and Methods in Physics Research Section A: Accelerators, Spectrometers, Detectors and Associated Equipment*, 767:281–288, 2014.
- [Lösel(2013)] P. Lösel. Performance Studies of Large Size Micromegas Detectors. Master's thesis, Ludwig-Maximilians-Universität München, 2013.
- [Lösel et al.(2015)] P. Lösel, O. Biebel, J. Bortfeldt, R. Hertenberger, R. Müller, and A. Zibell. Performance of a 1 m<sup>2</sup> Micromegas Detector Using Argon and Neon based Drift Gases. *PoS, EPS-HEP2015:232*, 2015.
- [LTSpice(2014)] LTSpice. Linear Technology. <http://www.linear.com/designtools/software/>, 2014. [Online; accessed 2016-02-23].
- [Moll(2013)] S. Moll. Entladungsstudien an Micromegas-Teilchendetektoren. Diploma thesis, Ludwig-Maximilians-Universität München, 2013.
- [Ntekas(2013)] Konstantinos Ntekas. Performance of Micromegas Detectors for Inclined Tracks and in Magnetic Fields. <http://indico.cern.ch/event/229907/session/7/>, 2013.

- [Nygren(1974)] D. R. Nygren. The Time-Projection Chamber - A new  $4\pi$  detector for charged particles. *PEP-144*, 1974.
- [Olive et al.(2014a)] K. A. Olive et al. Review of Particle Physics, 2014-2015. Review of Particle Properties. *Chin. Phys. C*, 38(arXiv:1412.1408):090001. 15 p, 2014a.
- [Olive et al.(2014b)] K.A. Olive et al. (Particle Data Group). *Chinese Physics*, C38(090001), 2014b.
- [Panasonic(2015)] Panasonic. Panasonic Electric Works AXK5SA3277YG CONN SOCKET BRD/BRD .5MM 130POS . <https://www.panasonic-electric-works.com/eu/>, 2015.
- [Poskus(2010)] Andrius Poskus. Energy Loss Of Alpha Particles In Gases. [http://web.vu.lt/ff/a.poskus/files/2013/06/ENP\\_No02.pdf](http://web.vu.lt/ff/a.poskus/files/2013/06/ENP_No02.pdf), 2010.
- [R. K. Carnegie(2005)] M. S. Dixit J. Dubeau D. Karlen J.-P. Martin H. Mes K. Sachs R. K. Carnegie. Resolution studies of cosmic-ray tracks in a TPC with GEM readout. *Nucl. Instrum. Methods Phys. Res., A*, 2005.
- [Raether(1964)] H. Raether. *Electron Avalanches and Breakdown in Gases*. Butterworths advanced physics series. Butterworths, 1964.
- [Raizer(1991)] Y. P. Raizer. *Gas Discharge Physics*. Springer, 1991.
- [RD51(2010)] RD51. What is SRS - RD 51 Scalable Readout System. [indico.cern.ch/event/77597/contribution/1/](http://indico.cern.ch/event/77597/contribution/1/), 2010.
- [Rinaldi(2011)] I. Rinaldi. *Investigation of novel imaging methods using therapeutic ion beams*. PhD thesis, Ruperto-Carola University of Heidelberg, 2011.
- [Schneider et al.(2004)] U. Schneider, J. Besserer, P. Pемler, M. Dellert, M. Moosburger, E. Pedroni, and B. Kaser-Hotz. First proton radiography of an animal patient. *Medical Physics*, 31(1046), 2004.
- [Sternheimer et al.(1984)] R.M. Sternheimer, M.J. Berger, and S.M. Seltzer. Density effect for the ionization loss of charged particles in various substances. *Atomic Data and Nuclear Data Tables*, 30(2):261–271, March 1984.
- [Veenhof(2010)] R. Veenhof. Garfield - simulation of gaseous detectors. <http://garfield.web.cern.ch/garfield/>, Sep 2010.
- [Zibell(2010)] A. Zibell. Pulsformanalyse an MDT-Myondetektoren. Diploma thesis, Ludwig-Maximilians-Universität München, 2010.
- [Ziegler et al.(2010)] J. F. Ziegler, M. D. Ziegler, and J. P. Biersack. SRIM - The stopping and range of ions in matter (2010). *Nucl. Instrum. Methods Phys., B*, 268:1818–1823, June 2010.

# Appendix A

## Tracking Methods

### A.1 $\chi^2$ -Minimization

The fit of a two parameter function, such as a straight line  $x(z) = az + b$ , to a set of data points  $(z_i, x_i)$ ,  $i = 1, \dots, n$  can be performed analytically [Horvat, 2005].

The parameters  $a$  and  $b$  can be determined by minimizing the  $\chi^2$  function

$$\chi^2 = \sum_{i=1}^n w_i (x_i - az_i - b)^2, \quad (\text{A.1})$$

where  $w_i$  is the weight of a given data point. The weights for the track fit in a Microegas reference system are given by an estimate of the spatial resolution  $\tilde{\sigma}_i$ , with  $w_i = 1/\tilde{\sigma}_i^2$ . Thus,

$$\chi^2 = \sum_{i=1}^n \frac{1}{\tilde{\sigma}_i^2} (x_i - az_i - b)^2. \quad (\text{A.2})$$

From the minimization requirements  $\frac{\delta\chi^2}{\delta a} = 0$  and  $\frac{\delta\chi^2}{\delta b} = 0$  follows

$$\begin{aligned} \chi^2 &= \sum_{i=1}^n \frac{z_i}{\tilde{\sigma}_i^2} (x_i - az_i - b), \\ \chi^2 &= \sum_{i=1}^n \frac{1}{\tilde{\sigma}_i^2} (x_i - az_i - b). \end{aligned} \quad (\text{A.3})$$

We can now define parameters  $g_1$ ,  $g_2$  and  $\Lambda_{11}$ ,  $\Lambda_{12}$  and  $\Lambda_{22}$  with

$$\begin{aligned} (g_1, g_2) &= \sum_{i=1}^n \frac{x_i(1, z_i)}{\tilde{\sigma}_i^2}, \\ (\Lambda_{11}, \Lambda_{12}, \Lambda_{22}) &= \sum_{i=1}^n \frac{x_i(1, z_i, z_i^2)}{\tilde{\sigma}_i^2}. \end{aligned} \quad (\text{A.4})$$

Inserting Eq. A.4 into Eq. A.3 gives

$$\begin{aligned} \Lambda_{11}b + \Lambda_{12}a &= g_1, \\ \Lambda_{12}b + \Lambda_{22}a &= g_2. \end{aligned} \quad (\text{A.5})$$

Slope  $a$  and intersect  $b$  of the track can now be determined by applying Cramers's rule, yielding

$$\begin{aligned} a &= \frac{\Lambda_{11}g_2 - \Lambda_{12}g_1}{D} \\ &\text{and} \\ b &= \frac{\Lambda_{22}g_1 - \Lambda_{12}g_2}{D} \\ &\text{with} \\ D &= \Lambda_{11}\Lambda_{22} - \Lambda_{12}^2 . \end{aligned} \tag{A.6}$$

The uncertainty of the track fit  $\sigma_{\text{track}}$  can be determined at each detector position  $(z_i, x_i)$ , e.g. if needing it for the determination of the spatial resolution as described in section 4.7.3, given by

$$\sigma_{\text{track}}^2(z_i, x_i) = \text{Var}(b) + 2z_i \text{Covar}(b, a) + z_i^2 \text{Var}(a) . \tag{A.7}$$

For an approximation of the true spatial resolution  $\sigma_i$  with the estimate  $\tilde{\sigma}_i$  this leads to

$$\sigma_{\text{track}}^2(z_i, x_i) = \frac{1}{D} [\Lambda_{22} - 2z_i\Lambda_{12} + z_i^2\Lambda_{11}] . \tag{A.8}$$

A detailed derivation of the variance and covariance can be found in [Horvat, 2005].

## A.2 Kalman Filter Based Track Reconstruction

Consider a detector system consisting of  $n$  detector layers with registered hit positions  $\vec{x}_i(x_i, y_i, z_i)$ , for layer  $i = 0, \dots, n$ . The hits are reconstructed in the  $x - y$  detector plane, with  $z$  defining the detector position in the perpendicular direction. Consider the hit  $x_i$  measured by detector layer  $i$  in  $x$ -direction. The estimation of the local track at layer  $i$  can thus be described by the so called state estimation vector  $\vec{x}_i$  and the estimate covariance error matrix  $\mathbf{C}_i$ , with

$$\vec{x}_i = \begin{bmatrix} x_i \\ y_i \\ m_{x,i} \\ m_{y,i} \end{bmatrix} \quad \text{and} \quad \mathbf{C}_i = \begin{bmatrix} \text{var}(x) & \text{covar}(x, y) & \text{covar}(x, m_x) & \text{covar}(x, m_y) \\ \text{covar}(y, x) & \text{var}(y) & \text{covar}(y, m_x) & \text{covar}(y, m_y) \\ \text{covar}(m_x, x) & \text{covar}(m_x, y) & \text{var}(m_x) & \text{covar}(m_x, m_y) \\ \text{covar}(m_y, x) & \text{covar}(m_y, y) & \text{covar}(m_y, m_x) & \text{var}(m_y) \end{bmatrix} , \tag{A.9}$$

where  $m_{x,i}, m_{y,i}$  describes the slope of the track in the  $x$ - $z$ - and  $y$ - $z$  plane at detector position  $z_i$  of layer  $i$ , respectively. The  $4 \times 4$  error covariance matrix  $\mathbf{C}_i$  of the two independent variables  $x_i$  and  $y_i$  and their respective slopes describes the variances on the diagonal part of the matrix, whereas the off-diagonal encode correlations between the variables.

In the next step, the track information of layer  $i$ , encoded in the state estimation vector  $\vec{x}_i$ , is extrapolated to the next layer  $i + 1$  via multiplication with the transport matrix

$\mathbf{J}_{i+1}$ , thus yielding the state estimation vector  $\vec{x}_{i+1}$  with

$$\begin{aligned}
\vec{x}_{i+1} &= \mathbf{J}_{i+1} \cdot \vec{x}_i \\
&= \begin{bmatrix} 1 & 0 & \Delta z_{i,i+1} & 0 \\ 0 & 1 & 0 & \Delta z_{i,i+1} \\ 0 & 0 & 1 & 0 \\ 0 & 0 & 0 & 1 \end{bmatrix} \cdot \begin{bmatrix} x_i \\ y_i \\ m_{x,i} \\ m_{y,i} \end{bmatrix} \\
&= \begin{bmatrix} x_i + m_{x,i} \cdot \Delta z_{i,i+1} \\ y_i + m_{y,i} \cdot \Delta z_{i,i+1} \\ m_{x,i} \\ m_{y,i} \end{bmatrix} = \begin{bmatrix} x_{i+1} \\ y_{i+1} \\ m_{x,i} \\ m_{y,i} \end{bmatrix}
\end{aligned} \tag{A.10}$$

where  $\Delta z_{i,i+1} = z_{i+1} - z_i$  describes the distance between detector layers  $i$  and  $i + 1$ . The covariance matrix  $\mathbf{C}_{i+1}$  after transport to layer  $i + 1$  is then given by

$$\mathbf{C}_{i+1} = \mathbf{J}_{i+1} \cdot \mathbf{C}_i \cdot \mathbf{J}_{i+1}^\top, \tag{A.11}$$

defining the errors e.g. uncertainties at state  $i + 1$ . The residual  $\Delta_{\text{res}}^{i+1}$  between the measured hit  $x_{i+1,\text{meas}}$  in layer  $i + 1$  and the predicted hit  $x_{i+1}$  of Eq. (A.10) can thus be calculated:

$$\Delta_{\text{res } x,y}^{i+1} = (x_{i+1,\text{meas}}, y_{i+1,\text{meas}}) - \mathbf{H}^\top \cdot \vec{x}_{i+1} \tag{A.12}$$

with

$$\mathbf{H} = \begin{bmatrix} \cos(\alpha) \\ \sin(\alpha) \\ 0 \\ 0 \end{bmatrix} \tag{A.13}$$

describing the orientation of the measured hit, either in  $x$ - or  $y$ -direction, via the angle  $\alpha$  between the  $y$ -axis and the orientation of the measured strip. For a measured hit i.e. in the  $x$  direction,  $x_{i+1,\text{meas}}$ , the resulting angle  $\alpha=0$ , as the  $x$ -strips are always oriented in  $y$ -direction, thus

$$\begin{aligned}
\Delta_{\text{res } x}^{i+1} &= x_{i+1,\text{meas}} - \mathbf{H}^\top \cdot \vec{x}_{i+1} \\
&= x_{i+1,\text{meas}} - [1 \ 0 \ 0 \ 0] \cdot \begin{bmatrix} x_{i+1} \\ y_{i+1} \\ m_{x,i} \\ m_{y,i} \end{bmatrix} \\
&= x_{i+1,\text{meas}} - x_{i+1}.
\end{aligned} \tag{A.14}$$

The weight of the measured hit, used for fitting the track, is defined as the inverse sum of an estimate of the spatial resolution  $\sigma_{i+1}$  at layer  $i + 1$  and the covariance matrix  $\mathbf{C}_{i+1}$ , translated on the respective direction via multiplication with the  $1 \times 4$  rotation matrix  $\mathbf{H}$ , as defined in Eq. (A.13), yielding the weight  $w_{i+1}$

$$w_{i+1} = (\sigma_{i+1}^2 + \mathbf{H}^\top \mathbf{C}_{i+1} \mathbf{H})^{-1} \tag{A.15}$$

The update  $\vec{u}_{i+1}$  of the state estimate vector  $\vec{x}_{i+1}$ , after the measurement in layer  $i + 1$ , is then given by

$$\vec{u}_{i+1} = w_{i+1} \cdot \Delta_{\text{res } x,y}^{i+1} \cdot \mathbf{C}_{i+1} \cdot \mathbf{H}, \tag{A.16}$$

thus defining the updated state for layer  $i + 1$

$$\vec{x}_{i+1} = \vec{x}_{i+1} + \vec{u}_{i+1} \quad (\text{A.17})$$

and the updated estimate covariance matrix  $\mathbf{C}_{i+1}$

$$\mathbf{C}_{i+1} = \mathbf{C}_{i+1} - \mathbf{C}_{i+1} \cdot \mathbf{H} \cdot w_{i+1} \cdot \mathbf{H}^\top \cdot \mathbf{C}_{i+1} . \quad (\text{A.18})$$

$\chi_{i+1}^2$  can now be calculated after the measurement update in layer  $i + 1$ , following

$$\chi_{i+1}^2 = \frac{(\Delta_{\text{res,new}}^{i+1})^2}{v_{i+1}} , \quad (\text{A.19})$$

where

$$\Delta_{\text{res,new}}^{i+1} = \Delta_{\text{res x,y}}^{i+1} - \mathbf{H}^\top \cdot \vec{u}_{i+1} \quad (\text{A.20})$$

describes the new residual after the measurement update and

$$v_{i+1} = \sigma_{i+1}^2 - \mathbf{H}^\top \mathbf{C}_{i+1} \mathbf{H} \quad (\text{A.21})$$

includes the updated error information of the estimate covariance matrix  $\mathbf{C}_{i+1}$ .

For a calculated value of  $\chi_{i+1}^2 > 50$ , the measured hit of layer  $i + 1$  is not accepted for track fitting, marking the used as bad. The algorithm now searches for a matching cluster in layer  $i + 1$ , until  $\chi_{i+1}^2 < 50$ . If no matching cluster is found, the algorithm jumps back to layer  $i$  and searches for a matching cluster in this layer.

Assuming the algorithm converges after a finite number of steps reaching the last layer  $i = n$ , then the information of the resulting found track is saved in the state estimation vector  $\vec{x}_n^{\text{for}}$  and the corresponding estimate covariance matrix  $\mathbf{C}_n^{\text{for}}$ , respectively. *for* denotes that the algorithm performed the track finding procedure in the *forward* direction, searching from layer 0 to layer n, thus increasing the number of layer with each step.

In a next step, the algorithm repeats the track finding process, now starting in the last layer  $n$ , extrapolating the hit in the reverse direction into layer  $n - 1$ . The track parameters are saved in the state  $\vec{x}_0^{\text{rev}}$  and  $\mathbf{C}_0^{\text{rev}}$ , after completed search in the *reverse* direction, arriving at layer 0.

In a last step, the final track parameters are determined from the average of the reverse and forward search, yielding  $\mathbf{C}_i^{\text{mean}}$  and  $\vec{x}_i^{\text{mean}}$  at layer  $i$  with

$$\mathbf{C}_i^{\text{mean}} = \left( (\mathbf{C}_i^{\text{for}})^{-1} + (\mathbf{C}_i^{\text{rev}})^{-1} \right)^{-1} \quad (\text{A.22})$$

and

$$\vec{x}_i^{\text{mean}} = \mathbf{C}_i^{\text{mean}} \cdot \left( (\mathbf{C}_i^{\text{for}})^{-1} \cdot \vec{x}_i^{\text{for}} + (\mathbf{C}_i^{\text{rev}})^{-1} \cdot \vec{x}_i^{\text{rev}} \right)^{-1} . \quad (\text{A.23})$$

As the algorithm performs the track search consecutively at each detector position  $z_i$ , it is possible to include uncertainties of the track caused by multiple scattering of particles within layer  $i$ . The mean scattering angle  $d\Theta$  thus needs to be calculated as described in section 2.3, Eq. (2.10). After the measurement update of the estimate covariance matrix  $\mathbf{C}_i$  in layer  $i$ , the scattering angle  $d\Theta$  is then quadratically added to the variances of both track slopes  $m_x$  and  $m_y$ , encoded on the diagonal elements of  $\mathbf{C}_i$  in the 2nd and 3rd column, see Eq. (A.10). As a consequence, the track determined by the algorithm needs not necessarily to be straight. This allows for example comparing tracklets before and after a certain  $z$  position, as described in section 6.5.2.

# Acknowledgments

At this point, I would like to thank the people that supported me during the last year. I am truly sorry, if I missed anyone.

First of all, I would like to thank my supervisor Dr. Jonathan Bortfeldt. Without his excellent advice, continuous support and comments, this thesis would be much thinner.

I want to thank Prof. Dr. Otmar Biebel for giving me the opportunity to write this thesis. His door was always open for questions despite his many other, comprehensive tasks.

I want to thank Dr. Ralf Hertenberger for his support and fruitful advices.

I would like to thank the whole hardware group, Bernhard Flierl, Maximilian Hermann, Philipp Lösel, Ralph Müller, Chrysostomos Valderanis and Andre Zibell for the helpful discussions and the very agreeable atmosphere in the group.

Also thanks to Maximilian Dornieden, for supporting me with helpful comments about the English grammar.

Above all, I want to thank my family and friends for their continuous support during the last year and, especially, during the last weeks of this thesis. Thanks to my girlfriend Cathrin Grolig enduring my self, even when i was stressed and didn't have alot time for her.



# Declaration of academic integrity

I hereby declare, that this thesis is my own work and that I have not used any sources and aids other than those stated in the thesis.

Felix Klitzner

Munich, March 16, 2016